Studies of the physics and chemistry occurring in shock waves associated with regions of star formation

McCoey, Carolyn

Studies of the Physics and Chemistry occurring in Shock Waves associated with Regions of Star Formation

Carolyn M^{c}Coey

A thesis submitted in fulfilment of the
requirements for the degree of
Doctor of Philosophy

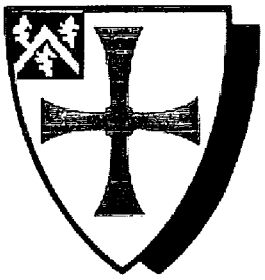

The University of Durham
Department of Physics
2004

Studies of the Physics and Chemistry occurring in Shock waves associated with Regions of Star Formation

Carolyn M^{c}Coey

Abstract

Herbig-Haro (HH) objects, which are observed in molecular, ionic and atomic line emission, are shocked regions within outflows associated with low mass star formation. A 1-D, planar shock code, MHD_VODE, which incorporates an extensive chemistry and calculates the population distributions of various important species throughout the shock wave, is used to model the H_2, [Fe II] and [C I] line intensities observed from 14 HH objects. It is found that models of non-equilibrium J-type shocks with magnetic precursors are required to reproduce the observed H_2 emission. These models have shock velocities in the range of 30–50 km s^{-1}, pre-shock densities of typically 10^4 cm^{-3} and ages of the order of a few hundred years. However, such models predict a low electron density and are not able to reproduce the observed [Fe II] and [C I] emission. The ionization of H following dissociation of H_2 in a J-type shock results in weak H_2 emission but can produce the ionization fraction required for the atomic and ionic forbidden line emission. Thus, an elementary representation of a bow shock, consisting of a J-type shock with a magnetic precursor and a J-type shock, respectively, proves successful in reproducing both the H_2 and [Fe II] emission. It is necessary to assume that Fe has previously been eroded from dust grains, probably by the earlier passage of a C-type shock wave. These findings are consistent with observations, which have suggested that HH outflows are episodic phenomena and that the emission from HH objects arises in bow shocks.

Contents

List of Figures

Declaration

I confirm that no part of the material offered has previously been submitted by me for a degree in this or in any other University. If material has been generated through joint work, my independent contribution has been clearly indicated. In all other cases material from the work of others has been acknowledged and quotations and paraphrases suitability indicated.

Carolyn M^{c}Coey
Durham, 1st June 2004

Acknowledgements

The work presented in this Thesis was carried out in collaboration with D. R. Flower, T. Giannini, B. Nisini, A. Caratti o Garatti and D. Lorenzetti. I thank David Flower, in particular, for his advice, tutition and time. Observations were performed and reduced by T. Giannini, B. Nisini, A. Caratti o Garatti and D. Lorenzetti. Images of the modelled regions were kindly supplied by Teresa Giannini, who also supplied the (otherwise unpublished) semi-empirical analysis of HH99B0. MHD_VODE is an on-going group project. However, Jacques Le Bourlot, Guillaume Pineau des Forêts and Sylvie Cabrit (and their students) have made significant contributions to the code in recent times. Finally, it is a pleasure to thank Malcolm Walmsley, for helpful comments regarding Sagittarius B2, and Michael Balogh, for extensive reading and comments on the text.

Chapter 1

Introduction

Stars form within dusty, dense molecular clouds in the interstellar medium (ISM). The process is characterised by accretion from a circumstellar disk onto the proto-star and by bipolar outflows of matter into the surrounding region. The process by which stars form is still uncertain but we can hope to improve our understanding by studying phenomena associated with star formation, such as outflows. In the case of stars that will evolve to become high mass ($\gg 1$ $M_\odot$), a stellar wind and an ultraviolet (UV) radiation field quickly develops and destroys the outflow. For this reason, outflows associated with high mass star formation are not easily observed. On the other hand, low mass (≈ 1 $M_\odot$) stars evolve more slowly so their outflows remain observable for timescales of 10^3–10^5 years (Bachiller, 1996) and are not complicated by the effects of a strong UV field. Therefore, outflows associated with low mass star formation provide an excellent opportunity to study the earliest stages of stellar evolution.

Strong evidence for the involvement of the accretion disk in the production of outflows comes from two observed characteristics of low mass star forming systems: excess emission from accretion is always associated with outflow activity; and the energy carried away by the outflow is comparable with that associated with the energy released by accretion of matter from the circumstellar disk (Cabrit & Raga, 2000; Hartigan et al., 1995). It is thought that the processes

of accretion and ejection (outflow) are interdependent and self-regulating. The formation of an accretion disk provides a mechanism by which to store energy and angular momentum during the early evolution of a star, while the outflow removes excess energy and momentum. It has become generally accepted that an interaction between the accretion disk and the magnetic field threaded through the disk is responsible for the launch of outflows. However, the details of the formation process of the outflow remain uncertain.

Outflows are generally slow, with bulk velocities of tens of kilometres per second, and poorly collimated. Jets, which are a phenomena that are strongly related to outflows, are faster (bulk velocities of typically hundreds of kilometres per second) and highly collimated. Jets and outflows, and the shocks they produce in the ambient medium, are ubiquitous phenomena that are observed on all scales within the Universe. They are associated with a diverse number of objects ranging from active galactic nuclei (AGN) through black hole X-ray transients, low- and high-mass X-ray binaries (possibly in the production of gamma ray bursts) and protoplanetary nebulae to low- and high-mass star formation. The physical conditions in all of these systems are very different and likewise the outflows associated with them have a wide range of characteristics. For example, the jets associated with AGN are highly relativistic, while the jets associated with low mass star formation, which are the simplest of the above phenomena, have much lower velocities of typically hundreds of kilometres per second. As with low mass stars, the mechanism responsible for driving these jets and outflows is still poorly understood. However, it is likely to be related to the accretion of matter and to the associated magnetic fields, which play a role in every system. It is possible that the same fundamental physics underlies all of these processes. Therefore, by studying and modelling outflows associated with low mass star formation, we may improve our understanding of both the dynamics of outflows and the processes occurring within them and the mechanism by which outflows, on all scales, form.

The study of outflows associated with low mass star formation (Herbig-Haro

outflows) have tended to investigate three aspects of the outflows: their morphology, their kinematics and their spectrophotometry. From the results of these studies, which shall be described in the next two Sections, it has become apparent that shocks are a common feature of these outflows. These shocked regions have a complex morphology that require a magnetohydrodynamical solution (MHD, Chapter 2) and, as shall be described in Chapter 3, drive a variety of chemical reactions that do not occur in quiescent environments. Detailed modelling of the emission from outflows, therefore, is a useful tool with which to place strong constraints on the molecular dynamics and MHD in star forming regions. In this Thesis, shock models, which are described in Chapter 4, are used to predict the H_2, [Fe II] and [C I] emission observed in 14 shocked regions in Herbig-Haro outflows (Chapter 5).

1.1 Characteristics of Herbig-Haro outflows

The study of outflows associated with low mass star formation began with the observations of Herbig (1951) and Haro (1952) of small nebulosities, with peculiar emission line optical spectra and high proper motions, in regions of star formation. These nebulosities, which have become known as Herbig-Haro (HH) objects, are now recognised as the manifestations of outflow activity from the forming star. The outflows are observed over a wide range of wavelengths, from the ultraviolet (UV) to the radio, which may highlight different components of the outflow. Bachiller (1996) gave a good review of the components of an outflow and of the HH objects themselves, which were reviewed by Reipurth & Bally (2001). We shall now consider first the outflow, then the HH objects.

1.1.1 Components of the outflow

Most of the mass in an outflow is contained in a relatively low velocity ($<$ 30 km s^{-1}, e.g., Bally & Lada, 1983), usually bipolar component consisting of molecular gas and, in particular, CO. This so-called 'CO outflow' is generally

poorly collimated material that is thought to have been swept up by an underlying jet, forming two cavities (Snell et al., 1980). Radio emission of CO is observed from the irregular lobes and incomplete shells surrounding these cavities. This molecular component is found around Young Stellar Objects (YSOs) of all masses and luminosities and so suggests a common formation mechanism. These outflows are observed to be time variable both in the radio emission and the optical. For example, L1551 (the prototypical CO outflow) shows evidence for four separate mass loss events separated by approximately 10^4 yr (Bachiller et al., 1994). Variability is also observed in the same outflow at visible wavelengths on timescales of 10^2–10^3 yr (Neckel & Staude, 1987; Campbell et al., 1988; Davis et al., 1995).

Another component of the HH outflow is a highly collimated jet (called an 'HH jet') observed at optical, radio and infrared (IR) wavelengths in neutral and ionized species, such as [O I], [C I], [S II], and [Fe II], and also molecular species such as H_2, NH_3 and H_3O^+. These jets consist of strings of HH objects and often consist of multiple bow shocks. The strongest jets, for example HH34 (Chernin & Masson, 1995), HH111 (Reipurth & Cernicharo, 1995), are associated with the weakest CO outflows. Conversely systems with strong CO outflows often show no sign of a jet or the jet can be observed only in the IR (Reipurth & Bally, 2001). This implies that in the latter case the jet is completely obscured. HH objects and jets are the subject of this Thesis and will be discussed in more detail in Section 1.1.2 below.

The HH jets are often observed to have the same orientation and length as the low velocity CO outflow, which is much wider than the HH jet. This has led to suggestions of a "unified theory" in which the CO outflow is entrained by bow shocks associated with the HH jet. Some evidence for this comes from a comparison of the morphologies of the CO emission and the terminating bow shock in some objects (e.g., L1157 Umemoto et al., 1992; Gueth et al., 1997). Proper motions indicate that the outflow velocities of HH objects gradually decrease with distance from the source, and this is probably best explained

as a loss of momentum due to entrainment of the ambient medium (Cabrit & Raga, 2000).

Similar jets are observed in only molecular emission lines, in particular those of CO, and are known as CO "bullets". Both HH objects and molecular "bullets" show a marked symmetry in their position and velocities with respect the outflow source, which suggests that they are caused by periodic bursts of matter from the star rather than the forming as a result of instabilities within the jet. Specifically, the inferred time between successive CO bullets (and HH objects) is typically 10^3 years (Reipurth, 1989; Bachiller, 1996). The similarity seen between characteristics of the HH objects and the molecular "bullets" is striking.

1.1.2 HH objects and jets

Morphology and dynamics

HH objects are small (20″-30″) nebulosities around regions of low mass star formation. Their shapes are generally amorphous but some objects (or a series of HH objects) form a bow shock shape, while others are elongated in the direction of the flow. They are often found in pairs to either side of a forming star. Alternatively, they are seen to form linear or gently wiggling chains, which may be connected by fainter emission and contain other compact knots. Together, these form the systems known as HH jets. These jets are highly collimated with length-to-width ratios of 10:1 or more and are parsec scale in length (Bally & Devine, 1994). The typical dynamical lifetimes of 10^4 years of the HH jets contrasts with the observed variability within them on timescales of 10^3 years. It seems likely, therefore, that the HH objects are not observed at equilibrium conditions (Pineau des Forêts et al., 1997; Smith & Mac Low, 1997; Chiéze et al., 1998).

HH objects show low-excitation spectra that indicate shock velocities of a few tens of kilometres per second at most. This appears at odds with the

supersonic bulk velocities of the jets, which are several hundreds of kilometre per second. Since the HH objects in the jets also show large proper motions, this invalidates an early idea that they form as highly oblique (and hence weak and stationary) recollimation shocks (e.g., Falle et al., 1987; Canto et al., 1989). There are three recently popular theories for the formation of HH objects within the jets. The first is that the outflow overruns and shocks clumps of gas in the ambient medium (Schwartz, 1978); however, this now seems unlikely given the regular spatial distribution of the HH objects along the jet axis. Another possibility is that instabilities [either hydrodynamic (e.g., Buehrke et al., 1988; Micono et al., 1998), magnetohydrodynamic (e.g., Stone & Hardee, 2000) or thermal (e.g., de Gouveia dal Pino & Opher, 1990)] in the jet excite a series of oblique travelling shocks. Finally, clumps of matter ejected from the forming star at different velocities can collide with each other to form an internal working surface (Raga et al., 1990). The fact that these HH jets are observed to contain multiple groups of HH objects is evidence for variability in their ejection velocities, ejection directions, and possibly mass loss rates and degree of collimation (e.g., Noriega-Crespo et al., 2002).

The most energetic and violent shock in the HH outflow, which is termed the "terminal working surface", occurs when the supersonic flow slams directly into the quiescent ambient medium. Both internal and terminal working surfaces consist of forward and reverse shocks, such as those observed in HH2 (Bally et al., 2002). The forward shock accelerates the material with which it collides, while the reverse shock, which is also known as a Mach disk, decelerates the supersonic flow (Hartigan et al., 1989). The forward shock may take the form of a bow shock, as in HH111, in which the surface is normal to the direction of the flow axis but becomes increasingly oblique away from the axis in the wings or wake. Proper motion studies of bow shocks have indeed shown that this is the case (Reipurth & Bally, 2001). A simple prediction for symmetric bow shocks is that high excitation lines should dominate at the apex and lower excitation lines should be strong along the wings; and indeed, high resolution images of HH objects with bow shock morphologies have shown that [Fe II]

(a high excitation species) emission arises in the apex, while lower excitation H_2 is seen in the wings. Some good examples of such objects are HH99 (Davis et al., 1999) and HH7 (Smith et al., 2003).

Line emission in the infrared

HH objects emit from the UV to the radio; the ability of IR transitions to probe regions of high extinction makes them particularly useful diagnostic tools. For example, some shocked knots (also known as condensations) are observed only at IR wavelengths. It has been suggested that these are regions where the extinction is particularly high. Although this possibility has yet to be formally established, it is supported by the fact that HH jets are observed to have highly variable extinction (Hartmann & Raymond, 1984).

Important line emission in the IR arises from transitions due to molecular, atomic and ionic species, such as H_2, [C I] and [Fe II]. IR Ro-vibrational transitions of H_2 are important tracers of HH outflows and are observed both in HH objects themselves and in a surrounding "cocoon" of gas between the HH jet and the CO outflow, which has been interpreted as the mixing layer where ambient gas is entrained (Davis & Eisloeffel, 1995). The 2.122 μm v=1-0 S(1) and 2.247 μm v=2-1 S(1) transitions are usually the strongest lines observed (the 2.122 μm transition is often of comparable strength to the Hα line in the same object) and are frequently used for mapping (e.g., HH111 Gredel & Reipurth, 1993, 1994; Davis et al., 1994). The value of H_2 as an observational diagnostic comes particularly from two features of its emission. The first is that it is a good indicator of shock activity because the first vibrational level is about 6000 K above the ground state; therefore, H_2 molecules become collisionally excited in dense regions at temperatures of few thousand kelvin. Secondly, because the transitions occur at IR wavelengths they are less affected by dust, allowing observations to probe deeper into obscured regions that are not observable at visible wavelengths.

Fe, and other elements that form refractory material, are depleted from the gas in the ISM on to solid dust grains (see Chapter 3 for further details). Therefore, the presence of [Fe II] emission is particularly interesting as it implies that dust grains have been eroded, probably by the passage of a shock wave (May et al., 2000). Naively, one might expect that strong shocks (characterised by higher ionization) would result in a higher gas phase abundance of Fe than weak shocks. However, studies of gas phase metal abundances in strong and weak shocks indicated a similar (and high) abundance of Fe (Beck-Winchatz et al., 1994, 1996; Böhm & Matt, 2001). One possible interpretation of this is that all HH objects undergo a strong shock at some point in their evolution, possibly during the launching of the jet.

As shall be discussed in Chapter 3, the rich line spectrum of [Fe II] provides an excellent tool with which to investigate the ionized component of shocked gas in HH objects. Almost all of the observed IR [Fe II] lines arise from four closely spaced levels in the a^4D term, making the lines insensitive to temperature, but a useful diagnostic of density. Furthermore, [Fe II] lines have a larger critical density than those of [S II] and [O III], which are observed at visible wavelengths, so [Fe II] lines allow us to probe more dense and more obscured regions of the outflows (Gredel, 1994, 1996). Indeed, the extinctions derived from [Fe II] lines indicate that the [Fe II] emission arises in regions that suffer from, typically, 1–2 magnitudes more extinction than the H_2 emission, which itself arises in more obscured regions than the optical emission (e.g., Nisini et al., 2002).

1.2 Previous work

The recognition, after studies of molecular line widths and shifts, that shocks play a fundamental role in producing HH objects (Schwartz, 1978; Elias, 1980) enabled a physical interpretation of their emission. Two- and three-dimensional magnetohydrodynamic simulations, especially those incorporating variable ejec-

tion mechanisms, are able to reproduce the morphological and kinematic characteristics of HH jets described in the previous Section, for example, that of HH32 (Raga et al., 2004). However, at present, it is too computationally expensive to incorporate into such models the full chemical and microscopic processes that have an important influence upon these outflows (see Chapter 3). Therefore, most of the investigations into such processes have been based on planar shock models, whose predictions may be compared with observed intensities, ratios and emission line profiles.

'Traditional' shock models are discontinuous (or 'J-type') and are solved by means of the Rankine-Hugoniot relations (see Chapter 2). Such models predict that H_2 will become fully dissociated at shock velocities above 25 km s^{-1} (Kwan, 1977). Therefore, the early models of HH objects were that of slow J-type shocks propagating through a pre-accelerated gas. Draine (1980), following on from work of Mullan (1971), showed that a shock propagating in a weakly ionized medium in the presence of a magnetic field is broadened, forming a precursor to the J-type shock. For a sufficiently large magnetic field, the velocity change across the shock is continuous and the peak temperature of the gas is much lower than in a J-type shock of the same speed (see Chapter 2 for more detail). Draine et al. (1983) showed that such shocks (known as continuous or 'C-type') were able to propagate at velocities of up to 40–50 km s^{-1} before H_2 dissociation occurs. The excitation conditions in C-type shocks were found to be able to explain that observed levels of H_2 emission in some HH objects. These models, and subsequent ones (for example, Smith & Brand, 1990; Kaufman & Neufeld, 1996a,b) assumed a static equilibrium when evaluating the degree of dissociation of H_2 within the shock wave. However, later work (Le Bourlot et al., 2002; Flower et al., 2003; Flower & Pineau des Forêts, 2003) has shown that when this (invalid) assumption is relaxed, shock velocities of 60–70 km s^{-1} may be attained.

Early planar shock models, whilst explaining the levels of emission in some HH objects, were unable to reproduce the range of excitation conditions and

line widths of H_2 observed in them (e.g., Carr, 1993; Hartigan et al., 1989). A proposed mechanism to reproduce the observed range of excitation conditions was that of a combination of two C-type planar shocks. In such models, the high excitation levels arise in a strong shock, while a weaker shock is responsible for the emission from low vibrational levels (e.g., Le Bourlot et al., 2002). An alternative is to assume pumping effects, such as fluorescence (Fernandes & Brand, 1995). These types of models have successfully reproduced the observed H_2 emission in some HH objects by increasing the population in the higher vibrational levels. More commonly, both C-type (Smith et al., 1991) and J-type (Smith, 1994) bow shock models have also successfully been applied to HH objects.

A related issue is that the emission from HH objects is observed both from species thought to require a high degree of ionization, such as [Fe II], and species expected to arise in a largely neutral medium, such as H_2. C-type shock models (of any variety) were not expected to be compatible with these observations because they do not strongly ionize the gas. However, to the best of our knowledge, this has not previously been verified. 'Fast' (or radiative) J-type shocks, such as those of Hollenbach & McKee (1989), which form a radiative and ionizing precursor to the shock front, were able to reproduce the observed [Fe II] emission but not that of H_2. This is because in such models H_2 is dissociated in the shock front and reforms in the cooling flow behind the shock. This process gives rise to H_2 emission that is some two orders of magnitude weaker than that expected from C-type shocks. Hartigan et al. (1987) constructed a bow shock model consisting of 43 radiative J-type planar shocks that was able to explain many aspects of the atomic and ionic emission observed at visible wavelengths towards HH objects but did not consider emission from molecular lines, such as H_2. The apparent inability of pure C- or J-type shock models to reproduce both the low and high excitation species simultaneously has lead to suggestions that the emission may form in combinations of the two. Three possible mechanisms, which have been proposed for HH7, are bow shocks (Smith et al., 2003), J-type shocks with magnetic

precursors (Carr, 1993; Gredel, 1994) or a combination of the two (Hartigan et al., 1989): all three mechanisms can produce the high excitation species in a dissociative region and the low excitation species in a continuous component.

From the above, it can be seen that although shock modelling of HH objects has met with many successes, we are still not able to confidently identify the dominant shock mechanism in a given case.

1.3 Motivation

The widely held opinion that species such as [Fe II] and H_2 arise in distinct shocks is based on comparisons with the predictions of 'fast' J-type shock models (commonly, observations are compared with the models of Hollenbach & McKee (1989)) and of C-type models such as those of Draine et al. (1983) and Kaufman & Neufeld (1996a,b). Such models assumed static equilibrium when evaluation the degree of dissociation of H_2 and allowed a maximum C-type shock velocity of only 40–50 km s^{-1} and, to the best of our knowledge, were never actually used to calculate [Fe II] emission. Certainly, cooling due to fine-structure transitions of [Fe II] are not included in the models cited above. Furthermore, the relative gas phase abundance of Fe in the widely cited J-type shock model of Hollenbach & McKee (1989) was taken to be 10^{-6} based on the depletions tabulated by Harris et al. (1984), and the elemental abundance of Allen (1983). Later work has indicated that Fe is almost entirely depleted onto the dust grains and has a much smaller relative gas phase abundance of 2.5×10^{-8} (Sofia & Meyer, 2001).

Recently Le Bourlot et al. (2002) and Flower et al. (2003) have developed a more sophisticated planar C-type shock model in which the evolution of the shock is followed self-consistently with the chemistry and H_2 level populations. In this model the maximum shock velocity can be higher, up to 60-70 km s^{-1}. In light of these developments, it seems advisable to revisit the question of the origin of the [Fe II] and H_2 emission. Furthermore, tremendous advances in

available instrumentation have greatly extended the number of IR [Fe II] transitions observed in HH objects. We can therefore make a detailed comparison with a number of HH objects to learn about the common physics.

Chapter 2

The physics of shock waves

The prevalence of shock waves in the interstellar medium (ISM) was discussed in Chapter 1. In particular, the presence of bright knots in outflows associated with low mass star formation (Herbig-Haro outflows) are believed to be shocked phenomena. Since the physics of shock waves is relatively well understood, it is possible to construct models that, in conjunction with atomic and chemical processes, can be compared with observations. This comparison allows us to constrain parameters related to the physical conditions in the ISM (e.g., temperature and density) and thus aid our understanding of the processes occurring within interstellar shocks. In this Chapter, the effect of a magnetic field upon the structure of a shock will be discussed, following the work of Draine (1980). The construction of a one-dimensional shock model, and the influence of parameters upon that model, will also be presented.

2.1 Effects of the magnetic field upon shock structure

Regions of star formation are permeated by magnetic fields, which can have various significant effects on physical processes within the ISM. In particular, magnetic fields influence the process of star formation by supporting the pre-stellar cloud against gravitational collapse (Pikel'Ner, 1967; Larson, 2003), and

by broadening shock waves (e.g., Mullan, 1971; Draine, 1980). In this Section, the latter effect and its implications for the shock structure are discussed.

The presence of a sufficiently strong magnetic field, perpendicular to the direction of propagation of a shock wave, allows ion magnetosonic waves to travel ahead of the shock front (Mullan, 1971; Draine, 1980). The resulting temperature rise ahead of the shock front damps the effects of the shock, as shall be described below. Draine (1980) categorised shocks according to the strength of the B-field and the size of the shock speed relative to the ion magnetosonic speed; his arguments are summarised below.

A shock wave is assumed to propagate in one dimension, at constant speed into a homogeneous medium: these are simplifying assumptions that do not affect the physics discussed here. Furthermore, the magnetic field is assumed to always be perpendicular to the direction of propagation of the shock. In a cloud of partially ionized gas, compressive waves travel through the medium as a result of collisions between, and within, the neutral and charged (i.e., ion and electron) fluids. Waves due to collisions within the neutral fluid travel through the medium at the neutral gas sound speed, $(\gamma n_{\rm n} kT/\rho_{\rm n})^{\frac{1}{2}}$. Disturbances in the ionized fluid travel more slowly than those in the neutral fluid because Lorentz forces cause the ions gyrate about the magnetic field lines. The speed at which waves travel in the ion fluid is given by the ion magnetosonic speed, $v_{\rm ims}$ (Spitzer, 1962; Draine, 1980)

$$v_{\rm ims} = \left(\frac{\left[\frac{B^2}{4\pi} + \gamma(n_{\rm i} + n_{\rm e})kT \right]}{(\rho_{\rm i} + \rho_{\rm e})} \right)^{\frac{1}{2}} . \qquad (2.1)$$

Here, B is the magnetic field strength, k is the Boltzmann constant, γ is the ratio of specific heats at constant pressure and volume, T is the temperature, c is the sound speed and $n_{\rm n}, n_{\rm i}, n_{\rm e}$ ($\rho_{\rm n}, \rho_{\rm i}, \rho_{\rm e}$) are the number (mass) densities of the neutrals, ions and electrons, respectively.

Both the neutral sound waves and ion magnetosonic waves become damped

when collisions between the charged and neutral fluid occur. Collisions between the charged and neutral fluids travel through the medium at the effective magnetosonic speed,

$$v_{\rm ms} = \left(\frac{\left[\frac{B^2}{4\pi} + \gamma(n_{\rm n} + n_{\rm i} + n_{\rm e})kT \right]}{(\rho_{\rm n} + \rho_{\rm i} + \rho_{\rm e})} \right)^{\frac{1}{2}}. \tag{2.2}$$

Waves at the effective magnetosonic speed have a very long wavelength and traverse the medium with little damping. For a shock to propagate through the medium, the shock velocity, $v_{\rm s}$, must be greater than $v_{\rm ms}$; the structure of the shock, however, depends upon $v_{\rm ims}$ and the strength of the magnetic field.

If there is no magnetic field then the charged fluid experiences no Lorentz forces and flows with the same velocity as the neutral fluid. The shock velocity in this case exceeds all the sound speeds in the medium and no disturbance can travel ahead of the shock front: a *discontinuous* or *J-type* shock occurs. In Figure 2.1, the temperature and velocity profiles of the gas, in the frame of the shock front, are plotted against time; panel a is an example of a J-type shock. The shock is discontinuous because the transitions at the point of the shock front occur on a scale of the order of the mean free path of the particles.

In the presence of a magnetic field, the charged fluid is compressed with the magnetic field lines and (due to the slowing of the ionized fluid by Lorentz forces) is compressed more gradually than the neutral fluid. The discontinuity in the charged fluid becomes gradually wider with increasing magnetic field and disappears when $v_{\rm s} < v_{\rm ims}$. When such a condition is met, the ion-electron magnetosonic waves propagate faster than the shock wave and can transmit information about the shock to the medium ahead of the shock front via collisions with the neutral and charged gas. As the ion magnetosonic waves travel ahead of the shock they compress the pre-shock B-field over their damping length and so form a magnetic precursor to the shock. For a moderate B-field the magnetic precursor is not large enough for the neutral fluid to be strongly

affected so a J-type shock front is still present in the neutral fluid while there is a continuous change in the charged fluid variables. The damping length, and hence the length of the magnetic precursor and the width of the shock wave, increases as the difference between v_s and v_{ims} increases, i.e., with increasing magnetic field or ionization fraction and with decreasing v_s. As the size of the magnetic precursor increases, more collisions between the neutral and charged fluids occur ahead of the shock front resulting in the transfer of energy and momentum to the neutral fluid. The compression ratio of the neutral fluid across the discontinuity is then reduced and a gradual change of velocity in the neutral fluid occurs ahead of the discontinuity. These types of shocks are *J-type shocks with magnetic precursors*, and two examples are shown in panels b and c of Figure 2.1, where the lower peak temperature and greater width of the shock wave compared with that of a J-type shock can be seen.

Above a critical value of magnetic field strength, B_{crit}, the discontinuity in the neutrals is also broadened sufficiently that the flow is everywhere continuous. The critical value of the magnetic field strength depends upon the density and ionization fraction of the gas as well as the shock velocity. This category of shock is a *continuous* or *C-type shock*, and an example is shown in Figure 2.1d. A comparison of the temperature profiles in Figure 2.1 shows that the effect of the magnetic field is to widen the shock wave and to reduce the peak temperature attained by the gas.

In the frame of the shock, the ion fluid always has a smaller velocity than the neutral fluid in the precursor, due to the effect of the magnetic field. This velocity difference between the fluids, known as ambipolar diffusion, velocity drift or (ion-neutral) streaming, is at its greatest at the peak of a shock wave and approaches the shock velocity. The effects of streaming will be discussed further in Chapter 3.

The above cases are examples of flows that have been allowed sufficient time to attain steady state. However, if that is not the case, the above types of shock can be thought of as stages within an evolutionary process (Pineau des

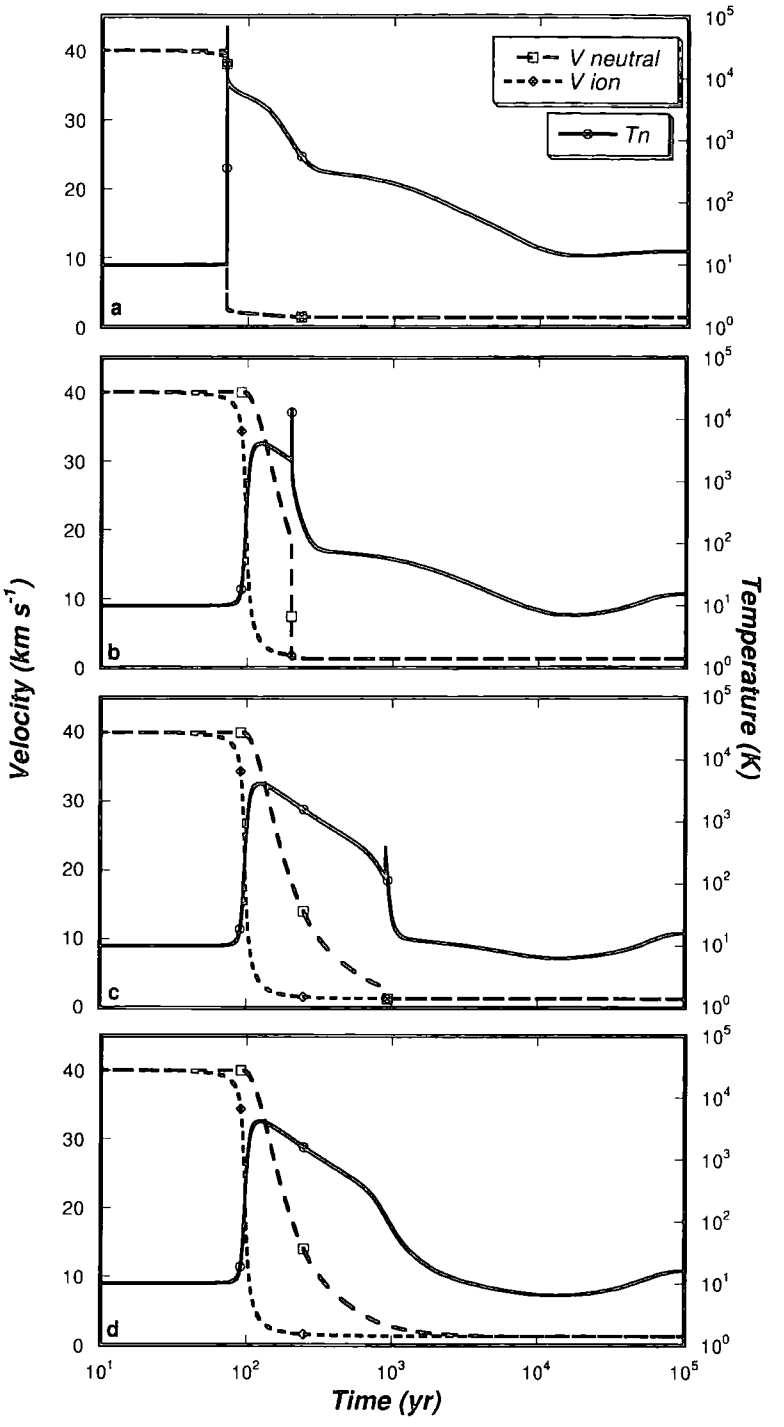

Figure 2.1: The evolutionary process from a J-type shock (panel a) to a C-type shock (panel d); the intermediary stages are represented by J-type shocks with magnetic precursors with ages of 200 yr (panel b) and 900 yr (panel c). Velocity and temperature profiles are plotted against time. The shock velocity is 40 km s^{-1}, $n_{\rm H} = 10^4$ cm^{-3} and the initial magnetic induction, B is 100 μG in all four cases. Calculations are performed in the frame of the shock: therefore, pre-shock gas is on the left-hand side of the Figure.

Forêts et al., 1997; Smith & Mac Low, 1997; Chiéze et al., 1998). A shock that is initially J-type broadens in the presence of a transverse magnetic field in the manner described above until a precursor develops. Over time, the precursor lengthens and the J-type discontinuity weakens due to the effect of the magnetic field. For example, in Figure 2.1b the discontinuity is responsible for the peak temperature attained in the shock wave; in contrast, the shock in Figure 2.1c is 700 years older and the temperature attained by the discontinuity is less than that at the peak of the precursor. Eventually, the J-type shock is sufficiently broadened that the steady-state solution of a C-type shock is obtained, as in Figure 2.1d. As Figures 2.1a–d indicate, a J-type shock with magnetic precursor can be considered as a J-type discontinuity introduced into a C-type shock profile at the point in the neutral fluid flow time, $t_{\rm n} = \int 1/v_{\rm n} dz$, that may be identified with the age of the shock (Flower & Pineau des Forêts, 1999; Flower et al., 2003).

2.2 Shock modelling

From the discussion in the previous Section regarding the effect of a magnetic field on the different fluids in the gas, it can be seen that when modelling a J-type shock in the absence of a magnetic field only a single fluid need be considered. In contrast, shocks in the presence of a magnetic field (C-type shocks and J-type shocks with magnetic precursors) require at least a two fluid treatment. If the ionization fraction of the gas is low, the electrons will thermalize at a different temperature to the ions and a three fluid treatment is necessary. In this section the treatments required for single and multi-fluid shocks are described.

2.2.1 J-type Shocks

In the simplest case, we can model the change of physical conditions in the gas in the absence of a magnetic field by consideration of the conservation of

mass, momentum and energy over a J-type shock front. This is expressed in the Rankine-Hugoniot relations:

$$\rho v = \sigma, \tag{2.3}$$

$$\rho v^2 + p = \zeta, \tag{2.4}$$

$$\frac{1}{2}v^2 + \frac{\gamma}{\gamma - 1}\frac{p}{\rho} = \xi. \tag{2.5}$$

Equation (2.3) refers to mass conservation; (2.4) to momentum flux and (2.5) to energy flux. The right-hand side in each case is a constant; v is the fluid velocity; ρ is the mass density of the fluid; p is the gas pressure and γ is the ratio of the specific heat capacities of the fluid. Equation (2.3) gives us a means to measure the strength of the shock, and can be rewritten as:

$$\rho_1 v_1 = \rho_2 v_2 \quad \text{or} \quad \frac{v_1}{v_2} = \frac{\rho_2}{\rho_1}, \tag{2.6}$$

where the subscript 1 refers to pre-shock parameters and 2 to post-shock; in the frame of the shock $v_1 = v_s$. From the velocity ratio, v_1/v_2, and the pre-shock parameters we can find the post-shock parameters (or vice versa). The ratio ρ_2/ρ_1 is known as the *compression ratio*: in monatomic gas, for which $\gamma = 5/3$, the compression ratio has a value of 4. Theoretically, diatomic (fully molecular, $\gamma = 7/5$) gas should have a compression ratio of 6, while gas that is a mix of atomic and molecular material should have a compression ratio between these two values. In fact, within the discontinuity the populations of the H_2 energy levels do not have time to thermalize. Therefore, $\gamma = 5/3$ should be adopted and the internal energy treated explicitly in the cooling flow (Flower et al., 2003).

This type of analysis is appropriate for a pure J-shock where there is no magnetic field. This, however, is unlikely to be a realistic assumption in the ISM and a more useful representation of the conservation equations, which also includes the effect of the magnetic field, B, is (following Field et al., 1968):

$$\frac{d}{dz}(\rho v) = 0 \tag{2.7}$$

$$\frac{d}{dz}\left[\rho v^2 + p + \left(\frac{B^2}{8\pi}\right) - \sigma_{xx\prime}\right] = 0 \tag{2.8}$$

$$\frac{d}{dz}\left[\rho v\left(\frac{1}{2}v^2 + U + \frac{\gamma}{\gamma - 1}\frac{p}{\rho}\right) + \frac{B^2}{4\pi}v + F_x - v\sigma_{xx\prime}\right] = 0 \tag{2.9}$$

$$\frac{d}{dz}\left(\frac{B}{\rho}\right) = 0. \tag{2.10}$$

Equations (2.7) - (2.9) are equivalent to equations (2.3) - (2.5) but apply over the whole flow rather than only at the discontinuity. The internal (rotational) energy term, U, in equation (2.9) is incorporated into the last term on the left-hand side of (2.5). The last term in equation (2.8), $\sigma_{xx\prime}$, is the viscous stress tensor and the last three terms in (2.9) are the Poynting vector, the radiative flux vector and the viscous energy flux. Equation (2.10) deals with the compression of the magnetic field.

These equations can be rearranged to find post-shock values of parameters such as velocity, density, temperature and magnetic induction. However, in the code, which is described in Chapter 4, an artificial viscosity term is instead included in the conservation equations presented below, which may then be integrated through the J-type shock. This process and the precautions that must be taken when using it are discussed in Chapter 4.

2.2.2 C-type Shocks and Magnetic Precursors

The conservation equations from above must be adapted for a two-fluid medium. One consequence of this model is that interactions between the two types of fluid can lead to changes in the particle number (and hence density, momentum and energy) of the fluids. In particular, chemical reactions can significantly affect the ionization fraction and hence the cooling of the gas (Flower et al., 1985; Pineau des Forêts et al., 1997). To model this, source terms are required;

these terms are the change per unit volume and time of the quantity under consideration and are discussed in Appendix A.2. The conservation equations for particle number density, mass density, momentum flux and energy flux for a multi-fluid medium have been well described in several papers (Flower et al., 1985; Flower & Pineau des Forêts, 1995; Flower et al., 2003) and are reproduced below. The subscript n refers to neutrals and i refers to ions.

Particle number conservation

The particle number conservation equations are

$$\frac{d}{dz}\left(\frac{\rho_{\rm n} v_{\rm n}}{\mu_{\rm n}}\right) = \mathcal{N}_{\rm n} \tag{2.11}$$

$$\frac{d}{dz}\left(\frac{\rho_{\rm i} v_{\rm i}}{\mu_{\rm i}}\right) = \mathcal{N}_{\rm i}, \tag{2.12}$$

where μ is the mean molecular weight and $\mathcal{N}$ is the number of particles created per unit volume and time.

In addition, the inclusion of chemical reactions, which alter the ionization of the gas and will be discussed in Chapter 3, means that the abundance, n_α, of each atomic and molecular species, α, must be followed over the shock wave. $\mathcal{C}_\alpha$, the rate, per unit volume and time, at which a species is being formed through chemical reactions is given by:

$$\frac{d}{dz}\left(n_\alpha v_\alpha\right) = \mathcal{C}_\alpha. \tag{2.13}$$

Mass conservation

As mass and charge are conserved, the source terms for the ion and neutral mass conservation equations, $\mathcal{P}$, are of equal value but opposite in sign

$$\frac{d}{dz}\left(\rho_{\rm n} v_{\rm n}\right) = \mathcal{P}_{\rm n} \tag{2.14}$$

$$\frac{d}{dz}\left(\rho_{\rm i} v_{\rm i}\right) = -\mathcal{P}_{\rm n}. \tag{2.15}$$

Momentum flux conservation

For the neutral fluid, the momentum conservation equation is given by:

$$\frac{d}{dz}\left(\rho_{\rm n} v_{\rm n}^2 + \frac{\rho_{\rm n} k T_{\rm n}}{\mu_{\rm n}}\right) = \mathcal{A}_{\rm n}. \tag{2.16}$$

The compression of the magnetic field must be taken into account when considering the ion fluid: the B-field is assumed to be coupled only to the ion fluid (the "frozen field" approximation). The magnetic flux within the shock wave is related to the pre-shock magnetic flux, B_0, via the following expression (Field et al., 1968):

$$B v_{\rm i} = B_0 v_{\rm s}. \tag{2.17}$$

Hence, the $B^2/8\pi$ in equation (2.8) becomes the last term in the following equation, where $\mathcal{A}$ is the rate of change of momentum flux per unit volume:

$$\frac{d}{dz}\left[\rho_{\rm i} v_{\rm i}^2 + \frac{\rho_{\rm i} k T_{\rm i}}{\mu_{\rm i}} + \frac{B_i^2}{8\pi}\left(\frac{v_{\rm s}}{v_{\rm i}}\right)^2\right] = -\mathcal{A}_{\rm n}. \tag{2.18}$$

Energy flux conservation

The energy conservation equation of the neutral fluid is given by:

$$\frac{d}{dz}\left(\frac{1}{2}\rho_{\rm n} v_{\rm n}^3 + \frac{5}{2}\frac{\rho_{\rm n} v_{\rm n} k T_{\rm n}}{\mu_{\rm n}} + \frac{\rho_{\rm n} v_{\rm n} U_{\rm n}}{\mu_{\rm n}}\right) = \mathcal{B}_{\rm n}, \tag{2.19}$$

where $U_{\rm n}$ is the mean internal energy per neutral particle. The dominant contribution to $U_{\rm n}$ in molecular shocks is from the rovibrational states of H_2

and so we can neglect this term in the ion fluid equation, in which we must again take account of the compression of the magnetic field. Here $\mathcal{B}$ is the rate of change per unit volume of contributions to the energy flux,

$$\frac{d}{dz}\left(\frac{1}{2}\rho_{\rm i}v_{\rm i}^3+\frac{5}{2}\frac{\rho_{\rm i}v_{\rm i}kT_{\rm i}}{\mu_{\rm i}}+\frac{v_{\rm s}^2}{u_{\rm i}}\frac{B_0^2}{4\pi}\right)=\mathcal{B}_{\rm i}. \tag{2.20}$$

To find the post-shock parameters from these equations they must be rearranged in the form dX/dz, where X is the dependent variable (v, T, ρ or n) and z is the independent distance variable: the rearranged forms can be found in Appendix A.1. The changes in the variables are continuous so these differential equations can be integrated through the shock to find post-shock parameters. The dependence of the variable, X, upon time is found from $1/X$ $\ln(dX/dz)$.

2.3 Effects of shock model parameters upon the shock structure

The passage of a shock wave through the interstellar medium results in compression and heating. H_2, which is the predominant constituent and coolant of the gas, can become dissociated, resulting in further heating. Radiative emission, following collisional excitation in the compressed gas, from H_2 and other atomic and ionic species causes the gas to cool again. The peak temperature attained and the width of the shock, which is related to the cooling time, depend strongly upon the type of shock wave, the shock velocity, the pre-shock density and the pre-shock magnetic flux. The degree of ionization in the pre-shock gas and, in the case of a J-shock with magnetic precursor, the age of the shock, are also significant parameters. The effects of these parameters upon the shock structure are discussed below.

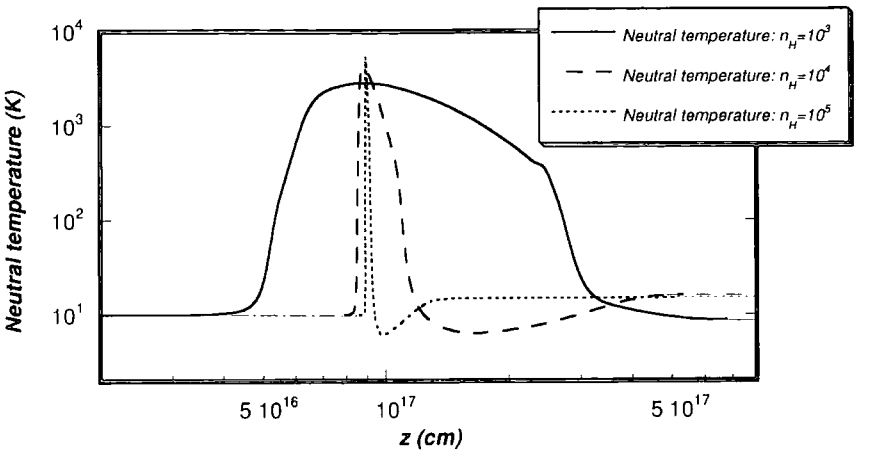

Figure 2.2: Temperature profiles for 40 km s^{-1} shocks of $n_H = 10^3$ (solid line), 10^4 (dashed line) and 10^5 (dotted line) cm^{-3}. The shock narrows and attains a higher peak temperature as pre-shock density increases.

2.3.1 Pre-shock density

The rate of collisions within a shock wave increases as density rises and this has the effect of strengthening the coupling between the charged and neutral fluids. As a result of the increased coupling, the maximum kinetic temperature attained by the neutral fluid and the rate at which v_n falls to the adiabatic sound speed, which rises with the temperature of the neutrals, both increase. Therefore the effect of increasing pre-shock density is to cause the peak temperature of the shock to rise and the shock width to decrease: this effect is illustrated in Figure 2.2.

2.3.2 Shock velocity

The peak temperature within a shock wave rises with an increase in the shock velocity because the energy flux of the shock wave is proportional to v_s^3 (see equations (2.19) and (2.20) in Section 2.2.2). In C-type shocks, higher shock velocities give rise to a greater compression and narrower shock width. The

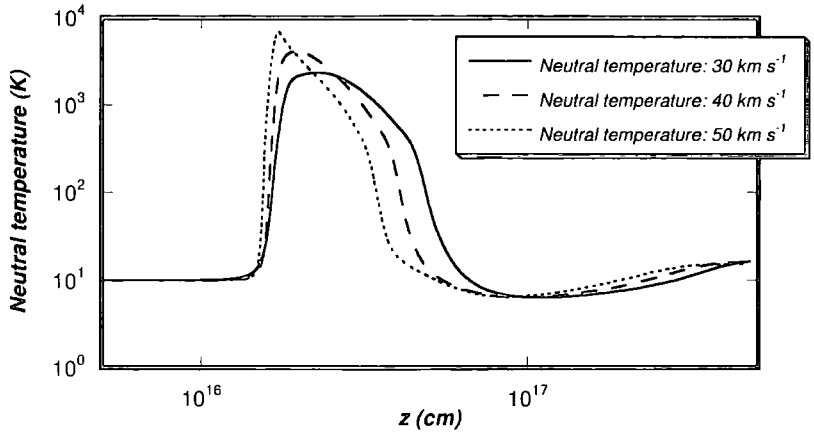

Figure 2.3: Temperature profiles for shocks of 30 (solid line), 40 (dashed line) and 50 (dotted line) km s^{-1} ($n_{\rm H}$ = 10^4 cm^{-3} and B = 100 μG in all three cases). The shock narrows and attains a higher peak temperature as shock velocity increases.

greater compression results in a higher rate of collisions (in particular between H and H_2, the dominant mechanism for excitation of H_2) and hence an increased cooling rate, which is more efficient than the rate of heating. Therefore, as the velocity of a C-type shock increases so does the rate at which the gas cools, resulting in a narrower shock wave. As an example, neutral temperature profiles from shock models with $n_{\rm H}$ = 10^4 cm^{-3}, B = 100 μG and shock velocities of 30, 40 and 50 km s^{-1} are shown in Figure 2.3.

J-type shocks have a larger compression ratio than C-type shocks and so, because adiabatic expansion is assumed, a J-type shock will produce a greater peak temperature than a C-type shock at the same velocity; see Figure 2.1. In the case of J-type shocks, a different behaviour with increasing shock velocity is observed to that described for C-type shocks above: the shock width first increases before decreasing again at a particular velocity ($v_{\rm s}$=25 km s^{-1} at $n_{\rm H}$=10^4 cm^{-3}, Flower et al., 2003). The initial increase in shock width is related to the greater amount of energy that must be dissipated by the shock wave: a higher peak temperature requires more time in order to cool. The

rate of dissociation of H_2 is greater and so the cooling less efficient in J-type shocks than C-type. As the shock velocity increases above a certain value, the degree of ionization in the gas increases and cooling via radiative decay following electron collisional excitation becomes important: the rate of cooling then increases with increasing shock speed and the shock width decreases.

Le Bourlot et al. (2002) defined the critical velocity, $v_{\rm crit}$, as the shock velocity at which sufficient H_2 dissociation occurs within a C-type shock wave that there is a rapid increase in the neutral temperature of the gas, which results in a sonic point (discontinuity) in the flow. These authors calculated $v_{\rm crit}$ for a range of densities and found that (assuming the magnetic field scales as $B(\mu{\rm G}) = [n_{\rm H}\ ({\rm cm}^{-3})]^{\frac{1}{2}}$ and neglecting the effects of external photons) the critical velocity decreased with increasing density, from 81 km s^{-1} at $n_{\rm H}=10^3$ cm^{-3} to 32 km s^{-1} at $n_{\rm H}=10^6$ cm^{-3}. As $n_{\rm H}$ increases the energy dissipated by the shock wave is less readily radiated away because the rate of cooling of the gas by radiative transitions of H_2 decreases from a quadratic to a linear dependence upon $n_{\rm H}$. Hence, the dissociation rate of H_2 increases and a sonic point is more readily attained.

2.3.3 Charged grains

The effect of the shock wave upon dust grains will be discussed in Chapter 3. Here, the influence of the grains on the shock structure, which was studied by Flower & Pineau des Forêts (2003), shall be briefly described. In a weakly ionized medium the charged grains, because of their relatively high mass density, constitute a significant fraction of the ionized mass. This means that charged grains contribute to the dynamics of the shock wave in two ways. Charged grains enhance the momentum transfer from the neutral to the ionized fluid, hence narrowing the shock wave. They also affect the magnetosonic speed, which must be greater than the shock velocity for a C-type shock to occur, by increasing the inertia of the ionized fluid. The latter effect was studied by Flower & Pineau des Forêts (2003) who found that, when the effects of

charged grains on the shock structure were considered, the magnetosonic speed in the pre-shock gas — and hence the maximum possible velocity of a shock — could be lower than $v_{\rm crit}$. The abundance of polycyclic aromatic hydrocarbons (PAHs), which are large molecules that can be considered as small grains and that carry most of the negative charge in the ionized fluid, is significant in these findings. For a relative PAH abundance of 10^{-6}, the maximum possible C-type shock velocity is determined by $v_{\rm crit}$, as above, for $n_{\rm H} > 10^4$ cm^{-3} but by the magnetosonic speed at lower densities. For example, Flower & Pineau des Forêts (2003) found that the maximum possible velocity of a C-type shock into gas with a pre-shock density of $n_{\rm H} = 10^4$ cm^{-3} was limited to the magnetosonic speed of approximately 60 km s^{-1} rather than the value of $v_{\rm crit} \approx$ 70 km s^{-1} found by consideration of collisional dissociation of H_2. At lower relative PAH abundances, the maximum possible C-type shock velocity was determined by the magnetosonic speed.

The outflows modelled in Chapter 5 are expected to undergo several shock events within their lifetimes. As shall be described in Chapter 3, one of the effects of the passage of a shock wave is to erode the dust grains, thereby reducing the mass of the dust grains and their influence on the inertia of the ionized fluid. The number and frequency of shocks experienced by an outflow and, hence, the mass of material remaining on the dust grains is not well constrained. Furthermore, the rates of grain charging are unsure. In view of these uncertainties, the effects of grain charging on the dynamics of a shock wave were not included in the work described in Chapter 5. However, the models presented there typically have shock velocities in the range 30–50 km s^{-1} and a pre-shock density of $n_{\rm H} = 10^4$ cm^{-3} and are, in any case, consistent with the findings of Flower & Pineau des Forêts (2003).

2.3.4 Magnetic fields

Increasing the value of the pre-shock value of the magnetic flux results in a larger ion magnetosonic speed. As the Alfvèn part of the ion magnetosonic

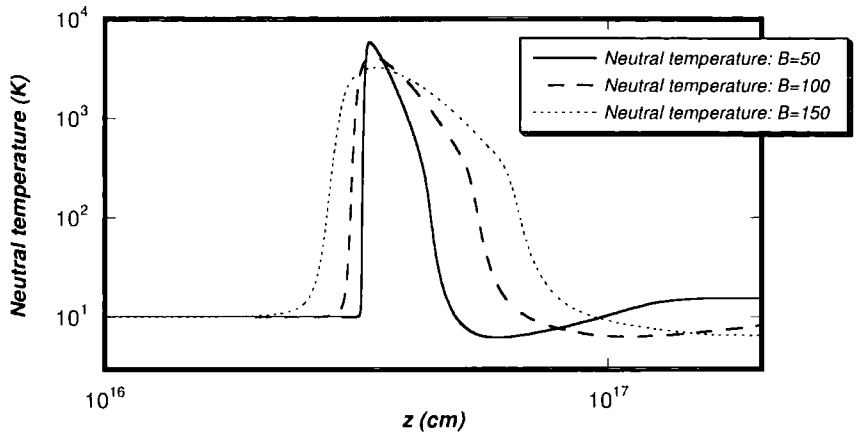

Figure 2.4: Temperature profiles for shocks with an initial magnetic induction of 50 μG (solid line), 100 μG (dashed line) and 150 μG (dotted line). The shock widens and attains a lower peak temperature as the initial magnetic induction increases.

sound speed increases, the effect is to broaden the shock wave and lower the peak temperature attained by the gas, as described in Section 2.1, in all types of shock waves. An important consequence of this is that the critical velocity of a C-type shock tends to increase with increasing pre-shock magnetic flux (Le Bourlot et al., 2002). The effect of increasing the initial magnetic flux from 50 μG to 150 μG on a 40 km s^{-1} C-type shock wave into gas with $n_{\rm H} = 10^4$ cm^{-3} is shown in Figure 2.4.

2.3.5 Photoionization effects

Photoionization of the pre-shock gas, perhaps due the presence of the background ultraviolet (UV) interstellar radiation field, leads to an increase the coupling between the neutral and the charged fluids, resulting in a narrower shock wave. An increased ionization fraction also results in a higher peak temperature, as described above. In the case of a C-type shock the effect of the increased ionization fraction is to reduce the value of $v_{\rm crit}$. In Figure 2.5 the effect of including photoionization processes on the temperature profile of a 40

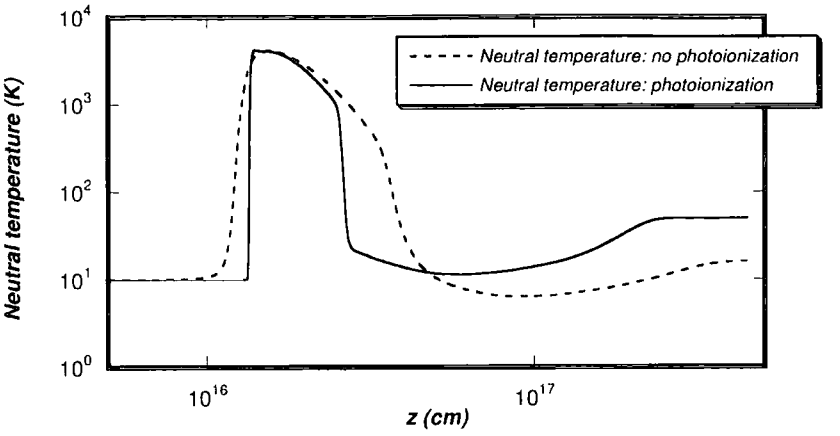

Figure 2.5: Temperature profiles for shocks including photoionization effects (solid line) and without photoionization effects (dashed line). When photoionization processes are included the peak temperature of the shock increases from 4160 K to 4240 K.

km s^{-1} C-type shock into gas with $n_H = 10^4$ cm^{-3} and $B = 100$ μG can be seen.

2.3.6 J-type shock with magnetic precursor: sensitivity of the model to age

The age of a J-type shock with magnetic precursor affects the peak temperature attained by the discontinuity and the width of the shock wave. Profiles of neutral temperature against time for shocks with v_s=40 km s^{-1}, n_H=10^4 cm^{-3} and B=100 μG at four stages of evolution from a J-type to a C-type shock wave are shown in Figures 2.1a–d. Figure 2.1a shows the profile of a J-type shock: the exact values of the peak temperature and the width of this shock are determined by the initial conditions as described above. In figures 2.1b–d the shock is old enough that a precursor heats, accelerates and compresses the gas, which can subsequently start to cool, ahead of the J-type discontinuity. Rapid cooling results in the termination of the shock wave soon after the point of the J-type discontinuity (see Figures 2.1b and c). Therefore, the age of the shock

determines the extent of the precursor, which lengthens over time, and hence the conditions within the gas in which the discontinuity occurs. At greater shock ages, the gas heated by the precursor has slowed (in the frame of the shock) and cooled significantly and so the discontinuity attains ever lower peak temperatures (see, for example, Figure 2.1c). Ultimately, the discontinuity is completely removed from the profile and the width and peak temperature of the resulting C-type shock depend upon the conditions as above.

Chapter 3

Microscopic physics of shock waves

The dynamical effects of a shock wave upon the ISM, and the effects of conditions within the gas upon the dynamics of the shock wave, were discussed in the previous Chapter. The effects of microscopic processes and shock waves upon each other can be similarly circular. When a shock passes through the interstellar medium the gas is heated and compressed so that H_2 becomes excited through collisions and some dissociation may also occur. H_2 deexcites through rotational-vibrational (ro-vibrational) transitions that also act to cool the gas; the progress of the shock wave is dependent upon the rate at which the gas cools. The velocities of particles in the medium are increased due to the shock so chemical reactions tend to occur at a greater rate. In particular, streaming drives ion-neutral reactions, which has significance for the shock structure, and endothermic reactions are also more likely to occur in a shock wave because more energy is available to them as the gas temperature rises. This temperature rise and subsequent fall after the passage of the shock alters the abundance of species in the medium, which can also significantly affect the cooling rate of the gas. In this Chapter, some aspects of the microscopic treatment of a shock wave most relevant to this Thesis will be presented. In Section 3.1 the assumed initial chemical composition of the gas and some of the most important processes, such as grain erosion, shall be discussed. The

emission treatment of H_2, [Fe II] and some other species is described in Section 3.2 and the effect of the shock on the H_2 emission will be dealt with in Section 3.3.

3.1 Chemical processes

Chemical reactions are inextricably intertwined with shock waves: the processes driven by the passage of the shock wave reactions alter the abundance of species and the ionization fraction of the gas, both of which affect the shock. A higher ionization fraction results in increased coupling of the charged and neutral fluids and gives rise to a narrower shock wave (Flower et al., 1985). The abundance of important coolants, such as H_2, can be changed through chemical reactions and atomic processes, particularly dissociation in the shock wave, and this affects the rate of cooling in the gas, which in turn influences the rate at which chemical reactions and other atomic processes can occur. The presence of dust grains allows the reformation of H_2 after the passage of the shock wave while the erosion of grains in the shock releases refractory species, such as SiO, Fe and Mg, into the gas phase: the line emission from these species can then be used as a tracer of shock activity. In this Section, the initial chemical conditions of the gas, some examples of shock chemistry and the erosion of dust grains will be discussed.

3.1.1 Initial chemical composition

The chemistry in the model involves over 1000 reactions between 138 species comprising the atoms, ions, molecules and free radicals of H, He, N, C, O, S, Si, Mg and Fe. The elemental abundances of these species are presented in Table 3.1. They are derived from studies of: meteors and the solar photosphere (Anders & Grevesse, 1989); diffuse interstellar clouds (Savage & Sembach, 1996); F and G stars (Sofia & Meyer, 2001); and embedded protostars (Gibb et al., 2000). Processes involving grains, electrons, photons, secondary pho-

Table 3.1: Initial elemental abundances, relative to $n_{\rm H} = n({\rm H}) + 2n({\rm H_2}) + n({\rm H^+})$, of the species included in the chemical model.

Species	Relative abundance
H	1
O	4.41×10^{-4}
C	3.55×10^{-4}
N	7.94×10^{-5}
He	10×10^{-1}
Mg	3.70×10^{-5}
S	1.86×10^{-5}
Si	3.37×10^{-5}
Fe	3.23×10^{-5}

tons, cosmic ray particles and polycyclic aromatic hydrocarbons (PAHs) are also included. PAHs tend to "mop up" electrons (i.e., the negative charge in the gas) through electron attachment reactions with neutrals (des Forêts et al., 1988) and, therefore, play an important role in changing the ionization fraction in the gas, and hence the structure of the shock wave. The initial PAH abundance used in this Thesis is 10^{-6}, unless otherwise stated. The effects of dust grains will be discussed in the next section: the initial grain/gas ratio, calculated from the sum of the abundances of species on the grains, is assumed to be 1.2×10^{-2} and the initial grain size distribution used is that deduced by Mathis et al. (1977). The gas is assumed to initially be in chemical equilibrium and the initial electron abundance is determined from the difference in the abundances of positive and negative ions, by the requirement of overall charge neutrality in the gas. Cosmic ray ionization, which gives rise to secondary photons, is assumed to occur at a rate of $\zeta = 5 \times 10^{-17}$ s^{-1} while photon reaction rates correspond to the mean interstellar background UV radiation field (Draine, 1978). The initial abundances of all the chemical species considered for gas with a density of $n_{\rm H} = 10^4$ cm^{-3} and for which photoionization effects have been included is given, as an example, in Appendix B, where the full list of chemical reactions considered in the model can also be found.

3.1.2 Shock chemistry

As an example of the chemistry that may occur in a shock wave, the formation of H_2O and CO, which become important coolants as H_2 is dissociated in a C-type shock wave, are described below (see also Flower, 1989).

Within a shock wave, the temperature rise of the gas may be sufficient to drive the neutral-neutral reactions

$$O + H_2 \rightarrow OH + H \tag{3.1}$$

and

$$OH + H_2 \rightarrow H_2O + H, \tag{3.2}$$

whose rate coefficients are temperature-dependent (Cohen & Westberg, 1983) and can be expressed as

$$k_{3.1} = 1.55 \times 10^{-13} \left(\frac{T}{300}\right)^{2.8} e^{(-2980/T)} \text{ cm}^3 \text{ s}^{-1}$$

$$k_{3.2} = 9.54 \times 10^{-13} \left(\frac{T}{300}\right)^{2.0} e^{(-1490/T)} \text{ cm}^3 \text{ s}^{-1}$$

OH can react with C^+, which may have been produced by cosmic ray photoionization of C.

$$C^+ + OH \rightarrow CO^+ + H \tag{3.3}$$

The CO^+ produced in 3.3 may react with H_2 to form HCO^+,

$$CO^+ + H_2 \rightarrow HCO^+ + H \tag{3.4}$$

while H_2O may also react with C^+ to form HCO^+,

$$C^+ + H_2O \rightarrow HCO^+ + H \tag{3.5}$$

which then dissociatively recombines to form CO

$$HCO^+ + e \rightarrow CO + H. \tag{3.6}$$

Table 3.2: Initial relative abundances of core species.

Core species	Relative abundance
O**	1.40×10^{-4}
Si**	3.37×10^{-5}
Mg**	3.70×10^{-5}
Fe**	3.23×10^{-5}
C**	1.63×10^{-4}

Table 3.3: Initial relative abundances of mantle species.

Mantle species	Relative abundance
H_2O*	1.03×10^{-4}
CO*	8.27×10^{-6}
CO_2*	1.34×10^{-5}
CH_4*	1.55×10^{-6}
NH_3*	1.55×10^{-5}
CH_3OH*	1.86×10^{-6}
H_2CO*	6.2×10^{-6}
HCO_2H*	7.24×10^{-6}
OCS*	2.07×10^{-7}
H_2S*	3.72×10^{-6}

3.1.3 Dust grains

Dust grains significantly affect both the chemical composition of the medium and the photons travelling through it. The absorption of photons by dust grains results in the extinction of emission from an astrophysical body: extinction laws (e.g., Seaton, 1979; Rieke & Lebofsky, 1985) are used to account for this effect. Dust grains can subsequently re-emit photons at longer wavelengths leading to an observed reddening of the emission, which can be corrected by adjusting observed line ratios to be consistent with that expected by theory. For example, the ratio of the [Fe II] 1.644 μm and 1.257 μm lines, which originate from the same upper level, is dependent only upon the Einstein A-values for each transition and is expected to have a value of 1.04 (Nussbaumer &

Storey, 1988). The observed ratio, in conjunction with an extinction law, can then be used to determine the extinction by the lines (Gredel, 1994). Dust grains are also responsible for the scattering and polarisation of photons and deplete refractory elements, such as Fe, Mg, Si and C, from the ISM. Finally, grains are involved in a three body reaction with two H atoms to form H_2: the grain is the third particle required to carry away the excess energy (as phonon excitation within the grain).

In the model, dust grains are assumed to consist of a tightly bound core made of particles or compounds of the heavier elements, such as carbon, silicon, magnesium and iron. It is assumed that the grain cores are composed of graphite or a representative silicate, in the form of olivine, $MgFeSiO_4$. The initial relative abundances of the grain core species used in the model are listed in Table 3.2: the values used are from the work of Anders & Grevesse (1989). The temperatures in the dense molecular clouds that star formation occurs in are so low (on the order of 10s of Kelvin) that a mantle, consisting of ices such as H_2O, NH_3 and CH_4 forms around the core. The initial relative abundances of the mantle species are listed in Table 3.3 and are taken from Gibb et al. (2000).

The influence of the magnetic field upon the dynamics of the charged fluid (discussed in Chapter 2) has consequences on microscopic scales. In particular, the slowing of the charged fluid in relation to the neutrals is responsible for the erosion of dust grains. The icy mantles tend to sputter off the dust grains as the the velocity difference develops in the initial stages of a shock. Cosmic ray impact can also remove the grain mantles via desorption. The cores are much more tightly bound and require greater energies than are available from the heating associated with the shock in order to break them up. Molecular outflows are situated within clouds of dense, dusty gas and so are largely (although not necessarily completely) shielded against strong UV radiation. Therefore, there is little photoionization of the grains and so there exists an attraction at long range between grains and electrons, due to polari-

sation effects. The resulting potential features a well in which an electron can be trapped; giving the grain a net negative charge that repulses any further electrons. In the presence of a magnetic field, Lorentz forces will cause the charged particles (and therefore the grains) in a moving gas to gyrate about the field lines while the neutrals are unaffected. The result of this is that the charged particles, which move with the B-field, are slowed and, as mentioned in Chapter 2, a velocity difference between the neutrals and ions builds up. This effect means that, in the reference frame of the shock, the neutrals can have a greater kinetic energy than the charged particles and, in particular, a greater kinetic energy than the grains. If the energy difference is sufficient, particles can be knocked off the surface of the dust grains. May et al. (2000) showed that in C-type shocks typical to the ISM the velocity difference can be sufficient that collisions between dust grains and neutrals can remove up to 50% of the grain constituents.

3.2 H_2 and other atomic and ionic line emission

Cooling of the gas occurs largely through ro-vibrational transitions of H_2. However, during the passage of a shock wave, the temperature and density of the gas increase, H_2 is dissociated and H begins to be ionized. As a consequence, the contribution of radiative cooling by H_2 decreases and that of other molecular and atomic species, such as H_2O, CO, O, C and Fe^+, assumes greater importance. In particular, cooling due to O and Fe^+ becomes important after the peak of strongly dissociative J-type shocks. Therefore, models of H_2, other molecular species, atomic and ionic emission are required.

3.2.1 H_2 emission

The hydrogen molecule, which consists of two protons and two electrons, is the simplest (neutral) molecule that exists. The attractive state ($^1\Sigma_g^+$) that results when two n=1, l=0 ground state hydrogen atoms approach each other is the ground state of the H_2 molecule. The bound hydrogen atoms exhibit two types of motion: vibration along the bond and (end over end) rotation about the midpoint of the inter-nuclear axis. The H_2 ground state contains 14 bound vibrational (v) states, which are each split into a number of rotational (J) states. Therefore an energy level of H_2 is described by its rotational-vibrational (rovibrational) state, (v, J). The homonuclear nature of H_2 means that it does not have a permanent dipole moment and so dipole transitions between different vibrational and rotational levels are forbidden in the electronic ground state. However, electric quadrupole transitions may occur, which have selection rules $\Delta J = 0, \pm 2$, with $J = 0 \rightarrow 0$ also forbidden. Ro-vibrational transitions are labelled according to the vibrational transition, the difference in J (with O, Q, and S representing ΔJ =+2, 0, and -2, respectively) and the final rotational level. For example, the 2.122 μm transition from $v = 1 \rightarrow v = 0$ and $J = 3 \rightarrow 1$ is represented as 1-0 S(1). The spontaneous transition probabilities of the ro-vibrational transitions, which are emitted in the IR, are small but are compensated by the high abundance of H_2 to make it the most important coolant in the ISM.

The population densities of each state are calculated taking into account the processes that create or destroy H_2 and those that transfer population within the molecule: namely, collisional excitation and de-excitation; spontaneous radiative decay; collisional dissociation and ionization; and reformation of H_2 on grains. The details and rates of these processes are well described by Le Bourlot et al. (2002) and Flower et al. (2003), and are only briefly summarised here, below. The distribution of population among 150 rovibrational levels of H_2 (i.e. up to $(v = 8, J = 3)$ $E_{vJ} = 3.9 \times 10^4$ K) are calculated for all objects in Chapter 5. The equations for the H_2 level populations are solved in parallel

with the chemical and dynamical conservation equations. This approach is essential to ensure the accuracy of the computed H_2 column densities, because the level populations do not respond instantaneously to changes in the physical state of the gas.

Population transfer due to collisions with H, H_2, He and grains is taken into account using the data of Le Bourlot et al. (1999) and Pineau des Forêts et al. (2001). Le Bourlot et al. (2002) noted that, at $T_n = 1000$ K, the rates coefficients for vibrational transitions induced by collisions with H are approximately two orders of magnitude larger than those for H_2 or He. The limit of quantal calculations is reached at $E(v, J) = 20,000$ K. Above this energy only collisions with H and grains are considered. The rate coefficients used are the quasi-classical trajectory calculations of Mandy & Martin (1993); Martin & Mandy (1995) and Pineau des Forêts et al. (2001), respectively. The spontaneous decay rates of Abgrall & Roueff (1989) and Roueff (private communication) were adopted.

The ionization of H_2 clearly reduces the total population densities but the ionization of both H and He also removes perturbers of H_2 from the gas, which has consequences for the excitation of H_2. The rate coefficients for the collisional ionization of H and H_2 by streaming ions are calculated in the manner described by Le Bourlot et al. (2002) and are given by

$$1.1 \times 10^{-13} \exp[-179160/T_{\rm eff}(H_2)] \text{ cm}^3 \text{ s}^{-1} \tag{3.7}$$

for H_2, and

$$1.3 \times 10^{-13} \exp[-157890/T_{\rm eff}(H)] \text{ cm}^3 \text{ s}^{-1} \tag{3.8}$$

for H. The rate coefficient for the ionization of He, which was not considered in Le Bourlot et al. (2002), is given by

$$1.1 \times 10^{-13} \exp[-285328/T_{\rm eff}(He)] \text{ cm}^3 \text{ s}^{-1} \tag{3.9}$$

The effective temperature takes account of the energy imparted to the collision due to ion-neutral streaming in addition to the thermal energy of the gas. As

an example, the expression for the effective temperature for collisions between an H atom and an ion, i, is given

$$T_{\rm eff}({\rm H}) = \frac{m_{\rm H} m_{\rm i} (v_{\rm n} - v_{\rm i})^2}{3k(m_{\rm H} + m_{\rm i})} + \frac{m_{\rm H}\, T_{\rm i} + m_{\rm i}\, T_{\rm n}}{m_{\rm H} + m_{\rm i}}. \tag{3.10}$$

Collisional ionization of H and H_2 by electrons is also considered; see Le Bourlot et al. (2002) for the rate coefficients.

H_2 is assumed to be dissociated in collisions with atoms and ions (Wilgenbus et al., 2000) and with H, H_2, He (Le Bourlot et al., 2002) and electrons (Flower et al., 1996, section 2.1). Le Bourlot et al. (2002) adapted the rate coefficient of Dove & Mandy (1986) to allow for the excitation energy $E(v, J)$ of the initial ro-vibrational level (v, J), which acts to increase the rate of dissociation. The rate coefficient adopted is

$$\frac{1.0 \times 10^{-10}}{n({\rm H_2})} \sum_{v,J} n(v, J) \exp\{-[56644 - E(v, J)]/T_{\rm n}\} \ {\rm cm^3\ s^{-1}}, \tag{3.11}$$

where $n({\rm H_2}) \sum_{v,J} n(v, J)$ is the population density of the ro-vibrational level (v, J). H_2 is also destroyed in chemical reactions: for example, H_2 reacts with O to form OH, which itself reacts with a further H_2 molecule to form H_2O.

H_2 is destroyed through collisions and chemical processes in the shock wave but reformed on grain surfaces at a rate

$$n({\rm H})\, n({\rm gr})\, \pi r_{\rm gr}^2 \left[\frac{8kT_{\rm eff}}{\pi m_{\rm H}(1 + T_{\rm eff}/30)}\right]^{0.5} ({\rm cm^{-3}\ s^{-1}}), \tag{3.12}$$

where

$$T_{\rm eff} = \frac{m_{\rm H}(v_{\rm n} - v_{\rm i})^2}{3k} + T_{\rm n}. \tag{3.13}$$

The energy associated with reformation of H_2 on grains, which occurs in the wake of the shock wave over approximately 10^3 yr, gives rise to a "knee" in the temperature profile at $T_{\rm n} \approx 300$ K after which the gas continues to cool to the equilibrium value. The extent to which the gas is heated depends upon how the energy associated with reformation (up to the dissociation energy of the H_2 molecule, 4.4781 eV) is assumed to be distributed. The energy can: go into

populating the energy levels of the molecule; provide kinetic energy for the H_2 molecule, which then goes into heating the gas; or be absorbed back into the grain as phonons. The simplest assumption to make is that the available energy is split equally among the three possibilities. Alternatively, the internal energy can be calculated by summing the products of the level populations and the energy of each level: the remaining energy is split between the kinetic energy of the molecule and the energy going into the grain. Four assumptions that can be made regarding the distribution of population in the H_2 molecule as it leaves the grain are:

- The energy levels are populated in proportion to a Boltzmann distribution at 1.4927 eV, which is 1/3 of the dissociation energy of H_2 (4.4781 eV);
- The population is assumed to be excited to the dissociation limit or last bound state, v=14, J=6 (Black & van Dishoeck, 1987);
- The population forms initially in the J=0 and 1 rotational levels of the ν=6 vibrational level (Black & van Dishoeck, 1987): an ortho-to-para ratio of 3:1 is assumed;
- The levels are populated in proportion to the density of the local population.

The effects of these assumptions on the H_2 excitation diagram are discussed later in this Chapter, in Section 3.3. Once the internal energy is calculated according to one of the four assumptions above, there are two possible assumptions that can be made regarding how the remaining energy is split between kinetic energy of the H_2 molecule and energy that is absorbed by the grain. The simplest assumption is that half of the remaining energy (4.4781 eV - internal energy) goes into kinetic energy of the molecule and half is absorbed by the grain. Alternatively, the kinetic energy is given by the lesser of 1/3 of the dissociation energy (1.4927 eV) and (4.4781 eV - internal energy). In

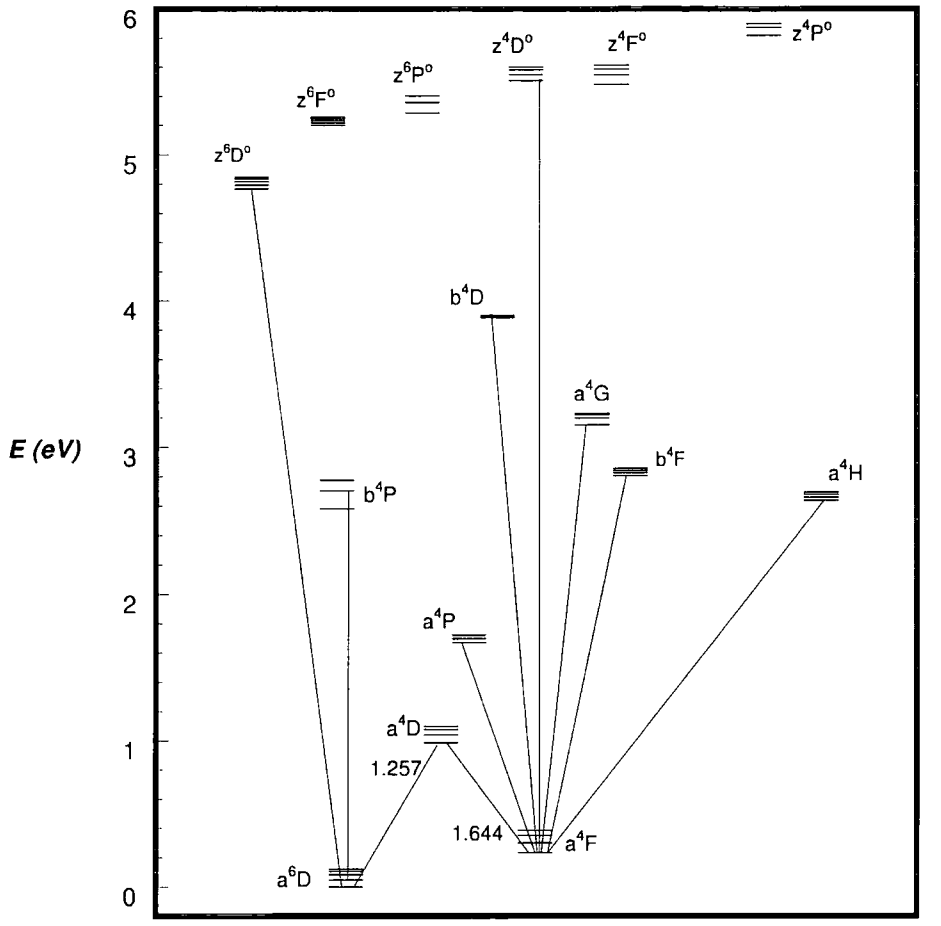

Figure 3.1: Energy level diagram for Fe^+. The strongest transition from each of the even parity terms is marked. The odd parity terms decay most strongly to terms with the same multiplicity and the strongest transitions from the z^6D^o and z^4D^o terms are marked as examples. The strongest observed IR transitions, the 1.257 and 1.644 μm lines, are also indicated.

practice, this means that unless the internal energy is greater than 2/3 of the dissociation energy, which may occur if the H_2 was assumed to form off the grain in highly excited states, the kinetic energy will be 1/3 of the dissociation energy.

3.2.2 [Fe II] emission

The rich energy structure of Fe^+, (see Figure 3.1) means that iron transitions are observed over a wide range of wavelengths — from the far IR to the X-

ray — in a wide variety of astrophysical sources, making it an important tool for astrophysics. The low ionization potential (7.87 eV) of iron means that, once it has been eroded from grain cores, it is rapidly ionized via charge transfer reactions with ions; H^+ in particular but also other ions such as H_3O^+ and H_3^+. Within a C-type shock the electron density is sufficiently small (of order $10^{-5} \times n_H$) that the timescale for ionization via charge transfer is short compared with the timescale for electron recombination of Fe^+ to Fe. Instead, recombination with PAHs are the dominant mechanism for recombination of Fe^+. Within a J-type shock, the electron abundances are comparable to that of H^+, which is the most abundant ion in a J-type shock wave, and radiative recombination with electrons becomes the dominant mechanism for converting Fe^+ to Fe. The timescale for ionization via charge transfer reactions with H^+ is much shorter than that for radiative electron recombination; at the peak of a 50 km s^{-1}, n_H=10^4 cm^{-3} J-type shock, where the temperature is of order 10^5 K, the timescales for these processes are approximately 5×10^{-4} yr and of the order 10 yr, respectively. Furthermore, in such a J-type shock, the timescale for ionization of Fe^+ to Fe^{2+} (of order 10^{-3} yr), via charge transfer reactions with H^+, is an order of magnitude larger than the rate of electron recombination of Fe^{2+} to Fe^+ (Kingdon & Ferland, 1996). Therefore, iron is expected to be in the form of Fe^+ within a shock wave.

Singly ionized iron has twenty five electrons in the ground state electronic configuration $1s^22s^22p^63s^23p^63d^64s$. The first 18 electron are in a stable core, $1s^22s^22p^63s^23p^6$, and are expected to remain inactive. The typical energies of collisions within the region surrounding a low mass star are such that the electron in the $4s^1$ subshell or even an electron in the $3d^6$ subshell can become excited to, in theory, any of the higher levels of the ion. Once the ion has been excited above the ground state it will then decay radiatively or collisionally; radiative decay is the process that gives rise to the observed emission lines. In IR observations of outflows, [Fe II] is observed only in lines from the a^4D term. The strongest of these are the 1.257 μm and the 1.644 μm lines, which share the same upper energy level and, hence, can be used to calculate the

extinction of the gas (e.g., Gredel, 1994). The proximity of the levels in the a^4D term mean that the [Fe II] lines are only weakly sensitive to temperature (the levels in the a^4D term lie at $1.1–1.3\times10^4$ K).

In the model of Fe^+, transitions among the 19 energy levels that arise from the a^6D, a^4F, a^4D, a^4P and b^4P terms are considered. The rates of collisional and radiative transitions determine the relative Fe^+ level populations at each point in the model and the absolute populations are found by multiplying by the gas phase abundance of Fe^+. Line intensities can then be calculated from the level populations. The spontaneous radiative transition probabilities computed by Nussbaumer & Storey (1988) are adopted; however, these data extend only to the a^4P term and so the data of Quinet et al. (1996) are used for transitions arising in the b^4P term. Excitation via collisions with the 'heavy' neutrals of H_2, H and He are included in the model. No quantal calculations of rate coefficients are available so a classical approximation based on the 'orbiting model' is used. However, electron spin conservation rules mean that only H, the least abundant of the three perturbers, is able to excite Fe^+ out of the ground state and so collisions with these perturbers are not efficient enough to excite Fe^+ to the degree observed in astrophysical shocks. (A more detailed discussion and a description of the classical approximation are given in Appendix C.1.) Instead, collisions with electrons in regions with a high fractional ionization are considered to be a more likely mechanism for excitation of Fe^+. The electron collision strengths of Zhang & Pradhan (1995) are adopted.

Statistical equilibrium can be assumed in the calculations of the Fe^+ level populations: the timescale for population changes of the ion are, unlike those for H_2 (see Section 3.2.1 above), on shorter timescales than those for dynamical changes within the shock wave. A simple comparison of the timescales of these processes clearly demonstrates the validity of the assumption of statistical equilibrium. The flow time through a shock wave is determined by the time taken for the gas to first be heated by the passage of the shock and then to cool back to pre-shock temperatures. The latter process is dominated by the

rate at which H_2, the dominant coolant of the gas, reforms on grain surfaces. Therefore, in the case of a J-type shock, in which the gas can be assumed to be almost instantaneously heated, the flow time through the shock wave is essentially that of the reformation time of H_2; approximately 10^3 years. This can be compared with the timescales for excitation of Fe^+ and for radiative decay out of those excited levels. Nussbaumer & Storey (1988) found a decay rate of $4.83\times\ 10^{-3}$ s^{-1} for the 1.257 μm transition, which implies that the timescale for this process is of the order of 10^{-5} years. The rate of collisional excitation (cm^{-3} s^{-1}) of Fe^+, which is calculated from the deexcitation rate and assuming detailed balance, is given by

$$q_{ik} = \frac{8.63 \times 10^{-6} \Upsilon_{ki}}{\omega_k T_e^{1/2}} e^{\left(\frac{-E_{ki}}{T_e}\right)} \frac{\omega_k}{\omega_i}. \tag{3.14}$$

The 1.257 μm line corresponds to a transition between the first (i) and tenth (k) energy levels of Fe^+. The Maxwellian-averaged collision strength, Υ_{ki}, for this transition is 11 (Zhang & Pradhan, 1995) while ω_k=8 and ω_i=10; ω=(2j+1), where ω is the statistical weight and j is the angular momentum quantum number. E_{ki}, the energy difference between the two levels, is 1.1 $\times$ 10^4 K (Corliss & Sugar, 1982). Taking the temperature and electron number density attained in the cooling flow after the discontinuity (where the [Fe II] emission arises) of a 50 km s^{-1}, $n_H = 10^4$ cm^{-3} J-type shock of T_e=10^4 K and n_e=10^4 cm^{-3}, respectively, the timescale for collisional excitation of Fe^+ is found to be 10^{-4} years. Therefore, changes in the Fe^+ level populations occur on timescales of at least 7–8 orders of magnitude shorter than that associated with the flow time of a shock wave and the assumption of statistical equilibrium is valid.

All of the observed [Fe II] IR transitions are from the a^4D term, which lies at an energy of approximately 1 eV (10^4 K) above the ground state: see Figure 3.1. In order to correctly calculate the populations of the levels of this and other terms, it is necessary to ensure that all significant cascade effects have been included. The highest level of the five terms considered lies at an energy of approximately 3 eV (3×10^4 K), which is lower than the peak temperatures

(of order 10^5 K) attained in J-type shock models. The inclusion of higher energy terms, and in particular the a^4H, b^4F, a^4G and b^4D terms, which decay preferentially to the a^4F term, could conceivably change the distribution of population in the a^4D term. As a check on the convergence of the model results, a 50 km s^{-1} J-type shock model was run, including all of the 142 energy levels for which Zhang & Pradhan (1995) provided data, i.e. levels up to 11.5 eV (1.3×10^5 K) above ground. The set of radiative transition probabilities was extended by means of the data of Quinet et al. (1996), up to the b^4D term, and of Nahar (1995) for the odd parity terms above this. The overall effect of including these terms is small: the intensities of the [Fe II] lines which are observed were reduced, but by no more than 10%, which is to be compared with the estimated uncertainty of 20% in the observed line intensities (see Chapter 5). It is concluded that the basis of 19 levels is sufficient to model the observed [Fe II] emission lines, given the current observational uncertainties.

3.2.3 Other species

Shock activity is also traced by emission lines of abundant molecular, atomic and ionic species, such as CO, H_2O, OH, NH_3, (rotational transitions) and the atoms and ions of C, N, O, S and Si (fine structure transitions). The cooling rates of CO, H_2O, OH and NH_3 are calculated using an approximation described in Le Bourlot et al. (2002), which agrees well with the 'escape probability' approach described by Neufeld & Kaufman (1993) for CO and H_2O over the peak of the shock wave. Calculations, assuming statistical equilibrium (which can be justified in the same way as for Fe^+ above), of level populations are performed for the first five levels of the atoms and ions of C, N, O, S and Si in order to calculate the emission from the strongest observed lines. The calculations for all of these species take into account radiative decay as well as collisional excitation by electrons, H, H^+, He and the ortho and para forms of H_2. Two lines of [C I], the 0.983 and 0.985 μm transitions, are often observed in conjunction with [Fe II] emission in HH outflows. In order to calculate the

intensities of these lines, the five energy levels in the ^{3}P, ^{1}D and ^{1}S terms of C are considered. Fits to the calculated rates for the excitation of [C I], which were taken from the literature, were required; these fits and the references are listed in Appendix C.3.

3.3 H_2 Excitation Diagram: the dependence upon shock model parameters

The excitation diagram (also know as Boltzmann plot or rotation diagram) is a plot of natural log of column density, N, divided by statistical weight, g, against the energy, E, of the upper level of a transition (in kelvin). The relative populations of two levels i and j are related by their statistical weights and the Boltzmann factor

$$\frac{n_i}{n_j} = \frac{g_i}{g_j}\exp(-E_{ji}/kT), \tag{3.15}$$

where E_{ji} is the difference in energy (in eV) of the two levels. The statistical weight, g, is the product of the rotational statistical weight, $(2J + 1)$, and the nuclear spin statistical weight, which has values of 1 and 3 for ortho and para rotational levels (J), respectively. Therefore, these diagrams are useful diagnostic tools: the gradient of the values of $\ln(N/g)$ is inversely proportional to the temperature of the gas. For example, if the gas is completely thermalized the values of $\ln(N/g)$ will fall along a straight line on the diagram. A shock wave excites the gas over a ranges of temperatures and the departure from LTE is exhibited as a curve on the excitation diagram that may display deviation from the median line. The values of $\ln(N/g)$ and the extent of the departure from LTE exhibited in the excitation diagram provide useful constraints for shock models. Below, the effects of the shock type, the shock parameters and the assumptions made regarding H_2 on the excitation diagram are discussed.

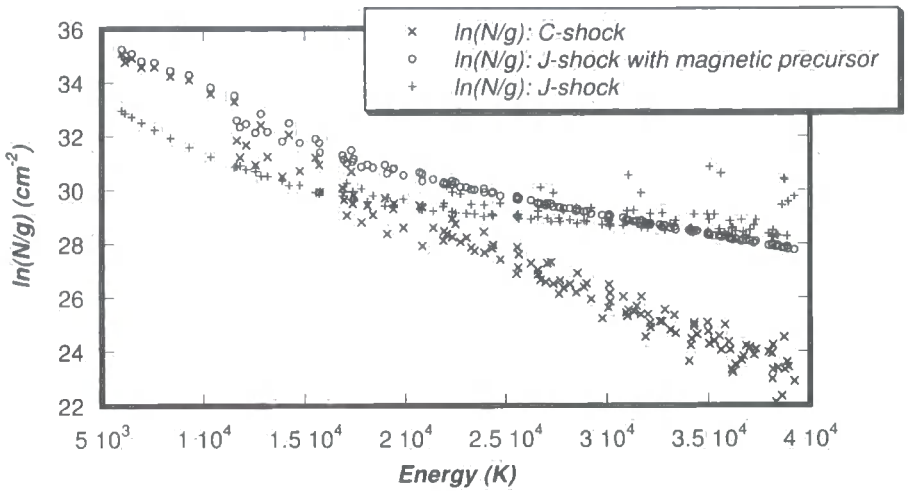

Figure 3.2: H_2 excitation diagrams for 40 km s^{-1}, $n_H = 10^4$ cm^{-3} C-type (crosses), 200 yr J-type with magnetic precursor (circles) and J-type (upright crosses) shocks.

3.3.1 Shock type

The values of $\ln(N/g)$ are determined by excitation conditions within the gas, which are strongly dependent upon the type of shock wave. In a J-type shock the strong coupling between the neutral and charged fluids results in a strong, discontinuous rise in the temperature and density of the gas. This results in a high rate of collisions and hence a tendency towards LTE: the excitation diagram tends to a smooth curve that closely follows the median line. The broadening of a C-type shock by a magnetic field gives rise to lower rates of collisions and greater divergences from LTE than in a J-type shock, and this is reflected in the greater departure from the median curve in the excitation diagram. The high rates of H_2 dissociation that can occur in a J-type shock result in weaker H_2 emission than in an equivalent C-type shock (one with the same shock velocity, pre-shock density, etc.) and, therefore, lower values of $\ln(N/g)$ for low energy vibrational levels, in particular v=1. On the other hand, the higher temperatures attained in a J-type shock tend to result in greater population of the vibrational levels at high energies (especially above

v=2) than in an equivalent C-type shock, see Figure 3.2.

A J-type shock with a magnetic precursor can be considered to be a combination of a C-type shock and a J-type shock, and this is reflected in the excitation diagram. The v=0, 1 levels are largely populated due to the precursor and exhibit the departure from LTE and the values of $\ln(N/g)$ seen from an equivalent C-type shock. The higher energy levels are populated immediately after the discontinuity and tend to follow the shape and values of $\ln(N/g)$ seen from a equivalent J-type shock, see Figure 3.2.

Regardless of the type of shock, most of the H_2 population remains in the v=0 vibrational manifold because radiative cascade tends to shift population down from higher energy vibrational levels. In addition, population within each vibrational level tends to accumulate in the lowest energy rotational level following rotationally inelastic collisions (Flower et al., 2003).

3.3.2 Shock parameters

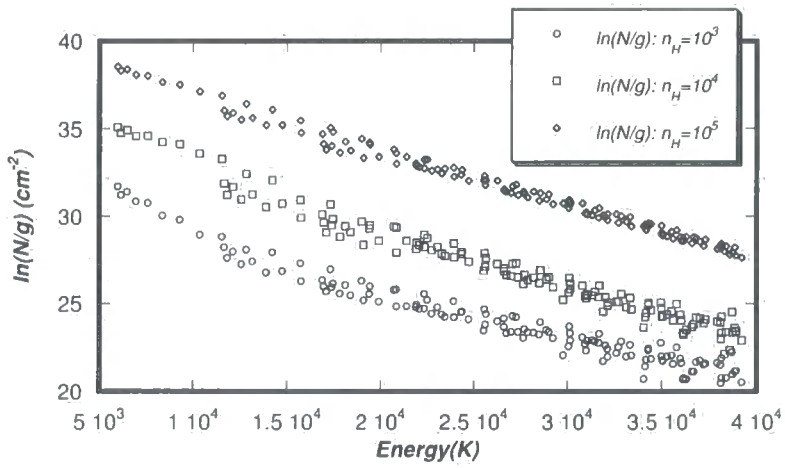

Figure 3.3: H_2 excitation diagrams for 40 km s^{-1} shocks with $n_{\rm H} = 10^3$ (circles), 10^4 (squares) and 10^5 (diamonds) cm^{-3}. Column density increases with increasing pre-shock density.

Figure 3.3 demonstrates that low pre-shock gas densities result in smaller ex-

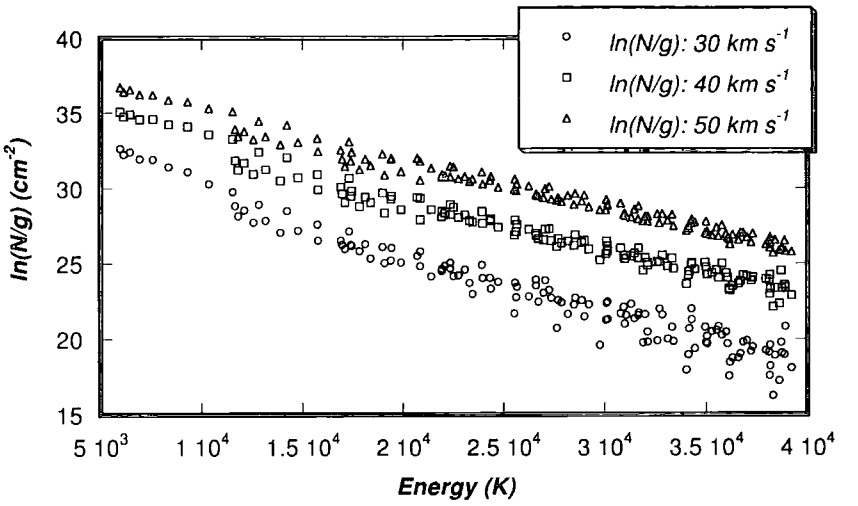

Figure 3.4: H_2 excitation diagrams for 30 (circles), 40 (squares) and 50 (triangles) km s^{-1} shocks ($n_H = 10^4$ cm^{-3}. Column density increases with shock velocity.

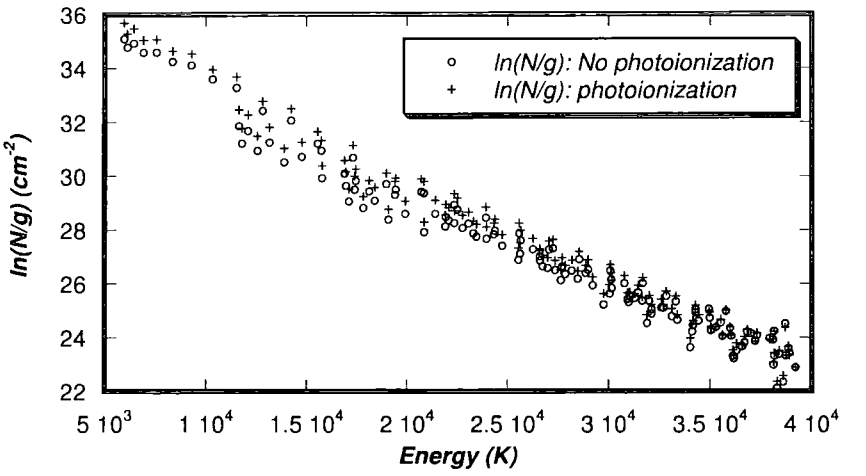

Figure 3.5: H_2 excitation diagrams for 40 km s^{-1}, $n_H = 10^4$ cm^{-3} C-type shocks with (squares) and without (upright crosses) the effects of photoionization. The inclusion of photoionization increases the tendency to thermalization.

cited state column densities and greater departures of the level populations from LTE; this is due to low rates of collisional excitation of H_2 molecules. For a given density, the shock speed is the main factor determining the column

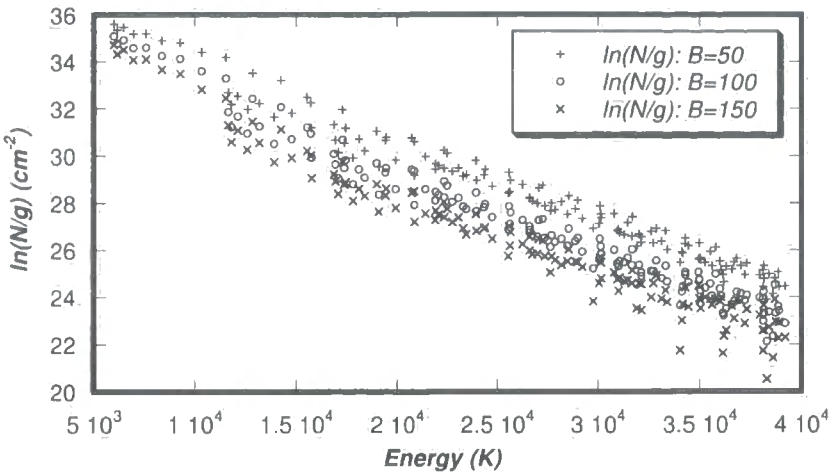

Figure 3.6: H_2 excitation diagrams for 40 km s^{-1} C-type shocks ($n_H = 10^4$ cm^{-3}) with an initial magnetic induction of 50 (upright crosses), 100 (squares) and 150 (crosses) μG. As the initial magnetic field tends to decreases the peak temperature attained in the shock wave and reduces the H_2 column densities.

densities (see Figure 3.4): an increase in the shock speed tends to result in larger column densities. Indeed, the model is so sensitive to the shock speed that a change of the order of 1 km s^{-1} in v_s can make a significant difference to the excitation diagram. The age of a J-type shock with magnetic precursor affects differentially the population densities of the more highly excited levels: the younger the object, the closer is the shock wave to being J-type and the higher are the column densities of the more highly excited rovibrational levels. Furthermore, the populations of these levels tend to be closer to LTE. The presence of a background radiation field leads to an increase in the degree of ionization of the gas and hence in the strength of the coupling between the neutral and the charged fluids. This results in a narrower shock wave and so the H_2 populations are closer to LTE, see Figure 3.5. Finally, increasing the initial magnetic flux widens the shock wave and a lower peak temperature and density are attained. The effect of this on the H_2 excitation diagram is shown in Figure 3.6: the rates of excitation into H_2 levels, and hence the populations in these levels, tend to be slightly decreased. The effects of the assumptions re-

garding the internal energy of the H_2 molecule described in Section 3.2.1 above are not large and only have an effect in the higher energy levels, which can be seen in Figure 3.7. Assumptions 1 and 3 (labelled 'iforH2=1' and 'iforH2=3', respectively) lead to a similar distribution among the rotational levels but, because it is less selective, assumption 1 gives rise to populations among the higher energy levels that are nearer to LTE. The assumption that 1/3 of the dissociation energy goes into populating the H_2 energy levels ('iforH2=0') gives rise to a more thermalized distribution of population than the previous two cases. However, assumption 4 ('iforH2=4') is the least selective of all and increases the tendency to a Boltzmann distribution of the local population according to local conditions and therefore gives rise to a more nearly thermal distribution than assumptions 1 and 3.

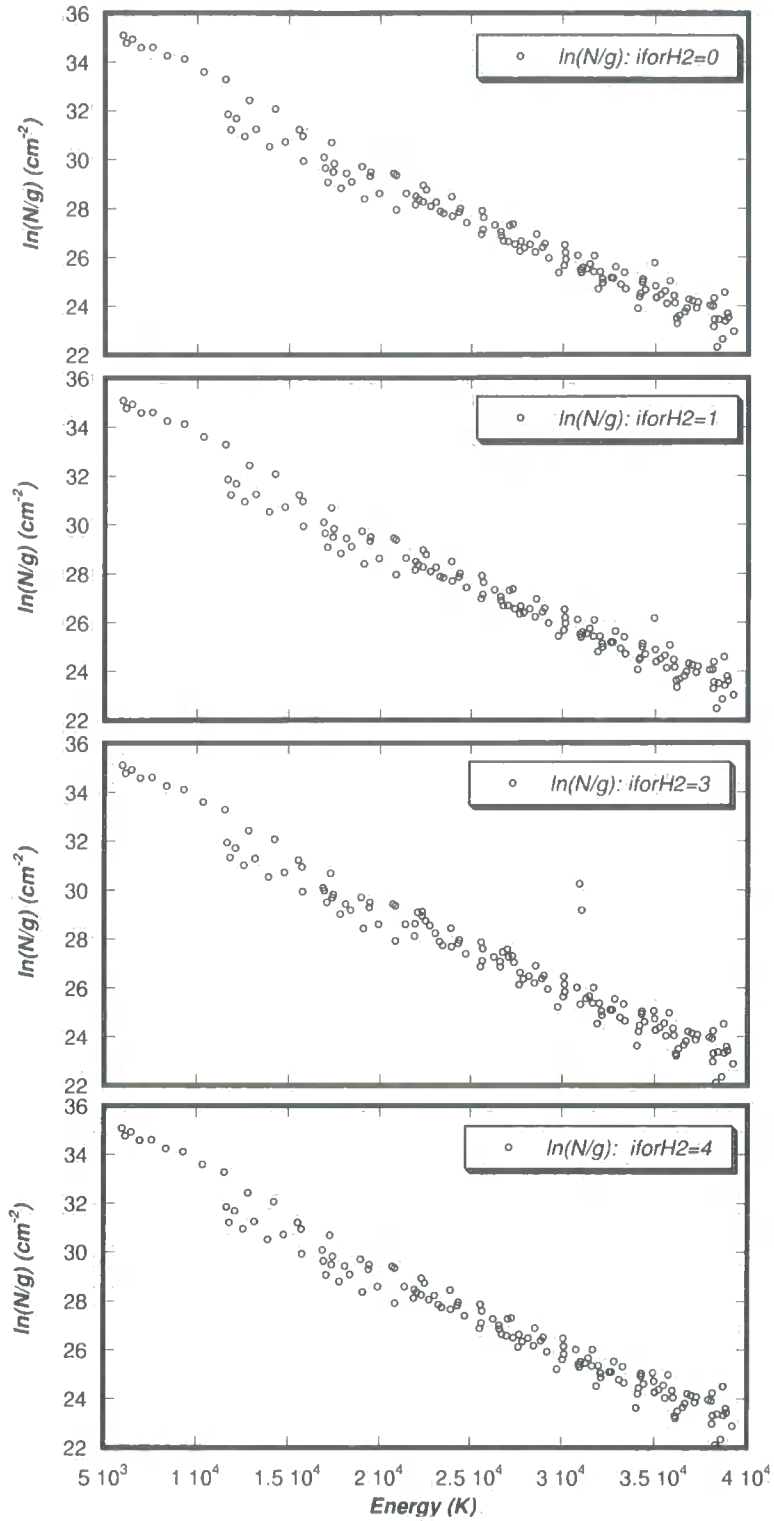

Figure 3.7: The effect of the assumed internal energy of the H_2 molecule can be seen in the higher energy levels in the H_2 excitation diagram.

Chapter 4

Computer code and approach to modelling

In this Chapter, the capabilities and limitations of the computer code used, MHD_VODE, are discussed in Section 4.1. The code and the processes it models are also well described in Le Bourlot et al. (2002) and Flower et al. (2003); only the most relevant assumptions and checks of accuracy used in the modelling of shock waves are presented here. The approach taken in order to determine the best model for the observed emission is also described in Section 4.2.

4.1 MHD_VODE

It is assumed that the shock propagates into a homogeneous medium and, in order that modelling may be carried out in one spatial dimension, that the flow is locally plane parallel. When modelling shocks, the stationary shock frame is used; that is, the gas is considered to flow into a stationary shock front at the shock speed. It is also assumed that the magnetic field is 'frozen' into the electron-ion fluid. Finally, only the components of the magnetic field perpendicular to the shock are considered as this is the only direction in which the field is compressed.

MHD_VODE is used to calculate the structure (i.e., temperature, velocity, density) of a shock wave and the emission expected from it: in particular, the IR ro-vibrational transitions of H_2 and the IR lines from atomic and ionic species, such as [Fe II] and [C I]. MHD_VODE solves the magnetohydrodynamical equations for the three fluids (neutral, positively and negatively charged) in parallel with an extensive chemical network, which links 138 species by more than 1000 reactions. It includes the effects of large molecules such as polycyclic aromatic hydrocarbons (PAHs) on chemical reactions. The influences of grains on both the charged fluid (via collisions) and the abundance of refractory species (via sputtering, erosion, adsorption and desorption) are calculated. The line intensities are derived from a comprehensive treatment of the populations of rovibrational levels of H_2 and other species. MHD_VODE is capable of modelling steady-state C- and J-type shocks and also non-equilibrium J-type shocks with magnetic precursors. In addition, it can be used to calculate the chemical equilibrium conditions in the pre-shock gas. It should be noted that at the time the work presented in Appendices G and F was carried out the code was capable only of modelling C-type shock waves.

The code treats the 'discontinuity' in both J-type shocks and J-type shocks with magnetic precursors by introducing an artificial viscosity term, $\rho l^2 (dv/dz)^2$, into the energy and momentum conservation equations of the neutral fluid (Richmyer & Morton, 1957; Flower et al., 2003):

$$\frac{d}{dz}\left[\rho v^2 + nkT + \frac{B^2}{8\pi} + \rho l^2 \left(\frac{dv}{dz}\right)^2\right] = 0, \tag{4.1}$$

and

$$\frac{d}{dz}\left(v\left[\frac{1}{2}\rho v^2 + \frac{5}{2}nkT + \frac{B^2}{4\pi} + nU + \rho l^2 \left(\frac{dv}{dz}\right)^2\right]\right) = E, \tag{4.2}$$

where $n = \rho/\mu$ is the number density of the gas and E is the energy source term. The length parameter, l, is the thickness of the 'discontinuity'. Care should be taken that l is of the same order as the characteristic length scale of elastic collisions in the gas so that the transition from pre- to post-shock

is adiabatic. If l is too large, inelastic collisions may occur and the heating of the gas underestimated (Chiéze et al., 1998); l must be small enough that the shock is able to attain the peak temperature predicted by the Rankine-Hugoniot relations.

Once the 'discontinuity' has been passed the artificial viscosity becomes negligible and it is dropped from the conservation equations; the change in the flow velocity and its first derivative are kept continuous at this point. Downstream of the 'discontinuity', the neutral fluid continues to fall in velocity; however, if $v_{\rm n} < v_{\rm i}$, in the frame of the shock, the solution becomes unphysical. Transfer of momentum from the neutral to the charged fluid is responsible for maintaining the compression of the magnetic field, and if $v_{\rm n} < v_{\rm i}$ then this cannot occur and the magnetic field cannot remain compressed. Therefore, at the point where $v_{\rm n} = v_{\rm i}$ the code changes to single-fluid mode, which causes the neutral and charged fluids to be fully coupled and prevents the divergence of the fluid velocities that would occur if $v_{\rm n} < v_{\rm i}$: see Flower et al. (2003) for more detail.

The integration of the stiff differential equations A.1–A.10 given in Appendix A.1 is performed by the VODE package (Brown et al., 1989), which uses variable step sizes to account for the widely differing characteristic length scales of the parameters (v, T, n and ρ). Equations A.1–A.10 describe an initial value problem and the initial values used, which should be derived from observation and upon which the final outcome of the modelling depends, are defined in an input file (input_mhd.in). As an illustration, relevant extracts of input_mhd.in, relating to dynamical and computational parameters, are reproduced below. In what follows, each variable will be discussed in the order that it appears in the input file.

```
!---- shock parameters ------------------------------------------
C         ! shock type : 'C' or 'J', Steady state : 'S'
3         ! Nfluids : 1, 2 or 3
1.0D0     ! Bbeta: Bfield = Bbeta * sqrt(nH)
40.0      ! Vs: shock speed (km/s)
1.0e3     ! Vn - Vi initial (cm s-1)
3.0       ! op_H2: initial H2 ortho/para ratio
10.00     ! T(n,i,e): initial gas temperature (K)
1.0D4     ! nH_init: initial value for n(H) +2.0n(H2) +n(H+) (cm-3)
15        ! Tgrains: initial grain temperature (K)
!---- environment -----------------------------------------------
5.0D-17   ! Zeta: cosmic ray ionization rate (s-1)
1.D0      ! RAD:  flux radiation (multiplicative factor)
0.D0      ! Av:   initial extinction (magnitudes)
!---- numerical parameters --------------------------------------
150       ! NH2_lev: Number of H2 levels included
50        ! NH2_lines_out: Max number of H2 lines in output file
BOTH      ! H_H2_flag: H-H2 collisions : DRF, MM or BOTH
4         ! iforH2: Formation on grain model (1, 3, 4)
2         ! ikinH2: Kinetic energy of H2 newly formed (1,2)
1.00D10   ! XLL: characteristic viscous length (cm)
1.85D5    ! timeJ: shock age (years)
1.00D5    ! duration_max: max. shock duration (years)
-----------------------------------------------------------------
```

Shock parameters

The shock and environmental parameters define the initial conditions of both the shock and the medium through which the shock wave passes. The first two parameters define the type of shock and the number of fluids ('Nfluids') considered in the integration. As explained in Chapter 2, a C-type shock ('C') should be run with 2 or 3 fluids, while both a J-type shock ('J') and

the steady state equilibrium run ('S'), which is used to calculate the chemical equilibrium conditions and is not a shock, require only 1 fluid. To run a J-type shock with magnetic precursor the flag 'C' and a multi-fluid model should be selected in order to accurately calculate the structure of the precursor. Computationally, 'single fluid mode' means that the dynamical parameters in the ion and electron fluids are set equal to those in the neutral fluid: $v_{\rm i} = v_{\rm n}$ and $T_{\rm i} = T_{\rm e} = T_{\rm n}$. In the two-fluid mode, the electron temperature is set equal to the ion temperature, $T_{\rm e} = T_{\rm i}$, while $T_{\rm n}$ has a distinct value. In the three-fluid mode differential equations are solved for all fluids and, initially, the three temperatures are not equal.

The scaling relation $B(\mu{\rm G}) = b[n_{\rm H}(cm^{-3})]^{0.5}$ is adopted in order to calculate the initial magnetic flux, where b is 'Bbeta' in the input file. Ideally, b should be determined observationally, but this is not generally feasible. The value of $b \approx 1$ is consistent with equipartition of magnetic energy: therefore, 'Bbeta' = 1 is used in the modelling work presented in this Thesis, unless stated otherwise.

The charged fluid velocity should always be smaller than that of the neutral fluid; therefore, initial velocities are required for both the neutral and charged fluids. In practice, what is done is to assign the shock velocity, 'Vs', to the neutral fluid and to subtract a small number from this to give the charged fluid velocity. If the shock velocity is very much larger than the initial velocity difference between the fluids, as is the case for the models presented in Chapter 5 and Appendices G and F, the code is not sensitive to this parameter. The shock velocity is input in km s^{-1} while the velocity difference is given in cm s^{-1}: the value of 10^3 cm s^{-1} that is found in the reproduction of the input file above was used throughout.

The initial ortho-to-para ratio of H_2 is set by 'op_H2'. In the cold gas of a molecular cloud the equilibrium value of the ortho-to-para ratio is small (< 0.1 at $T < 25$ K). In the hot gas produced by a shock wave, para-H_2 is converted to ortho-H_2 by nuclear spin changing reactions with H^+. As shown by Wilgenbus

et al. (2000), the local ortho:para ratio increases to a value of 3 immediately behind the shock wave (assuming that it has become thermalized through proton transfer reactions with H^+ and H_3^+). The observations of ro-vibrational H_2 emission from HH objects comprise emission lines from H_2 levels of both ortho (J odd) and para (J even) symmetry and hence reflect the variation of the ortho:para ratio through the shock wave. However, the observations do not yield N(ortho)/N(para), as the contributions from the levels of the vibrational ground state, whose populations become significant in the cooling flow, are not generally observable. Rather, the observations (of excited vibrational levels) reflect the value of the ortho:para ratio in the region of the hot gas in which the corresponding levels are preferentially excited and where the ortho-to-para ratio is expected to have the LTE value of 3. For this reason 'op_H2' was taken to be 3 in all the modelling work presented in this Thesis. Any systematic departure of the ortho:para ratio from its value in LTE would manifest itself as a downwards displacement of the ortho levels in the excitation diagram (cf. Wilgenbus et al., 2000); no such shift was discernible in the comparison with the models presented in Chapter 5.

The initial temperatures of the gas and grains can be specified; however, unless a very low velocity shock is modelled these parameters do not, in practice, have an important effect because the 'memory' of these temperatures is rapidly lost in the passage of the shock wave. Of more importance is the initial density, which is important in determining the rate of collisions in the gas. The steady state equilibrium conditions (the relative abundances of chemical species), which are dependent upon the assumed density should be calculated for each new density before a shock model is run.

Environment

The three environmental parameters refer to the rate of cosmic ray ionization ('zeta'), the strength of the ultraviolet background radiation field ('rad') and the amount of extinction in the gas cloud ('Av'). The cosmic ray ionization

rate above, ζ=5×10^{-17} s^{-1}, was used in all models. The parameter for the strength of the background radiation field is a multiplicative one and a value of 1 corresponds to the mean background interstellar UV radiation field of Draine (1978). 'Av' refers to the extinction between a source of UV radiation and the object being modelled: a value of 0 indicates no extinction. The effect of photionization processes, which are perhaps induced by the background interstellar UV radiation field, on the fit of the model to the observations was investigated for every object considered. For want of more specific information, rates corresponding to the mean interstellar background UV radiation field and zero extinction were assumed in every instance: further details are discussed in Section 4.2.

Numerical parameters

The number of H_2 levels, 'NH2_lev', included in the model should be enough that the cooling is accurately modelled. However, using a large number of levels can slow down the calculation considerably. Population transfer in collisions with H_2 and He (Le Bourlot et al., 1999), with grains (Pineau des Forêts et al., 2001) and with H (Le Bourlot et al., 1999) and (Mandy & Martin, 1993; Martin & Mandy, 1995)) is taken into account. The data for rates of collision between H and H_2 comprises two sets: quantum calculations for the first 50 energy levels, up to an energy of approximately 20 000 K above the ground state ($v = 0$, $J \leq 16$; $v = 1$, $J \leq 13$; $v = 2$, $J \leq 10$; $v = 3$, $J \leq 8$) (Le Bourlot et al., 1999) and quasi-classical trajectory calculations for 318 energy levels of H_2 up to an energy of approximately 40 000 K ($v = 0$, $J \leq 38$ to $v = 14$, $J \leq 4$) (Mandy & Martin, 1993; Martin & Mandy, 1995). It is possible to use only the quantal determinations of the rate coefficients by selecting the 'DRF' flag, whilst the data of Mandy & Martin (1993) and Martin & Mandy (1995) may be used by selecting the 'MM' flag; alternatively, a composite of the two data sets, which consists of the rate coefficients of Le Bourlot et al. (1999) for the first 50 levels and the rate coefficients of Mandy & Martin (1993); Martin &

Mandy (1995) for higher energy levels, can be used by selecting 'BOTH'. The number of H_2 lines written to the output file is limited by 'NH2_lines_out'.

As discussed in Chapter 3, the energy associated with the reformation of H_2 on the surface of grains (up to the dissociation energy of the H_2 molecule, 4.4781 eV) is split between populating the H_2 energy levels, the kinetic energy of the molecule as it leaves the grain and phonon excitations in the grain. Five assumptions regarding the distribution of the population in the H_2 molecule as it leaves the grain were described in Chapter 3: it is to these assumptions that the flag 'iforH2' refers:

iforH2 = 0 1.4927 eV goes into populating the H_2 molecule as the energy released by the formation of H_2 is split equally between the grain, the kinetic energy of the molecule and the internal energy of the molecule;

iforH2 = 1 The energy levels are populated in proportion to a Boltzmann distribution at 1.4927 eV, which is 1/3 of the dissociation energy of H_2 (4.5 eV);

iforH2 = 3 The population forms initially in the J=0 and 1 rotational levels of the v=6 vibrational level (Black & van Dishoeck, 1987): an ortho-to-para ratio of 3:1 is assumed;

iforH2 = 4 The levels are populated in proportion to the local population density.

One other possible assumption, that the H_2 is populated in the final bound state (Black & van Dishoeck, 1987), is not used because it causes numerical problems for the code.

Two assumptions regarding the proportion of the energy associated with reformation of H_2 (minus the internal energy) going into the kinetic energy of the molecule were also discussed in Chapter 3. The flag 'ikinH2' is used to select these assumptions:

ikinH2 = 1 The difference between the formation and internal energies is split equally between the kinetic energy and the energy going into the grain;

ikinH2 = 2 The lesser of (4.4781 eV - internal energy) and 1.4927 eV (1/3 of dissociation energy) goes into kinetic energy.

As discussed in Chapter 3, 'iforH2'=4 and 'ikinH2'=2 are the least selective assumptions and all of the modelling presented in this Thesis has been performed using these values.

Some parameters deal with numerical aspects of the code that should not be 'built in', such as the characteristic length scale used in the artificial viscosity, XLL, for which appropriate values typically range between 10^9–10^{12} cm. Other parameters, which are not discussed here, relate to the precision at which calculations are made and limits to the size of the output files.

Two timescales are associated with J-type shocks with magnetic precursors: the flow time at which the 'discontinuity' is introduced ('timeJ') and the maximum duration of the shock wave ('duration_max'). The maximum duration of the shock wave should be long enough that the gas has time enough to cool down to equilibrium conditions, which is set by the timescale for the slowest reactions, such as the formation of H_2 on grains. Typically, 10^5 years is sufficient for any type of shock (including C- and J-type) while 10^7 years is more appropriate for a static equilibrium calculation, in which there is no compression and little heating so reactions proceed at a slower rate than in a shock. The position of the 'discontinuity' is calculated explicitly in a J-type shock wave while there is no 'discontinuity' introduced into a C-type shock wave or the static equilibrium calculation: therefore, 'TimeJ' should be set greater than 'duration_max' for these types of calculations.

There are various checks that can be made on the accuracy and reliability of the calculation: here the most relevant to this project are listed. It was ensured

that mass, momentum and energy are conserved and it was also verified that the artificial viscosity plays a significant role only within the 'discontinuity' and that the change in temperature and density over the 'discontinuity' agree with that expected from the Rankine-Hugoniot relations. At each step in the integration we also check that the sum of the relative level populations of the all the species for which level populations are calculated is equal to one. Finally, for the atomic and ionic species, we check that the thermal energy going into exciting the species is equal to the radiative energy emitted.

4.2 Approach to Modelling

In Chapter 5, modelling of H_2, [Fe II] and [C I] emission observed towards HH outflows is described. It was found that it was not possible to reproduce the observed atomic and ionic emission with the same shock model used for the H_2 emission: a higher degree of ionization was required. Pure J-type shocks can provide the levels of ionization, notably of H, required to model the atomic and ionic emission. Accordingly, it was suggested that the atomic and ionic emission may arise in regions of higher ionization, distinct from those responsible for the H_2 emission: at the apex of a bow shock or in a reverse shock, within the jet, for example. This mechanism, and the bow shock theory in particular, has become favoured as high resolution observations have shown that HH objects often display a bow shock shape with ionic emission seemingly slightly displaced from the H_2 emission, for example HH99 (Davis et al., 1999) and HH7 (Smith et al., 2003). The combination of a pure J-type shock and either a pure C-type shock, or a J-type shock with magnetic precursor, may be viewed as an elementary representation of a bow shock. For objects in which both H_2 and [Fe II] were observed, such a composite model was employed, while models containing a C-type shock component were used for objects that were observed only in H_2 emission. In what follows, the process by which the H_2 emission was simulated and the constraints upon the J-type shock component are explained.

4.2.1 Models of H_2 emission

The optimal values of the shock speed and pre-shock gas density were determined by comparison of the model predictions (calculated in a grid in the ranges $v_s = 0$–v_{crit} km s^{-1} and 10^3–10^6 cm^{-3}, respectively) with observations. The shock velocity at which at discontinuity occurs in the flow is defined as v_{crit} (see Chapter 2 for more detail). Two additional parameters are the age of the shock wave, which determines the extent of the magnetic precursor, and the degree of ionization in the pre-shock gas, which may be affected by, for example, the background ultraviolet radiation field. It is often assumed that HH outflows are shielded from UV radiation by the molecular clouds in which they reside. However, work presented in this Thesis has shown that HH outflows may be affected by nearby UV sources or other sources of ionizing radiation and that, in such cases, the model fits to the observed H_2 emission can be improved by the inclusion of photoionization effects (see Chapter 5 and Giannini et al., 2004; M^{c}Coey et al., 2004). In addition (and as discussed in the Introduction), the cavities that occur in star forming molecular clouds can be quite low-density ($n_H \approx 10^4$ cm^{-3}) and it could also be envisaged that weak UV sources, such as Herbig Ae stars, within the cloud could also affect emission from outflows. Furthermore, Gredel (1994) suggested that X-rays from T Tau stars in dark clouds could similarly photoionize the gas in star forming regions: although it should be noted that photoionization due to X-rays are not included in the model. Accordingly, the effect of including photoionization upon the fit of the models to the observations of every HH object considered was systematically investigated. The influence of photoionization processes on the degree of ionization in the gas was simulated by including reactions for species with ionization potentials less than that of H (13.6 eV): that is, C, S, Fe and Si. For want of more specific information, rates corresponding to the mean interstellar UV radiation field in the solar neighbourhood (Draine, 1978) were adopted.

When comparing model predictions with observations, it is important to re-

member that several quite different models (e.g., low pre-shock density and high shock velocity compared with high pre-shock density and low shock velocity) can produce quite similar (although not identical) excitation conditions. Therefore, data spanning a wide range of energies are required to identify a unique model. Observed quantities are typically line fluxes/intensities and can also yield column densities (divided by statistical weight), which can be presented graphically as excitation diagrams. Shock excitation in astrophysical outflows, particularly that in HH outflows, is marked by the large number of H_2 ro-vibrational transitions observed. The abundance of H_2 lines and the effects of the shock parameters upon the excitation diagram, which were described in Chapter 3, makes them an especially useful tool for constraining possible models. The fitting of a model to the excitation diagram is done interactively and by eye. In general, a good fit is achieved through systematic application of the following considerations:

- The strongest emphasis is placed on the fit of the model to the most accurately measured values of $\ln(N/g)$, which are typically those derived from transitions from low lying energy levels.

- Each type of shock produces quite a distinct excitation diagram. If the population lies close to the median curve and is nearly thermalized, then a J-type shock or a very young J-type shock with a magnetic precursor will be an appropriate model. Divergence from LTE and little population in the higher energy levels indicate that either a C-type shock or a more evolved J-type shock with magnetic precursor is required.

- The divergence from LTE is also strongly affected by the pre-shock density: high pre-shock densities result in a more thermalized distribution of populations.

- For a given pre-shock density, the values of $\ln(N/g)$ are more sensitive to the shock velocity than any other parameter.

- H_2 emission from an object that has not reached equilibrium may have characteristics of emission from both C- and J-type shocks: in other words, a J-type shock with magnetic precursor. The population in the higher energy levels is increased (or decreased) by introducing the 'discontinuity' at an earlier (or later) flow time.

- Finally, the inclusion of photoionization processes increases the tendency to LTE and can also cause the population in the $v = 1$ levels to increase.

4.2.2 Models of atomic and ionic emission

The atomic and ionic emission is assumed to arise in a J-type shock. Under 'normal' interstellar conditions, Fe is strongly depleted from the gas phase, and most of the elemental abundance of Fe (3.23×10^{-5}: Anders & Grevesse (1989)) is to be found in the grains, probably in the form of silicates. However, this equilibrium abundance of gas phase Fe is much smaller than that found from analysis of observed [Fe II] lines and so is too small to reproduce observed emission: therefore, the gas phase abundance of Fe must be increased by the release of Fe from grains. In shock waves, dust grains may be shattered in grain–grain collisions (Jones et al., 1994, 1996; Flower & Pineau des Forêts, 2003). However, this process breaks large grains into smaller grains, rather than releasing elements such as Fe into the gas phase. In a J-type shock, all fluids flow at the same velocity and, because the rate of grain erosion is assumed to be directly dependent upon the velocity difference between the fluids, grain erosion does not occur in J-type shocks in the context of the model. On the other hand, the velocity difference between the neutral and charged fluids in C-type shock waves gives rise to collisions between neutrals, such as CO, and charged grains which are sufficiently energetic to result in the erosion of the refractory grain cores (May et al., 2000). Thus, if a C-type shock wave, or a J-type shock with a magnetic precursor, has passed previously through a given region, the fraction of Fe in the gas phase could be significant (providing that there has been insufficient time for grains to reform). For dynamically young

objects, such as those we study and which are subject to episodic events on time scales of the order of 500–1000 yr or less (e.g., Reipurth & Bally, 2001) it seems reasonable to treat the gas phase abundance of Fe as a variable.

J-type shocks which cause significant ionization of H are highly dissociative and do not produce strong emission in H_2. Nonetheless, the combined H_2 emission from the pure J-type shock and the H_2 model must remain consistent with that observed. Furthermore, the pure J-type shock should have a pre-shock density similar to that of the corresponding H_2 model and should include photoionization effects if the H_2 model does (although this is less significant in the context of the J-type component).

In the models found for each object (and listed in Table 5.1 in Chapter 5), a J-type shock with emission consistent with the model of H_2 emission was first found and then the initial gas phase abundance of Fe was varied in order to reproduce the observed [Fe II] emission. The intensities of the [Fe II] lines are relatively insensitive to changes in temperature above 10^4 K, because the levels from which emission arises are close together at $1.1–1.3\times10^4$ K above ground. Consequently, the [Fe II] lines are more sensitive to the abundance of Fe in the gas phase than to the shock velocity, once this is sufficient to give rise to partial ionization of hydrogen.

Chapter 5

Astrophysical Applications: Herbig-Haro Outflows

Shock models were used to reproduce the IR (0.98–2.5 μm) H_2, [Fe II] and [C I] emission observed towards 14 objects observed in HH outflows (HH72A, HH72D, HH26A, HH25C, HH320A, Knot 4, HH120, HH111F, HH240A and HH99, which comprises five knots labelled A, B0, B1, B2 and B3). The modelling work presented here uses the observations of Nisini et al. (2002); Giannini et al. (2004); M^{c}Coey et al. (2004), who obtained spectra in the 0.98–2.5 μm range of HH outflows. It should be noted that the modelling results presented here for HH72A, HH26A, HH25C, HH320A and HH99 derives largely from the published material of Giannini et al. (2004) and (M^{c}Coey et al., 2004).

General modelling results are given in the forthcoming Section, while model results and discussion specific to each object are presented in Sections 5.2.1-5.2.7. The modelling results are discussed in a more general sense in the final Section (5.3) of this Chapter.

5.1 General results

It was found that non-equilibrium J-type shock models with magnetic precursors were required in order to model the H_2 emission in all of the the objects

except for HH25C. Steady state C-type shocks underestimated the populations in the higher energy levels, while J-type shocks underestimated the population in the lower energy levels. Taking HH99B3 as an example, the excitation diagrams resulting from C- and J-type shocks are plotted with the observations in Figure 5.1; these shock models have the same velocity as that used for the J-type shock with magnetic precursor, whose fit to the observations is shown in Section 5.2.7 below.

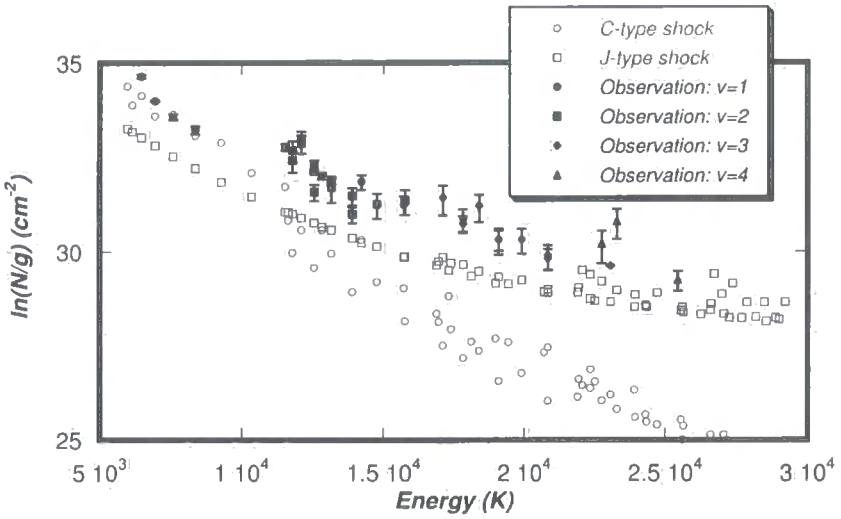

Figure 5.1: A demonstration that neither pure C- or J-type shocks can reproduce the observed H_2 emission in HH99B3.

However, it was not possible to reproduce the observed atomic and ionic emission with the J-type with magnetic precursor shock models used for the H_2 emission. The [Fe II] and [C I] lines were underestimated by several orders of magnitude because the degree of ionization in the shock ($x_e \approx 10^{-5}$) is too low for collisions with electrons (or H) to cause sufficient excitation of Fe^+ or C. Instead, it was found that pure J-type shocks can provide the necessary levels of ionization, notably of H, to reproduce the observed [Fe II] and [C I] emission. On the basis of observations, it has been suggested that atomic and ionic emission may arise in regions of higher ionization, distinct from those responsible for the H_2 emission: at the apex of a bow shock or in a reverse

shock, within the jet, for example (e.g., Smith et al., 1991; Davis et al., 1999; Smith et al., 2003). The combination of a pure J-type shock and either a pure C-type shock, or a J-type shock with magnetic precursor, may be viewed as an elementary representation of a bow shock. Attempts to reproduce the observed emission (molecular, atomic and ionic) using such a combination of models proved successful and shall be presented in Sections 5.2.1–5.2.7 below. These elementary bow shock models required that Fe be present in greater than 'normal' abundances in the gas phase, perhaps as a result of grain erosion by a previous shock: this assumption was discussed in the previous Chapter.

The model parameters (the age used in the models of H_2 emission, the percentage of Fe in the gas phase used in the J-type shock models and the shock velocities and pre-shock densities for both types of model) for each object are listed in Table 5.1. The H_2 lines fluxes observed in the regions of HH72, HH26, HH320 and HH99 are listed in Appendix E; the observations towards HH120, HH111F and HH240 are published in Nisini et al. (2002). The predicted [Fe II] and [C I] line intensities are listed with those observed, for comparison, in Appendix D.

Table 5.1: Parameters for models of H_2 emission and for J-type shock models used for each object. No J-shock component was modelled for objects in which less than two [Fe II] lines were observed.

	Model of H_2 emission				J-type shock		
Object	v_s (km s^{-1})	n_H (cm^{-3})	Age (yr)	Photo-ionization	v_s (km s^{-1})	n_H (cm^{-3})	%Fe in gas phase
HH72A	31	10^4	165	Yes	44	10^4	23
HH72D	30	10^4	185	Yes	-	-	-
HH26A	50	10^4	70	Yes	50	10^4	6
HH25C (model 1)	45	10^4	> 260	Yes	-	-	-
HH25C (model 2)	27	10^5	> 680	Yes	-	-	-
HH320A	39	10^4	220	No	-	-	-
Knot 4	40	10^4	220	No	-	-	-
HH120	49	10^4	70	Yes	50	10^4	34
HH111F	36	10^4	100	Yes	39	10^5	8
HH240A	40	10^4	100	Yes	50	10^5	8
HH99A	34	5×10^3	350	Yes	50	5×10^3	12
HH99B0	34	10^4	130	Yes	50	10^4	25
HH99B1 (slit 1)	30	10^4	190	Yes	50	10^4	1
HH99B1 (slit 2)	30	10^4	165	Yes	50	10^4	24
HH99B2	33	10^4	125	Yes	50	10^4	71
HH99B3	33	10^4	115	Yes	50	10^4	37

5.2 Comparisons of model predictions with observations

5.2.1 L1660 region: HH72A and HH72D

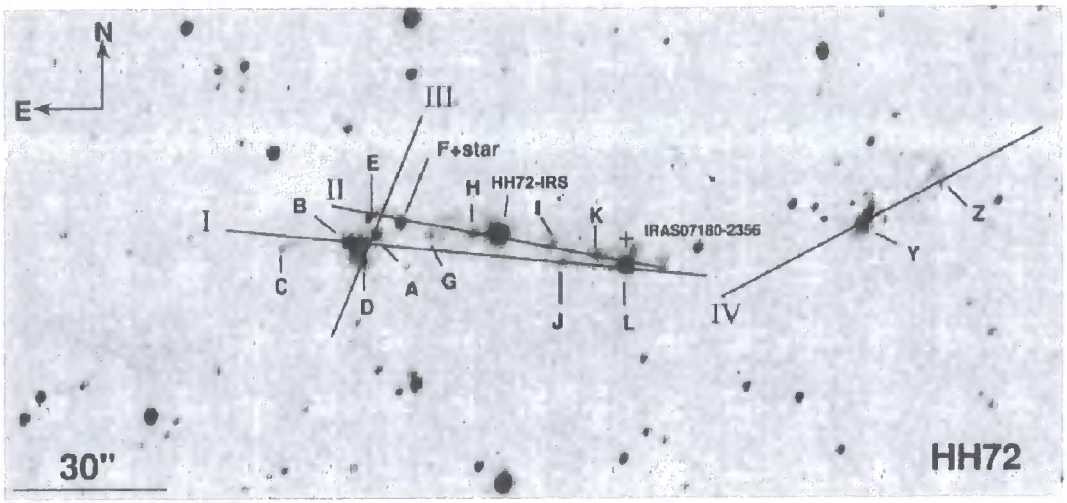

Figure 5.2: (Figure 2 of Giannini et al. (2004)) H_2 2.122 μm image of the L1660 region with SOFI slits superimposed. HH72-IRS, the source of the outflow is indicated by a cross.

The L1660 region, in which the HH72 outflow resides, is a bright-rimmed core illuminated by the young OB cluster NGC2362 in Vela (Reipurth & Graham, 1988), and lies at a distance of $\approx$ 1500 pc (Hilton & Lahulla, 1995). An E-W, poorly collimated outflow (Schwartz et al., 1988) is present in the region, driven by the intermediate mass class 1 source HH72-IRS (Reipurth et al., 1993, $L_{bol} \approx 170 L_{\odot}$). The chain of HH objects (HH72 A–C) was discovered by Reipurth & Graham (1988), who suggested that the L1660 region is slowly being destroyed by the UV emission from the OB cluster. Figure 5.2 shows the SOFI 2.12 μm image of the region (Giannini et al., 2004), where, together with the HH objects, several knots (or condensations) are recognizable (HH72 D-Z). Three distinct chains of objects, which are overlaid by slits I, II and IV in the image (Figure 5.2, can be seen and perhaps suggest some precession in the outflow source. HH72A, B and D appear to form a bow shock shape with HH72B at the apex and HH72D seemingly lying further away from the

apex than HH72A. HH72C lies further out from HH72-IRS than HH72 A, B and D and may perhaps be the result of an earlier outflow event. Giannini et al. (2004) found that the strongest H_2 emission arose in HH72A and B (with HH72B exhibiting the stronger emission of the two) but that HH72A was strongest in [Fe II] emission. As the [Fe II] lines are of particular interest to this study, it was decided to model the emission from HH72A. Giannini et al. (2004) found that the condensation HH72D exhibited the strongest and richest H_2 spectrum of all the condensations in the region and, in order to investigate any differences between HH objects and condensations, the H_2 emission from HH72D was also modelled.

HH72A

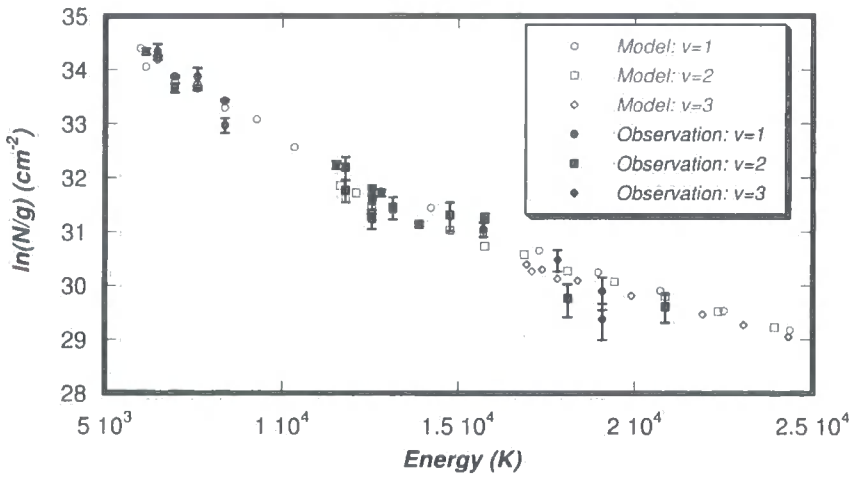

Figure 5.3: Observed and computed excitation diagrams for HH72A. Transitions from the $v = 1$, $v = 2$ and $v = 3$ vibrational manifolds are denoted by circles, squares and diamonds, respectively. Open symbols represent the models and filled symbols the observational results.

In Figure 5.3 the excitation diagrams derived from the model (open symbols) and the observations (corresponding filled symbols) are shown. The observations extend up to approximately 2×10^4 K above ground and include v=1, 2

and 3 vibrational levels. At successive vibrational thresholds, the observational points do not depart notably from the median curve, indicating that there is a high degree of thermalization at the local temperature. Models with initial densities less than 10^4 cm^{-3} yield lower column densities which diverge more evidently from the median curve at each vibrational threshold. Conversely, models with initial densities higher than 10^4 cm^{-3} produce level populations which are closer to LTE, but the curvature of the Boltzmann plot is not consistent with that observed. This analysis was used in the determination of the best-fitting model for each object.

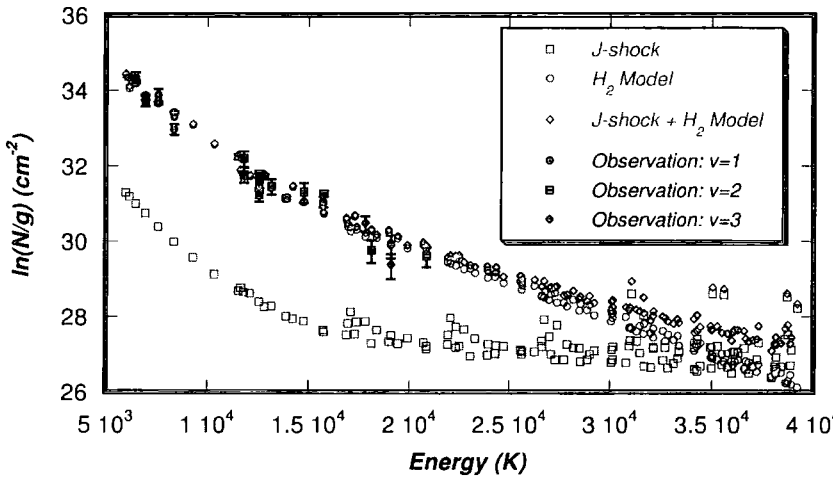

Figure 5.4: Excitation diagrams from the models of H_2 emission and pure J-type shock component for HH72A. The effect of the J-type shock is seen from the sum of the two components, denoted "J-shock + H_2 model"). The contribution to the H_2 emission from the J-type shock is not significant over the range of the observations.

The excitation diagrams from the pure J-type shock model and the J-type shock with magnetic precursor model are plotted in Figure 5.4 together with their sum. It can be seen that the contribution to the H_2 emission from the J-type shock is not significant over the observed range of excitation energies; only above 3×10^4 K does the H_2 emission from the J-type shock become important.

It may also be illuminating to consider the excitation diagram of the Fe^+ level

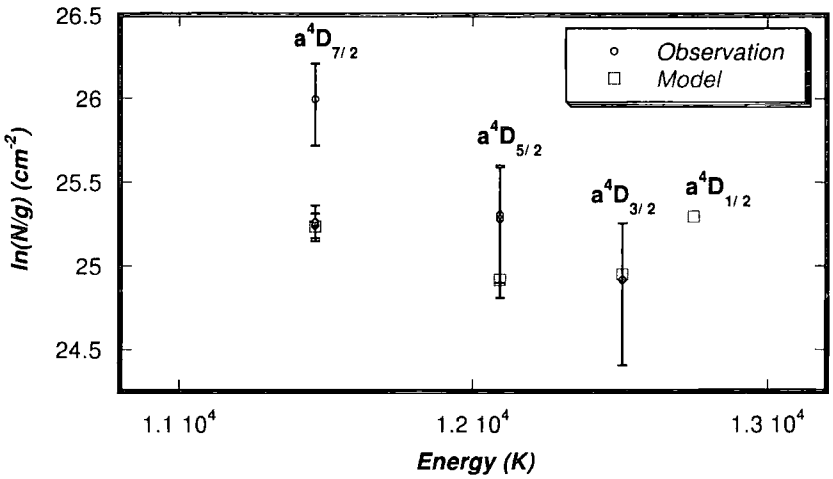

Figure 5.5: Excitation diagrams from unblended observed lines of [Fe II] with S/N>3 (circles), compared with the predictions of the models (squares) for HH72A.

populations predicted by the model (squares) and derived from observation (circles), which is shown in Figure 5.5 where each level of the a^{4}D term is labelled for reference. In theory, the values of $\ln(N/g)$ derived from the observations should be the same for each transition from the same level. Clearly, this is not this case: there is a factor of about 2 between values of $\ln(N/g)$ derived from transitions from the a^{4}D$_{7/2}$ level. Similar discrepancies are evident for almost all the objects discussed in this Thesis. It seems likely that the problem is either an observational one or related to the reddening correction. For the three energy levels from which transitions are observed, the model predictions lie within the error bars and the spread of the observational points. The model predicts that most of the Fe^+ population should lie in the a^{4}D$_{1/2}$ level (the highest energy level of the a^{4}D term): a prediction that does not seem to be borne out by the observations, which show no transitions from that level. The intensities of transitions from the a^{4}D$_{1/2}$ level (the 1.271 and 1.664 μm lines) are observed to be less than the lowest intensity of any [Fe II] line observed towards HH72A (6.9×10^{-5} erg cm^{-2} s^{-1}) for most objects (see Table D.2 in Appendix D). This may suggest that the intensity of transitions from

the $a^4D_{1/2}$ level may be below the detection limit for HH72A.

The intensities of [Fe II] and [C I] lines predicted by the model are compared with those observed in Table D.2 in Appendix D. The computed [Fe II] intensities are all within the error bars of the the observed intensities with the exception of the 1.321 μm line, which is underestimated by the model. However, it should be noted that this transition arises from the same energy level as the 1.644 and 1.257 μm lines, whose strong emission are well modelled. Furthermore, the population computed for this energy level is in very good agreement with that derived from these two observed line intensities. In contrast, the population derived from the observed 1.321 μm line intensity seems anomalously large. Finally, the [C I] lines poorly modelled: they are underestimated by up to a factor of 7.

HH72D

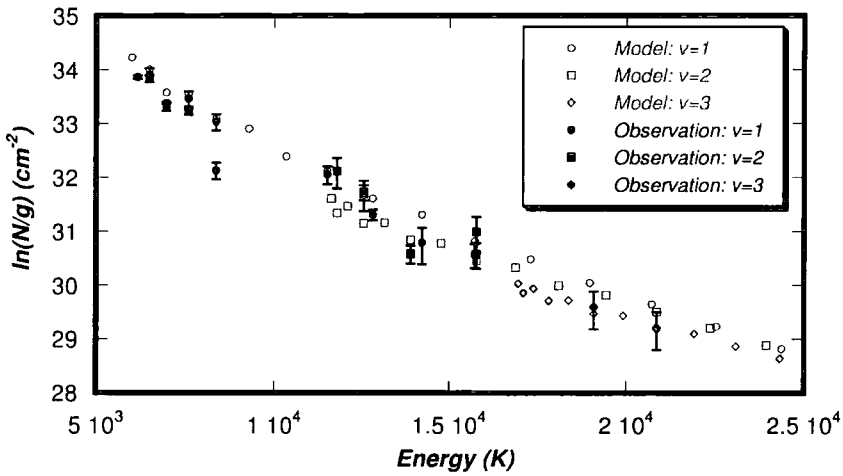

Figure 5.6: Observed and computed excitation diagrams for HH72D. Transitions from the $v = 1$, $v = 2$ and $v = 3$ vibrational manifolds are denoted by circles, squares and diamonds, respectively. Open symbols represent the models and filled symbols the observational results.

The H_2 excitation diagram for HH72D is very similar to that of HH72A (see

Figure 5.6): H_2 emission is observed from the same vibrational levels, up to the same energy, and the degree of LTE is similar. In fact, the range of vibrational levels from which H_2 emission is observed from HH72D is unusual in this outflow: all of the other condensations exhibit H_2 emission from $v \leq 2$ (see Table E.3 in Appendix E). The values of $\ln(N/g)$ are slightly lower for HH72D especially at higher energies and this is reflected in the model for HH72D, which has a slightly lower shock speed and greater age than that found for HH72A. The similarity of the models for the H_2 emission and the proximity of HH72A and HH72D implies that the molecular gas in both objects is excited under the same conditions, possibly by the same shock wave.

5.2.2 HH24-26 region: HH26A and HH25C

Located in the L1630 Orion dark cloud (d $\approx$ 400 pc Anthony-Twarog, 1982), the HH24-26 region is an active site of star formation, rich in young stellar objects at different evolutionary stages. Two low luminosity, Class 0 protostars (Andre et al., 2000), HH24MMS (Chini et al., 1993, L_{bol}=5$L_\odot$) and HH25MMS (Bontemps et al., 1995, L_{bol}=6$L_\odot$) drive distinct compact jets, traced by means of both the 2.12 μm H_2 line and CO mm transitions (e.g., Gibb & Little, 1998), while the Class I protostar HH26IR (Davis et al., 1997, L_{bol}=28.8$L_\odot$) gives rise to the more extended molecular outflow (Gibb & Heaton, 1993). Herbig-Haro objects (HH24, HH25 and HH26) are associated with each of these three sources. Imaging in the 2.12 μm H_2 rovibrational line (Davis et al., 1997, see Figure 5.7) reveals a string of shocked condensations along the axis of the HH25MMS and HH26IR outflows, which lie orthogonally to each other and intersect near to HH25C. Both of these outflows describe an arc which may be due to density gradients in the region; large scale magnetic fields; or, the proper motions of HH25MMS and HH26IR (Davis et al., 1997). The curvature is unlikely to be due to wandering of the jets, which tends to result in an S-shaped curvature of the outflow. Far infrared spectra of the region were obtained by Benedettini et al. (2000), who interpreted the observed emission

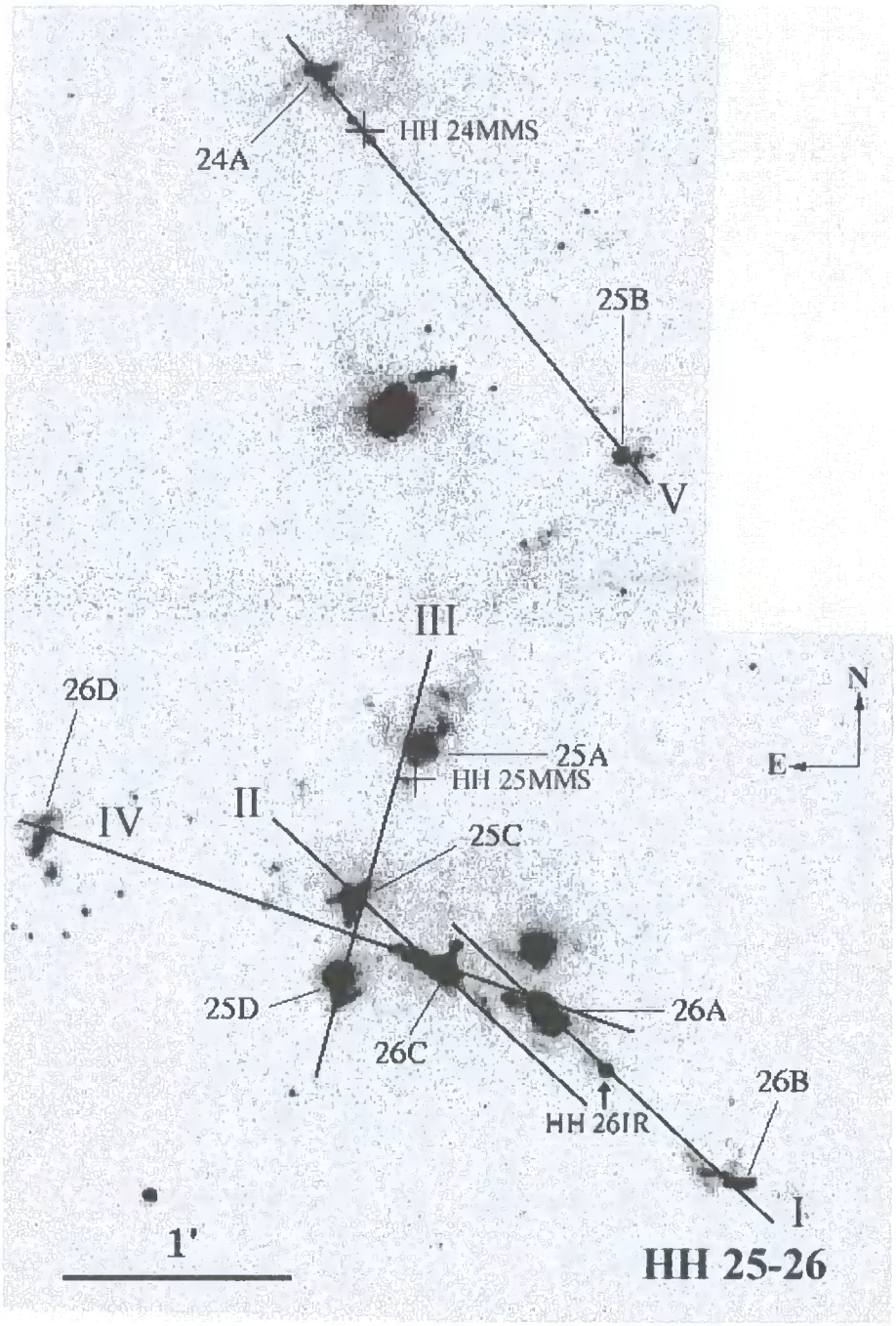

Figure 5.7: (Figure 1 of Giannini et al. (2004)) The positions of the SOFI slits of Giannini et al. (2004) are superimposed on the H_2 2.122 μm of Davis et al. (1997). The exciting sources of the outflows, HH24MMS, HH25MMS and HH26IR, are indicated by crosses.

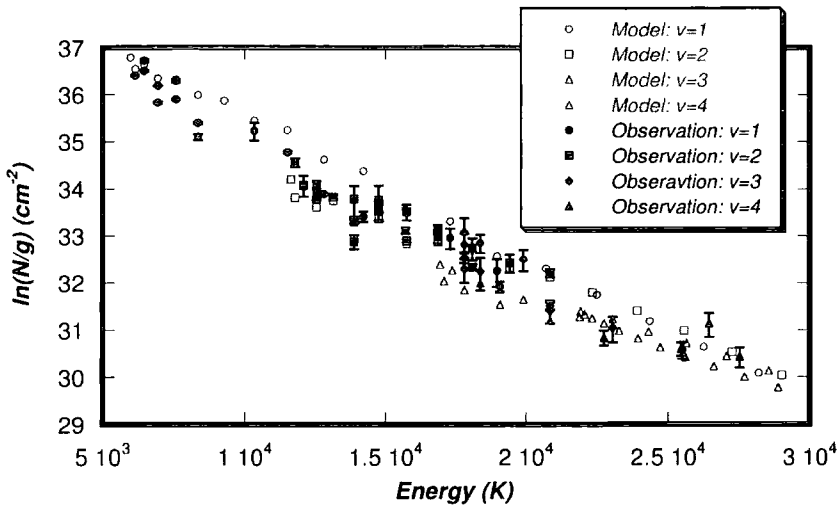

Figure 5.8: Observed and computed excitation diagrams for HH26A. Transitions from the $v = 1$, $v = 2$, $v = 3$ and $v = 4$ vibrational manifolds are denoted by circles, squares, diamonds and triangles, respectively. Open symbols represent the models and filled symbols the observational results.

(from [O I], CO, H_2O and H_2 lines) as due to a mixture of both C- and J-type shocks. Giannini et al. (2004) found that the HH object HH26A was the richest in both H_2 and [Fe II] lines in the region and, therefore, the most suitable candidate for modelling work. HH25C is a typical condensation, and the richest such object in the region. Comparison with HH26C, an HH object which exhibits a similar spectrum over the v=1 and 2 levels to HH25C, showed that emission from $v = 3$ and 4 levels might be expected from HH25C; Giannini et al. (2004) concluded that this indicated different excitation conditions for HH25C and HH26C.

HH26A

The observed points in the H_2 excitation diagram extend, in the case of HH26A, to almost 3×10^4 K and include emission from the $v = 1$–4 vibrational states: see Figure 5.8. The column densities are larger than observed in HH72A, implying a higher shock speed, and show a similar degree of departure from

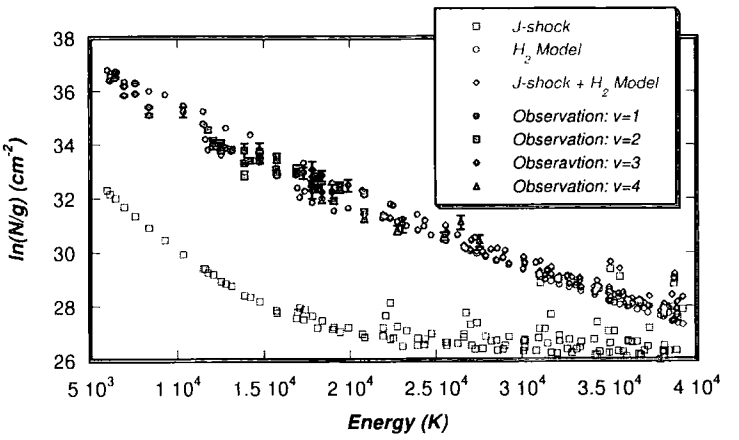

Figure 5.9: Excitation diagrams from the models of H_2 emission and pure J-type shock components for HH26A. The effect of the J-type shock is seen from the sum of the two components, denoted "J-shock + H_2 model"). The contribution to the H_2 emission from the J-type shock is not significant over the range of the observations.

LTE. The higher shock speed used for HH26A results in a higher rate of H_2 cooling and so the shock is narrower than HH72A; it is for this reason that the model of HH26A has a smaller age than HH72A.

The model of HH26A yields column densities of levels with $v = 1$ which exceed the observations beyond approximately 10^4 K (cf. Figure 5.8); this is symptomatic of a more general tendency of the models to overestimate the populations of the levels in the $v = 1$ manifold. Such a tendency may point to an overestimation of the rates of vibrationally inelastic $v = 0 \rightarrow v = 1$ collisions. The model of HH26A has the highest shock speed of all the objects considered and hence has the largest fractional abundance of H, owing to collisional dissociation of H_2. As the rate coefficients for vibrational excitation of H_2 by H are much larger than for excitation by He or H_2, a larger H abundance exacerbates the effect of any systematic error in the H-H_2 collisional rate coefficients. However, it should be stressed that there is no independent evidence to confirm the existence of such a systematic error.

The excitation diagrams from the J-type shock, the model for the H_2 emission

and their sum are plotted in Figure 5.9. The J-type shock makes no significant contribution to the H_2 emission over the range of the observations and only becomes important above 3.5×10^4 K. Only the two strongest lines of [Fe II], 1.644 and 1.257 μm, are observed towards HH26A. The predicted intensities of these lines lie within the error bars of the observations. Both of these lines originate in the same energy level, thus, an excitation diagram would not be instructive. The [C I] lines are, once again, underestimated but to a lesser extent than for HH72A. However, it is of note that the column density of C predicted by the J-type shock model for HH26A of 3.8×10^{17} cm^{-2} is exactly the upper limit to the column density found by Gibb & Little (1998).

HH25C

HH25C is an condensation which is observed in v=1 and 2 lines of H_2, at excitation energies extending up to $\approx 1.5 \times 10^4$ K, beyond which there are only upper limits on the line intensities and the column densities of the corresponding levels. No [Fe II] or [C I] emission was observed towards HH25C.

Two models of HH25C could be found, whose parameters are given in Table 5.1. Both the models are of C-type shocks in steady state, and the flow time through the shock wave provides only a lower limit to its age. The models are compared with the observations of HH25C in Figure 5.10. Regarding the levels which are definitely observed, with excitation energies less than about 1.5×10^4 K, the model with the lower density (and higher shock speed) provides perhaps a better fit: the column densities of the v=1 levels are overestimated and those of the $v = 2$ levels are underestimated to a greater extent by the higher density (and lower velocity) model 2. On the other hand, the predictions of the higher density model are more consistent with the observational upper limits at excitation energies above 1.5×10^4 K. Straight line fits to the theoretical data yield excitation temperatures of 2770 K for model 1 and 2130 K for model 2; the latter result is more consistent with the value of $\approx$ 2300 K obtained by fitting to the observational data.

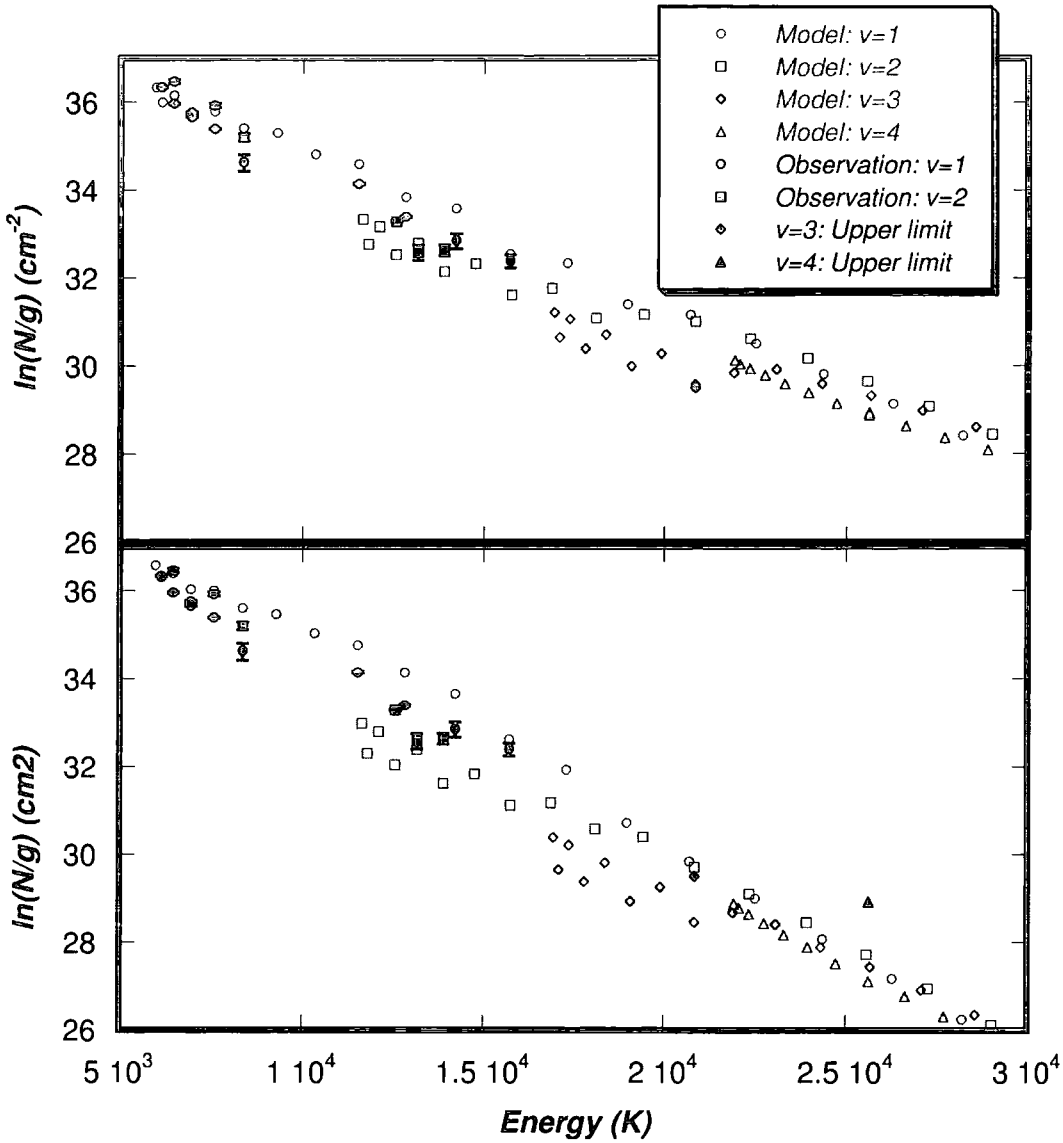

Figure 5.10: Observed and computed excitation diagrams for HH25C. Transitions from the $v = 1$ and $v = 2$ vibrational manifolds are denoted by circles and squares, respectively. Open symbols represent the models and filled symbols the observational results.

5.2.3 BHR71 region: HH320A and Knot 4

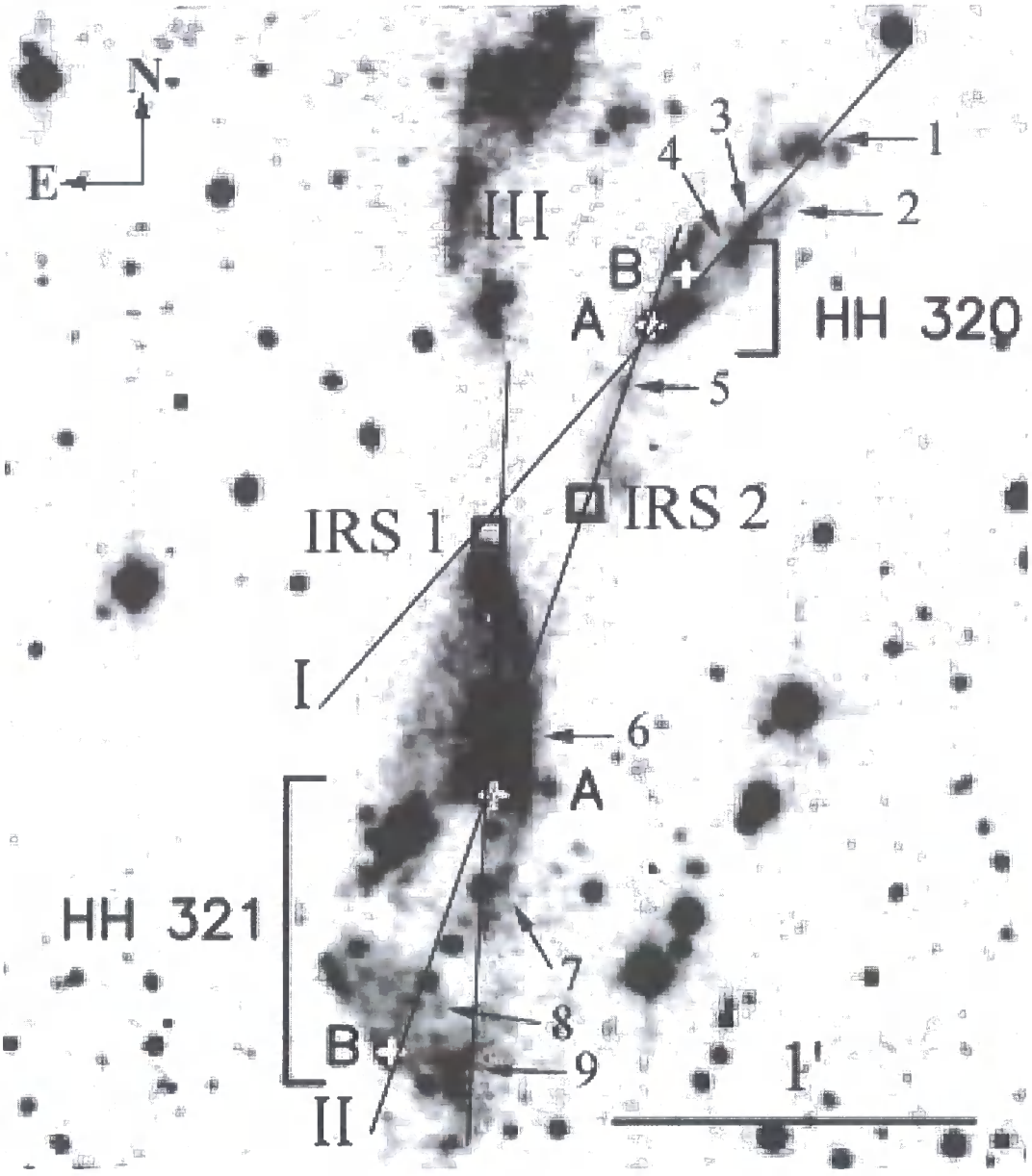

Figure 5.11: (Figure 3 of Giannini et al. (2004)). The positions of the SOFI slits of Giannini et al. (2004) are superimposed on the H_2 2.12 μm image of BHR71 of Bourke (2001). The two driving sources IRS1 and IRS2 are indicated by rectangles and, together with HH objects 320A/B and 321A/B, the pure H_2 emission knots identified by Bourke (2001) are labelled 1–9.

Figure 5.11 shows the H_2 2.12μm image by Bourke (2001) of the Bok globule BHR71 (Bourke et al., 1995), which is located at a distance of $\approx$ 200 pc (Sei-

densticker & Schmidt-Kaler, 1989). An embedded binary protostellar system, separated by $\approx$ 3400 AU, has been found in the region (Bourke, 2001). One of the two sources has been identified as a Class 0 protostar, IRS 1, ($L_{bol} \approx 9 L_{\odot}$) by means of 1.3 mm observations (Bourke et al., 1997); ISO mid-IR maps led to the discovery of the possibly more evolved source IRS 2 (Bourke, 2001). A recent study by Lemaire et al. (2002) suggests the presence of a circumstellar disk around this object. A large scale CO outflow, where a shock enhanced chemistry has been revealed (Garay et al., 1998) and which is associated with HH321A and B, is driven by IRS1 along the North-South direction. IRS2 gives rise to a more compact outflow, which is associated with HH320A and B, with an inclination $\approx$-36°. Optical [S II] images revealed HH associations (HH320 and HH321) along both the CO outflows (Corporon & Reipurth, 1997); the lack of Hα emission observed by these authors towards these objects indicates that they have a low degree of ionization. Indeed, Giannini et al. (2004) detected only H_2 emission towards the BHR71 region. They found HH320A exhibited the strongest and richest spectrum and that the strongest condensation in that outflow was Knot 4: therefore, these objects were selected for modelling.

HH320A

Levels of the first six vibrational states, with excitation energies extending to over 3×10^4 K, are observed: see Figure 5.12. The column densities observed for two levels ($(v = 3, J = 7)$, $E = 20\ 857$ K and $(v = 3, J = 9)$, $E = 23\ 070$ K) fall significantly below the mean curve in the excitation diagram. The level at $E = 20\ 857$ K has been observed twice, in two different transitions: one observation falls on the median curve, while the other, as already stated, falls below it and out of line with the remaining $v = 3$ levels. It is possible that this discrepancy arises from systematic errors (perhaps related to atmospheric absorption) in the observations and that the misalignment of the observational point at $E = 23\ 070$ K level is attributable to a similar effect. Photoionization effects were not found to enhance the fit of the model to the observations,

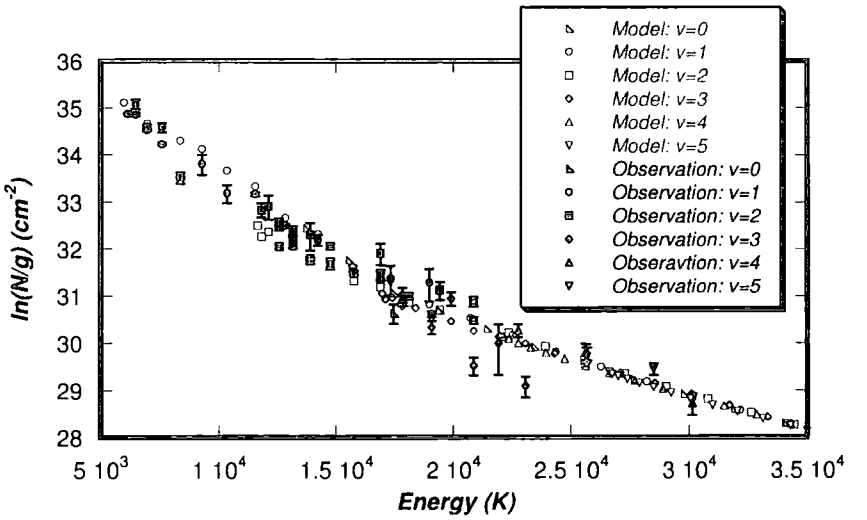

Figure 5.12: Observed and computed excitation diagrams for HH320A. Transitions from the $v = 0$, $v = 1$, $v = 2$, $v = 3$, $v = 4$ and $v = 5$ vibrational manifolds are denoted by right-facing triangles, circles, squares, diamonds, triangles and downwards triangles, respectively. Open symbols represent the models and filled symbols the observational results.

and their absence results in a wider shock wave than is the case for the other objects and thence to a greater shock age.

No atomic or ionic emission is observed towards the BHR71 region. In fact, the model is consistent with such a situation: the [Fe II] emission flux of order 10^{-18} erg cm^{-2} s^{-1} predicted by the shock model is below the detection limit of the observations: the lowest flux observed is of order 10^{-15} erg cm^{-2} s^{-1} (T. Giannini, private communication). However, the absence of both [Fe II] and [C I] lines, which were observed towards all other HH objects discussed, is particularly surprising. Here some possible reasons as to why these lines are not observed are given.

Perhaps the most extreme possibility is that there is very little Fe and C present in the gas phase of the BHR71 region because they are mainly in solid (and, in the case of C, in molecular) form, which would imply that the dust grains have undergone little erosion. Whilst such a situation cannot be discounted

by the observations of Giannini et al. (2004), it seems unlikely because the H_2 emission suggests that the gas has been been subjected to a strong shock.

Emission from [C I] and [Fe II] would not be observed if C and Fe^+ were ionized by collisions, photons or charge transfer reactions; but it should be noted that no lines of Fe^{2+} are observed in this region (there are no lines of C^+ at IR wavelengths). Furthermore, the very high [S II]/Hα ratio found by Corporon & Reipurth (1997) indicates that the region is of low excitation. The energies required for ionization of C and Fe^+ (11.26 eV and 16.16 eV, respectively) are such that, if collisional or photoionization is invoked, emission should be expected from other ions (for example, [N II]) that are not observed. Charge transfer ionization of C to C^+ is ineffective and Fe^{2+} rapidly recombines via charge transfer recombination reactions with H (Kingdon & Ferland, 1996). For these reasons, it seems unlikely that ionization is responsible for the absence of [C I] and [Fe II] emission.

Collisional deexcitation of the lines could be responsible for their relative weakness. The rate of electron collisional deexcitation of the [Fe II] and [C I] lines is of order 10^{-7} and 10^{-9} cm^3 s^{-1}, respectively: by comparison, the radiative decay rates are of order 10^{-3} s^{-1} for [Fe II] and 10^{-4} s^{-1} for [C I]. Therefore, in order for collisional deexcitation to dominate radiative decay, n_e must be greater than 10^4 or 10^5 cm^{-3}, respectively, which, in contrast to observation, would imply that hydrogen is fully ionized.

An alternative and more probable explanation is that the atomic and ionic emission arises in the apex of a bow shock or a reverse shock in the jet, where the gas has a high degree of ionization. In either case, the region of atomic and ionic emission would be small, and it is possible that the slits did not encompass fully the emitting areas. A further possibility is that the region around the HH320 has too low a degree of ionization for a J-type shock to occur at all: there are no sources of UV photons or X-rays near by and the outflow is deeply embedded in the molecular cloud, which makes penetration by a background UV radiation field unlikely. If this were the case, then the Fe

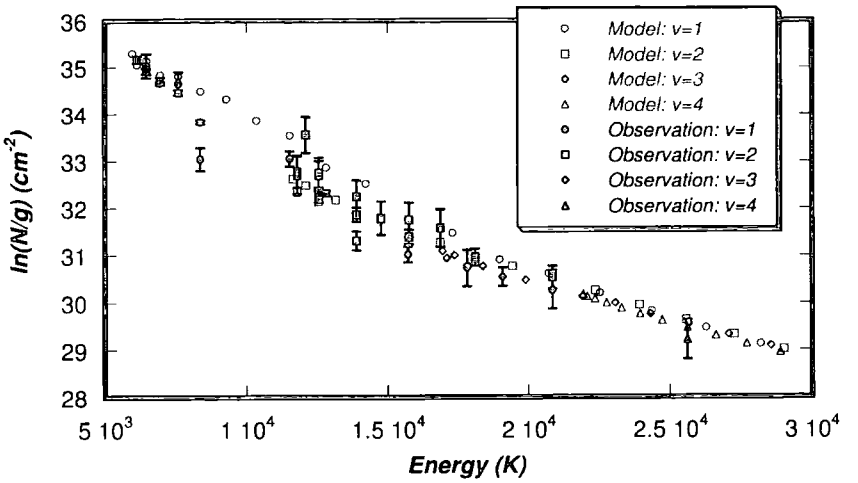

Figure 5.13: Observed and computed excitation diagrams for Knot 4. Transitions from the $v = 1$, $v = 2$, $v = 3$ and $v = 4$ vibrational manifolds are denoted by circles, squares, diamonds and triangles, respectively. Open symbols represent the models and filled symbols the observational results.

in the gas phase may not be sufficiently excited to emit strongly.

As an aside, it is interesting that [S II] is observed at optical wavelengths Corporon & Reipurth (1997) but not in the IR. The IR transitions originate in the fourth and fifth energy levels ($E > 3.5 \times 10^4$ K) of S^+, while the optical transitions originate in lower levels ($E < 2.1 \times 10^4$ K): this may place an upper limit on the temperature of the gas in the region. The peak temperature attained in the shock model is less than 2 $\times 10^4$ K.

Knot 4

Knot 4 is the final condensation that was studied and, as for HH320A, no atomic or ionic emission was observed towards this object. The H_2 emission from this object is observed over a slightly narrower range than for HH320A: there are transitions from four vibrational levels and up to an energy of 2.5 $\times 10^4$ K, see Figure 5.13. Two ($v = 1$, $J = 5$) observational points at 8.37×10^3 K, which theoretically should have the same value of $\ln(N/g)$ but

do not coincide over the range of their error bars, seem to be outliers and are not considered in the modelling process. The degree of LTE is the same as for HH320A but column densities are slightly higher. Therefore, the model for Knot 4 has the same age and density as for HH320A but a slightly higher shock velocity.

5.2.4 HH120

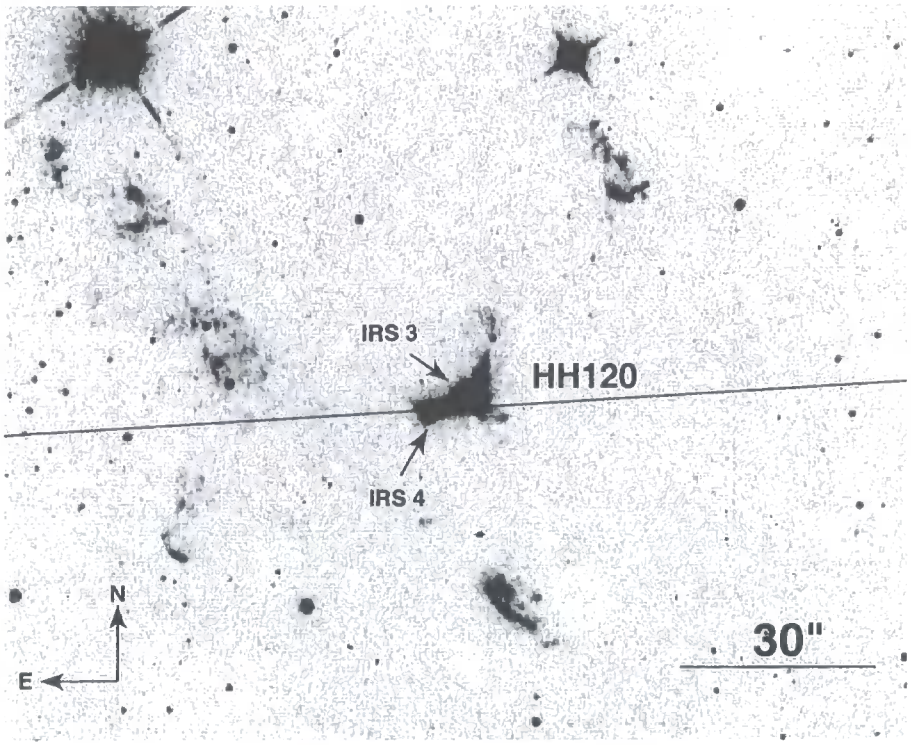

Figure 5.14: (Figure 3 of Nisini et al. (2002)). H_2 2.122 μm image of HH120 with SOFI slit superimposed. IRS3 and the outflow driving source, IRS4, (Pettersson, 1984) are also labelled.

HH120 forms part of the Cometary Globule CG30 ($d \approx$400 pc Brandt et al., 1971), which is thought to consist of HH120 and a reflection nebula (Pettersson, 1984), and is excited by a young source, IRS4 (Pettersson, 1984) associated with FIR source IRAS 08076–3556 (see Figure 5.14). CG30 is itself situated in the Gum Nebula, an H II region, which is excited by UV radiation sources, the of4 star, η Pup, and the WC star, γ^2 Vel, (Reynolds, 1976; Weaver et al., 1977).

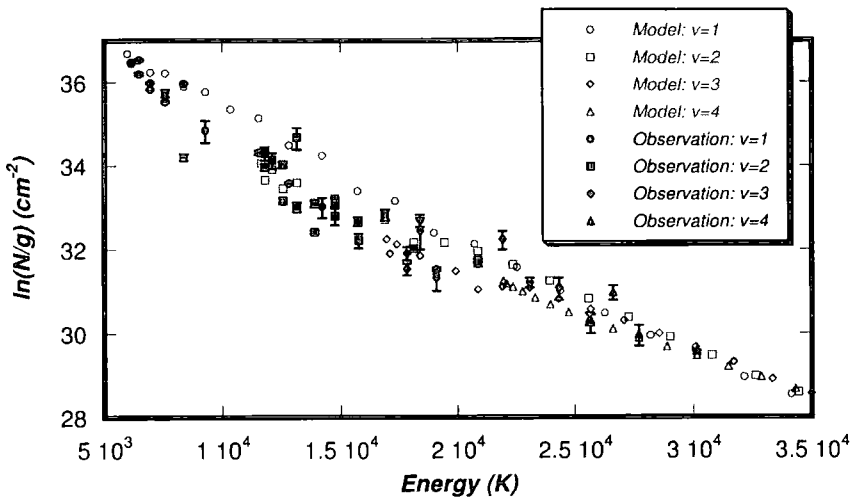

Figure 5.15: Observed and computed excitation diagrams for HH120. Transitions from the $v = 1$, $v = 2$, $v = 3$ and $v = 4$ vibrational manifolds are denoted by circles, squares, diamonds and triangles, respectively. Open symbols represent the models and filled symbols the observational results.

Hodapp & Ladd (1995) found evidence for outflows in the HH120 region (but not for one associated with HH120) that showed multiple shocks at slightly different angles from the assumed source of each outflow. They suggested that this might be evidence for a wandering or precessing jet. The [Fe II] and H_2 emission are slightly displaced from each other in HH120 and Gredel (1994) suggested that a J-type shock with a magnetic precursor could be responsible for this and that the high ionization fraction of 0.1 derived by Pettersson (1984) would be sufficient for a J-type shock to propagate in the region. Gredel (1994) also suggested that OB stars or X rays from T Tau stars in dark clouds could provide the UV radiation necessary to ionize the gas to this degree. Nisini et al. (2002) considered that the rich [Fe II] spectra observed towards HH120 indicated the presence of a strong J-type shock wave.

The H_2 emission from HH120 is observed over 4 vibrational levels and up to $3{\times}10^4$ K; see Figure 5.15. The excitation diagram for this object is very similar to that of HH26A and this is reflected in the similarity of the models, which

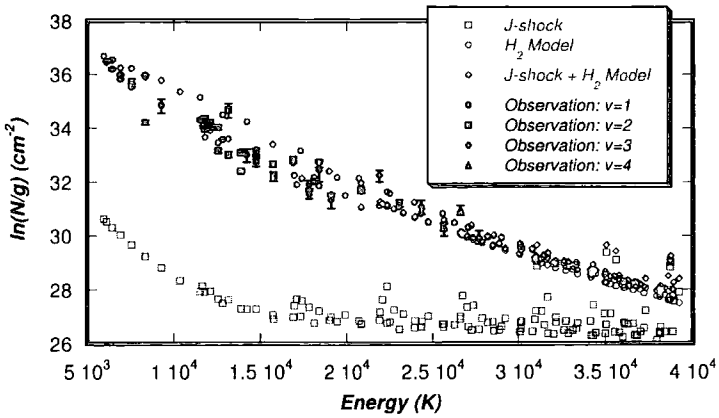

Figure 5.16: Excitation diagrams from the model of the H_2 emission and pure J-type shock component for HH120 . The effect of the J-type shock is seen from the sum of the two components, denoted "J-shock + H_2 model"). The contribution to the H_2 emission from the J-type shock is not significant over the range of the observations.

are listed in Table 5.1. It should be noted that the v=1 level populations are also overestimated by the model for HH120.

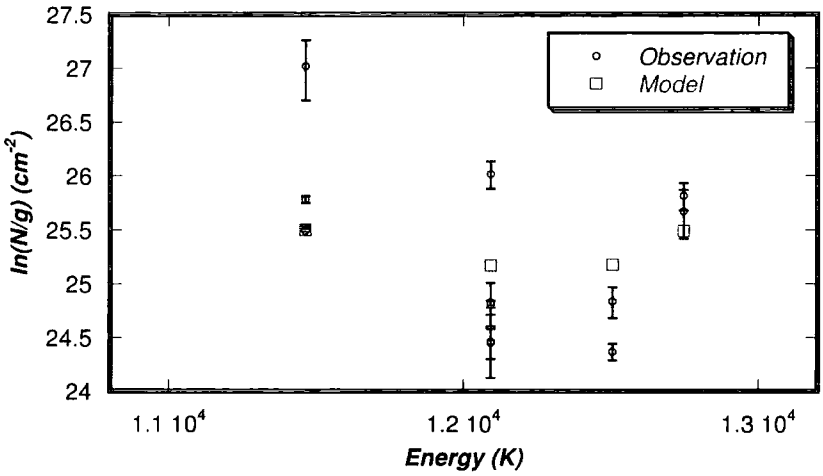

Figure 5.17: Excitation diagrams from unblended lines of [Fe II] with S/N>3 (circles), compared with the predictions of the models (squares) for HH120.

The J-type shock for the atomic and ionic emission observed towards HH120

makes no significant contribution to the H_2 emission over the range of the observations but does become important above 3.5×10^4 K; see Figure 5.16. [Fe II] emission is observed from all four energy levels in the a^4D term and over a wider range of wavelengths than previous objects considered. Therefore, a more thorough analysis of the ability of the model to reproduce the observed [Fe II] emission is possible for this object. The predicted level populations are within the error bars and the spread in the observational points in the [Fe II] excitation diagram for all but the third energy level, $a^4D_{3/2}$, which the model overestimates (see Figure 5.17). Most of the predicted [Fe II] intensities are within a factor of two of that observed: the exceptions are the 1.248, 1.328, 1.600, 1.677, 1.800 and 1.810 μm lines. The 1.248 μm line is blended with the 1.247 μm H_2 2-0 Q(3) emission line, while the 1.800 and 1.810 μm lines lie at wavelengths that suffer from poor atmospheric transmission. The other line intensities are exceeded by the model predictions by a little over a factor of two and two of these transitions (1.328 and 1.677 μm) originate in the $a^4D_{5/2}$ level, whose population is over estimated by the model. The [C I] lines are underestimated by a factor of 2–3.

5.2.5 HH111F

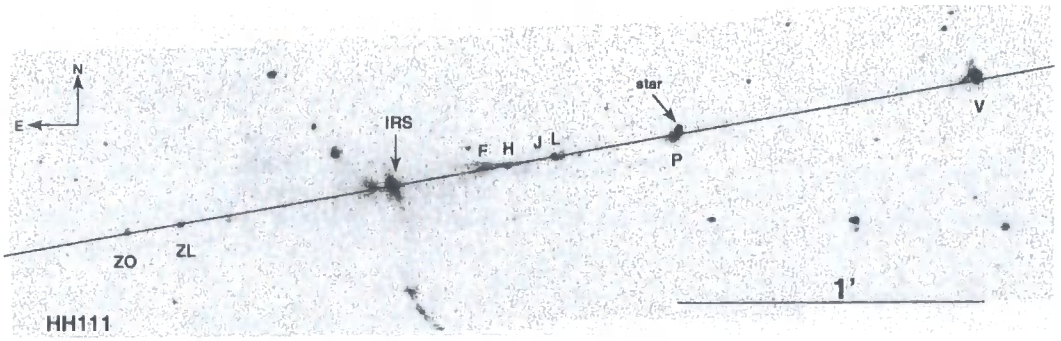

Figure 5.18: (Figure 1 of Nisini et al. (2002)). H_2 2.122 μm image of HH111 (from Davis et al., 1994). The SOFI slit is superimposed and the knots identified, following the nomenclature of Gredel & Reipurth (1994). The outflow driving source is approximately 3″ to the east of the IRS source. The high degree of collimation of the outflow and the symmetry of the knots about the outflow source are apparent.

The extremely well–collimated HH111 outflow is situated in the L1617 cloud at a distance about 460 pc Reipurth (1989) and is driven by a 25 $L_{\odot}$ class 1 source, IRAS 05491+2047 which is also a VLA source (Reipurth, 1989). The red (east) lobe is more obscured in the optical than the blue (west) but distribution of knots along the lobes show remarkable symmetry in the IR suggesting episodic emission (Reipurth, 1989; Gredel & Reipurth, 1994). The series of knots along both lobes of the outflow trace a sinuous path, which is ascribed to variations in the velocity and opening angle of the jet (Reipurth et al., 1997), and high spatial resolution observations of the blue lobes indicate that the HH objects (F–V) have a bow shock structure (Nisini et al., 2002). Optical emission-line velocity maps of HH111V have shown that the pre-shock material is flowing away from the driving source at about 300 km s^{-1} suggesting that HH111V is moving into an even earlier ejection (Morse et al., 1993). This theory is supported by the mm observations of Cernicharo & Reipurth (1996), who found several compact, high-velocity CO bullets further out along the flow axis. Further evidence comes from the HST WFPC2 Hα and [S II] $\lambda\lambda$6716, 6713 observations of Reipurth et al. (1997) from which they concluded that the outflow overruns previously ejected jet material. Their observations also showed bow shock structures along the outflow. Nisini et al. (2002) found that the [Fe II] emission peaks at HH111F and decrease moving away from the source and that generally both the atomic/ionic and molecular emission indicates that excitation decreases away from the source. The strength of the [Fe II] lines observed towards HH111F motivated the modelling work described below.

The H_2 emission from HH111F is observed in only the v=1 and 2 levels up to an energy of just over 1.4 $\times 10^4$ K. Only three transitions from the v=2 level are observed (see Figure 5.19); however, the degree of LTE, even in these few levels, is such that it was clear that the $n_{\rm H} = 10^4$ cm^{-3}, $v_{\rm s}$=36 km s^{-1} model with an age of 100 yr that was adopted is the best for the object.

A J-type shock that was compatible with the both H_2 and [Fe II] observations

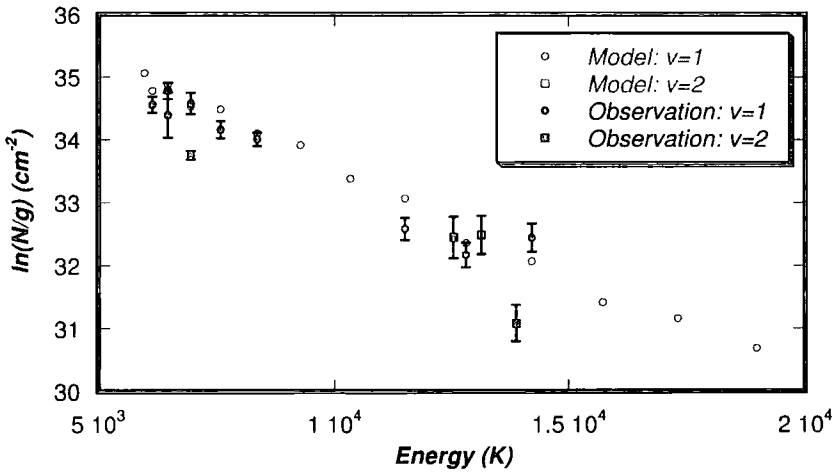

Figure 5.19: Observed and computed excitation diagrams for HH111F. Transitions from the $v = 1$ and $v = 2$ vibrational manifolds are denoted by circles and squares, respectively. Open symbols represent the models and filled symbols the observational results.

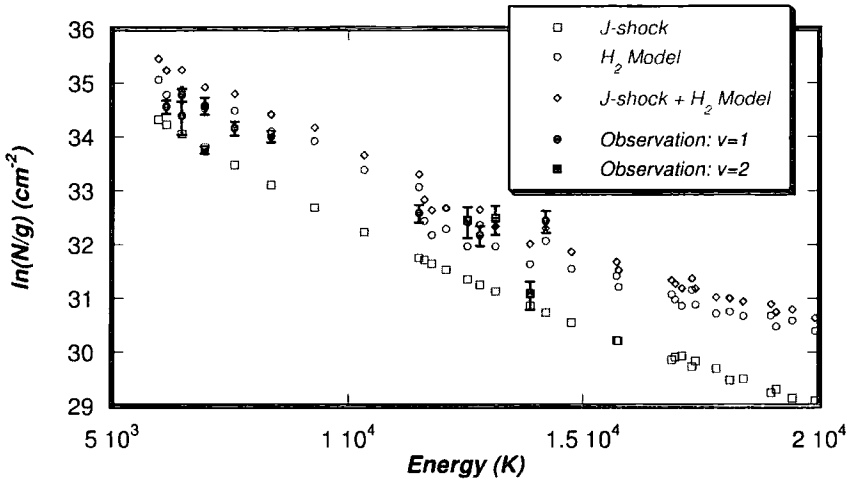

Figure 5.20: Excitation diagrams from the models of H_2 emission and pure J-type shock component for HH111F. The effect of the J-type shock is seen from the sum of the two components, denoted "J-shock + H_2 model"). The contribution to the H_2 emission from the J-type shock is significant over the range of the observations.

could not be found. In Figure 5.20 the excitation diagram from the J-type shock model that was most successful is plotted with that from the model for the H_2 emission. The contribution from the J-type shock causes the combined model to exceed the observations.

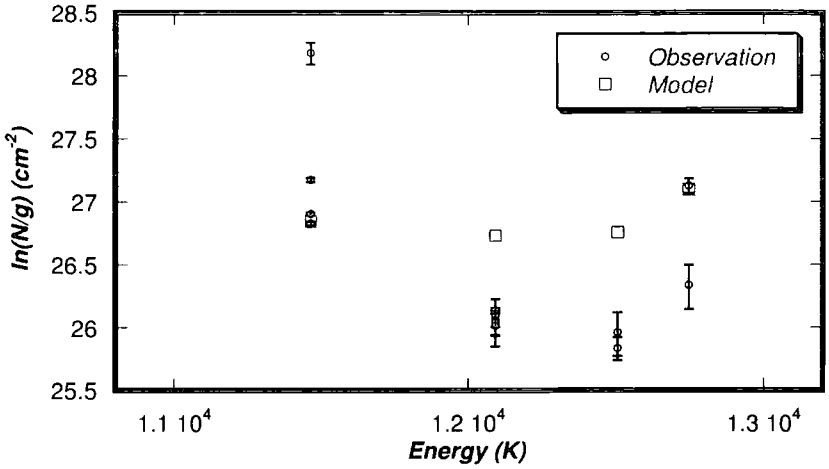

Figure 5.21: Excitation diagrams from unblended lines of [Fe II] with S/N>3 (circles), compared with the predictions of the models (squares) for HH111F.

The population predicted for the first and fourth ($a^4D_{7/2}$ and $a^4D_{1/2}$) levels of Fe^+ are in good agreement with the populations derived from observations. The model overestimates the population in the second and third ($a^4D_{5/2}$ and $a^4D_{3/2}$) levels.

5.2.6 HH240A

Located in the core of L1634, a dark cloud in Orion (distance $\approx$ 500 pc (Hodapp & Ladd, 1995)), the HH240 outflow is driven by IRAS 05173-0555 (Cohen et al., 1985), a class 0 deeply embedded source with $L_{\rm bol} \approx 17 L_\odot$ (Reipurth et al., 1993; Davis et al., 1997). The region was first detected in H_2 by Schwartz et al. (1987). At optical wavelengths, only the HH object nearest the source, HH240A also known as RN040, is visible (e.g., Bohigas et al., 1993). In the

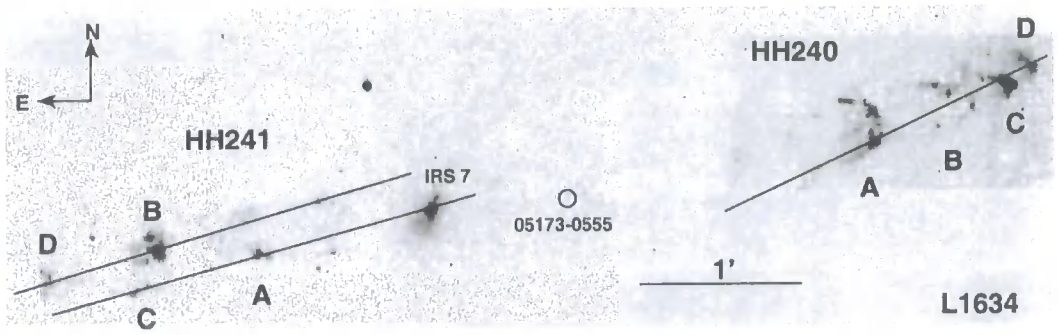

Figure 5.22: (Figure 2 of Nisini et al. (2002)). H_2 2.122μm image of the L1634 region with the SOFI slit superimposed. The knots in the HH240/241 chains are labelled following the nomenclature of Davis et al. (1997). The bow shock nature of the knots in the HH240 chain and the symmetry of the outflow about the source, IRAS05173-0555, are apparent.

IR, the outflow emerges (see Figure 5.22), and can be seen to consist of a series of knots associated with HH241 (A–D) that make up the eastern (red-shifted) lobe while HH240 A–D comprise the western (blue-shifted) lobe. The bow shock structure of the knots, in particular in HH240 (see Figure 5.22), and the filamentary and sinuous nature of the outflow also become apparent in the IR. The symmetry in the red and blue lobes with respect to the driving source is suggestive of periodic eruptions while the curvature of the outflow might suggest a precession of the jet. The IR spectroscopic observations of Nisini et al. (2002) showed that the atomic and ionic emission ([Fe II], [C I], [N I], [S II], [S III]) was only present in the two objects nearest to the source, HH240A and HH241A, from which they concluded that the excitation in the outflow decreased with distance from the source. Furthermore, they considered that the higher degree of [Fe II] excitation nearer the source was due to a higher degree of ionization rather than a higher density. The [Fe II] emission they detected was strongest towards HH240A: therefore, modelling work of this object was undertaken.

H_2 emission is observed up to the fourth vibrational level and to an energy of 2.5×10^4 K. Two v=1 observational points at 8.37×10^3 K ($J = 5$) and 1.73×10^4 K ($J = 12$) seem to be outliers (see Figure 5.23) and are not taken

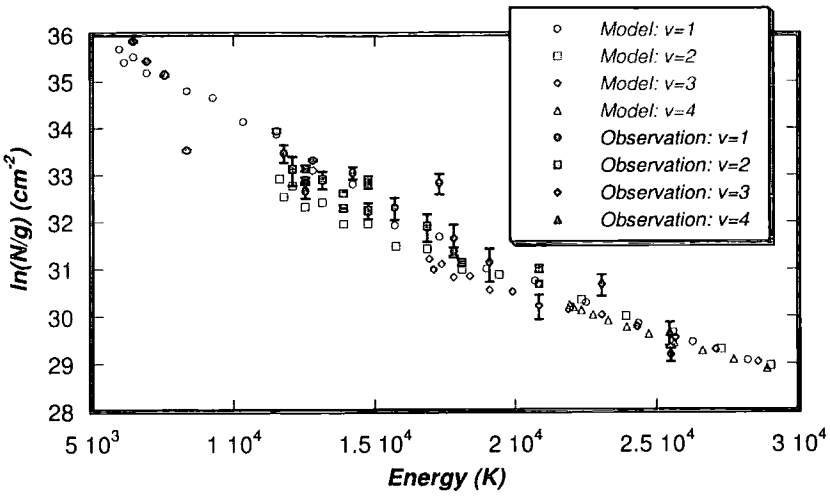

Figure 5.23: Observed and computed excitation diagrams for HH240A. Transitions from the $v = 1$, $v = 2$, $v = 3$ and $v = 4$ vibrational manifolds are denoted by circles, squares, diamonds and triangles, respectively. Open symbols represent the models and filled symbols the observational results.

into account when modelling.

The J-type shock found for the [Fe II] emission contributes to the H_2 emission of the combined model (J-type shock plus J-type shock with magnetic precursor) over the range of the observations but is still within the error bars and the spread of the points, see figure 5.24.

The J-type shock predicts populations that are in good agreement with those derived from observations for the first two energy levels but exceeds the populations observed in the $a^4D_{3/2}$ and $a^4D_{1/2}$ levels. Comparison between the observed and predicted [Fe II] line intensities, as should be expected, reflect this trend.

5.2.7 HH99

The HH99 region, a Herbig-Haro complex in the RCrA molecular core (d $\approx$ 130 pc Marraco & Rydgren, 1981) comprises what appears to be a bow shock

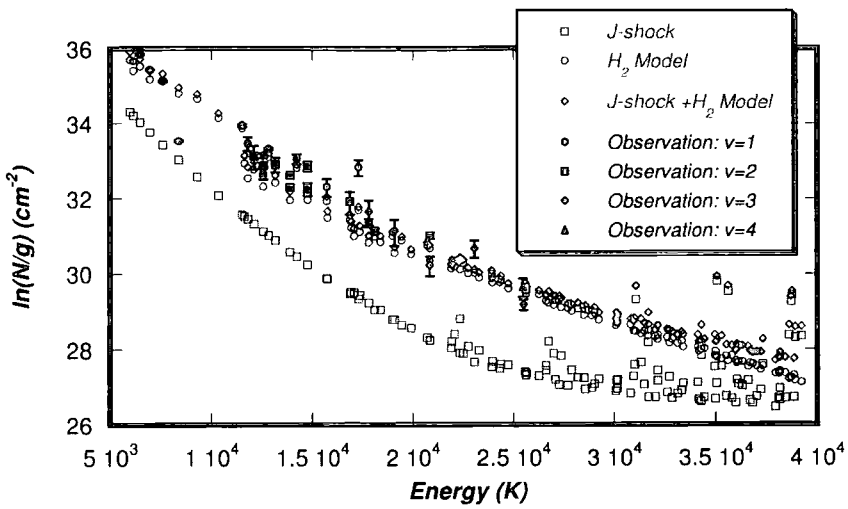

Figure 5.24: Excitation diagrams from the models of H_2 emission and pure J-type shock component for HH240A. The effect of the J-type shock is seen from the sum of the two components, denoted "J-shock + H_2 model"). The contribution to the H_2 emission from the J-type shock is not significant over the range of the observations.

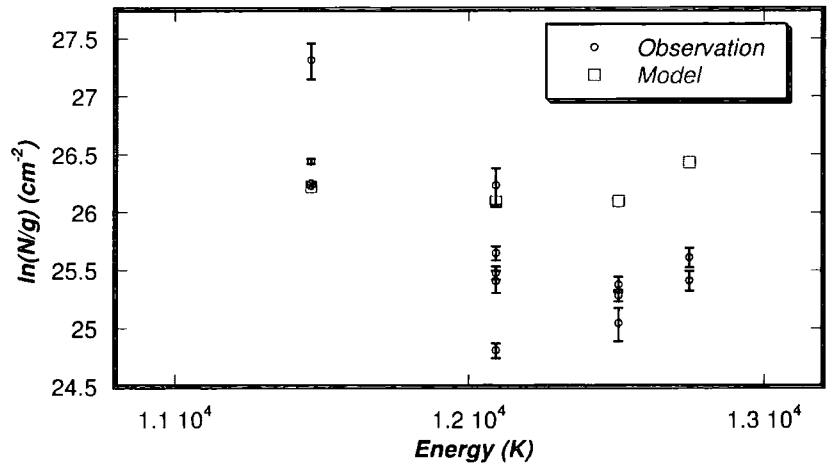

Figure 5.25: Excitation diagrams from unblended lines of [Fe II] with S/N>3 (circles), compared with the predictions of the models (squares) for HH240A.

(HH99B) and a bright wing feature (HH99A), which may have arisen as a result of the interaction of the flow with a dense ambient clump or cloudlet

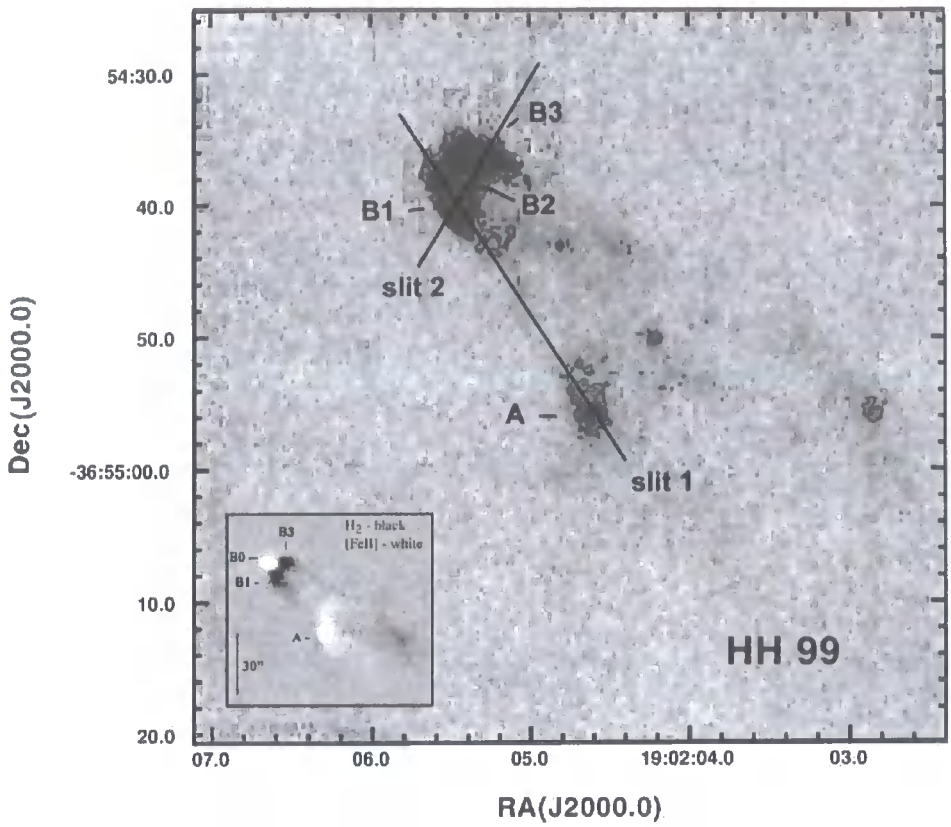

Figure 5.26: (Figure 2 of M^{c}Coey et al. (2004)). The H_2 (2.122 μm) image (not continuum subtracted) obtained at ESO-NTT with the SOFI IR camera. The knots of HH99 are labelled and slit positions are superposed. Knot B0 has also been marked on Figure 1b of Davis et al. (1999), in the inset.

(Davis et al., 1999). On the basis of optical images and high resolution spectra, Hartigan & Graham (1987) suggested that the HH99 complex is the red-shifted lobe of the HH100 flow, powered by the embedded protostar HH 100IR. More recently, near infrared images have demonstrated that the bow shock defines a direction consistent with the position of the infrared source IRS 9 and the pre-main sequence star R CrA (Wilking et al., 1997). The low resolution K-spectrum of HH99B3 and echelle spectra of the H_2 2.122 μm line have been obtained by Davis et al. (1999), who also imaged the HH99 region in the 1.644 μm line of [Fe II] and found strong emission towards the head of the shock (HH99B0) and in HH99A. M^{c}Coey et al. (2004) found a rich H_2 spectrum (up to $v = 4$) and strong atomic and ionic emission, particularly that of [Fe II],

towards HH99B0. They also found strong H_2 emission towards the other knots ($v \leq 3$ for the other knots in HH99B and $v = 1, 2$ towards HH99A) along with weaker atomic and ionic emission, in the raw data, than observed towards HH99B0.

H_2 emission

Table 5.2: Parameters of possible shock excitation models for H_2 emission that include photoionization effects. H_2 was observed to emit over a narrower energy range in HH99 than other objects considered in this Chapter and for this reason it was more difficult to constrain the models of H_2 emission for HH99. However, other observational considerations, which are described in the text, indicate that the models in bold face below (and in Table 5.1) are the most consistent with observation.

Object	v_s	n_H^a	Age
	km s^{-1}	cm^{-3}	yr
HH99A[1]	50	10^3	$> 3\times10^3$
HH99A[2]	**34**	$\mathbf{5\times10^3}$	**350**
HH99A[3]	28	10^4	250
HH99A[4]	12	10^5	40
HH99B0	**34**	$\mathbf{10^4}$	**130**
HH99B0	18	10^5	40
HH99B1(slit 1)	55	10^3	400
HH99B1(slit 1)	**30**	$\mathbf{10^4}$	**190**
HH99B1(slit 2)	53	10^3	200
HH99B1(slit 2)	**30**	$\mathbf{10^4}$	**165**
HH99B2	55	10^3	200
HH99B2	**33**	$\mathbf{10^4}$	**125**
HH99B3	**33**	$\mathbf{10^4}$	**115**

Notes:
[a] $n_H = n(H) + 2n(H_2)$
[1], [2], [3], [4] Models 1, 2, 3 and 4 for HH99A

As noted by Davis et al. (1999), and as can be seen in Figure 5.26, the mor-

phology of the HH99B complex is suggestive of a bow shock. A bow shock can be modelled approximately as a sequence of planar shock fronts, for which the effective shock speed varies with the angle of attack. In the present study, a dissociative J-type shock is assumed to occur at the apex of the bow, and J-type shocks with magnetic precursors to dominate in the wings.

The observed emission lines of H_2 of M^{c}Coey et al. (2004) alone are usually insufficient to determine uniquely the shock parameters, notably the shock speed and age and the pre-shock gas density; measurements of the (weaker) lines from levels of still higher excitation, particularly from higher vibrational manifolds, would be required to do so. However, when other observational constraints are taken into account, the range of possible models, which are listed in Table 5.2, is more closely circumscribed. First, previous echelle spectroscopy by Davis et al. (1999) provides some constraints on the shock velocity for the knots HH99B1 and HH99B3. Second, it seems reasonable to require that the pre-shock parameters for all the knots which are physically associated should be similar. Third, the models of the H_2 emission should be compatible with the J-type shock models which reproduce the [Fe II] and [C I] emission lines.

The HH99B bow shock complex is physically connected, and it is reasonable to expect similar pre-shock conditions in all the models of the associated knots. Models with a pre-shock gas density $n_{\rm H} = 10^4$ cm^{-3}, which included photoionization reactions, were found to yield the most consistent fits to the observations of all the HH objects in this complex: accordingly, these models were adopted. The shock velocities of such models were deduced to be about 30 km s^{-1} for all the objects, and the evolutionary ages derived from the models of B0, B2 and B3 were about 120 yr (see Table 5.1). The observations of B1 from slits 1 and 2 were modelled separately from each other and yielded a similar age (but a greater age than for the other objects). HH99B1 forms part of the head and one wing of the putative bow shock (see Figure 5.26); it is the only part of the bow shock whose emission was measured along the wing

(in slit 1), rather than across the head. In addition, the portion of HH99B1 captured in slit 2 lies further back from the apex of the bow shock than any other object (see Figure 5.26). As the H_2 emission weakens along the wing with distance from the apex, it might be anticipated that HH99B1 should exhibit a lower degree of excitation, consistent with a greater evolutionary age than for the other objects in the complex.

A further constraint on v_s in HH99B1 and HH99B3 can be derived from the echelle spectroscopy of Davis et al. (1999). Using the H_2 2.122 μm line, they measured a FWHM of 15–20 km s^{-1} in B1 and 20–40 km s^{-1} in B3. These observations provide some indication of the flow speed of the neutral gas in the region of the shock in which the lines are excited; but it should be noted that the observed line profiles were not deconvolved from the instrumental profile and that there are (uncertain) line–of–sight projection effects. It is perhaps notable that the shock velocity of the model for HH99B3 is in good agreement with the measured FWHM, whilst the narrower profile observed in B1 favours the lower velocity model (i.e. $v_s = 30$ km s^{-1}) of the two considered for this knot.

HH99A is separated by from HH99B by some 25″ and so the constraint on density need not be applied so rigorously: it would seem reasonable to require that photoionization effects still be included and only such models are considered here. Davis et al. (1999) suggested that HH99A could be either the edge of the HH99B bow shock or a clump of gas which has been overrun by the bow shock. In the latter case, HH99A should have a greater evolutionary age than HH99B. Alternatively, HH99A could be the result of a separate outflow event. Referring to Table 5.2, it can be seen that three possible models of HH99A, labelled 1, 2 and 3 in the Table, are more evolved than the corresponding models of HH99B; this is consistent with HH99A being a clump of gas which has been overrun. The fourth possible model (model 4 in Table 5.2) is consistent with a much more recent outflow event: the gas behind the bow shock will continue to be compressed as it cools.

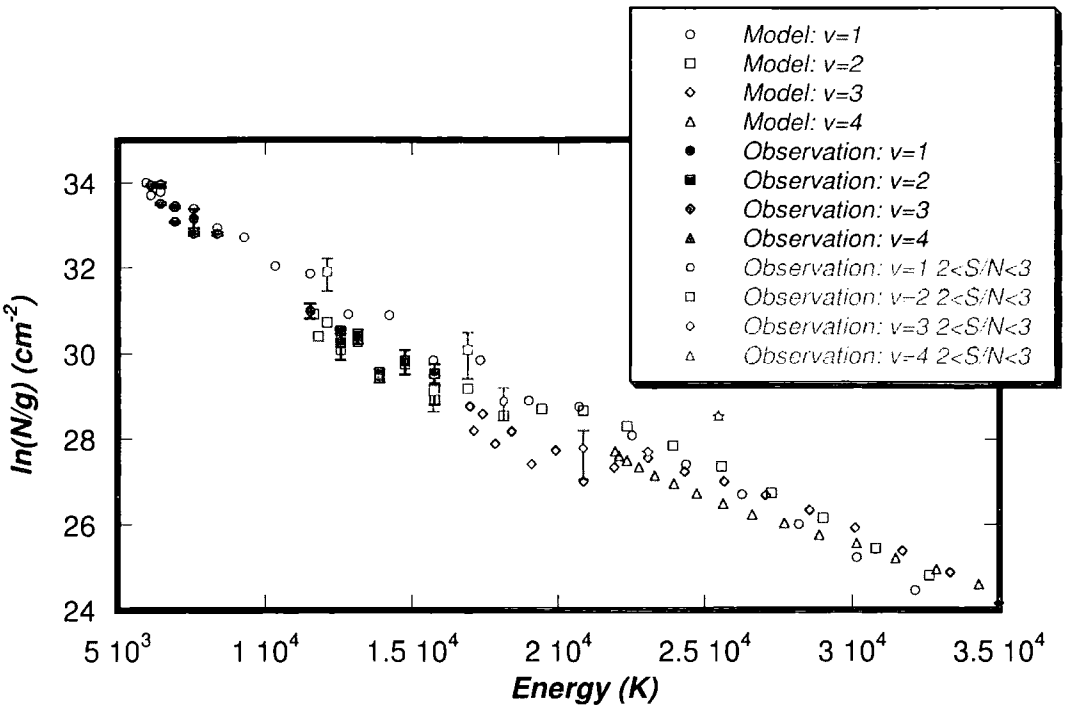

Figure 5.27: Observed and computed excitation diagrams for HH99A (model 1). Transitions from the $v = 1$, $v = 2$, $v = 3$ and $v = 4$ vibrational manifolds are denoted by circles, squares, diamonds and triangles, respectively. Open symbols represent the models and filled symbols the observational results, with S/N> 3 (black) and 2 <S/N< 3 (grey).

The H_2 emission lines observed towards HH99A arise from levels with excitation energies up to approximately 2.5×10^4 K. However, observations with S/N > 3 extend only up to 1.5×10^4 K, as compared with 2–2.5×10^4 K for the HH99B objects. The lower S/N of the lines of high excitation from HH99A compromises attempts to refine the models further. The excitation diagrams derived from models (open symbols) and observations (corresponding filled symbols) are shown in Figures 5.27–5.35. The results for models 1–4 of HH99A and the models adopted for the HH99B bow shock complex are plotted.

[Fe II] and [C I] emission

In the models of J-type shocks, $v_s = 50$ km s^{-1} was adopted, together with the pre-shock densities used in the models for H_2 emission, to be found in Table

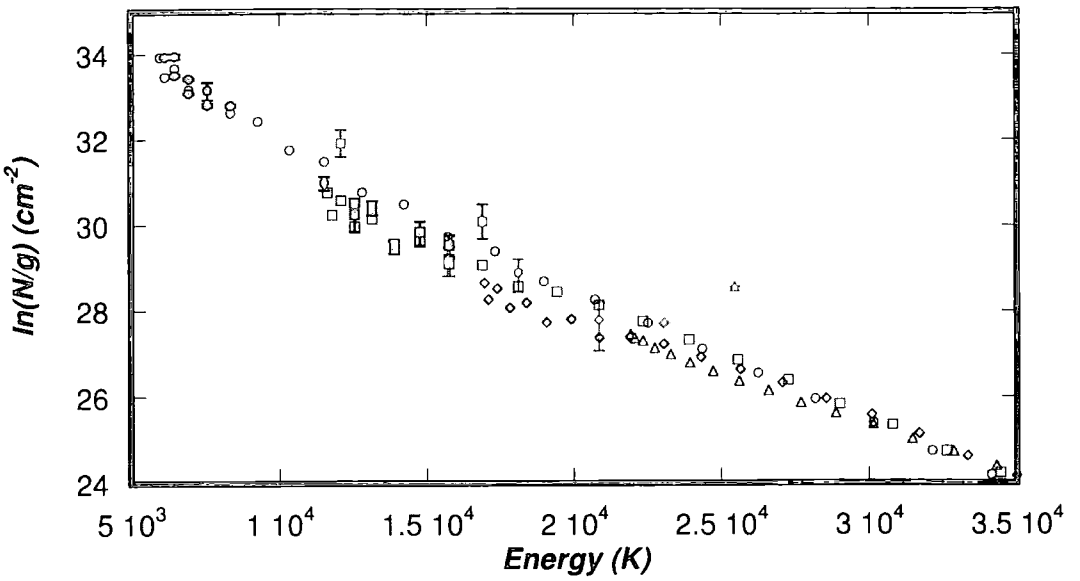

Figure 5.28: Observed and computed excitation diagrams for HH99A (model 2). Transitions are denoted by the same symbols as in Figure 5.27.

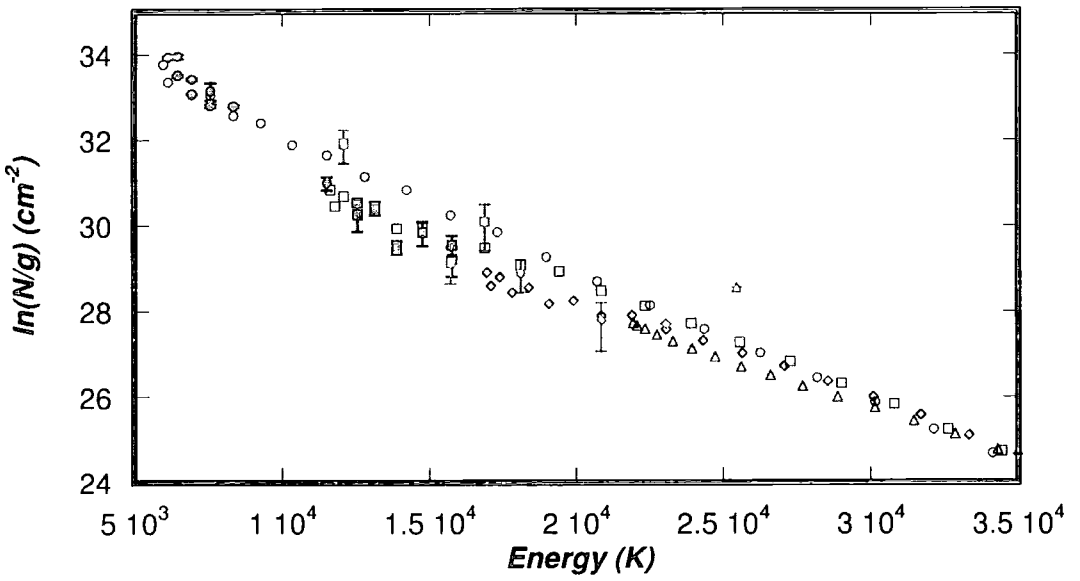

Figure 5.29: Observed and computed excitation diagrams for HH99A (model 3). Transitions are denoted by the same symbols as in Figure 5.27.

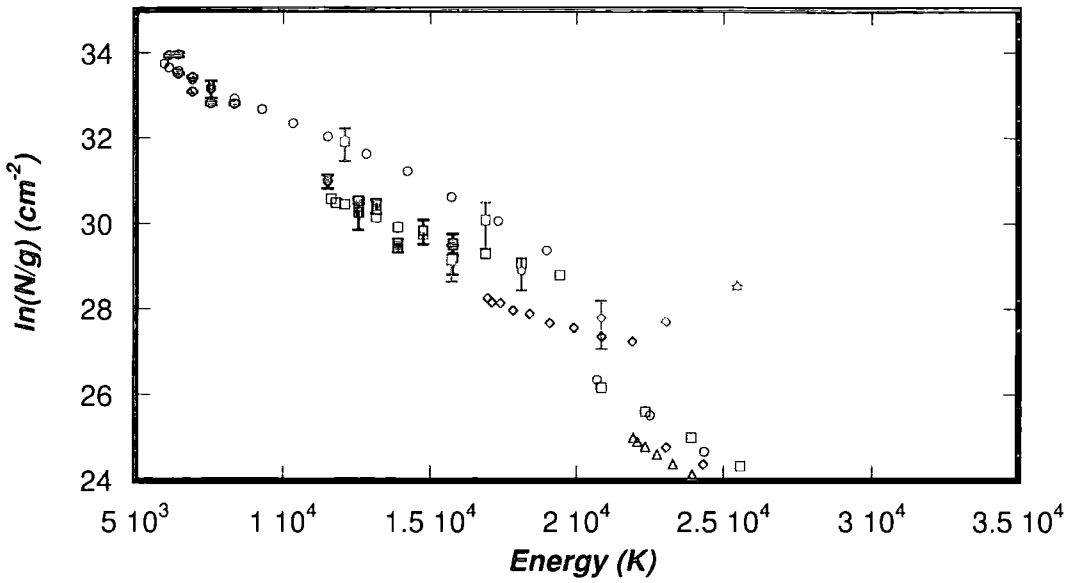

Figure 5.30: Observed and computed excitation diagrams for HH99A (model 4). Transitions are denoted by the same symbols as in Figure 5.27.

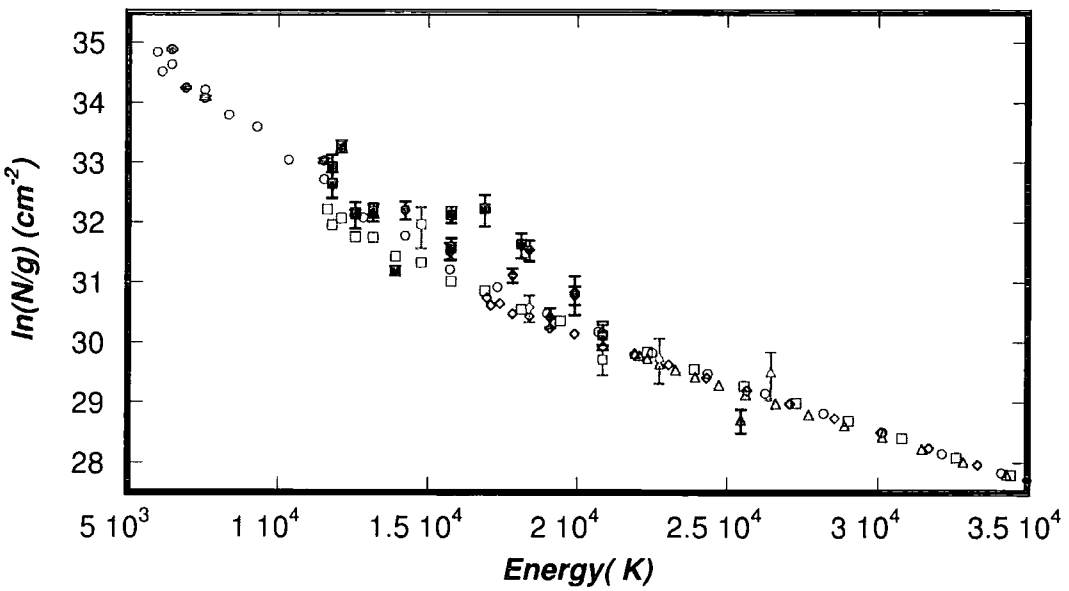

Figure 5.31: Observed and computed excitation diagrams for HH99B0. Transitions are denoted by the same symbols as in Figure 5.27.

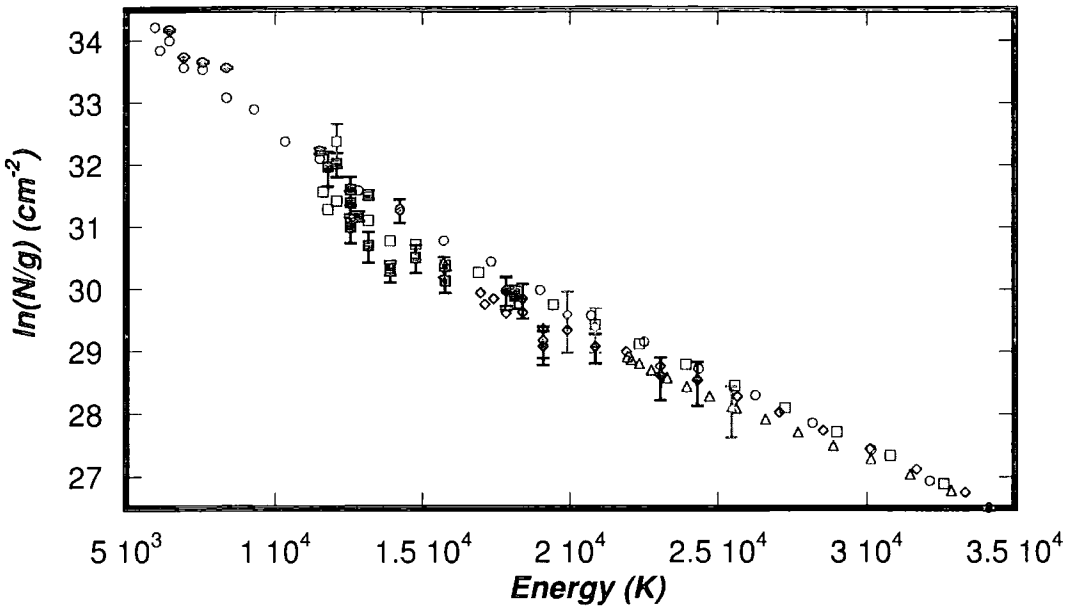

Figure 5.32: Observed and computed excitation diagrams for HH99B1 (slit 1). Transitions are denoted by the same symbols as in Figure 5.27.

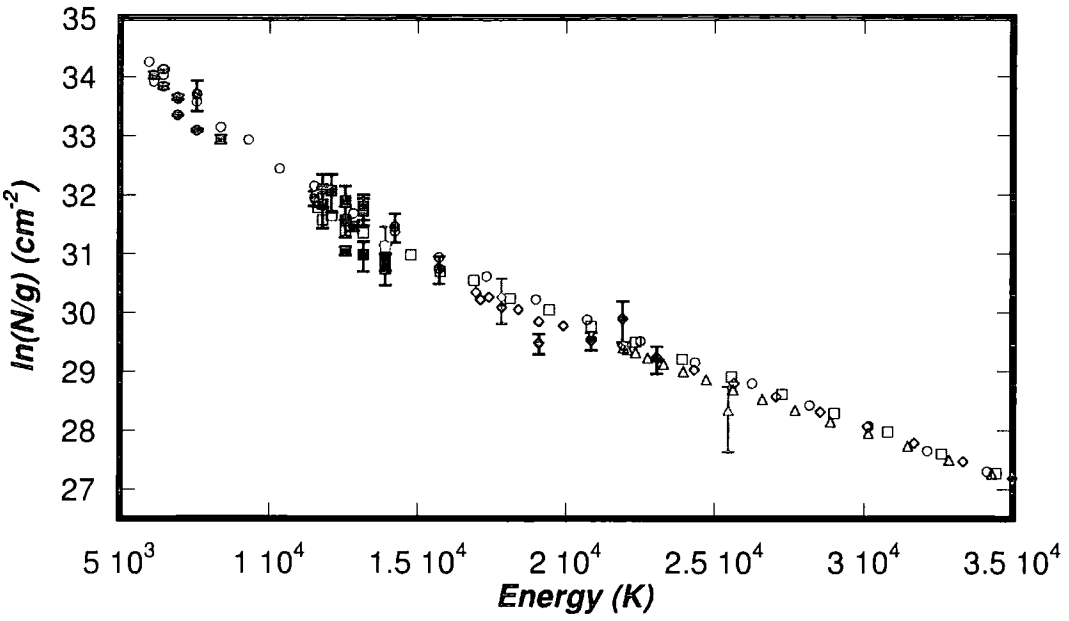

Figure 5.33: Observed and computed excitation diagrams for HH99B1 (slit 2). Transitions are denoted by the same symbols as in Figure 5.27.

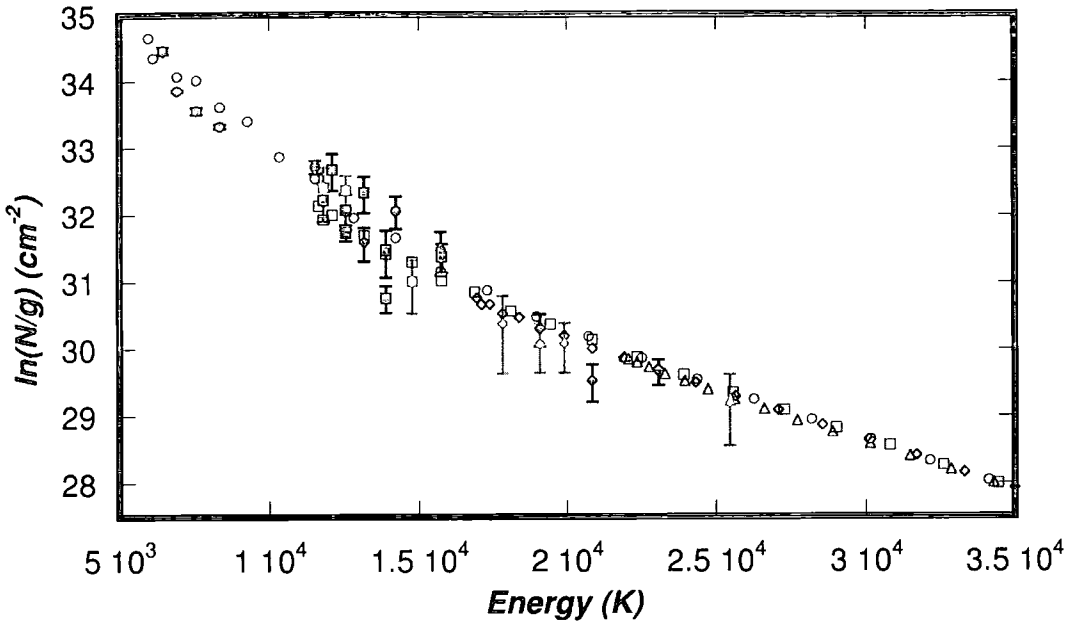

Figure 5.34: Observed and computed excitation diagrams for HH99B2. Transitions are denoted by the same symbols as in Figure 5.27.

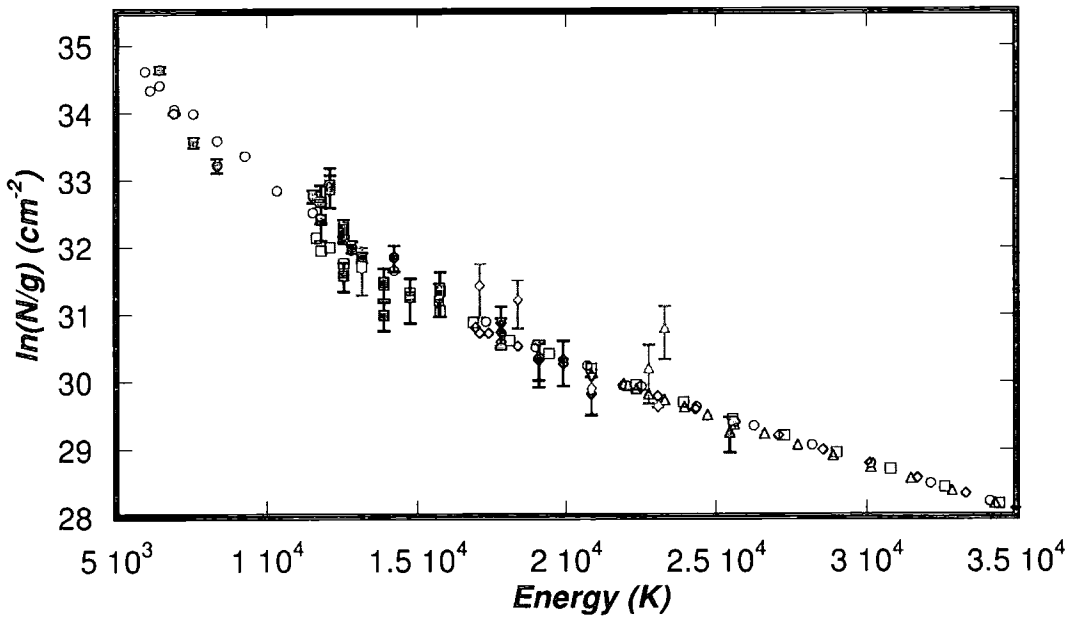

Figure 5.35: Observed and computed excitation diagrams for HH99B3. Transitions are denoted by the same symbols as in Figure 5.27.

5.2. Only the gas phase abundance of Fe differentiated the models: see column 3 in Table 5.4.

A comparison of the predicted and observed intensities of both [Fe II] and [C I] lines is presented in Table D.2 in Appendix D, where only unblended lines of [Fe II] are included. The predictions of the model are in reasonably good agreement with the observations; the intensities of most of the lines are reproduced to within a factor of 2 (or are consistent with the upper limits for [C I] observed with slit 2). In particular, transitions from the $a^4D_{7/2}$ term of Fe^+ are generally reproduced well, especially the strong 1.257 and 1.644 μm lines. On the other hand, the intensity of the 1.248 μm line (from the $a^4D_{3/2}$ term) observed in HH99B3 is underestimated by more than an order of magnitude. It is possible that this line is partially blended with the nearby 1.247 μm H_2 2-0 Q(3) line, which is comparable or stronger in intensity. Although these lines show distinct peaks in the spectrum, they are separated by only 9 Å (T. Giannini, private communication) and the deblending process may not be completely accurate for such a small separation and some contribution from the 1.247 μm line may remain. Consideration of Figure 5.41, in which the observations of [Fe II] emission lines in the form of an excitation diagram are presented and compared with the predictions of the model, supports this theory. The value of $\ln(N/g)$ derived from the 1.248 μm transition, at 1.25×10^4 K, lies at 28.4 cm^{-2} compared with a value of 25.7 cm^{-2} derived from another observed transition from the same energy level (1.279 μm) and with which the value of $\ln(N/g)$ predicted by the model (25.1 cm^{-2}) is in reasonable agreement.

In the upper panel of Figure 5.42, the excitation diagrams deriving from the J-type shock model and the model for the H_2 emission of HH99B2 are plotted, together with their sum. It can be seen that the contribution to the H_2 emission from the J-type shock is not significant over the observed range of excitation energies; only above 3×10^4 K does the H_2 emission from the J-type shock become important. The shock wave is sufficiently narrow that not all of the

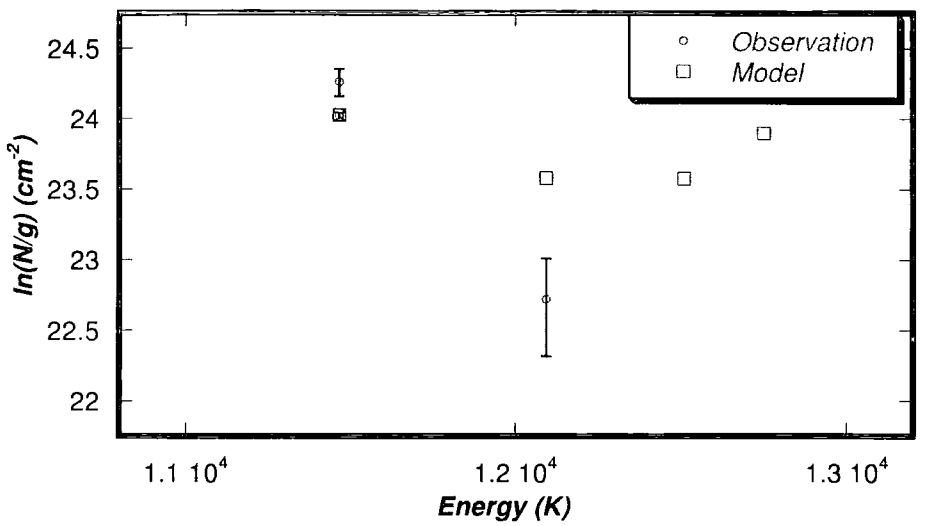

Figure 5.36: Excitation diagrams from unblended lines of [Fe II] with S/N>3 (circles), compared with the predictions of the models (squares), for HH99A (model 2). Only unblended lines observed with a S/N>3 were used when preparing this Figure.

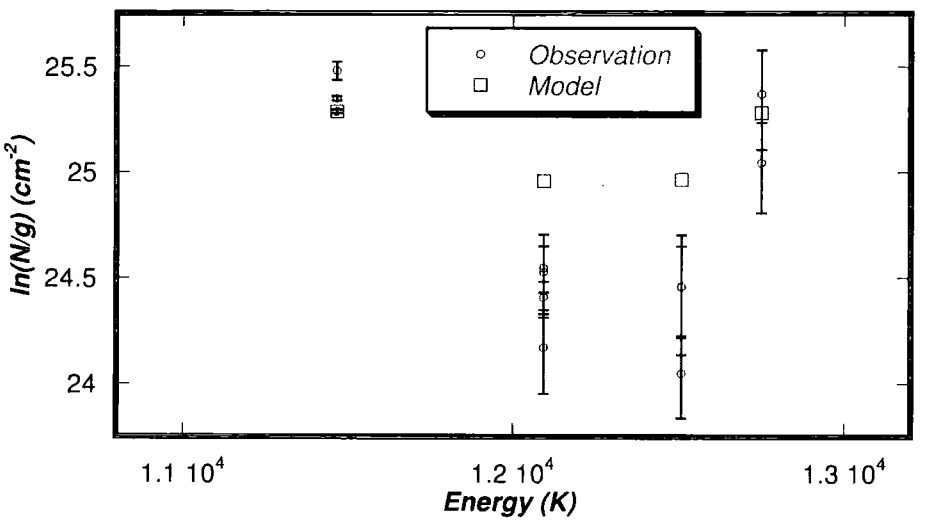

Figure 5.37: Excitation diagrams from unblended lines of [Fe II] with S/N>3 (circles), compared with the predictions of the models (squares), for HH99B0. Only unblended lines observed with a S/N>3 were used when preparing this Figure.

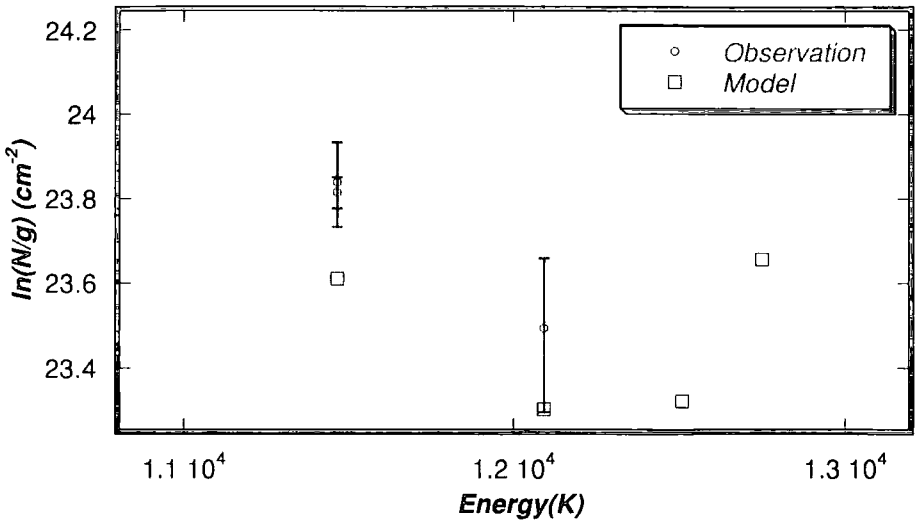

Figure 5.38: Excitation diagrams from unblended lines of [Fe II] with S/N>3 (circles), compared with the predictions of the models (squares), for HH99B1 (slit 1). Only unblended lines observed with a S/N>3 were used when preparing this Figure.

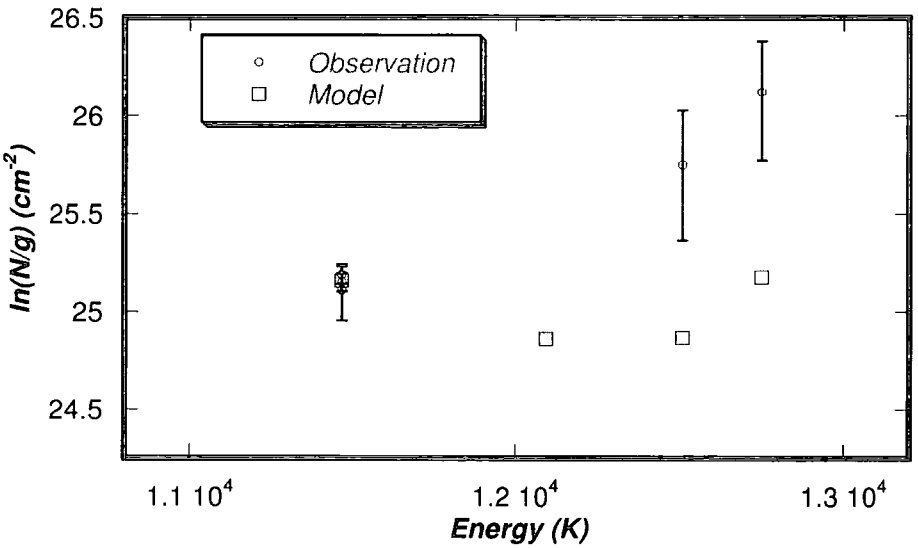

Figure 5.39: Excitation diagrams from unblended lines of [Fe II] with S/N>3 (circles), compared with the predictions of the models (squares), for HH99B1 (slit 2). Only unblended lines observed with a S/N>3 were used when preparing this Figure.

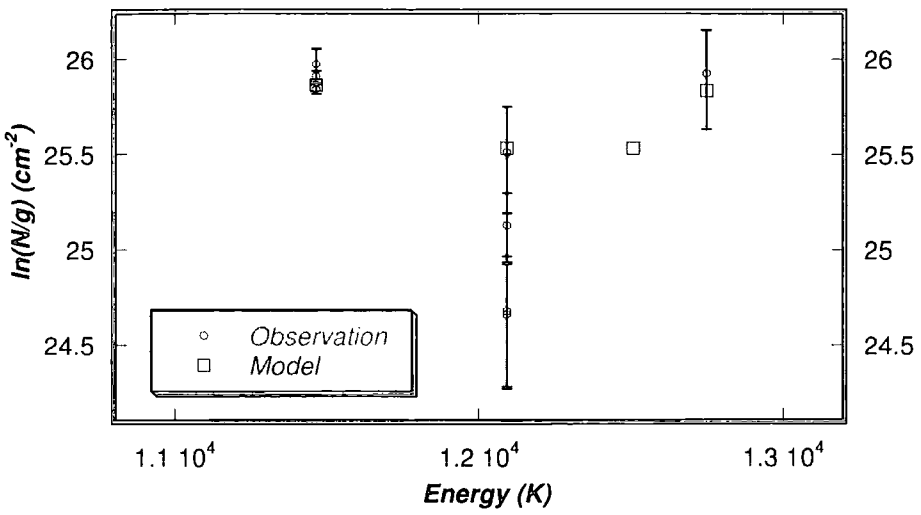

Figure 5.40: Excitation diagrams from unblended lines of [Fe II] with S/N>3 (circles), compared with the predictions of the models (squares), for HH99B2. Only unblended lines observed with a S/N>3 were used when preparing this Figure.

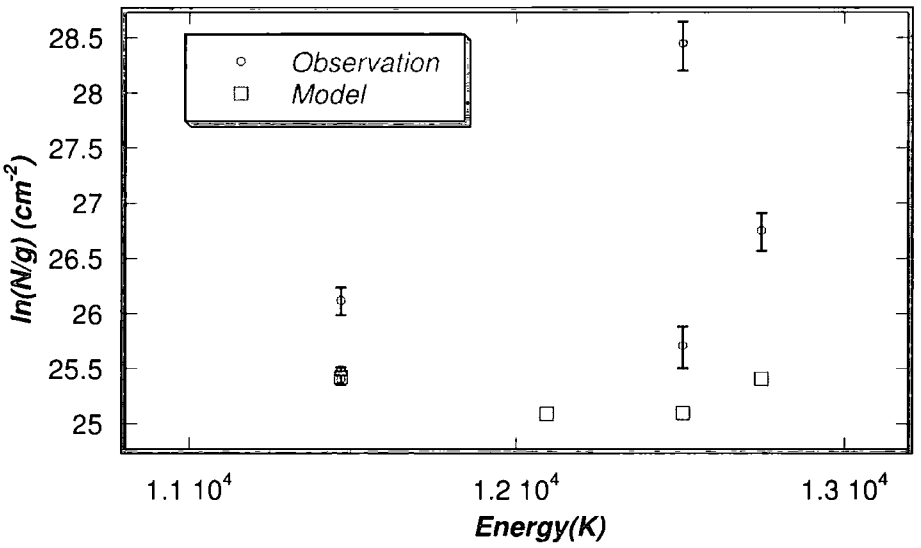

Figure 5.41: Excitation diagrams from unblended lines of [Fe II] with S/N>3 (circles), compared with the predictions of the models (squares), for HH99B3. Only unblended lines observed with a S/N>3 were used when preparing this Figure.

excited levels have time to thermalize, and this results in the scatter about the median curve that can be seen in the upper panel of Figure 5.42 (this effect is observed in all the J-type shock models and is discussed further in Section 5.3). Observational upper limits for HH99B2 are also plotted in the upper panel of Figure 5.42; they fall well above the model predictions. Similar results were obtained for the other models of HH99B models and are not shown here. The H_2 emission observed towards HH99A exhibits lower excitation than is seen in the bow shock complex. In the case of HH99A, the emission from the J-type shock becomes significant above 2.2×10^4 K (see Figure 5.42, lower panel). This contribution provides a means of discriminating between the models for the H_2 emission of HH99A. When the contribution from the J-type shock is added to that from models 1 and 3 ($n_{\rm H}$ = 10^3 and 10^4 cm^{-3}, respectively), the upper limit to the column density of the v = 3 level at $2.3\times$ 10^4 K is exceeded. In the case of model 2, this upper limit is not violated. Furthermore, no J-type shock model that was compatible with model 4 ($n_{\rm H}$=10^5 cm^{-3}) could be found. Therefore, only the combination of model 2 and the J-type shock associated with it (that is, a 50 km s^{-1} shock with $n_{\rm H}$ = 5×10^3 cm^{-3}) is considered further.

From the angular distance between HH99A and the HH99B complex (25″, see Figure 5.26) and the ages of the shock models, and assuming a distance to HH99 of d = 130 pc Marraco & Rydgren (1981)), a jet speed can be estimated. Taking 120 years as a typical age for the main body of the HH99B complex, and the age of 350 yr from model 2 of HH99A, a jet speed of 70 km s^{-1} is found. This value is similar to the speeds of 80–120 km s^{-1} derived by Davis et al. (1999) from bow shock models (which provided kinematic and spectroscopic data but did not consider the chemistry and atomic processes included in the models presented here) of the HH99 system.

The rapid and substantial dissociation of H_2 at the peak of these J-type shock models reduces significantly the rate of cooling by H_2, and atomic/ionic cooling, for example of Fe^+ and O, following electron collisional excitation, can

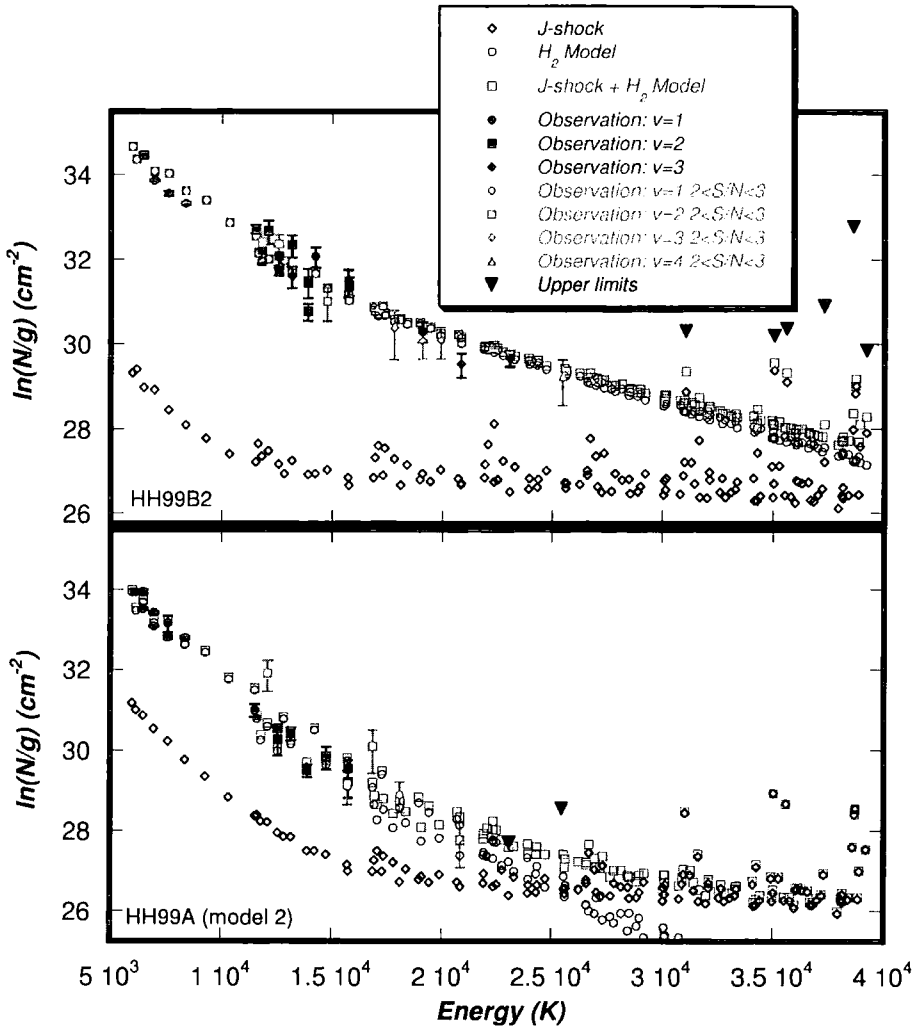

Figure 5.42: Excitation diagrams from the models of H_2 emission and pure J-type shock components for HH99B2 (upper panel) and model 2 of HH99A (lower panel). The effect of the J-type shock is seen from the sum of the two components, denoted "J-shock + H_2 model"). The contribution to the H_2 emission from the J-type shock is not significant over the range of the observations of HH99B2 but becomes possibly significant for HH99A, when the observational upper limits for transitions from levels with excitation energies above 2.2×10^4 K are taken into account.

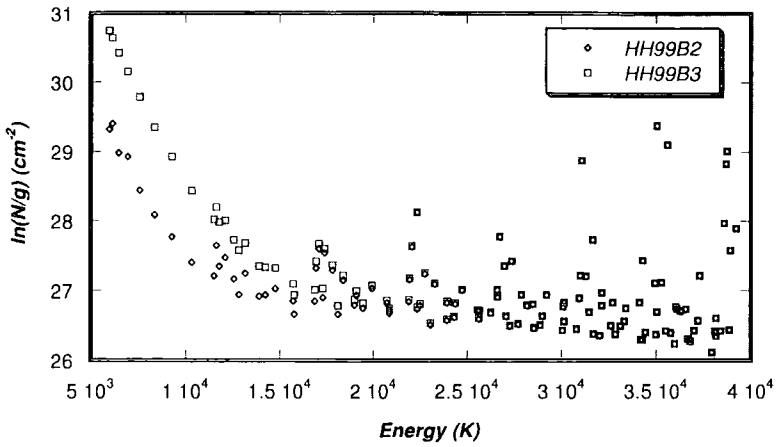

Figure 5.43: The gas phase abundance of Fe is the only parameter which changes between these models of HH99B2 (71%) and HH99B3 (37%). The effect of the different rates of cooling by Fe^+ in the post-shock gas is reflected in the H_2 $v = 1$ level populations.

become important. The effect of cooling by Fe^+ is seen, in the post-shock gas, in the region where the temperature drops below 10^4 K. At such temperatures only the $v = 1$ H_2 levels are significantly populated: the most important contribution to the higher vibrational level populations occurs immediately after the discontinuity. The effect of the cooling due to Fe^+, which becomes more pronounced as the gas phase abundance of Fe^+ increases, is to reduce the populations of the $v = 1$ H_2 energy levels. By way of an illustration, the excitation diagrams from the J-type shock models of B2 and B3 are compared, in Figure 5.43. The only difference between the models is the fraction of Fe in the gas phase (71% for HH99B2 and 37% for HH99B3). It may be seen that the higher gas phase abundance of Fe in the model of HH99B2 results in lower populations of the $v = 1$ energy levels. It should be noted that this effect is not observationally significant: the contribution to the H_2 emission by the $v = 1$ levels in the pure J-type shock is insignificant compared with that of the J-type shock with magnetic precursor.

A comment should be made regarding the abundances of Fe assumed to be in the gas phase for each model. It might be reasonable to assume that the gas

phase abundance of Fe should be the same for each object, given the proximity of the knots in HH99: clearly, this is not the situation described by the J-type shock models. The abundance of Fe used in the model is driven solely by the strength of the observed [Fe II] lines, which may be affected by inclination effects. It should be remembered that a bow shock is a 3-dimensional object: here the bow is being modelled in two dimensions by a combination of planar shock waves.

5.3 General discussion

5.3.1 Models of H_2 emission

Generally, the models of the H_2 emission provide a good fit to the values of the column densities and the degree of thermalization over the range of the observations. Any specific issues are discussed on a case-by-case basis in Sections 5.2.1–5.2.7 above. However, some care should be taken because the model does not take into account the angle of inclination of the outflow. As shall now be demonstrated, this introduces some uncertainty into the calculation of the flux from a radiating shock.

Consider a set of orthogonal axes, x, y and z, in which a shock is assumed to travel in the z-direction, the 'height' and 'thickness' of the shocked region are then measured in the y and x directions, respectively; see Figure 5.44. The emissivity of a transition from states $l \rightarrow k$ is given by

$$j = n_l \, A_{l \rightarrow k} \, (E_l - E_k) \text{ erg cm}^{-3} \text{ s}^{-1}, \tag{5.1}$$

thus, the total energy emitted per unit time is

$$\int j \, \mathrm{d}V \text{ erg s}^{-1}, \tag{5.2}$$

where $\mathrm{d}V = \mathrm{d}x \, \mathrm{d}y \, \mathrm{d}z$ is a volume of radiating gas. As the emission is assumed to be isotropic, the energy per unit area at the distance, d, of the Earth is

$$F = \frac{\int j \, \mathrm{d}V}{4\pi \, d^2} = \frac{\int j \, \mathrm{d}x \, \mathrm{d}y \, \mathrm{d}z}{4\pi \, d^2} \text{ erg s}^{-1} \text{ cm}^{-2} \tag{5.3}$$

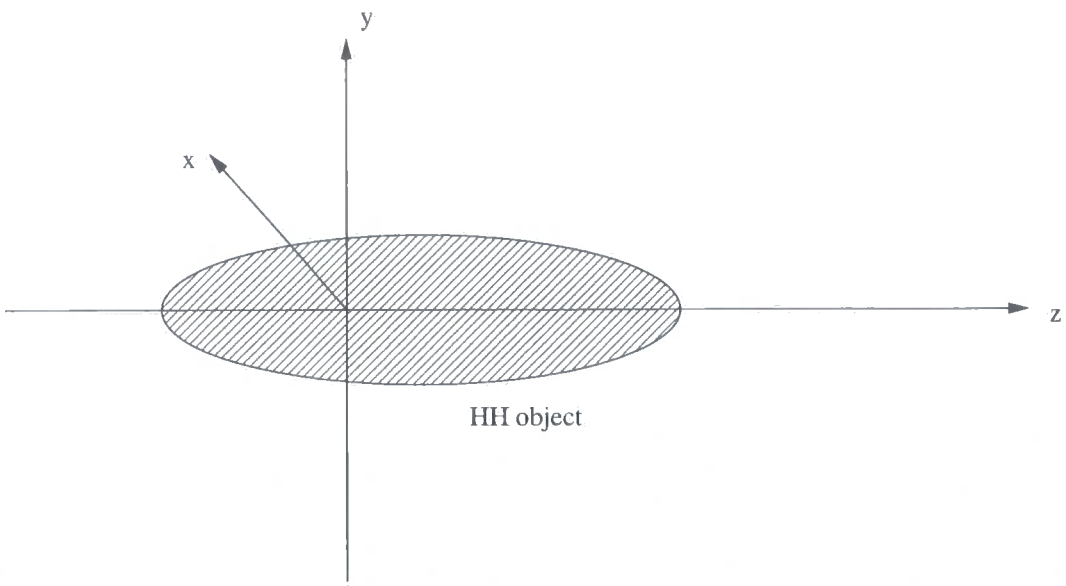

Figure 5.44: A shock is assumed to propagate in the z direction. The 'height' and 'thickness' of the HH object are measured in the y and x directions, respectively.

If the line of sight is along the axis of the jet (z) and the emission is uniform in the x and y directions, the flux is given by

$$F = \int \frac{\mathrm{d}A}{4\pi\, d^2} \int j\, \mathrm{d}z, \tag{5.4}$$

where $\mathrm{d}A = \mathrm{d}x\ \mathrm{d}y$. But, $\mathrm{d}A/d^2 = \mathrm{d}S$, an element of solid angle. Therefore,

$$\begin{aligned} F &= \frac{\int \mathrm{d}S \int j\, \mathrm{d}z}{4\pi} \\ &= S\, \frac{\int j\, \mathrm{d}z}{4\pi} \end{aligned} \tag{5.5}$$

Then

$$F = \theta_y \theta_x\, \frac{\int j\, \mathrm{d}z}{4\pi}, \tag{5.6}$$

where θ_y and θ_x are the angular extent of the HH object in the y and x directions, respectively, while $\int j\, \mathrm{d}z/4\pi$ is calculated by the code. This situation, in which the shock propagates towards the line of sight, is assumed by the code and in this case, θ_y and θ_x can be directly measured from their angular extent on the sky. However, outflows are more easily, and thus more frequently, observed when they lie in the plane of the sky (perpendicular to the z-axis). In

this case, θ_y can be measured, while dz is calculated by the code but is also the only other measured extent of the object on the sky: θ_x is unknown. In order to calculate the flux θ_x must be estimated. (A further uncertainty, which applies to both situations considered here, is associated with the distance to the source.) In practice, and for lack of better information, what is done is to assume θ_x is the same as the observed extent of the HH object in the z direction. For chains of HH objects, such as in the HH111 outflow, where the HH objects are seen to have a jet-like morphology and are elongated along the direction of the outflow, this assumption may result in an overestimate of the flux of radiation. In less collimated outflows, such as HH240, and in bow shocks, such as HH99, HH objects appear to be more amorphous and the neglect of geometrical effects may not be so important.

The characteristic length of the shock wave, which is determined by the distance over which the ion and neutral velocities differ is calculated along the z axis. As HH outflows tend to be observed in the plane of the sky, the models may be tested by comparing the characteristic length of the shock wave with the observed dimension of the source. As the outflows are unlikely to lie completely within the plane of the sky, this can only be an order of magnitude comparison. In Table 5.3 the size (in cm) of each object in the slit, derived from the angular size of the object in the slit and distance (columns 1 and 2), is compared with the characteristic shock length given by the model. The angular sizes were taken from measurements at the telescope for HH72A and HH99 (T. Giannini, private communication) and from the images of the sources published in Nisini et al. (2002) and Giannini et al. (2004) for the other objects. Generally, the agreement between the two lengthscales is good. Although this is only an order of magnitude comparison, it is perhaps worthy of note that, of the possible models for HH25C and HH99A, models 1 and 2, respectively, produce length scales closest to those observed.

A pre-shock density of 10^4 cm^{-3} is required for the majority of the objects modelled and the pre-shock density is always in the range 10^3–10^5 cm^{-3}. It is

Table 5.3: Comparisons between object size on the sky and characteristic length scale of the shock model.

Object	Angular size	Distance	Size on sky	Model prediction
	(″)	(pc)	(10^{16} cm)	
HH72A	3	1500	3.5	2
HH72D	1.5	1500	7	1.2
HH26A	15	400	9	0.6
HH25C (model 1)	12	400	7	1.1
HH25C (model 2)	12	400	7	0.5
HH320A	11	200	3	1.6
Knot 4	4	200	1.2	1.5
HH120	13	400	8	0.6
HH111F	3.3	460	2.3	0.9
HH240A	16	500	12	0.8
HH99A (model 1)	11.3	130	2.2	6.3
HH99A (model 2)	11.3	130	2.2	2.4
HH99A (model 3)	11.3	130	2.2	1.5
HH99A (model 4)	11.3	130	2.2	0.1
HH99B0	5.8	130	1.1	1
HH99B1 (slit 1)	12.4	130	2.4	1.3
HH99B1 (slit 2)	4.1	130	0.8	1.2
HH99B2	1.5	130	0.3	1
HH99B3	4.2	130	0.8	0.9

possible that it is only under such conditions that the effects of the shock wave associated with the outflow can be observed. It could be expected that very few HH objects should be found in a low density environment: star forming regions are, by their nature, relatively dense. It may be somewhat surprising, then, that higher pre-shock densities are not found. One possible reason could be that HH objects tend to form in cavities that have been swept out by a wind from the forming star.

In addition to that from HH objects, the emission from three condensations (HH72D, HH25C and Knot 4) was also modelled. Condensations are thought to be HH objects that suffer from a greater extinction than their optically

visible counterparts. The models found for the condensations were strikingly similar to the models found for the HH objects, particularly for HH72A and HH320A. These findings suggest that HH objects and condensations are subject to similar, or even the same, shock mechanisms.

5.3.2 Models of [Fe II] and [C I] emission

The errors in the observed [Fe II] line intensities given in Table D.2 in Appendix D are the rms of the local baseline multiplied by the instrumental profile width. Two further errors, relating to flux calibration and inter-calibration over the two grisms used in the spectroscopy, of the order of 10% each should be added, giving a total error of up to 20% (Giannini et al., 2004; Nisini et al., 2002). It might be expected that the agreement between observed and predicted intensities for the 1.257 μm line should be good because, as the strongest and often most tightly constrained line, it was the most used guide in selecting the model: however, it is encouraging that this process generally also reproduces the 1.644 μm line intensity well. The 1.800 and 1.810 μm line intensities are never successfully modelled; however, they lie at wavelengths that suffer from poor atmospheric transmission (Nisini et al., 2002). Some of the weaker, and therefore more uncertain, observed transitions, such as the 1.328, 1.745 and 1.295 μm lines, are also generally not well modelled. The model predictions for the remaining lines, in particular the 1.321 and 1.534 μm lines, are usually within 20–50% of the observed value.

The intensities of the [C I] lines are reproduced without modification of the pre-shock abundance of C in the gas phase. Approximately 1/3 of the elemental C abundance is already in the gas phase, in the form of CO, which is dissociated at high temperature in reactions with H, producing C and OH. At the peak temperature of the 50 km s$-$1 J-type shocks, 99% of the H_2 has been dissociated to H, and nearly all of the CO to C (Hollenbach & McKee, 1989).

$$CO + H \rightarrow OH + C$$

This approach seems to work relatively well for the data obtained from slit 1 of HH99 and for HH99B0 in particular, although the model overestimates the intensity of the [C I] lines for HH99B1 by more than a factor of two. Unfortunately, the spectrum from slit 2 for HH99 suffered from noise around 0.98 μm and only upper limits could be obtained for the [C I] lines, which the model predictions are consistent with but much smaller than. In the other objects, the [C I] emission is stronger than that found in slit 1 of HH99 and the model underestimates the observations by more than a factor of two in almost all cases (the 0.985 μm line in HH26A is reproduced to within 50%). This underestimation of the [C I] line intensities by the model suggests that C should be treated the same way as Fe. Carbon is bound in grains as graphite and it is quite reasonable to expect that, if Fe is released into the gas phase by a previous shock wave, then C should be be also, although some carbon would desorb back onto grain mantles, in the form of CO, CO_2, CH_4 and other ices, as the post shock gas cools.

Nisini et al. (2002) and Giannini et al. (2004) performed a semi-empirical analysis using the observed [Fe II] lines in order to estimate n_e, n(Fe) and x_e for the objects observed in those papers. Their analysis requires at least one of the 1.644 μm/1.600 μm, 1.644 μm/1.534 μm and 1.644 μm/1.677 μm line ratios, which are slightly sensitive to density variations, in order to estimate n_e, and observations of [S II] and [N I] to estimate n(Fe) and x_e. This semi-empirical analysis is dependent upon the electron temperature, which must be assumed. In the case of the HH99 region, the complete analysis was only possible for HH99B0: however, values of n_e could be estimated for HH99A, HH99B1 (slit 1) and HH99B2 (T. Giannini, private communication) and this was also the case for HH26A. In Table 5.4, the values of n(Fe) (see below), n_e and x_e predicted by the J-type shock models and those found from semi-empirical analysis (where possible) are compared. Overall, the two sets of predictions are quite consistent with each other, which perhaps supports the hypothesis that the [Fe II] emission arises in a J-type shock. The predictions from the J-type shock model for HH99B0 are not in good agreement with

those from the semi-empirical analysis: in particular, the gas phase abundance of Fe predicted by the J-type shock model of 25% is smaller than the 50–100% abundance predicted by the semi-empirical analysis while the density is larger. The ionization fraction predicted by the J-type shock model is in agreement with that predicted by the semi-empirical analysis but the latter is not very tightly constrained. However, the lower abundance of gas phase Fe and ionization fraction in the J-type shock model, in relation to those derived from semi-empirical analysis, are compensated by a higher electron density, so the two models predict similar levels of excitation of Fe^+. Finally, the electron density of 2.5×10^3 cm^{-3} found from the semi-empirical analysis for HH99A favours model 1, which has an electron density of 3.2×10^3 cm^{-3}. Unfortunately, it was possible to predict only the electron density from the semi-empirical analysis for HH99A: the full analysis may have allowed a more certain discrimination between the three J-type shock models for that object.

In the context of the model, no erosion of grains occurs in J-type shocks so the the only change in the gas phase abundance of Fe is that due to the compression of the shock wave. Furthermore, and as discussed in Chapter 3, the rates of ionization of Fe to Fe^+ via charge transfer reactions with ions are such that Fe is rapidly ionized to Fe^+ and remains in that form for the range of temperatures over which [Fe II] emission occurs. Therefore, the initial percentage gas phase abundance of Fe, which is quoted in column 8 of Table 5.1 and column two of Table 5.4, is the same abundance of Fe^+ in the peak emission regions of the shock model.

None of the J-type shock models described above significantly contribute to the H_2 emission over the range of the observations but can begin to do so above 3×10^4 K. In particular, the population in high vibrational levels, (v=6, $J = 1$) (E=3.106×10^4 K), ($v = 7, J = 1$) (E=3.506×10^4 K) and ($v = 8, J = 1$) (E=3.871×10^4 K) for example, lie well above the median line of the excitation diagrams of the J-type shock models (see, for example, Figure 5.42). Population in the ($v = 8, J = 1$) level would tend to vibrationally cascade into the

Table 5.4: Comparison between values of Fe gas phase abundance, electron density and ionization fraction derived from semi-empirical analysis of observations and model predictions.

Object	% Fe in gas phase		n_e (cm^{-3})		x_e	
	Observed	Model	Observed	Model	Observed	Model
HH72A	20–35	23	5×10^4	1.3×10^4	<0.25	0.07
HH26A	–	5	$<5\times10^4$	3.3×10^4	–	0.16
HH120	20–60	34	$0.5–1\times10^4$	2.4×10^4	0.1[1]	0.14
HH111F	20–60	8	$0.8–2\times10^4$	5.1×10^4	0.1[2]	0.04
HH240A	60–100	8	3×10^4	2.8×10^5	0.85–0.95	0.13
HH99A (model 1)	–	100	2.5×10^3	3.2×10^3	–	0.15
HH99A (model 2)	–	12	2.5×10^3	1.6×10^4	–	0.15
HH99A (model 3)	–	1	2.5×10^3	2.4×10^4	–	0.14
HH99B0	50–100	25	$3–6\times10^3$	2.4×10^4	<0.9	0.14
HH99B1 (slit 1)	–	1	2.5×10^4	2.4×10^4	–	0.14
HH99B1 (slit 2)	–	23	–	2.4×10^4	–	0.14
HH99B2	–	71	$8–15\times10^3$	2.4×10^4	–	0.14
HH99B3	–	31	–	2.4×10^4	–	0.14

Notes: [1] Pettersson (1984)
[2] Bacciotti & Eislöffel (1999)

$(v = 7, J = 1)$ level and thence into the $(v = 6, J = 1)$ level and similar levels below. In the 50 km s^{-1} J-type shocks used for HH99, the time for which the gas is heated above 3×10^4 K is approximately 6×10^{-3} yr. This may be compared with the decay time of these levels which is of the order of 0.1 yr (Abgrall & Roueff, 1989, , Roueff, private communication). Therefore, the passage of the shock wave is rapid enough that the higher energy levels do not have time to thermalize and their population remains elevated as seen above.

Chapter 6

Conclusions

Modelling of the emission from outflows associated with low mass star formation was undertaken using a state-of-art shock code, MHD_VODE, (Le Bourlot et al., 2002; Flower et al., 2003, and references therein). The intensities of H_2, [Fe II] and [C I] emission lines observed towards 14 HH objects by Nisini et al. (2002); Giannini et al. (2004); M^{c}Coey et al. (2004) have been used to constrain the parameters of shock models. The main conclusions of this work are as follows:

- It was found that the excitation diagrams derived from the observed H_2 emission in the HH objects can be reproduced by non-equilibrium models of J-type shocks with magnetic precursors and ages of typically 100–200 years. The shock velocities range from about 30 to about 50 km s^{-1}, and the pre-shock gas densities are of the order of 10^4 cm^{-3}. For all the HH objects in which [Fe II] emission was observed, the fit to the H_2 emission was improved by the inclusion of photoionization effects. In general, it was found that observations of H_2 lines from energy levels with $v > 2$ are required to constrain the models of H_2 emission;

- The same planar models that were used to fit the H_2 emission systematically underestimated both the [Fe II] and [C I] lines intensities observed in the HH objects. Instead a higher ionization fraction, such as that

produced in a J-type shock, was required. Such a combination of excitation conditions is expected from a bow shock. An elementary bow shock model was constructed in which the atomic and ionic emission originates in a J-type shock at the dissociative apex of the bow, while the H_2 emission arises in the wings from the J-type shock with magnetic precursor shocks discussed above;

- In order to reproduce the observed [Fe II] emission, it is necessary to assume an elevated abundance of Fe in the gas phase, perhaps as the result of grain erosion in a previous shock wave. This assumption is supported by observations which indicate that variability within HH outflows occurs on time scales of a factor of ten shorter than the lifetime of the outflow. Predictions of the J-type shock models of the abundance of Fe in the gas phase, the electron density and the ionization fraction of the gas are also consistent with estimates derived from semi-empirical analysis of observations of atomic and ionic lines from HH objects;

- The intensities of the [Fe II] emission lines are reproduced satisfactorily by pure J-type shocks. In particular, the computed intensities of the [Fe II] 1.257 μm and 1.644 μm lines, the strongest of the observed transitions, are in good agreement with the observations;

- The [C I] line intensities are reasonably well reproduced by the J-type shocks for HH99, which has the weakest observed [C I] emission of all the HH objects considered, but underestimated by more than a factor of two for most of the other objects considered. It is suggested that C, which, like Fe, is bound up in grain cores, should also be assumed to have been eroded from grains in a previous shock wave.

Investigation of the J-type shock models showed that Fe^+ becomes a significant coolant in the gas after the discontinuity (owing to dissociation of H_2 to H), in the region where the temperature drops below 10^4 K. The effect of the cooling due to Fe^+, which becomes more pronounced as the gas phase abundance of

Fe^+ increases, is to reduce the populations of the $v = 1$ H_2 energy levels. However, this effect is not observationally significant. The contribution of the J-type shock to the H_2 emission over the range of the observations is negligible compared to that from the J-type shock with magnetic precursor, as should be expected from the apex of a bow shock. On the other hand, above 3×10^4 K the H_2 emission from the J-type shock can become stronger than that from the models for the H_2 emission. The temperature of the gas falls so rapidly after the discontinuity that the higher energy H_2 levels, which are populated in the post-shock gas immediately after the discontinuity, do not have time to thermalize. The predictions of the J-type shock component are consistent with observed upper limits at such energies for HH99B2.

Overall, the findings listed above are consistent with the conclusions that HH outflows are episodic phenomena and that the emission from HH objects arises in bow shocks, with the atomic and ionic emission lines being produced at the apex and the H_2 emission lines in the wings.

Appendix A

Differential equations and source terms

A.1 Differential equations

The velocity, temperature, mass density and particle number density are integrated throughout the shock wave for each fluid. The conservation equations in Chapter 2 were given in a general form that contained charged fluid terms, which were the sum of the terms for positive and negative ions together with those for electrons. Here, the differential equations are given in the specific form used in MHD_VODE and neutral particles, positively charged ions, negatively charged ions and electrons are considered separately. Note that charge neutrality is assumed so the number density of the positively charged ions is given by the sum of the number densities of the negatively charged ions and the electrons. In order that the shock parameters can be integrated, the conservation equations for particle number, mass, momentum and energy in a multi-fluid medium (Equations 2.11–2.20 in Section 2.2.2 of Chapter 2) must be rearranged into the form of differential equations for v, T, ρ and n. The form of the differential equations below follow that of Heck et al. (1990); the source terms, which are discussed in the next Section, are as in Sections 2.2.2 in Chapter 2 with the subscripts n, i, neg and e denoting the neutral fluid, positive ions, negative ions and electrons, respectively.

$$\frac{d}{dz}v_{\mathrm{n}} = \frac{\left(2\mathcal{P}_{\mathrm{n}}v_{\mathrm{n}}^2 - \frac{5}{2}\mathcal{A}_{\mathrm{n}}v_{\mathrm{n}} + \mathcal{B}_{\mathrm{n}}\right)}{\left(\frac{5}{2}n_{\mathrm{n}}kT_{\mathrm{n}} - \frac{3}{2}\rho_{\mathrm{n}}v_{\mathrm{n}}^2\right)} \tag{A.1}$$

$$\frac{d}{dz}v_{\mathrm{i}} = \frac{\left(-2\mathcal{P}_{\mathrm{n}}v_{\mathrm{i}}^2 + \frac{5}{2}\mathcal{A}_{\mathrm{n}}v_{\mathrm{i}} + \mathcal{B}_{\mathrm{i}} + \mathcal{B}_{\mathrm{neg}} + \mathcal{B}_{\mathrm{e}}\right)}{\left[\frac{5}{2}n_{\mathrm{i}}k\left(T_{\mathrm{i}} + T_{\mathrm{e}}\right) + \frac{3}{2}\left(\frac{v_{\mathrm{s}}}{v_{\mathrm{i}}}\right)^2\frac{B_0^2}{4\pi} - \frac{3}{2}\left(\rho_{\mathrm{i}} + \rho_{\mathrm{neg}}\right)v_{\mathrm{i}}^2\right]} \tag{A.2}$$

$$\frac{d}{dz}\rho_{\mathrm{n}} = \frac{\left(\mathcal{P}_{\mathrm{n}} - \rho_{\mathrm{n}}\frac{d}{dz}v_{\mathrm{n}}\right)}{v_{\mathrm{n}}} \tag{A.3}$$

$$\frac{d}{dz}\rho_{\mathrm{i}} = \frac{-\left(\mathcal{P}_{\mathrm{n}} + \rho_{\mathrm{i}}\frac{d}{dz}v_{\mathrm{i}}\right)}{v_{\mathrm{i}}} \tag{A.4}$$

$$\frac{d}{dz}\rho_{\mathrm{neg}} = \frac{\left(\mathcal{P}_{\mathrm{neg}} - \rho_{\mathrm{neg}}\frac{d}{dz}v_{\mathrm{i}}\right)}{v_{\mathrm{i}}} \tag{A.5}$$

$$\frac{d}{dz}T_{\mathrm{n}} = \frac{\left(\mathcal{A}_{\mathrm{n}} - \mathcal{P}_{\mathrm{n}}v_{\mathrm{n}} - \frac{\mathcal{N}_{\mathrm{n}}kT_{\mathrm{n}}}{v_{\mathrm{n}}} + \frac{kT_{\mathrm{n}}}{v_{\mathrm{n}}}n_{\mathrm{n}}\frac{dv_{\mathrm{n}}}{dz} - \rho_{\mathrm{n}}v_{\mathrm{n}}\frac{dv_{\mathrm{n}}}{dz}\right)}{(kn_{\mathrm{n}})} \tag{A.6}$$

$$\frac{d}{dz}T_{\mathrm{i}} = \frac{\left(-\frac{1}{2}\mathcal{P}_{\mathrm{n}}v_{\mathrm{i}}^2 - \frac{3}{2}\mathcal{N}_{\mathrm{i}}kT_{\mathrm{i}} - \mathcal{A}_{\mathrm{i}}v_{\mathrm{i}} + \mathcal{B}_{\mathrm{i}} - n_{\mathrm{i}}kT_{\mathrm{i}}\frac{dv_{\mathrm{i}}}{dz}\right)}{\left(\frac{3}{2}kn_{\mathrm{i}}v_{\mathrm{i}}\right)} \tag{A.7}$$

$$\frac{d}{dz}T_{\mathrm{e}} = \frac{\left(\frac{1}{2}\mathcal{P}_{\mathrm{neg}}v_{\mathrm{i}}^2 - \frac{3}{2}\mathcal{N}_{\mathrm{i}}kT_{\mathrm{e}} - \left(\mathcal{A}_{\mathrm{i}} + \mathcal{A}_{\mathrm{e}}\right)v_{\mathrm{i}} + \left(\mathcal{B}_{\mathrm{neg}} + \mathcal{B}_{\mathrm{e}}\right) - n_{\mathrm{i}}kT_{\mathrm{e}}\frac{dv_{\mathrm{i}}}{dz}\right)}{\left(\frac{3}{2}k\,n_{\mathrm{i}}v_{\mathrm{i}}\right)} \tag{A.8}$$

$$\frac{d}{dz}n_{\mathrm{n}} = \frac{\left(\mathcal{N}_{\mathrm{n}} - n_{\mathrm{n}}\frac{dv_{\mathrm{n}}}{dz}\right)}{v_{\mathrm{n}}} \tag{A.9}$$

$$\frac{d}{dz}n_{\mathrm{i}} = \frac{\left(\mathcal{N}_{\mathrm{i}} - n_{\mathrm{i}}\frac{dv_{\mathrm{i}}}{dz}\right)}{v_{\mathrm{i}}} \tag{A.10}$$

These differential equations are integrated numerically and the order in which this occurs is important. As can be seen above, dv/dz appears in all the other differential equations so equations (A.1) and (A.2) must be solved before any others.

A.2 Source terms

The source terms provide the change in number and mass density, momentum and energy per unit volume per unit time and are calculated for each step of the integration. Draine (1980), Flower et al. (1985) and Flower et al. (1986) gave the expressions for the source terms used in the code and here they are reproduced.

Number density

The rate at which an atomic or molecular species, α, is produced in chemical reactions per unit volume and time was denoted by $\mathcal{C}_\alpha$ in Chapter 2. Therefore, the total number of neutral and ionized particles created per unit volume and time, respectively, are

$$\mathcal{N}_\mathrm{n} = \sum_{\substack{\alpha, \\ \text{neutral} \\ \text{species}}} \mathcal{C}_\alpha \tag{A.11}$$

and

$$\mathcal{N}_\mathrm{i} = \sum_{\substack{\alpha, \\ \text{ionized} \\ \text{species}}} \mathcal{C}_\alpha. \tag{A.12}$$

Mass density

The rate at which the mass of an atomic or molecular species, m_α, is transferred from the the ionized to the neutral fluid through the same chemical processes

and so is given by

$$\mathcal{P}_{\rm n} = \sum_{\substack{\alpha, \\ \text{neutral} \\ \text{species}}} \mathcal{C}_\alpha \, m_\alpha \tag{A.13}$$

and, similarly for the ions

$$\mathcal{P}_{\rm i} = \sum_{\substack{\alpha, \\ \text{ionized} \\ \text{species}}} \mathcal{C}_\alpha \, m_\alpha. \tag{A.14}$$

Conservation of mass requires that $\mathcal{P}_{\rm i} = -\mathcal{P}_{\rm n}$.

Momentum

Momentum transfer between the neutral and ionized fluids occurs via reactive ion-neutral collisions, which occurs at a rate $\mathcal{A}_{\rm n}^{\rm coll}$ and elastic ion-neutral scattering, which occurs at a rate of $\mathcal{A}_{\rm n}^{\rm scat}$. The source term for momentum transfer from the ionized to the neutral, $\mathcal{A}_{\rm n}$ is given by the sum of $\mathcal{A}_{\rm n}^{\rm coll}$ and $\mathcal{A}_{\rm n}^{\rm scat}$: conservation of momentum implies that $\mathcal{A}_{\rm i} = -\mathcal{A}_{\rm n}$.

Set

$$\mathcal{C}_\alpha = \sum_\beta \mathcal{C}_{\alpha\beta} \tag{A.15}$$

where $\mathcal{C}_{\alpha\beta}$ is the rate at which species α is created or destroyed through a chemical reaction β. The rate of momentum transfer resulting from ion-neutral collisions is calculated assuming that species α is created or destroyed at the centre of mass velocity, v_β^{CM}, of reaction β.

$$\mathcal{A}_{\rm n}^{\rm coll} = \sum_{\substack{\alpha, \\ \text{neutral} \\ \text{species}}} \sum_\beta \mathcal{C}_{\alpha\beta} \, m_\alpha \, v_\beta^{CM} \tag{A.16}$$

Elastic ion-neutral scattering is assumed to occur at a rate of

$$\sigma_{\rm in} = 2.41 \, \pi \left(\frac{e^2 \alpha_{\rm n}}{\mu_{\rm in} v_{\rm in}^2} \right)^{\frac{1}{2}} \tag{A.17}$$

(Osterbrock, 1961), where e is the charge of the electron, α_n is the polarizability of the neutral, $\mu_{in} = \mu_i\mu_n/(\mu_i + \mu_n)$ is the reduced mass of ion-neutral system and v_{in} is the relative velocity of the ion and neutral particles. The cross section rate coefficient is

$$\langle\sigma v\rangle_{in} = 2.41\,\pi \left(\frac{e^2\alpha_n}{\mu_{in}}\right)^{\frac{1}{2}} \tag{A.18}$$

and the transfer of momentum from the ion to the neutral fluid occurs at a rate of

$$\mathcal{A}_n^{scat} = \frac{\rho_n\rho_i}{\mu_n + \mu_i}\langle\sigma v\rangle_{in}(v_i - v_n) \tag{A.19}$$

Electron-neutral scattering provides a negligible contribution to momentum transfer due to the small mass of the electron.

Energy

There are several ways in which energy is assumed to be transferred between fluids: as kinetic energy resulting from chemical reactions, $\mathcal{B}^{kin}$; as enthalpy due to formation and destruction processes, $\mathcal{B}^{th}$; as heating or cooling due to energy defects of chemical reactions, $\mathcal{B}^{chem}$; and as heating or cooling due to ion-neutral, electron-neutral and electron-ion scattering, $\mathcal{B}^{i-n}$, $\mathcal{B}^{e-n}$ and $\mathcal{B}^{e-i}$, respectively. The total heating/cooling rate per unit volume and time for each of the fluids is given by the sum of these contributions.

The transfer of mass between the ionized and neutral fluids that occurs as a result of chemical reactions also gives rise to a transfer of kinetic energy. Kinetic energy is transferred to the neutral fluid at a rate

$$\mathcal{B}_n^{kin} = \sum_{\substack{\alpha, \\ \text{neutral} \\ \text{species}}} \sum_{\beta} \mathcal{C}_{\alpha\beta}\,\frac{1}{2} m_\alpha\, v_\beta^{2\,CM} \tag{A.20}$$

and to the ionized fluid at a rate

$$\mathcal{B}_i^{kin} = \sum_{\substack{\alpha, \\ \text{ionized} \\ \text{species}}} \sum_{\beta} \mathcal{C}_{\alpha\beta}\,\frac{1}{2} m_\alpha\, v_\beta^{2\,CM}. \tag{A.21}$$

The small electron mass means that the contribution from the electrons is negligible.

The destruction ($\mathcal{C}_{\alpha\beta} < 0$) and formation ($\mathcal{C}_{\alpha\beta} > 0$) of atomic and molecular species, for example via dissociation and recombination, results in transfer of enthalpy between the ionized and neutral fluids. The destruction and formation processes should be considered separately and the rate at which enthalpy is added to the neutral fluid is given by

$$\mathcal{B}_{\rm n}^{\rm th} = \sum_{\substack{\alpha, \\ \text{neutral} \\ \text{species}}} \left[\sum_{\substack{\beta, \\ \mathcal{C}_{\alpha\beta}>0}} \frac{3}{2} k \frac{T_{\rm i} + T_{\rm e}}{2} \mathcal{C}_{\alpha\beta} + \sum_{\substack{\beta, \\ \mathcal{C}_{\alpha\beta}<0}} \frac{3}{2} k T_{\rm n} \mathcal{C}_{\alpha\beta} \right]. \tag{A.22}$$

For the ions and electrons the rate of energy input is given by

$$\mathcal{B}_{\rm i}^{\rm th} = \sum_{\substack{\alpha, \\ \text{ionized} \\ \text{species}}} \left[\sum_{\substack{\beta, \\ \mathcal{C}_{\alpha\beta}>0}} \frac{3}{2} k T_{\rm n} \mathcal{C}_{\alpha\beta} + \sum_{\substack{\beta, \\ \mathcal{C}_{\alpha\beta}<0}} \frac{3}{2} k T_{\rm i} \mathcal{C}_{\alpha\beta} \right] \tag{A.23}$$

and

$$\mathcal{B}_{\rm e}^{\rm th} = \sum_{\substack{\alpha, \\ \text{ionized} \\ \text{species}}} \sum_{\substack{\beta, \\ \mathcal{C}_{\alpha\beta}<0}} \frac{3}{2} k T_{\rm e} \mathcal{C}_{\alpha\beta} \tag{A.24}$$

Cosmic-ray ionization of H results in an injection of non-thermal electrons that are subsequently thermalized via collisions. The rate at which this process adds energy to the electron fluid is taken to be $\delta E \zeta \rho_{\rm n} / \nu_{\rm n}$, where δE is the mean energy per cosmic-ray ionization (Spitzer & Scott, 1969) and ζ is the cosmic-ray ionization rate, which is taken to be 5×10^{-17} s^{-1}. This process is not significant in a shock wave but it is included for the sake of completeness.

The energy defects, ΔE, of chemical processes may also result in the transfer of energy between the ionized fluids. The source term for the heating (or cooling) of the neutral fluid is

$$\mathcal{B}_{\rm n}^{\rm chem} = \sum_{\substack{\alpha, \\ \text{neutral} \\ \text{species}}} \sum_{\substack{\beta, \\ \mathcal{C}_{\alpha\beta}>0}} \frac{M_\beta - m_\alpha}{M_\beta} \Delta E_\alpha \mathcal{C}_{\alpha\beta} \tag{A.25}$$

where M_β is the total mass of the products of the reaction β. The source term for the heating (or cooling) of the ion fluid, $\mathcal{B}_{\rm i}^{\rm chem}$, has the same form but instead involves a summation over the ionized species.

Ion-neutral, electron-neutral and electron-ion scattering also give rise to a transfer of heat among the fluids. Elastic scattering on the ions heats the neutral fluid at the rate

$$\mathcal{B}_{\rm n}^{\rm i-n} = \frac{\rho_{\rm n}\rho_{\rm i}}{\mu_{\rm n}\mu_{\rm i}}\langle\sigma v\rangle_{\rm in}\frac{2\mu_{\rm n}\mu_{\rm i}}{\mu_{\rm n}+\mu_{\rm i}}\{\frac{3}{2}k(T_{\rm i}-T_{\rm n})+\frac{1}{2}(v_{\rm i}-v_{\rm n})(\mu_{\rm i}\mu_{\rm i}+\mu_{\rm n}\mu_{\rm n})\} \quad \text{(A.26)}$$

and conservation of energy implies that $\mathcal{B}_{\rm i}^{\rm i-n} = -\mathcal{B}_{\rm n}^{\rm i-n}$. The heating of the neutral fluid by electron neutral scattering has a similar form but is simplified because $m_{\rm e} << \mu_{\rm n}$,

$$\mathcal{B}_{\rm n}^{\rm e-n} = \frac{\rho_{\rm n}\rho_{\rm e}}{\mu_{\rm n}}\langle\sigma v\rangle_{\rm en}2m_{\rm e}\{\frac{4}{2}k(T_{\rm e}-T_{\rm n})+\frac{1}{2}\mu_{\rm n}v_{\rm n}(v_{\rm i}-v_{\rm n})\} \quad \text{(A.27)}$$

where the scattering cross section is taken to be independent of energy and is given by

$$\langle\sigma v\rangle_{\rm en} = 10^{-15}\left(\frac{8kT_{\rm e}}{\pi m_{\rm e}}\right)\,{\rm cm}^2. \quad \text{(A.28)}$$

Again, conservation of energy implies that $\mathcal{B}_{\rm e}^{\rm e-n} = -\mathcal{B}_{\rm n}^{\rm e-n}$. Coulomb scattering on ions heats the electron fluid at a rate

$$\mathcal{B}_{\rm e}^{\rm e-i} = \frac{4e^4}{\mu_{\rm i}kT_{\rm e}}\left(\frac{2\pi m_{\rm e}}{kT_{\rm e}}\right)^{\frac{1}{2}}\ln\Lambda\left(\frac{\rho_{\rm i}}{\mu_{\rm i}}\right)^2 k(T_{\rm i}-T_{\rm e}) \quad \text{(A.29)}$$

(c.f. Spitzer, 1962), where

$$\Lambda = \frac{3}{2e^3}\left(\frac{k^3T_{\rm e}^3\mu_{\rm i}}{\pi\rho_{\rm i}}\right)^{\frac{1}{2}}. \quad \text{(A.30)}$$

Cooling of all three fluids can also occur via emission of photons, following collisional excitation. Ro-vibrational transitions of H_2 are important for cooling the gas while fine-structure transitions of Fe^+ in particular and also the atoms and ions of C, S, O, N and Si can play a role in cooling the gas immediately after the discontinuity in a J-type shock. These processes are discussed in Chapter 3 and further details are given in Appendix C.1.

Appendix B

Chemistry

B.1 Initial species abundances

Table B.1: Initial abundances, relative to $n_{\mathrm{H}} = 10^4$ cm^{-3}, of all species considered in the model, in which photoionization effects are considered. Grain mantle and core species are labelled with a single and a double asterisk, respectively.

Species	Relative abundance	Species	Relative abundance
H	9.645×10^{-05}	H^+	1.430×10^{-09}
H_2	5.000×10^{-01}	H_2^+	2.284×10^{-12}
He	1.000×10^{-01}	H_3^+	1.110×10^{-09}
C	1.480×10^{-06}	He^+	9.427×10^{-10}
CH	1.975×10^{-08}	C^+	6.999×10^{-07}
CH_2	4.906×10^{-08}	CH^+	1.469×10^{-14}
CH_3	7.814×10^{-12}	CH_2^+	5.713×10^{-13}
CH_4	3.908×10^{-11}	CH_3^+	4.558×10^{-11}
O	4.453×10^{-05}	CH_4^+	3.776×10^{-18}
O_2	1.167×10^{-08}	CH_5^+	4.056×10^{-14}
OH	3.846×10^{-09}	O^+	1.085×10^{-14}
H_2O	3.837×10^{-09}	O_2^+	1.041×10^{-14}
CO	7.944×10^{-05}	OH^+	9.143×10^{-14}
CO_2	4.123×10^{-12}	H_2O^+	1.103×10^{-13}
C_2	2.325×10^{-08}	H_3O^+	2.828×10^{-12}
C_2H	2.266×10^{-08}	CO^+	7.657×10^{-15}
C_2H_2	1.549×10^{-09}	HCO^+	4.380×10^{-11}
C_3	3.125×10^{-11}	HCO_2^+	4.080×10^{-17}

Table B.1: *(Continued.)*

Species	Relative abundance	Species	Relative abundance
C_3H	8.470×10^{-10}	C_2^+	7.700×10^{-15}
C_3H_2	9.992×10^{-10}	C_2H^+	2.730×10^{-14}
CH_3OH	1.000×10^{-16}	$C_2H_2^+$	6.212×10^{-12}
H_2CO	1.000×10^{-16}	$C_2H_3^+$	1.518×10^{-14}
HCO_2H	1.000×10^{-16}	C_3^+	1.032×10^{-13}
N	5.234×10^{-05}	C_3H^+	3.681×10^{-12}
NH	1.756×10^{-09}	$C_3H_2^+$	4.979×10^{-13}
NH_2	3.437×10^{-08}	$C_3H_3^+$	6.132×10^{-13}
NH_3	3.620×10^{-10}	N^+	1.352×10^{-13}
CN	1.867×10^{-07}	NH^+	7.439×10^{-15}
HCN	1.694×10^{-08}	NH_2^+	2.251×10^{-13}
HNC	4.986×10^{-09}	NH_3^+	6.928×10^{-12}
N_2	5.662×10^{-06}	NH_4^+	4.393×10^{-13}
NO	8.966×10^{-10}	CN^+	1.970×10^{-15}
S	7.825×10^{-06}	C_2N^+	1.395×10^{-11}
SH	1.375×10^{-11}	HCN^+	5.704×10^{-14}
H_2S	2.633×10^{-12}	H_2CN^+	6.604×10^{-12}
CS	7.189×10^{-07}	H_2NC^+	4.539×10^{-14}
SO	7.231×10^{-10}	H_2CO^+	2.262×10^{-42}
SO_2	4.273×10^{-13}	N_2^+	3.061×10^{-15}
OCS	1.321×10^{-14}	N_2H^+	2.361×10^{-12}
Si	1.405×10^{-16}	NO^+	8.792×10^{-13}
SiH	1.243×10^{-19}	HNO^+	2.921×10^{-16}
SiH_2	2.080×10^{-24}	S^+	6.159×10^{-06}
SiH_3	1.497×10^{-30}	SH^+	8.963×10^{-12}
SiH_4	7.146×10^{-29}	H_2S^+	2.353×10^{-16}
SiO	8.129×10^{-18}	H_3S^+	8.982×10^{-16}
SiO_2	5.100×10^{-23}	CS^+	3.327×10^{-13}
Mg	1.000×10^{-16}	HCS^+	9.775×10^{-12}
Fe	6.417×10^{-09}	SO^+	6.574×10^{-12}
FeO	3.341×10^{-19}	HSO^+	6.224×10^{-16}
FeH	9.977×10^{-17}	HSO_2^+	2.478×10^{-19}
FeOH	9.977×10^{-17}	$HOCS^+$	6.300×10^{-18}
$C_{54}H_{18}$	2.418×10^{-07}	Si^+	1.352×10^{-15}
C_6	1.000×10^{-16}	SiH^+	2.551×10^{-22}
C_{60}	3.072×10^{-12}	SiH_2^+	3.604×10^{-22}

Table B.1: *(Continued.)*

Species	Relative abundance	Species	Relative abundance
H_2O^*	1.029×10^{-04}	SiH_3^+	4.161×10^{-27}
CO^*	8.271×10^{-06}	SiH_4^+	3.109×10^{-37}
CO_2^*	1.339×10^{-05}	SiH_5^+	1.220×10^{-33}
CH_4^*	1.549×10^{-06}	SiO^+	2.044×10^{-23}
NH_3^*	1.549×10^{-05}	$SiOH^+$	1.634×10^{-21}
CH_3OH^*	1.859×10^{-05}	Fe^+	8.570×10^{-09}
H_2CO^*	6.199×10^{-06}	FeO^+	9.977×10^{-17}
HCO_2H^*	7.240×10^{-06}	FeH^+	9.977×10^{-17}
OCS^*	2.069×10^{-07}	$FeOH^+$	1.987×10^{-25}
H_2S^*	3.720×10^{-06}	$C_{54}H_{18}^+$	3.434×10^{-11}
O^{**}	1.399×10^{-04}	C_{60}^+	2.733×10^{-15}
Si^{**}	3.370×10^{-05}	C_{54}^+	1.000×10^{-16}
Mg^{**}	3.700×10^{-05}	$C_{54}H_{18}^-$	7.583×10^{-07}
Fe^{**}	3.230×10^{-05}	C_{60}^-	6.796×10^{-11}
C^{**}	1.629×10^{-04}	C_{54}^-	1.000×10^{-16}

B.2 Chemical reactions

In this Section, all of the chemical reactions included in the model are listed as they are in the code. The rate ($cm^3\ s^{-1}$) at which a reaction occurs is generally given by $k = \gamma \times (T/300)^{\alpha} \times \exp(-\beta/T)$, where γ, α and β, respectively, are listed in the final three columns. Electrons, grains, photons, cosmic-ray photons and secondary photons are denoted by 'ELECTR', 'GRAIN', 'PHOTON', 'CRP' and 'SECPHO', respectively.

```
H       H       =H2                                 8.14D-17  0.5
H       ELECTR  =H+       ELECTR  ELECTR  9.20D-10  0.5  157890.0
H2      ELECTR  =H2+      ELECTR  ELECTR  1.40D-09  0.5  179160.0
H       H+      =H+       H+      ELECTR  1.30D-13  0.5  157890.0
H       H3+     =H3+      H+      ELECTR  1.30D-13  0.5  157890.0
H       He+     =He+      H+      ELECTR  1.30D-13  0.5  157890.0
H       H3O+    =H3O+     H+      ELECTR  1.30D-13  0.5  157890.0
H       H3S+    =H3S+     H+      ELECTR  1.30D-13  0.5  157890.0
```

```
H       HCO+    =HCO+    H+      ELECTR   1.30D-13  0.5   157890.0
H       Fe+     =Fe+     H+      ELECTR   1.30D-13  0.5   157890.0
H       NH3+    =NH3+    H+      ELECTR   1.30D-13  0.5   157890.0
H       NH4+    =NH4+    H+      ELECTR   1.30D-13  0.5   157890.0
H       S+      =S+      H+      ELECTR   1.30D-13  0.5   157890.0
H       SiOH+   =SiOH+   H+      ELECTR   1.30D-13  0.5   157890.0
H       O2+     =O2+     H+      ELECTR   1.30D-13  0.5   157890.0
H2      H+      =H+      H2+     ELECTR   1.10D-13  0.5   179160.0
H2      H3+     =H3+     H2+     ELECTR   1.10D-13  0.5   179160.0
H2      He+     =He+     H2+     ELECTR   1.10D-13  0.5   179160.0
H2      H3O+    =H3O+    H2+     ELECTR   1.10D-13  0.5   179160.0
H2      H3S+    =H3S+    H2+     ELECTR   1.10D-13  0.5   179160.0
H2      HCO+    =HCO+    H2+     ELECTR   1.10D-13  0.5   179160.0
H2      Fe+     =Fe+     H2+     ELECTR   1.10D-13  0.5   179160.0
H2      NH3+    =NH3+    H2+     ELECTR   1.10D-13  0.5   179160.0
H2      NH4+    =NH4+    H2+     ELECTR   1.10D-13  0.5   179160.0
H2      S+      =S+      H2+     ELECTR   1.10D-13  0.5   179160.0
H2      SiOH+   =SiOH+   H2+     ELECTR   1.10D-13  0.5   179160.0
H2      O2+     =O2+     H2+     ELECTR   1.10D-13  0.5   179160.0
He      H+      =H+      He+     ELECTR   1.10D-13  0.5   285328.0
He      H3+     =H3+     He+     ELECTR   1.10D-13  0.5   285328.0
He      He+     =He+     He+     ELECTR   1.10D-13  0.5   285328.0
He      H3O+    =H3O+    He+     ELECTR   1.10D-13  0.5   285328.0
He      H3S+    =H3S+    He+     ELECTR   1.10D-13  0.5   285328.0
He      HCO+    =HCO+    He+     ELECTR   1.10D-13  0.5   285328.0
He      Fe+     =Fe+     He+     ELECTR   1.10D-13  0.5   285328.0
He      NH3+    =NH3+    He+     ELECTR   1.10D-13  0.5   285328.0
He      NH4+    =NH4+    He+     ELECTR   1.10D-13  0.5   285328.0
He      S+      =S+      He+     ELECTR   1.10D-13  0.5   285328.0
He      SiOH+   =SiOH+   He+     ELECTR   1.10D-13  0.5   285328.0
He      O2+     =O2+     He+     ELECTR   1.10D-13  0.5   285328.0
```

```
H2       ELECTR =ELECTR  H       H          2.00D-09  0.5  116300.0
H2       H      =H       H       H          1.00D-10  0.0   52000.0
H2       He     =He      H       H          1.00D-11  0.0   52000.0
H2       H2     =H2      H       H          1.25D-11  0.0   52000.0
H2       H+     =H+      H       H          3.00D-11  0.5   52000.0
H2       H3+    =H3+     H       H          3.00D-11  0.5   52000.0
H2       He+    =He+     H       H          3.00D-11  0.5   52000.0
H2       H3O+   =H3O+    H       H          3.00D-11  0.5   52000.0
H2       H3S+   =H3S+    H       H          3.00D-11  0.5   52000.0
H2       HCO+   =HCO+    H       H          3.00D-11  0.5   52000.0
H2       Fe+    =Fe+     H       H          3.00D-11  0.5   52000.0
H2       NH3+   =NH3+    H       H          3.00D-11  0.5   52000.0
H2       NH4+   =NH4+    H       H          3.00D-11  0.5   52000.0
H2       S+     =S+      H       H          3.00D-11  0.5   52000.0
H2       SiOH+  =SiOH+   H       H          3.00D-11  0.5   52000.0
H2       O2+    =O2+     H       H          3.00D-11  0.5   52000.0
C54H18   ELECTR =C54H18- PHOTON              1.00D-07  0.00      0.0
C54H18+  ELECTR =C54H18  PHOTON              3.30D-06 -0.50      0.0
C54H18+  C54H18-=C54H18  C54H18              3.00D-09 -0.50      0.0
C54H18-  H+     =C54H18  H                   7.50D-08 -0.50      0.0
C54H18-  H3+    =C54H18  H2      H          2.20D-08 -0.50      0.0
C54H18-  H3+    =C54H18  H       H    H     2.20D-08 -0.50      0.0
C54H18-  He+    =C54H18  He                  3.80D-08 -0.50      0.0
C54H18-  C+     =C54H18  C                   2.20D-08 -0.50      0.0
C54H18-  H3O+   =C54H18  H2O     H          1.70D-08 -0.50      0.0
C54H18-  H3S+   =C54H18  H2S     H          1.30D-08 -0.50      0.0
C54H18-  NH4+   =C54H18  NH3     H          1.80D-08 -0.50      0.0
C54H18-  HCO+   =C54H18  CO      H          1.40D-08 -0.50      0.0
C54H18-  HCS+   =C54H18  CS      H          1.10D-08 -0.50      0.0
C54H18-  Si+    =C54H18  Si                  1.40D-08 -0.50      0.0
C54H18-  Fe+    =C54H18  Fe                  1.00D-08 -0.50      0.0
```

C54H18-	S+	=C54H18	S			1.30D-08	-0.50	0.0
C54H18	H+	=C54H18+	H			4.40D-09	0.00	0.0
C54H18	H3+	=C54H18+	H2	H		1.30D-09	0.00	0.0
C54H18	H3+	=C54H18+	H	H	H	1.30D-09	0.00	0.0
C54H18	He+	=C54H18+	He			2.20D-09	0.00	0.0
C54H18	C+	=C54H18+	C			1.30D-09	0.00	0.0
C54H18	H3O+	=C54H18+	H2O	H		1.00D-09	0.00	0.0
C54H18	H3S+	=C54H18+	H2S	H		7.40D-10	0.00	0.0
C54H18	NH4+	=C54H18+	NH3	H		1.00D-09	0.00	0.0
C54H18	HCO+	=C54H18+	CO	H		8.20D-10	0.00	0.0
C54H18	HCS+	=C54H18+	CS	H		6.50D-10	0.00	0.0
C54H18	Si+	=C54H18+	Si			8.30D-10	0.00	0.0
C54H18	Fe+	=C54H18+	Fe			5.90D-10	0.00	0.0
C54H18	S+	=C54H18+	S			7.80D-10	0.00	0.0
C54H18-	H	=C54H18	H	ELECTR		3.30D-09	0.00	5500.0
C54H18-	C	=C54H18	C	ELECTR		9.60D-10	0.00	5500.0
C54H18-	CH	=C54H18	CH	ELECTR		9.60D-10	0.00	5500.0
C54H18-	O	=C54H18	O	ELECTR		8.30D-10	0.00	5500.0
C54H18-	OH	=C54H18	OH	ELECTR		8.30D-10	0.00	5500.0
C54H18	SECPHO	=C54H18+	ELECTR			2.00D+04	0.00	140000.0
C54H18-	SECPHO	=C54H18	ELECTR			2.00D+04	0.00	140000.0
C60	ELECTR	=C60-	PHOTON			6.900D-5	0.50	0.0
C60-	H+	=C60	H			1.60D-06	0.50	0.0
C60-	H3+	=C60	H2	H		4.61D-07	0.50	0.0
C60-	H3+	=C60	H	H	H	4.61D-07	0.50	0.0
C60-	He+	=C60	He			8.00D-07	0.50	0.0
C60-	C+	=C60	C			4.61D-07	0.50	0.0
C60-	H3O+	=C60	H2O	H		3.66D-07	0.50	0.0
C60-	H3S+	=C60	H2S	H		2.70D-07	0.50	0.0
C60-	NH4+	=C60	NH3	H		3.76D-07	0.50	0.0
C60-	HCO+	=C60	CO	H		2.96D-07	0.50	0.0

C60-	HCS+	=C60	CS	H		2.38D-07	0.50	0.0
C60-	Si+	=C60	Si			3.01D-07	0.50	0.0
C60-	Fe+	=C60	Fe			2.13D-07	0.50	0.0
C60-	S+	=C60	S			2.82D-07	0.50	0.0
C60	H+	=C60+	H			1.60D-06	0.50	0.0
C60	H3+	=C60+	H2	H		4.61D-07	0.50	0.0
C60	H3+	=C60+	H	H	H	4.61D-07	0.50	0.0
C60	He+	=C60+	He			8.00D-07	0.50	0.0
C60	C+	=C60+	C			4.61D-07	0.50	0.0
C60	H3O+	=C60+	H2O	H		3.66D-07	0.50	0.0
C60	H3S+	=C60+	H2S	H		2.70D-07	0.50	0.0
C60	NH4+	=C60+	NH3	H		3.76D-07	0.50	0.0
C60	HCO+	=C60+	CO	H		2.96D-07	0.50	0.0
C60	HCS+	=C60+	CS	H		2.38D-07	0.50	0.0
C60	Si+	=C60+	Si			3.01D-07	0.50	0.0
C60	Fe+	=C60+	Fe			2.13D-07	0.50	0.0
C60	S+	=C60+	S			2.82D-07	0.50	0.0
C60+	ELECTR	=C60	PHOTON			6.900D-5	0.50	0.0
C60	SECPHO	=C60+	ELECTR			0.63D+08	0.00	140000.0
C60-	SECPHO	=C60	ELECTR			0.41D+09	0.00	140000.0
C60-	C60	=C60	C54-	C6		7.000D-7	0.50	200000.0
C60+	C60	=C60	C54+	C6		7.000D-7	0.50	200000.0
H	CRP	=H+	ELECTR			4.60D-01	0.00	0.0
He	CRP	=He+	ELECTR			5.00D-01	0.00	0.0
H2	CRP	=H+	H	ELECTR		4.00D-02	0.00	0.0
H2	CRP	=H	H			1.50D+00	0.00	0.0
H2	CRP	=H2+	ELECTR			9.60D-01	0.00	0.0
C	CRP	=C+	ELECTR			1.80D+00	0.00	0.0
O	CRP	=O+	ELECTR			2.80D+00	0.00	0.0
C	SECPHO	=C+	ELECTR			1.02D+03	0.00	140000.0
CH	SECPHO	=C	H			1.46D+03	0.00	140000.0

CH4	SECPHO	=CH3	H	4.68D+03	0.00	140000.0
CH+	SECPHO	=C	H+	3.52D+02	0.00	140000.0
OH	SECPHO	=O	H	1.02D+03	0.00	140000.0
H2O	SECPHO	=OH	H	1.94D+03	0.00	140000.0
O2	SECPHO	=O2+	ELECTR	2.34D+02	0.00	140000.0
O2	SECPHO	=O	O	1.50D+03	0.00	140000.0
CO2	SECPHO	=CO	O	3.42D+03	0.00	140000.0
C2	SECPHO	=C	C	4.74D+02	0.00	140000.0
C2H	SECPHO	=C2	H	8.16D+03	0.00	140000.0
C2H2	SECPHO	=C2H	H	1.03D+04	0.00	140000.0
C2H2	SECPHO	=C2H2+	ELECTR	2.62D+03	0.00	140000.0
C3	SECPHO	=C2	C	2.24D+03	0.00	140000.0
C3H	SECPHO	=C3	H	8.16D+03	0.00	140000.0
C3H2	SECPHO	=C3H	H	8.16D+03	0.00	140000.0
CO	SECPHO	=C	O	6.80D+02	1.20	140000.0
O	H2	=OH	H	1.55D-13	2.80	2980.0
CO	H	=OH	C	1.10D-10	0.50	77700.0
O2	H	=OH	O	1.63D-09	-0.90	8750.0
OH	H	=O	H2	7.00D-14	2.80	1950.0
OH	H2	=H2O	H	9.54D-13	2.00	1490.0
H2O	H	=OH	H2	5.24D-12	1.90	9265.0
C	H2	=CH	H	1.16D-09	0.50	14100.0
C	H	=CH	PHOTON	1.00D-17	0.00	0.0
CH	H2	=CH2	H	2.38D-10	0.00	1760.0
CH2	H2	=CH3	H	5.18D-11	0.17	6400.0
CH3	H2	=CH4	H	3.00D-10	0.00	5460.0
C2	H2	=C2H	H	1.60D-10	0.00	1419.0
C2H	H2	=C2H2	H	1.14D-11	0.00	950.0
CH	H	=C	H2	1.16D-09	0.50	2200.0
CH2	H	=CH	H2	4.70D-10	0.00	370.0
CH3	H	=CH2	H2	5.18D-11	0.17	5600.0

CH4	H	=CH3	H2		3.00D-10	0.00	6560.0
O2	C	=CO	O		3.30D-11	0.50	0.0
OH	CO	=CO2	H		4.40D-13	-1.15	390.0
OH	C	=CO	H		3.10D-11	-0.36	0.0
OH	O	=O2	H		3.10D-11	-0.36	0.0
CH	O	=HCO+	ELECTR		2.40D-14	0.50	0.0
CH	O	=CO	H		9.50D-11	0.50	0.0
CH2	O	=CO	H	H	2.00D-11	0.50	0.0
CH3	O	=CO	H2	H	1.80D-10	0.50	0.0
C2	O	=CO	C		5.00D-11	0.50	0.0
C2H	O	=CO	CH		1.00D-10	0.00	250.0
C3	O	=CO	C2		5.00D-11	0.50	0.0
C3H	O	=C2H	CO		5.00D-11	0.50	0.0
C3H2	O	=C2H2	CO		5.00D-11	0.50	0.0
C+	H	=CH+	PHOTON		7.00D-17	0.00	0.0
C+	H2	=CH2+	PHOTON		5.00D-16	0.00	0.0
C+	H2	=CH+	H		1.50D-10	0.00	4640.0
CH+	H	=C+	H2		1.50D-10	0.00	0.0
CH+	H2	=CH2+	H		1.20D-09	0.00	0.0
CH2+	H	=CH+	H2		1.20D-09	0.00	2700.0
CH2+	H2	=CH3+	H		7.00D-10	0.00	0.0
CH3+	H	=CH2+	H2		7.00D-10	0.00	10560.0
CH3+	H2	=CH5+	PHOTON		6.00D-15	0.00	0.0
CH3+	H2	=CH4+	H		2.00D-10	0.00	32500.0
CH4+	H	=CH3+	H2		2.00D-10	0.00	0.0
CH4+	H2	=CH5+	H		4.00D-11	0.00	0.0
CH5+	H	=CH4+	H2		4.00D-11	0.00	2200.0
H+	ELECTR	=H	PHOTON		2.90D-12	-0.74	0.0
H2+	ELECTR	=H	H		1.60D-08	-0.43	0.0
He+	ELECTR	=He	PHOTON		4.50D-12	-0.67	0.0
H3+	ELECTR	=H2	H		1.50D-07	-0.50	0.0

C+	ELECTR	=C	PHOTON		4.40D-12	-0.61	0.0
CH+	ELECTR	=C	H		1.50D-07	-0.42	0.0
CH2+	ELECTR	=C	H2		1.25D-07	-0.50	0.0
CH2+	ELECTR	=CH	H		1.25D-07	-0.50	0.0
CH3+	ELECTR	=CH2	H		1.75D-07	-0.50	0.0
CH3+	ELECTR	=CH	H2		1.75D-07	-0.50	0.0
CH4+	ELECTR	=CH3	H		3.00D-07	-0.50	0.0
CH4+	ELECTR	=CH2	H	H	3.00D-07	-0.50	0.0
CH5+	ELECTR	=CH	H2	H2	8.75D-08	-0.30	0.0
CH5+	ELECTR	=CH2	H2	H	8.75D-08	-0.30	0.0
CH5+	ELECTR	=CH3	H2		8.75D-08	-0.30	0.0
CH5+	ELECTR	=CH4	H		8.75D-08	-0.30	0.0
H+	H2	=H2+	H		6.40D-10	0.00	21300.0
H2+	H	=H+	H2		6.40D-10	0.00	0.0
H2+	H2	=H3+	H		2.10D-09	0.00	0.0
H3+	H	=H2+	H2		2.10D-09	0.00	20000.0
H+	O	=O+	H		6.00D-10	0.00	227.0
H+	OH	=OH+	H		2.10D-09	0.00	0.0
H+	O2	=O2+	H		1.20D-09	0.00	0.0
H+	H2O	=H2O+	H		8.20D-09	0.00	0.0
H+	CH	=CH+	H		1.90D-09	0.00	0.0
H+	CH2	=CH+	H2		1.40D-09	0.00	0.0
H+	CH2	=CH2+	H		1.40D-09	0.00	0.0
H+	CH3	=CH3+	H		3.40D-09	0.00	0.0
H+	CH4	=CH3+	H2		2.28D-09	0.00	0.0
H+	CH4	=CH4+	H		1.52D-09	0.00	0.0
H+	CO2	=HCO+	O		4.20D-09	0.00	0.0
H2+	C	=CH+	H		2.40D-09	0.00	0.0
H2+	O	=OH+	H		1.50D-09	0.00	0.0
H2+	CO	=HCO+	H		2.16D-09	0.00	0.0
H2+	CO	=CO+	H2		6.44D-10	0.00	0.0

H2+	OH	=OH+	H2		7.60D-10	0.00	0.0
H2+	H2O	=H2O+	H2		3.90D-09	0.00	0.0
H2+	H2O	=H3O+	H		3.40D-09	0.00	0.0
H2+	CH	=CH+	H2		7.10D-10	0.00	0.0
H2+	CH	=CH2+	H		7.10D-10	0.00	0.0
H2+	CH2	=CH3+	H		1.00D-09	0.00	0.0
H2+	CH2	=CH2+	H2		1.00D-09	0.00	0.0
H3+	O	=OH+	H2		8.00D-10	0.00	0.0
H3+	OH	=H2O+	H2		1.30D-09	0.00	0.0
H3+	CO	=HCO+	H2		1.70D-09	0.00	0.0
H3+	CO2	=HCO2+	H2		2.00D-09	0.00	0.0
H3+	H2O	=H3O+	H2		4.30D-09	0.00	0.0
H3+	C	=CH+	H2		2.00D-09	0.00	0.0
H3+	CH	=CH2+	H2		1.20D-09	0.00	0.0
H3+	CH2	=CH3+	H2		1.70D-09	0.00	0.0
H3+	CH3	=CH4+	H2		2.10D-09	0.00	0.0
H3+	CH4	=CH5+	H2		1.90D-09	0.00	0.0
He+	H2	=H+	H	He	1.10D-13	-0.24	0.0
He+	OH	=OH+	He		5.50D-10	0.00	0.0
He+	OH	=O+	H	He	5.50D-10	0.00	0.0
He+	H2O	=OH+	H	He	2.30D-10	-0.94	0.0
He+	H2O	=H2O+	He		4.86D-11	-0.94	0.0
He+	H2O	=H+	OH	He	1.64D-10	-0.94	0.0
He+	CO	=C+	O	He	1.50D-09	0.00	0.0
He+	O2	=O+	O	He	1.00D-09	0.00	0.0
He+	CO2	=CO+	O	He	7.70D-10	0.00	0.0
He+	CO2	=O+	CO	He	1.80D-10	0.00	0.0
He+	CO2	=C+	O2	He	4.00D-11	0.00	0.0
He+	CH	=C+	H	He	1.10D-09	0.00	0.0
He+	CH2	=C+	H2	He	7.50D-10	0.00	0.0
He+	CH2	=CH+	H	He	7.50D-10	0.00	0.0

He+	CH3	=CH+	H2	He		9.00D-10	0.00	0.0
He+	CH3	=CH2+	H	He		9.00D-10	0.00	0.0
He+	CH4	=H+	CH3	He		4.00D-10	0.00	0.0
He+	CH4	=CH+	H2	H	He	2.56D-10	0.00	0.0
He+	CH4	=CH2+	H2	He		8.48D-10	0.00	0.0
He+	CH4	=CH3+	H	He		8.00D-11	0.00	0.0
He+	CH4	=CH4+	He			1.60D-11	0.00	0.0
C+	OH	=CO+	H			8.00D-10	0.00	0.0
C+	OH	=H+	CO			8.00D-10	0.00	0.0
C+	H2O	=HCO+	H			2.43D-09	-0.63	0.0
C+	O2	=O+	CO			5.15D-10	0.00	0.0
C+	O2	=CO+	O			3.15D-10	0.00	0.0
C+	CO2	=CO+	CO			1.10D-09	0.00	0.0
C+	CH	=C2+	H			3.80D-10	0.00	0.0
C+	CH	=CH+	C			3.80D-10	0.00	0.0
C+	CH2	=CH2+	C			5.20D-10	0.00	0.0
C+	CH2	=C2H+	H			5.20D-10	0.00	0.0
C+	CH4	=C2H2+	H2			3.25D-10	0.00	0.0
C+	CH4	=C2H3+	H			9.75D-10	0.00	0.0
O+	H	=H+	O			6.00D-10	0.00	0.0
O+	H2	=OH+	H			1.20D-09	0.00	0.0
O2+	C	=CO+	O			5.20D-11	0.00	0.0
O2+	C	=C+	O2			5.20D-11	0.00	0.0
OH+	H2	=H2O+	H			1.01D-09	0.00	0.0
H2O+	H2	=H3O+	H			8.30D-10	0.00	0.0
H3O+	H	=H2O+	H2			6.10D-10	0.00	20500.0
H3O+	C	=HCO+	H2			1.00D-11	0.00	0.0
H3O+	CH	=CH2+	H2O			6.80D-10	0.00	0.0
H3O+	CH2	=CH3+	H2O			9.40D-10	0.00	0.0
O+	ELECTR	=O	PHOTON			3.40D-12	-0.64	0.0
O2+	ELECTR	=O	O			1.95D-07	-0.70	0.0

OH+	ELECTR	=O	H	3.75D-08	-0.50	0.0
H2O+	ELECTR	=OH	H	3.15D-07	-0.50	0.0
H3O+	ELECTR	=OH	H2	8.45D-07	-0.50	0.0
H3O+	ELECTR	=H2O	H	4.55D-07	-0.50	0.0
CH3+	O	=HCO+	H2	3.10D-10	0.00	0.0
CH3+	O	=H3+	CO	1.30D-11	0.00	0.0
CH5+	O	=H3O+	CH2	2.16D-10	0.00	0.0
CH5+	CO	=HCO+	CH4	9.90D-10	0.00	0.0
CH5+	H2O	=H3O+	CH4	3.70D-09	0.00	0.0
CO+	H2	=HCO+	H	1.30D-09	0.00	0.0
CO+	H	=H+	CO	7.50D-10	0.00	0.0
HCO+	H	=CO+	H2	1.30D-09	0.00	24500.0
HCO+	C	=CH+	CO	1.10D-09	0.00	0.0
HCO+	CH	=CH2+	CO	6.30D-10	0.00	0.0
HCO+	CH2	=CH3+	CO	8.60D-10	0.00	0.0
HCO+	CH3	=CH4+	CO	1.40D-09	0.00	9060.0
HCO+	CH4	=CH5+	CO	9.90D-10	0.00	4920.0
HCO+	H2O	=H3O+	CO	2.50D-09	0.00	0.0
HCO+	O2	=HCO2+	O	1.00D-09	0.00	1450.0
HCO2+	O	=HCO+	O2	1.00D-09	0.00	0.0
HCO+	OH	=HCO2+	H	1.00D-09	0.00	0.0
HCO2+	H	=HCO+	OH	1.00D-09	0.00	7500.0
HCO2+	CO	=HCO+	CO2	1.00D-09	0.00	0.0
HCO+	CO2	=HCO2+	CO	1.00D-09	0.00	5000.0
HCO2+	CH4	=CH5+	CO2	7.80D-10	0.00	0.0
CO+	ELECTR	=C	O	1.00D-07	-0.46	0.0
HCO+	ELECTR	=CO	H	2.40D-07	-0.69	0.0
HCO2+	ELECTR	=CO2	H	2.24D-07	-0.50	0.0
HCO2+	ELECTR	=CO	OH	1.16D-07	-0.50	0.0
C2+	H2	=C2H+	H	1.40D-09	0.00	0.0
C2+	H2	=H+	C2H	1.50D-09	0.00	1260.0

C2H+	H2	=C2H2+	H		1.70D-09	0.00	0.0
C2H2+	H2	=C2H3+	H		5.00D-10	0.00	800.0
C2+	ELECTR	=C	C		3.00D-07	-0.50	0.0
C2H+	ELECTR	=C2	H		1.35D-07	-0.50	0.0
C2H+	ELECTR	=CH	C		1.35D-07	-0.50	0.0
C2H2+	ELECTR	=C2H	H		1.50D-07	-0.50	0.0
C2H2+	ELECTR	=CH	CH		1.50D-07	-0.50	0.0
C2H3+	ELECTR	=C2H	H2		1.35D-07	-0.50	0.0
C2H3+	ELECTR	=CH2	CH		1.35D-07	-0.50	0.0
C2H3+	ELECTR	=C2H2	H		3.00D-08	-0.50	0.0
C3+	H2	=C3H+	H		3.00D-10	0.00	0.0
C3H+	H2	=C3H2+	H		1.00D-09	0.00	500.0
C3H+	H2	=C3H3+	PHOTON		3.00D-13	-1.0	0.0
C3H2+	H2	=C3H3+	H		1.00D-10	0.00	2000.0
C3+	ELECTR	=C2	C		3.00D-07	-0.50	0.0
C3H+	ELECTR	=C2	CH		1.50D-07	-0.50	0.0
C3H+	ELECTR	=C2H	C		1.50D-07	-0.50	0.0
C3H2+	ELECTR	=C3H	H		1.50D-07	-0.50	0.0
C3H2+	ELECTR	=C2H	CH		1.50D-07	-0.50	0.0
C3H3+	ELECTR	=C3H2	H		1.50D-07	-0.50	0.0
C3H3+	ELECTR	=C2H2	CH		1.50D-07	-0.50	0.0
H+	C2	=C2+	H		3.10D-09	0.00	0.0
H+	C2H	=C2+	H2		1.50D-09	0.00	0.0
H+	C2H	=C2H+	H		1.50D-09	0.00	0.0
H+	C2H2	=C2H+	H2		2.00D-09	0.00	0.0
H+	C2H2	=C2H2+	H		2.00D-09	0.00	0.0
H+	C3H	=C3+	H2		2.00D-09	0.00	0.0
H+	C3H	=C3H+	H		2.00D-09	0.00	0.0
H+	C3H2	=C3H+	H2		2.00D-09	0.00	0.0
H+	C3H2	=C3H2+	H		2.00D-09	0.00	0.0
He+	C2H	=C+	CH	He	5.10D-10	0.00	0.0

He+	C2H	=CH+	C	He	5.10D-10	0.00	0.0
He+	C2H	=C2+	H	He	5.10D-10	0.00	0.0
He+	C2H2	=CH+	CH	He	7.70D-10	0.00	0.0
He+	C2H2	=C2+	H2	He	1.61D-09	0.00	0.0
He+	C2H2	=C2H+	H	He	8.75D-10	0.00	0.0
He+	C2H2	=C2H2+	He		2.45D-10	0.00	0.0
He+	C3H	=C3+	H	He	2.00D-09	0.00	0.0
He+	C3H2	=C3H+	H	He	1.00D-09	0.00	0.0
He+	C3H2	=C3+	H2	He	1.00D-09	0.00	0.0
H3+	C2H	=C2H2+	H2		1.70D-09	0.00	0.0
H3+	C2H2	=C2H3+	H2		2.90D-09	0.00	0.0
H3+	C3H	=C3H2+	H2		2.00D-09	0.00	0.0
H3+	C3H2	=C3H3+	H2		2.00D-09	0.00	0.0
C+	C2H	=C3+	H		1.00D-09	0.00	0.0
C+	C2H2	=C3H+	H		2.20D-09	0.00	0.0
HCO+	C2H	=C2H2+	CO		7.80D-10	0.00	0.0
HCO+	C2H2	=C2H3+	CO		1.36D-09	0.00	0.0
HCO+	C3H	=C3H2+	CO		1.40D-09	0.00	0.0
HCO+	C3H2	=C3H3+	CO		1.40D-09	0.00	0.0
H3O+	C2H	=C2H2+	H2O		2.20D-10	0.00	4100.0
H3O+	C2H2	=C2H3+	H2O		1.00D-09	0.00	7330.0
H3O+	C3H	=C3H2+	H2O		2.00D-09	0.00	0.0
H3O+	C3H2	=C3H3+	H2O		3.00D-09	0.00	0.0
C2H2+	H2O	=H3O+	C2H		2.20D-10	0.00	0.0
C2H3+	H2O	=H3O+	C2H2		1.11D-09	0.00	0.0
C3H+	H2O	=HCO+	C2H2		2.48D-10	0.00	0.0
C3H+	H2O	=C2H3+	CO		2.02D-10	0.00	0.0
H+	Fe	=Fe+	H		7.40D-09	0.00	0.0
H3+	Fe	=Fe+	H2	H	4.90D-09	0.00	0.0
C+	Fe	=Fe+	C		2.60D-09	0.00	0.0
HCO+	Fe	=Fe+	CO	H	1.90D-09	0.00	0.0

H3O+	Fe	=Fe+	H2O	H	3.10D-09	0.00	0.0
O2+	Fe	=Fe+	O2		1.10D-09	0.00	0.0
Fe+	ELECTR	=Fe	PHOTON		3.70D-12	-0.65	0.0
N	CRP	=N+	ELECTR		2.10E+00	0.00	0.0
CN	SECPHO	=C	N		2.12D+04	0.00	140000.0
HCN	SECPHO	=CN	H		6.23D+03	0.00	140000.0
HNC	SECPHO	=CN	H		6.23D+03	0.00	140000.0
NH2	SECPHO	=NH	H		1.60D+02	0.00	140000.0
NH2	SECPHO	=NH2+	ELECTR		1.30D+03	0.00	140000.0
NH3	SECPHO	=NH2	H		2.63D+03	0.00	140000.0
H3	SECPHO	=NH	H2		1.08D+03	0.00	140000.0
NH3	SECPHO	=NH3+	ELECTR		1.15D+03	0.00	140000.0
NO	SECPHO	=N	O		9.64D+02	0.00	140000.0
NO	SECPHO	=NO+	ELECTR		9.88D+02	0.00	140000.0
N	H2	=NH	H		8.66D-10	0.50	14600.0
NH	H2	=NH2	H		5.25D-12	0.79	6700.0
NH2	H2	=NH3	H		6.22D-11	0.50	6300.0
CN	H2	=HCN	H		3.53D-13	3.31	756.0
NH	H	=N	H2		8.66D-10	0.50	2400.0
NH2	H	=NH	H2		5.25D-12	0.79	2200.0
NH3	H	=NH2	H2		6.22D-11	0.50	5700.0
NH	O	=OH	N		2.90D-11	0.50	0.0
NH2	O	=NH	OH		3.50D-12	0.50	0.0
NH3	O	=NH2	OH		2.50D-12	0.00	3020.0
CN	O	=CO	N		1.80D-11	0.50	50.0
NH3	OH	=NH2	H2O		2.30D-12	0.00	800.0
NH	C	=CN	H		1.10D-10	0.50	0.0
CH	N	=CN	H		2.10D-11	0.00	0.0
CN	N	=N2	C		7.30D-10	0.00	4500.0
NH	N	=N2	H		5.00D-11	0.50	0.0
OH	N	=NO	H		5.30D-11	0.00	50.0

O2	N	=NO	O	3.30D-12	1.00	3150.0
NO	C	=CN	O	1.10D-10	0.50	0.0
NO	N	=N2	O	3.40D-11	0.00	50.0
NO	O	=O2	N	7.50D-13	1.00	16000.0
HNC	H	=HCN	H	1.00D-10	0.50	200.0
HNC	O	=CO	NH	2.00D-10	0.50	200.0
HNC	OH	=H2O	CN	2.00D-10	0.50	200.0
HNC	O2	=CO2	NH	2.00D-11	0.50	2000.0
NH2	C	=HNC	H	2.00D-11	0.50	0.0
CH2	N	=HCN	H	2.00D-11	0.50	0.0
CH3	N	=HCN	H2	2.00D-11	0.50	0.0
CH5+	HNC	=C2H3+	NH3	1.00D-09	0.00	0.0
CH5+	HCN	=C2H3+	NH3	1.00D-09	0.00	5120.0
N+	H2	=NH+	H	8.40D-10	0.00	168.5
NH+	H2	=NH2+	H	1.27D-09	0.00	0.0
NH+	H2	=H3+	N	2.25D-10	0.00	0.0
NH2+	H2	=NH3+	H	2.70D-10	0.00	0.0
NH3+	H2	=NH4+	H	2.40D-12	0.00	0.0
NH+	H	=N+	H2	6.52D-10	0.00	0.0
NH2+	H	=NH+	H2	1.27D-09	0.00	24000.0
NH3+	H	=NH2+	H2	2.25D-10	0.00	12800.0
NH4+	H	=NH3+	H2	1.00D-09	0.00	11000.0
CN+	H2	=HCN+	H	1.00D-09	0.00	0.0
HCN+	H	=CN+	H2	1.00D-09	0.00	15800.0
HCN+	H2	=H2CN+	H	9.80D-10	0.00	0.0
H2CN+	H	=HCN+	H2	9.80D-10	0.00	34400.0
N2+	H2	=N2H+	H	2.00D-09	0.24	0.0
N2H+	H	=N2+	H2	2.10D-09	0.00	30300.0
N2H+	H2	=H3+	N2	1.80D-09	0.00	8300.0
H+	HNC	=H+	HCN	1.00D-09	0.00	0.0
H+	HCN	=H+	HNC	1.00D-09	0.00	7850.0

H+	NH	=NH+	H		2.10D-09	0.00	0.0
H+	NH2	=NH2+	H		2.90D-09	0.00	0.0
H+	NH3	=NH3+	H		5.20D-09	0.00	0.0
H+	CN	=CN+	H		2.10D-09	0.00	6150.0
H+	HCN	=HCN+	H		1.10D-08	0.00	0.0
H+	NO	=NO+	H		1.90D-09	0.00	0.0
He+	NH	=N+	H	He	1.10D-09	0.00	0.0
He+	NH2	=NH+	H	He	8.00D-10	0.00	0.0
He+	NH2	=N+	H2	He	8.00D-10	0.00	0.0
He+	NH3	=NH3+	He		2.64D-10	0.00	0.0
He+	NH3	=NH2+	H	He	1.76D-09	0.00	0.0
He+	NH3	=NH+	H2	He	1.76D-10	0.00	0.0
He+	CN	=C+	N	He	8.80D-10	0.00	0.0
He+	CN	=N+	C	He	8.80D-10	0.00	0.0
He+	HCN	=CN+	H	He	1.46D-09	0.00	0.0
He+	HCN	=CH+	N	He	6.20D-10	0.00	0.0
He+	HCN	=C+	NH	He	7.75D-10	0.00	0.0
He+	HCN	=N+	CH	He	2.48D-10	0.00	0.0
He+	HNC	=CN+	H	He	1.55D-09	0.00	0.0
He+	HNC	=C+	NH	He	1.55D-09	0.00	0.0
He+	N2	=N+	N	He	7.92D-10	0.00	0.0
He+	N2	=N2+	He		4.08D-10	0.00	0.0
He+	NO	=N+	O	He	1.38D-09	0.00	0.0
He+	NO	=O+	N	He	2.24D-10	0.00	0.0
H3+	NH	=NH2+	H2		1.30D-09	0.00	0.0
H3+	NH2	=NH3+	H2		1.80D-09	0.00	0.0
H3+	NH3	=NH4+	H2		9.10D-09	0.00	0.0
H3+	N	=NH2+	H		4.50D-10	0.00	0.0
H3+	CN	=HCN+	H2		1.00D-09	0.00	0.0
H3+	CN	=H2CN+	H		1.00D-09	0.00	0.0
H3+	HCN	=H2CN+	H2		9.50D-09	0.00	0.0

H3+	HNC	=H2CN+	H2	9.50D-09	0.00	0.0
H3+	N2	=N2H+	H2	1.30D-09	0.00	0.0
H3+	NO	=HNO+	H2	1.10D-09	0.00	0.0
H3O+	NH3	=NH4+	H2O	2.20D-09	0.00	0.0
H3O+	CN	=H2CN+	OH	4.50D-09	0.00	0.0
H3O+	HCN	=H2CN+	H2O	4.50D-09	0.00	0.0
H2CN+	H2O	=H3O+	HCN	4.50D-09	0.00	2460.0
H3O+	HNC	=H2CN+	H2O	4.50D-09	0.00	0.0
H2CN+	H2O	=H3O+	HNC	4.50D-09	0.00	10300.0
HCO+	NH	=NH2+	CO	6.40D-10	0.00	0.0
NH2+	CO	=HCO+	NH	6.40D-10	0.00	6100.0
HCO+	NH2	=NH3+	CO	8.90D-10	0.00	0.0
HCO+	NH3	=NH4+	CO	1.90D-09	0.00	0.0
HCO+	HCN	=H2CN+	CO	3.70D-09	0.00	0.0
HCO+	HNC	=H2CN+	CO	3.70D-09	0.00	0.0
HCO2+	NO	=HNO+	CO2	1.00D-10	0.00	0.0
C+	NH	=CN+	H	7.80D-10	0.00	0.0
C+	NH2	=HCN+	H	1.10D-09	0.00	0.0
C+	NH3	=NH3+	C	5.29D-10	0.00	0.0
C+	NH3	=H2NC+	H	7.80D-10	0.00	0.0
C+	NH3	=H2CN+	H	7.80D-10	0.00	0.0
C+	NH3	=HCN+	H2	2.08D-10	0.00	0.0
C+	HCN	=C2N+	H	3.40D-09	0.00	0.0
C+	HNC	=C2N+	H	3.40D-09	0.00	0.0
C+	NO	=NO+	C	3.40D-09	0.00	0.0
C+	NO	=N+	CO	9.02D-10	0.00	0.0
N+	CO	=C+	NO	9.02D-10	0.00	15400.0
O2+	N	=NO+	O	7.84D-11	0.00	0.0
O2+	NH3	=NH3+	O2	2.00D-09	0.00	0.0
O2+	NO	=NO+	O2	4.40D-10	0.00	0.0
CH2+	N	=HCN+	H	9.40D-10	0.00	0.0

C2H+	N	=C2N+	H	8.30D-10	0.00	0.0
CH3+	N	=HCN+	H2	6.70D-11	0.00	0.0
CH3+	N	=H2CN+	H	6.70D-11	0.00	0.0
C2H2+	N	=CH+	HCN	2.50D-11	0.00	0.0
C2H2+	N	=CH+	HNC	2.50D-11	0.00	2600.0
C2H2+	N	=C2N+	H2	2.25D-10	0.00	0.0
N+	O2	=O2+	N	2.81D-10	0.00	0.0
N+	O2	=NO+	O	2.37D-10	0.00	0.0
N+	O2	=O+	NO	3.30D-11	0.00	0.0
N+	CO	=CO+	N	8.25D-10	0.00	0.0
N+	CO	=NO+	C	1.46D-10	0.00	0.0
N+	NO	=NO+	N	4.51D-10	0.00	0.0
N+	NO	=N2+	O	7.95D-11	0.00	0.0
NH3+	H2O	=NH4+	OH	2.50D-10	0.00	0.0
NH4+	OH	=NH3+	H2O	2.50D-10	0.00	3400.0
N2H+	O	=OH+	N2	1.40D-10	0.00	3400.0
N2H+	H2O	=H3O+	N2	2.60D-09	0.00	0.0
N2H+	CO	=HCO+	N2	8.80D-10	0.00	0.0
HCO+	N2	=N2H+	CO	8.80D-10	0.00	11200.0
N2H+	CO2	=HCO2+	N2	1.40D-09	0.00	0.0
HCO2+	N2	=N2H+	CO2	1.40D-09	0.00	6400.0
N2H+	NH3	=NH4+	N2	2.30D-09	0.00	0.0
NH4+	N2	=N2H+	NH3	2.30D-09	0.00	44000.0
N2H+	NO	=HNO+	N2	3.40D-10	0.00	0.0
C2N+	NH3	=N2H+	C2H2	1.90D-10	0.00	0.0
C2N+	NH3	=H2CN+	HCN	1.70D-09	0.00	0.0
HNO+	C	=CH+	NO	1.00D-09	0.00	0.0
HNO+	CO	=HCO+	NO	1.00D-10	0.00	0.0
HNO+	CO2	=HCO2+	NO	1.00D-10	0.00	0.0
HNO+	OH	=H2O+	NO	6.20D-10	0.00	0.0
HNO+	H2O	=H3O+	NO	2.30D-09	0.00	0.0

```
NO+      Fe      =Fe+     NO              1.00D-09  0.00       0.0
N+       ELECTR  =N       PHOTON          3.80D-12 -0.62       0.0
NH+      ELECTR  =N       H               2.00D-07 -0.50       0.0
NH2+     ELECTR  =NH      H               1.50D-07 -0.50       0.0
NH2+     ELECTR  =N       H       H       1.50D-07 -0.50       0.0
NH3+     ELECTR  =NH2     H               3.00D-07 -0.50       0.0
NH4+     ELECTR  =NH2     H2              7.60D-07 -0.50       0.0
NH4+     ELECTR  =NH3     H               7.60D-07 -0.50       0.0
CN+      ELECTR  =C       N               1.80D-07 -0.50       0.0
C2N+     ELECTR  =C2      N               1.00D-07 -0.50       0.0
C2N+     ELECTR  =CN      C               2.00D-07 -0.50       0.0
HCN+     ELECTR  =CN      H               1.50D-07 -0.50       0.0
HCN+     ELECTR  =CH      N               1.50D-07 -0.50       0.0
N2+      ELECTR  =N       N               3.60D-08 -0.42       0.0
N2H+     ELECTR  =N2      H               1.70D-07 -1.00       0.0
H2CN+    ELECTR  =HCN     H               1.75D-07 -0.50       0.0
H2CN+    ELECTR  =HNC     H               1.75D-07 -0.50       0.0
H2NC+    ELECTR  =HNC     H               1.75D-07 -0.50       0.0
H2NC+    ELECTR  =NH2     C               1.75D-07 -0.50       0.0
NO+      ELECTR  =N       O               4.30D-07 -0.37       0.0
HNO+     ELECTR  =NO      H               3.00D-07 -0.50       0.0
SO      +SECPHO  =S       O               9.64D+02  0.00  140000.0
CS      +SECPHO  =S       C               2.12D+04  0.00  140000.0
SH      +SECPHO  =S       H               1.46D+03  0.00  140000.0
OCS     +SECPHO  =CO      S               1.07D+04  0.00  140000.0
H2S     +SECPHO  =S       H2              1.03D+04  0.00  140000.0
H2S     +SECPHO  =H2S+    ELECTR          3.39D+03  0.00  140000.0
SO2     +SECPHO  =SO      O               1.77D+03  0.00  140000.0
S       +H2      =SH      H               1.04D-10  .132    9620.0
SH      +H2      =H2S     H               6.41D-12  .087    8050.0
SH      +H       =S       H2              2.50D-11  0.00       0.0
```

H2S	+H	=SH	H2	1.29D-11	0.00	860.0
SO	+H	=OH	S	5.90D-10	-0.31	11100.0
SO2	+H	=SO	OH	9.25D-09	-0.74	14700.0
OCS	+H	=SH	CO	1.70D-11	0.00	2000.0
SH	+O	=SO	H	1.60D-10	0.00	100.0
SH	+O	=OH	S	1.70D-11	0.67	950.0
H2S	+O	=SH	OH	1.40D-11	0.00	1920.0
H2S	+OH	=SH	H2O	6.30D-12	0.00	80.0
CS	+O	=CO	S	2.70D-10	0.00	760.0
CS	+OH	=OCS	H	1.55D-13	1.12	800.0
S	+O2	=SO	O	5.19D-12	0.00	265.0
SO	+O	=S	O2	6.60D-13	0.00	2760.0
SO	+O2	=SO2	O	1.40D-12	0.00	2820.0
SO	+OH	=SO2	H	1.96D-10	-0.17	0.0
SO	+N	=NO	S	1.73D-11	0.50	750.0
SO	+C	=CO	S	7.20D-11	0.00	0.0
SO	+C	=CS	O	1.70D-10	0.00	0.0
SO2	+O	=SO	O2	9.27D-11	-0.46	9140.0
OCS	+O	=SO	CO	2.60D-11	0.00	2250.0
CH	+S	=CS	H	1.10D-12	0.00	0.0
CH	+S	=SH	C	1.73D-11	0.50	4000.0
OH	+S	=SO	H	1.00D-10	0.00	100.0
SH	+C	=CS	H	2.00D-11	0.00	0.0
SH	+C	=CH	S	1.20D-11	0.58	5880.0
SH	+CO	=OCS	H	5.95D-14	1.12	8330.0
S+	+H2	=SH+	H	2.20D-10	0.00	9860.0
SH+	+H2	=H2S+	H	1.90D-10	0.00	8500.0
SH+	+H2	=H3S+	PHOTO	1.00D-15	0.00	0.0
H2S+	+H2	=H3S+	H	1.40D-11	0.00	2300.0
CS+	+H2	=HCS+	H	4.80D-10	0.00	0.0
SH+	+H	=S+	H2	1.10D-10	0.00	0.0

H2S+	+H	=SH+	H2		2.00D-10	0.00	0.0
H3S+	+H	=H2S+	H2		6.00D-11	0.00	0.0
SO+	+H	=S+	OH		6.10D-10	0.00	11385.0
H+	+SH	=SH+	H		1.60D-09	0.00	0.0
H+	+SH	=S+	H2		1.60D-09	0.00	0.0
H+	+H2S	=H2S+	H		7.60D-09	0.00	0.0
H+	+CS	=CS+	H		4.90D-09	0.00	0.0
H+	+SO	=SO+	H		3.20D-09	0.00	0.0
H+	+OCS	=SH+	CO		5.90D-09	0.00	0.0
H3+	+S	=SH+	H2		2.60D-09	0.00	0.0
H3+	+SH	=H2S+	H2		1.90D-09	0.00	0.0
H3+	+H2S	=H3S+	H2		3.70D-09	0.00	0.0
H3+	+CS	=HCS+	H2		2.90D-09	0.00	0.0
H3+	+SO	=HSO+	H2		1.90D-09	0.00	0.0
H3+	+SO2	=HSO2+	H2		1.30D-09	0.00	0.0
H3+	+OCS	=HOCS+	H2		1.90D-09	0.00	0.0
He+	+SH	=S+	H	He	1.70D-09	0.00	0.0
He+	+H2S	=S+	H2	He	3.60D-09	0.00	0.0
He+	+H2S	=SH+	H	He	4.80D-10	0.00	0.0
He+	+H2S	=H2S+	He		3.10D-10	0.00	0.0
He+	+CS	=C+	S	He	1.30D-09	0.00	0.0
He+	+CS	=S+	C	He	1.30D-09	0.00	0.0
He+	+SO	=O+	S	He	8.30D-10	0.00	0.0
He+	+SO	=S+	O	He	8.30D-10	0.00	0.0
He+	+OCS	=CS+	O	He	7.60D-10	0.00	0.0
He+	+OCS	=S+	CO	He	7.60D-10	0.00	0.0
He+	+OCS	=CO+	S	He	7.60D-10	0.00	0.0
He+	+OCS	=O+	CS	He	7.60D-11	0.00	0.0
He+	+SO2	=S+	O2	He	8.60D-10	0.00	0.0
He+	+SO2	=SO+	O	He	3.44D-09	0.00	0.0
C+	+S	=S+	C		1.50D-09	0.00	0.0

C+	+SH	=CS+	H	1.10D-09	0.00	0.0
C+	+H2S	=HCS+	H	1.28D-09	0.00	0.0
C+	+H2S	=H2S+	C	4.25D-10	0.00	0.0
C+	+CS	=CS+	C	1.60D-09	0.00	700.0
C+	+SO	=S+	CO	2.60D-10	0.00	0.0
C+	+SO	=CS+	O	2.60D-10	0.00	0.0
C+	+SO	=SO+	C	2.60D-10	0.00	0.0
C+	+SO	=CO+	S	2.60D-10	0.00	0.0
C+	+OCS	=CS+	CO	1.60D-09	0.00	0.0
C+	+SO2	=SO+	CO	2.30D-09	0.00	0.0
CH+	+S	=S+	CH	4.70D-10	0.00	0.0
CH+	+S	=SH+	C	4.70D-10	0.00	0.0
CH+	+S	=CS+	H	4.70D-10	0.00	0.0
CH+	+SO	=OH+	CS	1.00D-09	0.00	0.0
CH+	+SO	=SH+	CO	1.00D-09	0.00	0.0
CH3+	+S	=HCS+	H2	1.40D-09	0.00	0.0
CH3+	+SO	=HOCS+	H2	9.50D-10	0.00	0.0
CH5+	+S	=SH+	CH4	1.30D-09	0.00	0.0
H3O+	+S	=SH+	H2O	3.20D-10	0.00	4930.0
H3O+	+H2S	=H3S+	H2O	1.90D-09	0.00	0.0
HCO+	+S	=SH+	CO	3.30D-10	0.00	0.0
HCO+	+SH	=H2S+	CO	8.20D-10	0.00	0.0
HCO+	+CS	=HCS+	CO	1.20D-09	0.00	0.0
HCO+	+SO	=HSO+	CO	7.50D-10	0.00	0.0
HCO+	+H2S	=H3S+	CO	1.60D-09	0.00	0.0
HCO+	+OCS	=HOCS+	CO	1.10D-09	0.00	0.0
O2+	+S	=SO+	O	5.40D-10	0.00	0.0
O2+	+S	=S+	O2	5.40D-10	0.00	0.0
O2+	+H2S	=H2S+	O2	1.40D-09	0.00	0.0
S+	+CH	=CS+	H	6.20D-10	0.00	0.0
S+	+CH2	=HCS+	H	1.00D-11	0.00	0.0

S+	+OH	=SO+	H	6.10D-10	0.00	0.0
S+	+OH	=SH+	O	2.90D-10	0.00	8820.0
S+	+SH	=SH+	S	9.70D-10	0.00	350.0
S+	+NO	=NO+	S	3.20D-10	0.00	0.0
S+	+NH3	=NH3+	S	1.60D-09	0.00	0.0
S+	+O2	=SO+	O	2.30D-11	0.00	0.0
NH3+	+H2S	=NH4+	SH	6.00D-10	0.00	0.0
HNO+	+S	=SH+	NO	1.10D-09	0.00	0.0
N2H+	+S	=SH+	N2	1.10D-09	0.00	0.0
SH+	+O	=SO+	H	2.90D-10	0.00	0.0
SH+	+O	=S+	OH	2.90D-10	0.00	0.0
SH+	+S	=S+	SH	9.70D-10	0.00	0.0
SH+	+C	=CS+	H	9.90D-10	0.00	0.0
SH+	+CH	=CH2+	S	5.80D-10	0.00	0.0
SH+	+OH	=H2S+	O	3.10D-10	0.00	7500.0
SH+	+OH	=H2O+	S	4.30D-10	0.00	9200.0
SH+	+H2O	=H3O+	S	6.30D-10	0.00	0.0
SH+	+H2S	=H2S+	SH	5.00D-10	0.00	1000.0
SH+	+H2S	=H3S+	S	5.00D-10	0.00	0.0
SH+	+NO	=NO+	SH	3.30D-10	0.00	0.0
SH+	+NH3	=NH3+	SH	5.25D-10	0.00	0.0
SH+	+NH3	=NH4+	S	9.75D-10	0.00	0.0
H2S+	+O	=SH+	OH	3.10D-10	0.00	0.0
H2S+	+O	=SO+	H2	3.10D-10	0.00	0.0
H2S+	+C	=HCS+	H	1.00D-09	0.00	0.0
H2S+	+S	=S+	H2S	1.10D-09	0.00	0.0
H2S+	+SH	=SH+	H2S	5.00D-10	0.00	0.0
H2S+	+NO	=NO+	H2S	3.70D-10	0.00	0.0
H2S+	+H2O	=H3O+	SH	8.10D-10	0.00	0.0
H2S+	+NH3	=NH4+	SH	1.36D-09	0.00	0.0
H2S+	+NH3	=NH3+	H2S	3.40D-10	0.00	0.0

H3S+	+NH3	=NH4+	H2S		1.90D-09	0.00	0.0
H3S+	+HCN	=H2CN+	H2S		1.90D-09	0.00	0.0
HCS+	+O	=HCO+	S		1.00D-09	0.00	0.0
SO+	+NH3	=NH3+	SO		1.30D-09	0.00	0.0
S+	+Fe	=Fe+	S		1.80D-10	0.00	0.0
SH+	+Fe	=Fe+	SH		1.60D-09	0.00	0.0
SO+	+Fe	=Fe+	SO		1.60D-09	0.00	0.0
H2S+	+Fe	=Fe+	H2S		1.80D-09	0.00	0.0
S+	+ELECTR	=S	PHOTON		3.90D-12	-0.63	0.0
SH+	+ELECTR	=S	H		2.00D-07	-0.50	0.0
H2S+	+ELECTR	=SH	H		1.50D-07	-0.50	0.0
H2S+	+ELECTR	=S	H	H	1.50D-07	-0.50	0.0
H2S+	+ELECTR	=H2S	PHOTON		1.10D-10	-0.70	0.0
H3S+	+ELECTR	=H2S	H		3.00D-07	-0.50	0.0
H3S+	+ELECTR	=SH	H2		1.00D-07	-0.50	0.0
CS+	+ELECTR	=C	S		2.00D-07	-0.50	0.0
HCS+	+ELECTR	=CS	H		7.00D-07	-0.50	0.0
SO+	+ELECTR	=S	O		2.00D-07	-0.50	0.0
HSO+	+ELECTR	=SO	H		2.00D-07	-0.50	0.0
HSO2+	ELECTR	=SO	H	O	1.00E-07	-0.50	0.0
HSO2+	ELECTR	=SO	OH		1.00E-07	-0.50	0.0
HOCS+	+ELECTR	=OH	CS		2.00D-07	-0.50	0.0
HOCS+	+ELECTR	=OCS	H		2.00D-07	-0.50	0.0
Si	+SECPHO	=Si+	ELECTR		3.00D+03	0.00	140000.0
SiO	+SECPHO	=Si	O		3.00D+03	0.00	140000.0
SiO2	+SECPHO	=SiO	O		3.00D+03	0.00	140000.0
SiH	+SECPHO	=Si	H		1.46D+03	0.00	140000.0
SiH4	+SECPHO	=SiH3	H		4.68D+03	0.00	140000.0
SiH4	H	=SiH3	H2		2.60D-11	0.00	1400.0
SiH3	H	=SiH2	H2		2.00D-11	0.00	0.0
SiH2	H	=SiH	H2		2.00D-11	0.00	0.0

SiH	H	=Si	H2		2.00D-11	0.00	0.0
SiH2	O2	=SiO	H2O		7.50D-12	0.00	0.0
SiH	O2	=SiO	OH		1.70D-10	0.00	0.0
SiH2	O	=SiO	H	H	5.00D-11	0.50	0.0
SiH	O	=SiO	H		4.00D-11	0.50	0.0
Si	O2	=SiO	O		2.70D-10	0.00	111.0
Si	OH	=SiO	H		1.00D-10	0.00	111.0
SiO	OH	=SiO2	H		1.00D-12	-0.70	0.0
Si+	H2	=SiH2+	PHOTON		3.00D-18	0.00	0.0
SiH+	H2	=SiH3+	PHOTON		3.00D-17	-1.00	0.0
SiH3+	H2	=SiH5+	PHOTON		1.00D-18	-0.50	0.0
Si+	H2	=SiH+	H		1.50D-10	0.00	14310.0
SiH+	H2	=SiH2+	H		1.20D-09	0.00	28250.0
SiH2+	H2	=SiH3+	H		7.00D-10	0.00	6335.0
SiH3+	H2	=SiH4+	H		2.00D-10	0.00	47390.0
SiH4+	H2	=SiH5+	H		1.00D-09	0.00	0.0
SiH+	H	=Si+	H2		1.90D-09	0.00	0.0
SiH2+	H	=SiH+	H2		1.20D-09	0.00	0.0
SiH3+	H	=SiH2+	H2		7.00D-10	0.00	0.0
SiH4+	H	=SiH3+	H		2.00D-10	0.00	0.0
SiH5+	H	=SiH4+	H2		4.00D-11	0.00	4470.0
SiO+	H2	=SiOH+	H		3.20D-10	0.00	0.0
H+	Si	=Si+	H		9.90E-10	0.00	0.0
H+	SiH	=SiH+	H		1.70E-09	0.00	0.0
H+	SiH	=Si+	H2		1.70E-09	0.00	0.0
H+	SiH2	=SiH2+	H		1.50E-09	0.00	0.0
H+	SiH2	=SiH+	H2		1.50E-09	0.00	0.0
H+	SiH3	=SiH3+	H		1.50E-09	0.00	0.0
H+	SiH3	=SiH2+	H2		1.50E-09	0.00	0.0
H+	SiH4	=SiH4+	H		1.50E-09	0.00	0.0
H+	SiH4	=SiH3+	H2		1.50E-09	0.00	0.0

H+	SiO	=SiO+	H		3.30E-09	0.00	0.0
He+	Si	=Si+	He		3.30E-09	0.00	0.0
He+	SiH	=Si+	H	He	1.80E-09	0.00	0.0
He+	SiH2	=SiH+	H	He	1.00E-09	0.00	0.0
He+	SiH2	=Si+	H2	He	1.00E-09	0.00	0.0
He+	SiH3	=SiH2+	H	He	1.00E-09	0.00	0.0
He+	SiH3	=SiH+	H2	He	1.00E-09	0.00	0.0
He+	SiH4	=SiH3+	H	He	1.00E-09	0.00	0.0
He+	SiH4	=SiH2+	H2	He	1.00E-09	0.00	0.0
He+	SiO	=Si+	O	He	8.60E-10	0.00	0.0
He+	SiO	=O+	Si	He	8.60E-10	0.00	0.0
He+	SiO2	=SiO+	O	He	5.00E-10	0.00	0.0
He+	SiO2	=Si+	O2	He	5.00E-10	0.00	0.0
C+	Si	=Si+	C		2.10E-09	0.00	0.0
C+	SiH2	=SiH2+	C		1.00E-09	0.00	0.0
C+	SiH3	=SiH3+	C		1.00E-09	0.00	0.0
C+	SiO	=Si+	CO		5.40E-10	0.00	0.0
C+	SiO2	=SiO+	CO		1.00E-09	-0.60	0.0
S+	Si	=Si+	S		1.60E-09	0.00	0.0
S+	SiH	=SiH+	S		4.20E-10	0.00	0.0
H3+	Si	=SiH+	H2		2.00E-09	0.00	0.0
H3+	SiH	=SiH2+	H2		2.00E-09	0.00	0.0
H3+	Si	=SiH2+	H		1.70E-09	0.00	0.0
H3+	SiH2	=SiH3+	H2		2.00E-09	0.00	0.0
H3+	SiH3	=SiH4+	H2		2.00E-09	0.00	0.0
H3+	SiH4	=SiH5+	H2		2.00E-09	0.00	0.0
H3+	SiO	=SiOH+	H2		2.00E-09	0.00	0.0
H3O+	Si	=SiH+	H2O		1.80E-09	0.00	0.0
H3O+	SiH	=SiH2+	H2O		9.70E-10	0.00	0.0
H3O+	SiH2	=SiH3+	H2O		2.00E-09	0.00	0.0
H3O+	SiO	=SiOH+	H2O		2.00E-09	0.00	0.0

HCO+	Si	=SiH+	CO		1.60E-09	0.00	0.0
HCO+	SiH	=SiH2+	CO		8.70E-10	0.00	0.0
HCO+	SiH2	=SiH3+	CO		2.00E-09	0.00	0.0
HCO+	SiH4	=SiH5+	CO		1.40E-09	0.00	0.0
HCO+	SiO	=SiOH+	CO		7.90E-10	0.00	0.0
Si+	OH	=SiO+	H		6.30E-10	0.00	0.0
Si+	H2O	=SiOH+	H		2.30E-10	-0.60	0.0
Si+	O2	=SiO+	O		1.00E-13	0.00	0.0
SiH+	O	=SiO+	H		4.00E-10	0.00	0.0
SiH+	NH3	=NH4+	Si		1.00E-09	0.00	0.0
SiH+	H2O	=H3O+	Si		8.00E-10	0.00	0.0
SiH2+	O	=SiOH+	H		6.30E-10	0.00	0.0
SiH2+	O2	=SiOH+	OH		2.40E-11	0.00	0.0
SiH3+	O	=SiOH+	H2		2.00E-10	0.00	0.0
SiH4+	H2O	=H3O+	SiH3		2.00E-09	0.00	0.0
SiH4+	CO	=HCO+	SiH3		1.00E-09	0.00	0.0
SiH5+	H2O	=H3O+	SiH4		2.00E-09	0.00	0.0
Si+	ELECTR	=Si	PHOTON		4.90E-12	-0.60	0.0
SiH+	ELECTR	=Si	H		2.00E-07	-0.50	0.0
SiH2+	ELECTR	=Si	H	H	2.00E-07	-0.50	0.0
SiH2+	ELECTR	=SiH	H		1.50E-07	-0.50	0.0
SiH2+	ELECTR	=Si	H2		1.50E-07	-0.50	0.0
SiH3+	ELECTR	=SiH2	H		1.50E-07	-0.50	0.0
SiH3+	ELECTR	=SiH	H2		1.50E-07	-0.50	0.0
SiH4+	ELECTR	=SiH3	H		1.50E-07	-0.50	0.0
SiH4+	ELECTR	=SiH2	H2		1.50E-07	-0.50	0.0
SiH5+	ELECTR	=SiH4	H		1.50E-07	-0.50	0.0
SiH5+	ELECTR	=SiH3	H2		1.50E-07	-0.50	0.0
SiO+	ELECTR	=Si	O		2.0E-07	-0.50	0.0
SiOH+	ELECTR	=SiO	H		1.50E-07	-0.50	0.0
SiOH+	ELECTR	=Si	OH		1.50E-07	-0.50	0.0

Mg**	+He	=GRAIN	He	Mg	1.221D-2	73.0	41.187
Fe**	+He	=GRAIN	He	Fe	1.151D-2	73.0	40.976
Si**	+He	=GRAIN	He	Si	1.224D-2	73.0	42.175
C**	+He	=GRAIN	He	C	1.224D-2	73.0	42.175
O**	+He	=GRAIN	He	O	5.348D-2	73.0	36.030
Mg**	+C	=GRAIN	C	Mg	2.935D-2	48.0	36.740
Fe**	+C	=GRAIN	C	Fe	2.386D-2	47.0	42.794
Si**	+C	=GRAIN	C	Si	2.698D-2	48.0	36.502
C**	+C	=GRAIN	C	C	2.698D-2	48.0	36.502
O**	+C	=GRAIN	C	O	1.054D-1	48.0	30.812
Mg**	+N	=GRAIN	N	Mg	2.935D-2	48.0	36.740
Fe**	+N	=GRAIN	N	Fe	2.386D-2	47.0	42.794
Si**	+N	=GRAIN	N	Si	2.698D-2	48.0	36.502
C**	+N	=GRAIN	N	C	2.698D-2	48.0	36.502
O**	+N	=GRAIN	N	O	1.054D-1	48.0	30.812
Mg**	+O	=GRAIN	O	Mg	2.884D-2	48.0	30.238
Fe**	+O	=GRAIN	O	Fe	4.116D-2	44.0	59.438
Si**	+O	=GRAIN	O	Si	3.373D-2	47.0	37.810
C**	+O	=GRAIN	O	C	3.373D-2	47.0	37.810
O**	+O	=GRAIN	O	O	1.006D-1	47.0	31.588
Mg**	+H2O	=GRAIN	H2O	Mg	2.884D-2	48.0	30.238
Fe**	+H2O	=GRAIN	H2O	Fe	4.116D-2	44.0	59.438
Si**	+H2O	=GRAIN	H2O	Si	3.373D-2	47.0	37.810
C**	+H2O	=GRAIN	H2O	C	3.373D-2	47.0	37.810
O**	+H2O	=GRAIN	H2O	O	1.006D-1	47.0	31.588
Mg**	+N2	=GRAIN	N2	Mg	2.093D-2	48.0	27.730
Fe**	+N2	=GRAIN	N2	Fe	4.324D-2	47.0	42.335
Si**	+N2	=GRAIN	N2	Si	2.217D-2	47.0	28.013
C**	+N2	=GRAIN	N2	C	2.217D-2	47.0	28.013
O**	+N2	=GRAIN	N2	O	1.149D-1	46.0	46.018
Mg**	+CO	=GRAIN	CO	Mg	2.093D-2	48.0	27.730

Fe**	+CO	=GRAIN	CO	Fe	4.324D-2	47.0	42.335
Si**	+CO	=GRAIN	CO	Si	2.217D-2	47.0	28.013
C**	+CO	=GRAIN	CO	C	2.217D-2	47.0	28.013
O**	+CO	=GRAIN	CO	O	1.149D-1	46.0	46.018
Mg**	+O2	=GRAIN	O2	Mg	2.093D-2	48.0	27.730
Fe**	+O2	=GRAIN	O2	Fe	4.324D-2	47.0	42.335
Si**	+O2	=GRAIN	O2	Si	2.217D-2	47.0	28.013
C**	+O2	=GRAIN	O2	C	2.217D-2	47.0	28.013
O**	+O2	=GRAIN	O2	O	1.149D-1	46.0	46.018
C	+GRAIN	=CH4*			1.00D+00	0.00	102.0
CH	+GRAIN	=CH4*			1.00D+00	0.00	102.0
CH2	+GRAIN	=CH4*			1.00D+00	0.00	102.0
CH3	+GRAIN	=CH4*			1.00D+00	0.00	102.0
CH4	+GRAIN	=CH4*			1.00D+00	0.00	102.0
O	+GRAIN	=H2O*			1.00D+00	0.00	102.0
OH	+GRAIN	=H2O*			1.00D+00	0.00	102.0
H2O	+GRAIN	=H2O*			1.00D+00	0.00	102.0
CO	+GRAIN	=CO*			1.00D+00	0.00	102.0
CO2	+GRAIN	=CO2*			1.00D+00	0.00	102.0
C2	+GRAIN	=CH4*	CH4*		1.00D+00	0.00	102.0
C2H	+GRAIN	=CH4*	CH4*		1.00D+00	0.00	102.0
C2H2	+GRAIN	=CH4*	CH4*		1.00D+00	0.00	102.0
C3	+GRAIN	=CH4*	CH4*	CH4*	1.00D+00	0.00	102.0
C3H	+GRAIN	=CH4*	CH4*	CH4*	1.00D+00	0.00	102.0
C3H2	+GRAIN	=CH4*	CH4*	CH4*	1.00D+00	0.00	102.0
NH	+GRAIN	=NH3*			1.00D+00	0.00	102.0
NH2	+GRAIN	=NH3*			1.00D+00	0.00	102.0
NH3	+GRAIN	=NH3*			1.00D+00	0.00	102.0
CN	+GRAIN	=CH4*	NH3*		1.00D+00	0.00	102.0
HCN	+GRAIN	=CH4*	NH3*		1.00D+00	0.00	102.0
HNC	+GRAIN	=CH4*	NH3*		1.00D+00	0.00	102.0

NO	+GRAIN	=H2O*	NH3*		1.00D+00	0.00	102.0
OCS	+GRAIN	=OCS*			1.00D+00	0.00	102.0
S	+GRAIN	=H2S*			1.00D+00	0.00	102.0
SH	+GRAIN	=H2S*			1.00D+00	0.00	102.0
H2S	+GRAIN	=H2S*			1.00D+00	0.00	102.0
CS	+GRAIN	=CH4*	H2S*		1.00D+00	0.00	102.0
SO	+GRAIN	=H2O*	H2S*		1.00D+00	0.00	102.0
CH4*	+H	=CH4	H	GRAIN	4.00D-05	0.00	2000.0
CH4*	+H2	=CH4	H2	GRAIN	1.00D-04	0.00	2000.0
CH4*	+He	=CH4	He	GRAIN	8.00D-04	0.00	2000.0
H2O*	+H	=H2O	H	GRAIN	4.00D-05	0.00	6000.0
H2O*	+H2	=H2O	H2	GRAIN	1.00D-04	0.00	6000.0
H2O*	+He	=H2O	He	GRAIN	8.00D-04	0.00	6000.0
CO*	+H	=CO	H	GRAIN	4.00D-05	0.00	1900.0
CO*	+H2	=CO	H2	GRAIN	1.00D-04	0.00	1900.0
CO*	+He	=CO	He	GRAIN	8.00D-04	0.00	1900.0
CO2*	+H	=CO2	H	GRAIN	4.00D-05	0.00	3100.0
CO2*	+H2	=CO2	H2	GRAIN	1.00D-04	0.00	3100.0
CO2*	+He	=CO2	He	GRAIN	8.00D-04	0.00	3100.0
NH3*	+H	=NH3	H	GRAIN	4.00D-05	0.00	3600.0
NH3*	+H2	=NH3	H2	GRAIN	1.00D-04	0.00	3600.0
NH3*	+He	=NH3	He	GRAIN	8.00D-04	0.00	3600.0
CH3OH*	+H	=CH3OH	H	GRAIN	4.00D-05	0.00	6000.0
CH3OH*	+H2	=CH3OH	H2	GRAIN	1.00D-04	0.00	6000.0
CH3OH*	+He	=CH3OH	He	GRAIN	8.00D-04	0.00	6000.0
H2CO*	+H	=H2CO	H	GRAIN	4.00D-05	0.00	6000.0
H2CO*	+H2	=H2CO	H2	GRAIN	1.00D-04	0.00	6000.0
H2CO*	+He	=H2CO	He	GRAIN	8.00D-04	0.00	6000.0
HCO2H*	+H	=HCO2H	H	GRAIN	4.00D-05	0.00	6000.0
HCO2H*	+H2	=HCO2H	H2	GRAIN	1.00D-04	0.00	6000.0
HCO2H*	+He	=HCO2H	He	GRAIN	8.00D-04	0.00	6000.0

OCS*	+H	=OCS	H	GRAIN	4.00D-05	0.00	6000.0
OCS*	+H2	=OCS	H2	GRAIN	1.00D-04	0.00	6000.0
OCS*	+He	=OCS	He	GRAIN	8.00D-04	0.00	6000.0
H2S*	+H	=H2S	H	GRAIN	4.00D-05	0.00	6000.0
H2S*	+H2	=H2S	H2	GRAIN	1.00D-04	0.00	6000.0
H2S*	+He	=H2S	He	GRAIN	8.00D-04	0.00	6000.0
CH4*	+CRP	=CH4	GRAIN		7.00D+01	0.00	0.0
H2O*	+CRP	=H2O	GRAIN		7.00D+01	0.00	0.0
CO*	+CRP	=CO	GRAIN		7.00D+01	0.00	0.0
CO2*	+CRP	=CO2	GRAIN		7.00D+01	0.00	0.0
NH3*	+CRP	=NH3	GRAIN		7.00D+01	0.00	0.0
CH3OH*	+CRP	=CH3OH	GRAIN		7.00D+01	0.00	0.0
H2CO*	+CRP	=H2CO	GRAIN		7.00D+01	0.00	0.0
HCO2H*	+CRP	=HCO2H	GRAIN		7.00D+01	0.00	0.0
OCS*	+CRP	=OCS	GRAIN		7.00D+01	0.00	0.0
H2S*	+CRP	=H2S	GRAIN		7.00D+01	0.00	0.0
C	+PHOTON	=C+	ELECTR		2.20D-10	0.00	0.0
S	+PHOTON	=S+	ELECTR		1.50E-10	0.00	0.0
Si	+PHOTON	=Si+	ELECTR		2.00D-09	0.00	0.0
Fe	+PHOTON	=Fe+	ELECTR		1.80D-10	0.00	0.0
CH+	+Fe	=Fe+	CH		2.60D-10	0.00	0.0
N+	+Fe	=Fe+	N		1.50D-09	0.00	0.0
CH3+	+Fe	=Fe+	CH3		2.40D-09	0.00	0.0
O+	+Fe	=Fe+	O		2.90D-09	0.00	0.0
NH3+	+Fe	=Fe+	NH3		2.30D-09	0.00	0.0
H2O+	+Fe	=Fe+	H2O		1.50D-09	0.00	0.0
C2H2+	+Fe	=Fe+	C2H2		2.00D-09	0.00	0.0
N2+	+Fe	=Fe+	N2		4.30D-10	0.00	0.0
Si+	+Fe	=Fe+	Si		1.90D-09	0.00	0.0
H2CO+	+Fe	=Fe+	H2CO		1.90D-09	0.00	0.0
Fe	+CRP	=Fe+	ELECTR		1.30D-17	0.00	1500.0

Fe	O2	=FeO	O		2.09E-10	0.00	10200.0
Fe	H2O	=FeO	H2		1.00E-10	0.00.	9300.0
Fe	OH	=FeO	H		1.00E-10	0.00	1550.0
FeO	H2	=FeOH	H		1.00E-10	0.00	12000.0
H3+	FeO	=FeOH+	H2		2.00E-09	0.00	0.0
He+	FeO	=Fe+	O	He	1.70E-09	0.00	0.0
FeOH+	ELECTR	=Fe	OH		3.00E-07	-0.50	0.0
C+	+ELECTR	=C			1.09D-11	-0.95	7490.0
O+	+ELECTR	=O			5.09D-14	0.13	1298.2
N+	ELECTR	=N			6.76D-11	-1.27	3997.8
C+	+H	=C	H+		9.28D-19	1.34	15917.0
He+	+H	=He	H+		5.60D-18	2.06	191.8
N+	+H	=N	H+		3.13D-12	-0.31	508.4
S+	+H	=S	H+		5.75D-16	1.25	27151.0
C	+H+	=C+	H		1.00D-14	0.0	0.0
S	+H+	=S+	H		1.00D-14	0.0	0.0
N	+H+	=N+	H		9.82D-12	-0.23	262.1

Appendix C

Atomic and ionic emission

C.1 Level population calculation of Fe^+

The model used to calculate the population distribution of Fe^+, which accounts for population transfer among the 19 energy levels above the ground state arising in the a^6D, a^4F, a^4D, a^4P and b^4P terms, was described in Chapter 3. The spontaneous radiative transition probabilities computed by Nussbaumer & Storey (1988), which extend to the a^4P term, were adopted and those of Quinet et al. (1996) for the b^4P term. Collisions with both neutral species and electrons were included; for deexcitation rate coefficients of the latter, the (Maxwellian-averaged, υ_{ji}) collision strengths of Zhang & Pradhan (1995) were used. It was stated in Chapter 3 that collisions with neutral species are not efficient in exciting Fe^+. Here the calculation of the population distribution will be described before the treatment regarding the neutral perturbers is presented and the reason for their ineffectiveness is explained in the next Section.

Calculations of the distribution of the level populations followed the formalism of Seaton (1968). For electrons, the deexcitation rate coefficient is:

$$q_{ij} = \frac{8.63 \times 10^{-6}\, \Upsilon_{ji}}{\omega_j\, T_e^{1/2}} \qquad (j > i)\,. \tag{C.1}$$

Assuming detailed balance, the excitation rate coefficient, q_{ij}, is found by multiplying the deexcitation rate, q_{ji}, by the ratio of statistical weights, ω,

and a Boltzmann factor

$$q_{ij} = \frac{\omega_j}{\omega_i} q_{ji} \exp\left(-E_{ji}/T\right) \qquad (j > i)\,, \tag{C.2}$$

where E_{ji} is the difference between the energies (in K) of the levels j and i. The probability of a transition from state i to j is then given by

$$d_{ji} = (q_{ij} + q_{ji})\, N_{\text{perturber}} + A_{ji}, \tag{C.3}$$

where $N_{\text{perturber}}$ is the number density of the perturber, which is the electron density (but H_2, H and He are also included, see later), and A_{ji} is the probability of spontaneous radiative decay from j to i. The probability of radiative excitation is negligible compared to the probability of collisional excitation so this term is neglected for $j < i$. (C.3) provides the elements of a matrix of transition probabilities in which the diagonal elements are zero. Assuming steady state and labelling the number of Fe^+ ions per unit volume in level i as N_i gives

$$\sum_{j \neq i} d_{ij} N_j = \sum_{j \neq i} d_{ji} N_i \tag{C.4}$$

Setting the diagonal elements to

$$d_{ii} = -\sum_{j \neq i} d_{ji}, \tag{C.5}$$

gives

$$\sum_j d_{ij} N_j = 0, \tag{C.6}$$

where the number density, N, of Fe^+ is given by

$$\sum_j N_j = N. \tag{C.7}$$

For convenience, and because we are computing the relative level populations, we can set N=1 and re-write the closure relation in (C.7) as

$$\sum_j d_{1,j} N_j = 1, \tag{C.8}$$

where $d_{1,j} = 1$ (for all j). Then, in matrix form,

$$\mathbf{d}\,\mathbf{N} = \begin{pmatrix} 1 \\ \vdots \\ 0 \end{pmatrix}, \quad \text{or,} \quad \mathbf{N} = \mathbf{d}^{-1} \begin{pmatrix} 1 \\ \vdots \\ 0. \end{pmatrix} \tag{C.9}$$

Thus, the level populations relative to the ground state are given by the first column of the inverse of the matrix, **d**. This method provides a check on the accuracy of the calculation: the sum of the level populations should be equal to one.

C.2 Neutral perturbers of Fe^+

In the case of the neutral perturbers, only collisions with the most abundant neutral species, H_2, H and He, were considered. We are not aware of any quantum mechanical calculations of cross sections for the electronic excitation of Fe^+ by these perturbers. Accordingly, the deexcitation rate coefficients were estimated using a simple classical approximation, which derives from the Langevin 'orbiting' model, adopting the polarizability, α, and reduced mass, M, appropriate to each perturber.

$$q_{ji} = \pi \left(\frac{\alpha}{M}\right)^{\frac{1}{2}} \qquad (j > i)\,. \tag{C.10}$$

These deexcitation rate coefficients can be incorporated into the matrix discussed above. The ground state term of Fe^+ is a sextet term while the other terms considered in the model of Fe^+ are all quartet terms. Population can be transferred among terms of the same spin via collisions with electrons, H, H_2 and He. However, assuming LS coupling, conservation of the total electron spin implies that the spin state of Fe^+ can be changed only by exchange of a bound and an incident electron with oppositely directed spins [if (weak) magnetic interactions are neglected]. Electron collisional excitation of the a^4D term, from which all observed emission arises, from the a^6D ground term proceeds via this electron exchange mechanism. In collisions between Fe^+ and H, a similar process of exchange can, in principle, take place, between one of the

bound electrons of the ion and the bound electron of the hydrogen atom. In the case of collisions with He, on the other hand, the ground state is a singlet, and exchange with an electron of opposite spin implies a transition to a triplet state. As the lowest energy triplet state of He lies almost 20 eV above ground, such events will be extremely rare under typical physical conditions in HH outflows. Finally, ground state H_2 is also a singlet, and the lowest energy triplet state is repulsive. Hence, transitions to the triplet state lead to dissociation of the molecule and require an energy input of more than 4.5 eV. For these reasons it was concluded that transitions involving a change of spin, including excitation of a^4D from a^6D, are induced at a significant rate only by collisions with electrons and H atoms. In the model, therefore, transfer of population between levels of differing spin is assumed to be effected only via collisions with electrons and H. For completeness and to accurately calculate the transfer of population within terms of the same spin, collisions with H_2 and He are included, although their effect is small. However, H is the least abundant of the three neutral perturbers in C-type shock waves and the work described in Chapter 5 showed that excitation of Fe^+ by H in C-component shocks, where the ionization fraction is low, is insufficient to reproduce the observed [Fe II] emission. Instead, excitation of Fe^+ by collisions with electrons in regions of high ionization are required.

C.3 Rates coefficients for fine-structure transitions of [C I]

In addition to comparisons with [Fe II] line intensities, the intensity of the [C I] $^1D_2$–$^3P_1$ 0.985 μm and [C I] $^1D_2$–$^3P_2$ 0.983 μm transitions predicted by the J-type shock models were compared with observation. The model for [C I] calculated the transfer of population between the five ^3P, ^1D and ^1S levels, which lie at energies of 0.0, 24, 62, 1.5 $\times 10^4$ and 3.1×10^4 K above the ground state, as a result of collisions with H, ortho- and para-H_2, He, H^+ and electrons and of spontaneous decay. The spontaneous decay rate coefficients of

Nussbaumer & Rusca (1979) were adopted. Fits to the rate coefficients for collisional excitation, which were taken from the literature, were performed by C. M^{c}Coey for electron collisions and by J. Le Bourlot for all others (private communication). In what follows the fit and original reference are given for each perturber. Each rate, $k_{\rm X}$, is calculated at the effective temperature for each perturber, X, which takes into account ion-neutral streaming. Therefore, the effective temperature for neutral-neutral collisions, such as with H, is the neutral temperature of the gas, $T_{\rm n}$, while for collisions with electrons the effective temperature is the electron temperature, $T_{\rm e}$. On the other hand, the effective temperature of ion-neutral collisions between H^+ and C is given by

$$T_{\rm eff}({\rm H}^+) = \frac{m_{\rm C}\, m_{\rm H+}(v_{\rm C} - v_{\rm H+})^2}{3k(m_{\rm C} + m_{\rm H+})} + \frac{m_{\rm C}\, T_{\rm H+} + m_{\rm H+}\, T_{\rm C}}{m_{\rm C} + m_{\rm H+}}. \qquad \text{(C.11)}$$

For clarity, the energy levels of [C I] are labelled in the following way:

Term	Label
$^3P_0$	1
$^3P_1$	2
$^3P_2$	3
$^1D_2$	4
$^1S_0$	5

Collisions with H (Launay & Roueff, 1977):

$$k_{\rm H}(1,2) = 1.01 \times 10^{-10} \times T_{\rm n}^{0.117} \qquad \text{(C.12)}$$

$$k_{\rm H}(1,3) = 4.49 \times 10^{-11} \times T_{\rm n}^{0.194} \qquad \text{(C.13)}$$

$$k_{\rm H}(2,3) = 1.06 \times 10^{-10} \times T_{\rm n}^{0.234} \qquad \text{(C.14)}$$

Collisions with H_2 (Schroder et al., 1991):

$$k_{\rm paraH_2}(1,2) = 0.80 \times 10^{-10} \qquad \text{(C.15)}$$

$$k_{\rm orthoH_2}(1,2) = 0.75 \times 10^{-10} \qquad \text{(C.16)}$$

$$k_{\rm paraH_2}(1,3) = 0.90 \times 10^{-10} \qquad \text{(C.17)}$$

$$k_{\rm orthoH_2}(1,3) = 3.54 \times 10^{-11} \times T_{\rm n}^{0.167} \qquad \text{(C.18)}$$

$$k_{\mathrm{paraH_2}}(2,3) = 2.00 \times 10^{-10} \tag{C.19}$$

$$k_{\mathrm{orthoH_2}}(2,3) = 5.25 \times 10^{-11} \times T_{\mathrm{n}}^{0.244} \tag{C.20}$$

Collisions with He (Staemmler & Flower, 1991):

$$k_{\mathrm{He}}(1,2) = 8.38 \times 10^{-12} \times T_{\mathrm{n}}^{0.159} \tag{C.21}$$

$$k_{\mathrm{He}}(1,3) = 5.98 \times 10^{-11} \times T_{\mathrm{n}}^{0.078} \tag{C.22}$$

$$k_{\mathrm{He}}(2,3) = 3.68 \times 10^{-11} \times T_{\mathrm{n}}^{0.041} \tag{C.23}$$

Collisions with H+ (Roueff & Le Bourlot, 1990):

$$\begin{aligned} k_{\mathrm{H^+}}(1,2) = {} & \log^{-1}\{-10.359 + 0.7959 \times \log[T_{\mathrm{eff}}(\mathrm{H^+})] \\ & -0.08748 \times \log^2[T_{\mathrm{eff}}(\mathrm{H^+})]\} \end{aligned} \tag{C.24}$$

$$\begin{aligned} k_{\mathrm{H^+}}(1,3) = {} & \log^{-1}\{-13.232 + 2.4171 \times \log[T_{\mathrm{eff}}(\mathrm{H^+})] \\ & -0.29151 \times (\log^2[T_{\mathrm{eff}}(\mathrm{H^+})]\} \end{aligned} \tag{C.25}$$

$$\begin{aligned} k_{\mathrm{H^+}}(2,3) = {} & \log^{-1}\{-11.290 + 1.7915 \times \log[T_{\mathrm{eff}}(\mathrm{H^+})] \\ & -0.23010 \times (\log^2[T_{\mathrm{eff}}(\mathrm{H^+})]\} \end{aligned} \tag{C.26}$$

Collisions with electrons (from Pequignot & Aldrovandi (1976) as compiled by Mendoza (1983)):

$$k_e(i,4) = 8.629 \times 10^{-6} \times \frac{(1.83 \times 10^{-4} \times T_{\mathrm{e}}^{0.444})}{g_4} \times \frac{g_i}{9} \tag{C.27}$$

$$k_e(i,5) = 8.629 \times 10^{-6} \times \frac{(9.86 \times 10^{-5} \times T_{\mathrm{e}}^{0.343})}{g_5} \times \frac{g_i}{9} \tag{C.28}$$

$$k_e(4,5) = 8.629 \times 10^{-6} \times \frac{2.77 \times 10^{-3}}{g_5} \tag{C.29}$$

where i level 1, 2 or 3 and g_i is the statistical weight of the level. The division by 9 comes about because of the degeneracy of the ^{3}P term.

Appendix D

Observed and calculated [Fe II] and [C I] line intensities

The observations are corrected for reddening, using the power law fit of Cardelli et al. (1989) to the data of Rieke & Lebofsky (1985), and adopting $R = 3.1$. The values used for the extinction were derived from the [Fe II] lines from the 1.644, 1.257, 1.321 μm lines, which all arise in the $a^4D_{7/2}$ level, and are listed below (Nisini et al. (2002); Giannini et al. (2004) and T. Giannini, private communication):

Table D.1: Values of extinction derived from [Fe II] lines

Object	A_v
HH72A	4.7±1.5
HH26A	6±5
HH120	3.2±1.3
HH111F	9.1±0.4
HH240A	2.5±0.8
HH99A	5±1
HH99B0	4±1
HH99B1 (slit 1)	7±1
HH99B1 (slit 2)	7±1
HH99B2	6±1
HH99B3	10±1

Table D.2: a. Comparison between observed (reddening corrected) and computed [Fe II] and [C I] line intensities in HH72A, HH26A and HH120

Object	Term	$\lambda(\mu m)$	Observed (I $\pm$ ΔI) (10^{-5} erg cm^{-2} s^{-1} sr^{-1})	Model
HH72A	[Fe II] $a^4D_{7/2} - a^6D_{9/2}$	1.257	39.0±2.9	38.8
	[Fe II] $a^4D_{7/2} - a^6D_{7/2}$	1.321	21.7±5.2	10.2
	[Fe II] $a^4D_{5/2} - a^6D_{3/2}$	1.328	6.87±2.8	4.77
	[Fe II] $a^4D_{5/2} - a^4F_{9/2}$	1.534	12.3±4.1	8.33
	[Fe II] $a^4D_{3/2} - a^4F_{7/2}$	1.600	6.44±2.6	6.65
	[Fe II] $a^4D_{7/2} - a^4F_{9/2}$	1.644	29.2±3.1	28.5
	[C I] $^1D_2 - ^3P_1$	0.983	68.5±34	9.93
	[C I] $^1D_2 - ^3P_2$	0.985	119±17	29.4
HH26A	[Fe II] $a^4D_{7/2} - a^6D_{9/2}$	1.257	13.3±5.3	12.4
	[Fe II] $a^4D_{7/2} - a^4F_{9/2}$	1.644	10.0±1.5	9.15
	[C I] $^1D_2 - ^3P_1$	0.983	28.0±9.9	13.1
	[C I] $^1D_2 - ^3P_2$	0.985	57.7±9.9	39.0
HH120	[Fe II] $a^4D_{7/2} - a^6D_{9/2}$	1.257	50.1±0.22	50.6
	[Fe II] $a^4D_{1/2} - a^6D_{1/2}$	1.271	5.88±0.74	4.25
	[Fe II] $a^4D_{3/2} - a^6D_{3/2}$	1.279	5.20±0.73	7.17
	[Fe II] $a^4D_{5/2} - a^6D_{5/2}$	1.295	7.18±1.4	10.1
	[Fe II] $a^4D_{7/2} - a^6D_{7/2}$	1.321	17.5±0.56	13.3
	[Fe II] $a^4D_{5/2} - a^6D_{3/2}$	1.328	2.99±0.42	6.15
	[Fe II] $a^4D_{5/2} - a^4F_{9/2}$	1.534	7.50±0.24	10.7
	[Fe II] $a^4D_{3/2} - a^4F_{7/2}$	1.600	3.72±0.29	8.35
	[Fe II] $a^4D_{7/2} - a^4F_{9/2}$	1.644	38.0±0.56	37.2
	[Fe II] $a^4D_{1/2} - a^4F_{5/2}$	1.664	4.98±1.1	4.16
	[Fe II] $a^4D_{5/2} - a^4F_{7/2}$	1.677	3.85±1.1	7.81
	[Fe II] $a^4D_{5/2} - a^4F_{5/2}$	1.800	12.5±1.6	5.37
	[Fe II] $a^4D_{7/2} - a^4F_{7/2}$	1.810	34.2±9.3	7.49
	[C I] $^1D_2 - ^3P_1$	0.983	23.3±1.1	9.12
	[C I] $^1D_2 - ^3P_2$	0.985	67.8±0.33	27.0

Notes: [a] 2<S/N<3
[b] Upper limit

Table D.2: b. Comparison between observed (reddening corrected) and computed [Fe II] and [C I] line intensities in HH111F and HH240A

Object	Term	$\lambda(\mu m)$	Observed (I $\pm$ ΔI) (10^{-5} erg cm^{-2} s^{-1} sr^{-1})	Model
HH111F	[Fe II] $a^4D_{7/2} - a^6D_{9/2}$	1.257	191.0±2.68	194.0
	[Fe II] $a^4D_{1/2} - a^6D_{1/2}$	1.271	21.9±1.29	21.3
	[Fe II] $a^4D_{3/2} - a^6D_{3/2}$	1.279	13.8±1.26	34.8
	[Fe II] $a^4D_{5/2} - a^6D_{5/2}$	1.295	24.1±2.41	48.2
	[Fe II] $a^4D_{7/2} - a^6D_{7/2}$	1.321	70.6±1.12	50.7
	[Fe II] $a^4D_{5/2} - a^6D_{3/2}$	1.328	14.3±2.20	29.3
	[Fe II] $a^4D_{5/2} - a^4F_{9/2}$	1.534	26.1±1.41	51.2
	[Fe II] $a^4D_{3/2} - a^4F_{7/2}$	1.600	18.3±3.16	40.6
	[Fe II] $a^4D_{7/2} - a^4F_{9/2}$	1.644	151.6±1.77	142.5
	[Fe II] $a^4D_{1/2} - a^4F_{5/2}$	1.664	9.74±1.72	20.8
	[Fe II] $a^4D_{5/2} - a^4F_{7/2}$	1.677	19.7±2.81	37.2
	[Fe II] $a^4D_{7/2} - a^4F_{7/2}$	1.810	109.1±9.49	28.7
	[C I] $^1D_2 - ^3P_2$	0.985	211±16.6	247
HH240A	[Fe II] $a^4D_{7/2} - a^6D_{9/2}$	1.257	105±0.40	104
	[Fe II] $a^4D_{1/2} - a^6D_{1/2}$	1.271	4.80±0.40	10.9
	[Fe II] $a^4D_{3/2} - a^6D_{3/2}$	1.279	7.96±0.40	18.0
	[Fe II] $a^4D_{5/2} - a^6D_{5/2}$	1.295	13.8±0.79	25.4
	[Fe II] $a^4D_{3/2} - 4^6D_{1/2}$	1.298	2.74±0.39	7.89
	[Fe II] $a^4D_{7/2} - a^6D_{7/2}$	1.321	33.9±0.77	27.2
	[Fe II] $a^4D_{5/2} - a^6D_{3/2}$	1.328	4.29±0.27	15.5
	[Fe II] $a^4D_{5/2} - a^4F_{9/2}$	1.534	17.3±1.00	27.0
	[Fe II] $a^4D_{3/2} - a^4F_{7/2}$	1.600	10.2±0.66	21.0
	[Fe II] $a^4D_{7/2} - a^4F_{9/2}$	1.644	79.1±0.65	76.5
	[Fe II] $a^4D_{1/2} - a^4F_{5/2}$	1.664	3.85±0.32	10.7
	[Fe II] $a^4D_{5/2} - a^4F_{7/2}$	1.677	9.88±0.96	19.6
	[Fe II] $a^4D_{5/2} - a^4F_{5/2}$	1.800	15.6±2.40	13.5
	[Fe II] $a^4D_{7/2} - a^4F_{7/2}$	1.810	45.9±7.00	15.4
	[C I] $^1D_2 - ^3P_1$	0.983	8.62±0.50	58.6
	[C I] $^1D_2 - ^3P_2$	0.985	42.6±2.8	174

Notes: [a] 2<S/N<3
[b] Upper limit

Table D.2: c. Comparison between observed (reddening corrected) and computed [Fe II] and [C I] line intensities in HH99 A–B1 (slit 1)

Object	Term	$\lambda(\mu m)$	Observed (I $\pm$ ΔI) (10^{-5} erg cm^{-2} s^{-1} sr^{-1})	Model
HH99A[1]	[Fe II] $a^4D_{7/2} - a^6D_{9/2}$	1.257	11.5±0.34	11.5
	[Fe II] $a^4D_{7/2} - a^6D_{7/2}$	1.321	3.83±0.37	3.02
	[Fe II] $a^4D_{7/2} - a^4F_{9/2}$	1.644	8.48±0.31	8.50
	[Fe II] $a^4D_{5/2} - a^4F_{7/2}$	1.677	0.676±0.23	1.59
	[C I] $^1D_2 - ^3P_1$	0.983	10.2±2.0	6.71
	[C I] $^1D_2 - ^3P_2$	0.985	30.1±1.9	19.9
HH99B0	[Fe II] $a^4D_{7/2} - a^6D_{9/2}$	1.257	40.8±0.34	40.8
	[Fe II] $a^4D_{1/2} - a^6D_{1/2}$	1.271	2.72±0.57	3.45
	[Fe II] $a^4D_{3/2} - a^6D_{3/2}$	1.279	3.49±0.97	5.80
	[Fe II] $a^4D_{5/2} - a^6D_{5/2}$	1.295	5.42±0.59	8.18
	[Fe II] $a^4D_{3/2} - 4^6D_{1/2}$	1.298	1.53±0.33	2.54
	[Fe II] $a^4D_{7/2} - a^6D_{7/2}$	1.321	13.0±0.57	10.7
	[Fe II] $a^4D_{5/2} - a^6D_{3/2}$	1.328	3.23±0.63	4.97
	[Fe II] $a^4D_{5/2} - a^4F_{9/2}$	1.534	5.01±0.39	8.68
	[Fe II] $a^4D_{3/2} - a^4F_{7/2}$	1.600	2.70±0.52	6.76
	[Fe II] $a^4D_{7/2} - a^4F_{9/2}$	1.644	31.9±0.36	30.0
	[Fe II] $a^4D_{1/2} - a^4F_{5/2}$	1.664	1.91±0.71[a]	3.38
	[Fe II] $a^4D_{5/2} - a^4F_{7/2}$	1.677	2.87±0.56	6.31
	[Fe II] $a^4D_{3/2} - a^4F_{5/2}$	1.711	1.19±0.41[a]	1.77
	[Fe II] $a^4D_{1/2} - a^4F_{3/2}$	1.745	1.84±0.43	1.68
	[Fe II] $a^4D_{3/2} - a^4F_{3/2}$	1.798	1.40±0.59[a]	3.06
	[C I] $^1D_2 - ^3P_1$ + [C I] $^1D_2 - ^3P_2$	0.983+0.985	37.2±3.2	40.1
HH99B1 (slit 1)	[Fe II] $a^4D_{7/2} - a^6D_{9/2}$	1.257	9.36±0.35	7.64
	[Fe II] $a^4D_{5/2} - a^4F_{9/2}$	1.534	2.01±0.36	1.66
	[Fe II] $a^4D_{7/2} - a^4F_{9/2}$	1.644	7.06±0.70	5.62
	[C I] $^1D_2 - ^3P_1$ + [C I] $^1D_2 - ^3P_2$	0.983+0.985	25.3±8.3	61.1

Notes: [1] Model 2 for HH99A.
[a] 2<S/N<3
[b] Upper limit

Table D.2: d. Comparison between observed (reddening corrected) and computed [Fe II] and [C I] line intensities in HH99 B1 (slit 2), B2 and B3

Object	Term	$\lambda(\mu m)$	Observed ($I \pm \Delta I$) (10^{-5} erg cm^{-2} s^{-1} sr^{-1})	Model
HH99B1 (slit 2)	[Fe II] $a^4D_{7/2} - a^6D_{9/2}$	1.257	35.7±1.7	35.9
	[Fe II] $a^4D_{7/2} - a^6D_{7/2}$	1.321	8.95±0.13	9.41
	[Fe II] $a^4D_{5/2} - a^4F_{9/2}$	1.534	3.13±0.13[a]	7.88
	[Fe II] $a^4D_{7/2} - a^4F_{9/2}$	1.644	27.2±0.12	26.4
	[Fe II] $a^4D_{5/2} - a^4F_{7/2}$	1.677	2.84±0.12[a]	5.73
	[Fe II] $a^4D_{3/2} - a^4F_{5/2}$	1.711	3.89±0.12	1.61
	[Fe II] $a^4D_{1/2} - a^4F_{3/2}$	1.745	3.90±0.12	1.52
	[C I] $^1D_2 - ^3P_1$ + [C I] $^1D_2 - ^3P_2$	0.983+0.985	200[b]	38.0
HH99B2	[Fe II] $a^4D_{7/2} - a^6D_{9/2}$	1.257	71.1±1.8	72.7
	[Fe II] $a^4D_{5/2} - a^6D_{5/2}$	1.295	6.18±2.1	14.5
	[Fe II] $a^4D_{7/2} - a^6D_{7/2}$	1.321	21.3±1.8	19.0
	[Fe II] $a^4D_{5/2} - a^6D_{3/2}$	1.328	3.69±1.2	8.84
	[Fe II] $a^4D_{5/2} - a^4F_{9/2}$	1.534	10.3±1.9	15.4
	[Fe II] $a^4D_{3/2} - a^4F_{7/2}$	1.600	4.31±1.5[a]	11.9
	[Fe II] $a^4D_{7/2} - a^4F_{9/2}$	1.644	56.1±1.5	53.5
	[Fe II] $a^4D_{1/2} - a^4F_{5/2}$	1.664	6.45±1.6	5.88
	[Fe II] $a^4D_{5/2} - a^4F_{7/2}$	1.677	11.0±3.0	11.2
	[Fe II] $a^4D_{3/2} - a^4F_{5/2}$	1.711	4.96±2.3[a]	3.13
	[C I] $^1D_2 - ^3P_1$ + [C I] $^1D_2 - ^3P_2$	0.983+0.985	94[b]	22.5
HH99B3	[Fe II] $a^4D_{3/2} - a^6D_{5/2}$	1.248	7.31±1.6	0.256
	[Fe II] $a^4D_{7/2} - a^6D_{9/2}$	1.257	45.7±2.0	46.7
	[Fe II] $a^4D_{1/2} - a^6D_{1/2}$	1.271	15.0±2.5	3.93
	[Fe II] $a^4D_{3/2} - a^6D_{3/2}$	1.279	12.2±2.3	6.62
	[Fe II] $a^4D_{7/2} - a^6D_{7/2}$	1.321	24.5±3.1	12.2
	[Fe II] $a^4D_{7/2} - a^4F_{9/2}$	1.644	36.8±0.80	34.4
	[C I] $^1D_2 - ^3P_1$ + [C I] $^1D_2 - ^3P_2$	0.983+0.985	269[b]	36.4

Notes: [a] 2<S/N<3
[b] Upper limit

Appendix E

Observed H_2 line fluxes

The fluxes of H_2, [Fe II], [C I] and other atomic and ionic species, uncorrected for reddening, observed towards the objects modelled in Chapter 5 are listed in Tables E.1–E.10. The observations were performed by T. Giannini, B. Nissini, A. Caratti o Garatti and D. Lorenzetti and are published in Nisini et al. (2002), Giannini et al. (2004) and M^{c}Coey et al. (2004).

Table E.1: Observed lines in HH25.

Term	$\lambda(\mu m)$	$F \pm \Delta F$ (10^{-14} erg cm^{-2} s^{-1})			
H_2 lines		HH25 A	HH25B	HH25 C	HH25 D
1–0 S(9)	1.688	···	···	3.6±0.5	···
1–0 S(8)	1.715	···	···	2.4±0.4	···
1–0 S(7)	1.748	···	0.85±0.07	14.1±0.2	···
1–0 S(6)	1.788	···	1.2±0.1	10.4±0.2	···
1–0 S(3)	1.958	···	···	36±1	···
2–1 S(4)	2.004	···	···	···	···
1–0 S(2)	2.034	1.0±0.1	2.0±0.1	18.9±0.3	···
2–1 S(3)	2.073	···	0.9±0.1	6.3±0.8	···
1–0 S(1)	2.122	2.7±0.1	6.07±0.06	48.0±0.3	1.0±0.3
2–1 S(2)	2.154	···	0.41±0.08	1.5±0.3	···
1–0 S(0)	2.223	0.9±0.1	1.9±0.1	10.8±0.1	···
2–1 S(1)	2.248	···	1.1±0.2	6.1±0.7	···
2–1 S(0)	2.355	···	···	···	···
1–0 Q(1)	2.407	···	4.0±0.3	44±1	···
1–0 Q(2)	2.413	···	2.7±0.3	20±1	···
1–0 Q(3)	2.424	···	2.9±0.4	37±1	···
1–0 Q(4)	2.437	···	7.7±0.5	18±1	···
1–0 Q(5)	2.455	···	12.4±0.5	30±1	···

Notes: [a]S/N between 2 and 3.

Table E.2: Observed lines in HH26.

Term	$\lambda(\mu m)$	$F \pm \Delta F$ (10^{-14} erg cm^{-2} s^{-1})			
H_2 lines		HH26 A	HH26 B	HH26 C	HH26 D
2–0 S(9)	1.053	5.3±0.5	···	4.7±0.4	···
2–0 S(8)	1.057	2.1±0.4	···	···	···
2–0 S(7)	1.064	5.4±0.3	···	3.5±0.3	···
2–0 S(6)	1.073	3.0±0.4	···	1.8±0.4	···
2–0 S(5)	1.085	7.0±0.3	···	4.7±0.4	···
2–0 S(4)	1.100	3.9±0.5	···	1.5±0.1	···
2–0 S(3)	1.117	4.1±0.6	···	1.3±0.2	···
3–1 S(9)	1.122	1.7±0.2	···	3.3±0.7	···
3–1 S(8)	1.124	···	···	1.4±0.5[a]	···
3–1 S(7)	1.130	3.2±0.8	···	3±1	···
2–0 S(2)+ 3–1 S(6)	1.138+1.140	6±1	···	5±1	···
3–1 S(5)	1.152	3.9±0.3	···	3.8±0.3	···
2–0 S(1)	1.162	4.7±0.6	···	3.4±0.5	···
3–1 S(4)	1.167	2.8±0.6	···	1.4±0.3	···
3–1 S(3)	1.186	3.6±0.4	···	3.5±0.2	···
2–0 S(0)+ 4–2 S(10)	1.189+1.190	2±1[a]	···	8.0±0.2	···
4–2 S(9)+ 4–2 S(8)	1.196+1.199	1.0±0.2	···	···	···
4–2 S(7)[1]	1.205	1.7±0.4	···	1.1±0.3	···
3–1 S(2)	1.207	2.2±0.4	···	···	···
4–2 S(6)	1.214	1.1±0.3	···	···	···
4–2 S(5)	1.226	1.6±0.2	···	1.6±0.4	···
3–1 S(1)	1.233	2.9±0.3	···	2.5±0.4	···
2–0 Q(1)	1.238	3.8±0.3	···	1.7±0.3	···
2–0 Q(2)+ 4–2 S(4)	1.242+1.242	1.9±0.3	···	2.0±0.6	···
2–0 Q(3)	1.247	3.6±0.3	···	2.4±0.4	···
2–0 Q(4)	1.254	1.0±0.4[a]	···	···	···
4–2 S(3)+ 3–1 S(0)+ 2–0 Q(5)	1.261+1.262-1.263	6.1±0.4	···	3.6±0.5	···

Notes : [1]This line for HH26C is blended with 3-1 S(2).
[2]This line for HH26C is blended with 2-0 Q(7).
[a]S/N between 2 and 3.

Table E.2: *(continued)* Observed lines in HH26.

Term	$\lambda(\mu m)$	$F \pm \Delta F$ (10^{-14} erg cm^{-2} s^{-1})			
H_2 lines		HH26 A	HH26 B	HH26 C	HH26 D
2–0 Q(6)	1.274	1.5±0.5	···	1.1±0.2	···
4–2 S(2)[2]	1.285	1.4±0.4	···	···	···
2–0 Q(7)	1.287	4.0±0.7	···	1.4±0.2	···
2–0 Q(8)	1.302	1.0±0.1	···	···	···
4–2 S(1)	1.311	0.8±0.1	···	···	···
2–0 Q(9)	1.319	2.2±0.5	···	···	···
3–1 Q(3)	1.324	1.5±0.4	···	···	···
3–1 Q(4)+ 2–0 O(3)	1.333+1.335	3.9±0.5	···	2.1±0.4	···
3–1 Q(5)+ 4–2 S(0)	1.342+1.342	2.3±0.4	···	1.2±0.3	···
3–1 O(5)	1.522	1.7±0.4	···	···	···
2–0 O(7)	1.546	0.6±0.2	···	···	···
2–0 O(8)+ 5–3 O(3)	1.610+1.613	0.9±0.2	···	···	···
1–0 S(11)	1.650	0.7±0.2	···	···	···
1–0 S(10)	1.666	0.9±0.2	···	···	···
1–0 S(9)	1.688	4.4±0.3	···	3.8±0.3	···
1–0 S(8)	1.715	2.5±0.3	1.2±0.1	2.5±0.3	···
1–0 S(7)	1.748	13.3±0.3	3±1	12.9±0.3	2.5±0.2
1–0 S(6)	1.788	11.3±0.3	2.6±0.2	9.1±0.3	1.7±0.2
1–0 S(3)	1.958	44±1	8±1	71±2	11±1
2–1 S(4)	2.004	3.5±0.6	···	1.9±0.5	···
1–0 S(2)	2.034	18.1±0.3	5±1	16.6±0.3	2.2±0.2
3–2 S(5)	2.066	1.2±0.3	···	···	···
2–1 S(3)	2.073	7.1±0.3	2.1±0.1	4.9±0.3	···
1–0 S(1)	2.122	47.0±0.4	12.6±0.3	42.6±0.3	5.9±0.1
2–1 S(2)	2.154	3.0±0.2	···	2.1±0.2	···
3–2 S(3)	2.201	1.7±0.2	···	1.5±0.2	···
1–0 S(0)	2.223	10.6±0.2	2.9±0.1	9.7±0.3	1.7±0.2
2–1 S(1)	2.248	5.8±0.2	1.9±0.2	4.4±0.2	1.1±0.2
3–2 S(2)	2.287	0.6±0.2	···	···	···

Notes: [a]S/N between 2 and 3.

Table E.2: *(continued)* Observed lines in HH26.

Term	$\lambda(\mu m)$	$F \pm \Delta F$ (10^{-14} erg cm^{-2} s^{-1})			
H_2 lines		HH26 A	HH26 B	HH26 C	HH26 D
4–3 S(3)	2.344	···	···	0.7±0.2	···
2–1 S(0)	2.355	1.3±0.3	···	···	···
3–2 S(1)	2.386	2.2±0.6	···	···	···
1–0 Q(1)	2.407	27±1	8±1	34±1	4±1
1–0 Q(2)	2.413	15±1	3±1	16±1	···
1–0 Q(3)	2.424	23±1	9±1	28±1	3±1
1–0 Q(4)	2.437	15±1	6±1	14±1	···
1–0 Q(5)	2.455	16±1	11±1	···	···
1–0 Q(6)	2.476	8±3[a]	···	···	···
1–0 Q(7)	2.500	22±4	···	···	···
Atomic and Ionic lines					
[C I] $^1D_2 - ^3P_1$	0.98	1.7±0.6	···	···	···
[C I] $^1D_2 - ^3P_2$	0.985	3.5±0.6	···	···	···
[S II] $^2P_{3/2} - ^2D_{3/2}$	1.029	1.5±0.2	···	···	···
[S II] $^2P_{3/2} - ^2D_{5/2}$+ [S II] $^2P_{1/2} - ^2D_{3/2}$	1.032+1.034	1.3±0.3	···	···	···
[Fe II] $a^4D_{7/2} - a^6D_{9/2}$	1.257	1.0±0.4[a]	···	···	···
[Fe II] $a^4D_{7/2} - a^4F_{9/2}$	1.644	1.3±0.2	···	···	···

Notes: [a]S/N between 2 and 3.

Table E.3: a) Observed lines in HH72A-B.

Term	$\lambda(\mu m)$	$F \pm \Delta F(10^{-15}$ erg cm^{-2} s$^{-1})$	
H_2 lines		HH72 A	HH72 B
2–0 S(9)	1.053	1.9±0.5	4±2[a]
2–0 S(7)	1.064	2.0±0.6	5±2[a]
2–0 S(6)	1.073	···	3±1
2–0 S(5)[b]	1.085	6.7±0.5	6.4±0.9
2–0 S(3)	1.117	···	4±1
3–1 S(9)	1.122	···	4±1
3–1 S(7)	1.130	···	6±2
2–0 S(2) + 3–1 S(6)	1.138+1.140	···	3.2±0.4
3–1 S(5)	1.152	1.1±0.5[a]	4.1±0.7
2–0 S(1)	1.162	1.7±0.3	···
3–1 S(3)	1.186	1.4±0.4	2.9±0.8
2–0 S(0) + 4–2 S(10)	1.189+1.190	···	1.4±0.6[a]
4–2 S(7)	1.205	···	1.1±0.5[a]
3–1 S(2)	1.207	···	1.0±0.4[a]
3–1 S(1)	1.233	1.8±0.4	2.3±0.6
2–0 Q(1)	1.238	1.2±0.3	2.0±0.4
2–0 Q(3)	1.247	1.5±0.3	3.2±0.6
3–1 S(0) + 2–0 Q(5)	1.262+1.263	1.6±0.4	4.1±0.6
4–2 S(2) + 2–0 Q(7)	1.285+1.287	1.2±0.5[a]	2.8±0.8
2–0 O(3)	1.335	1.4±0.3	4±2[a]
4–2 S(0)	1.342	1.0±0.3[a]	···
1–0 S(9)	1.688	2.7±0.4	3.6±0.7
1–0 S(8)	1.715	1.6±0.6[a]	1.9±0.4
1–0 S(7)	1.748	7.5±0.5	9.0±0.3
1–0 S(6)	1.788	4.4±0.3	7.5±0.9
1–0 S(3)	1.958	30.3±0.7	84±1
2–1 S(4)	2.004	1.9±0.5	···
1–0 S(2)	2.034	9.5±0.4	17.8±0.7
2–1 S(3)	2.073	4.0±0.2	4.9±0.6

Notes: [a]S/N between 2 and 3.
[b]Blend with [S I] $^1D_2$–$^3P_2$ (1.082μm) and HeI 1.083μm.

Table E.3: a) *(continued)* Observed lines in HH72A-B

Term	$\lambda(\mu m)$	$F \pm \Delta F(10^{-15}$ erg cm^{-2} s$^{-1})$	
H_2 lines		HH72 A	HH72 B
1–0 S(1)	2.122	22.9±0.4	35.9±0.6
2–1 S(2)	2.154	1.4±0.3	2.6±0.6
3–2 S(3)	2.201	1.1±0.3	2.6±0.9[a]
1–0 S(0)	2.223	5.4±0.2	10.4±0.6
2–1 S(1)	2.248	3.8±0.3	7.8±0.6
3–2 S(1)	2.386	2.3±0.9[a]	···
1–0 Q(1)	2.407	17±1	56±2
1–0 Q(2)	2.413	7±1	25±2
1–0 Q(3)	2.424	13±1	54±4
1–0 Q(4)	2.437	7±1	···
1–0 Q(5)	2.455	9±1	···
1–0 O(5)	3.235	···	12±4
0–0 S(13)	3.847	···	12±4
Atomic and Ionic lines			
[C I] $^1D_2 - ^3P_1$	0.983	4±2[a]	8±2
[C I] $^1D_2 - ^3P_2$	0.985	7±1	16±2
[S II] $^2P_{3/2} - ^2D_{3/2}$	1.029	3.5±0.4	···
[S II] $^2P_{3/2} - ^2D_{5/2}$+ [S II] $^2P_{1/2} - ^2D_{3/2}$	1.032+1.034	7.3±0.6	···
[N I] $^2P_{3/2,1/2} - ^2D_{5/2}$+ [N I] $^2P_{3/2,1/2} - ^2D_{3/2}$	1.040+1.041	8±2	···
Paγ	1.094	1.3±0.5[a]	···
[Fe II] a$^4D_{7/2} - a^6D_{9/2}$	1.257	4.1±0.3	3.9±0.4
Paβ	1.282	2.4±0.5	0.8±0.3[a]
[Fe II] $a^4D_{7/2} - a^6D_{7/2}$	1.321	2.5±0.6	···
[Fe II] $a^4D_{5/2} - a^6D_{3/2}$	1.328	0.8±0.3[a]	···
[Fe II] $a^4D_{5/2} - a^4F_{9/2}$	1.534	1.8±0.6	···
[Fe II] $a^4D_{3/2} - a^4F_{7/2}$	1.600	1.0±0.4[a]	···
[Fe II] $a^4D_{7/2} - a^4F_{9/2}$	1.644	4.7±0.5	3.1±0.4

Notes: [a]S/N between 2 and 3.

Table E.3: b) Observed lines in HH72: Knots D-G.

Term	$\lambda(\mu m)$	$F \pm \Delta F(10^{-15}$ erg cm^{-2} s$^{-1})$		
H_2 lines		HH72 D	HH72 E	HH72 G
2–0 S(9)	1.053	2.6±0.9[a]	···	···
2–0 S(7)	1.064	2.4±0.8	···	···
2–0 S(5)	1.085	2.8±0.6	···	···
3–1 S(5)	1.152	1.6±0.5	···	···
2–0 S(1)	1.162	2.4±0.9[a]	···	···
3–1 S(3)	1.186	1.4±0.5[a]	···	···
4–2 S(5)	1.226	0.9±0.3	···	···
2–0 Q(1)	1.238	13.5±0.4	···	···
2–0 Q(3)	1.247	13.6±0.4	···	···
4–2 S(2) + 2–0 Q(7)	1.285+1.287	13.1±0.4	···	···
2–0 Q(9)	1.319	18.1±0.6	···	···
1–0 S(9)	1.688	2.4±0.5	···	···
1–0 S(8)	1.715	1.2±0.4	···	···
1–0 S(7)	1.748	7.1±0.7	3.9±0.4	1.6±0.1
1–0 S(6)	1.788	5.2±0.8	4.1±0.4	1.6±0.2
1–0 S(3)	1.958	30±4	16±2	13±2
2–1 S(4)	2.004	···	1.5±0.5	···
1–0 S(2)	2.034	8.7±0.5	8.7±0.6	3.9±0.5
2–1 S(3)	2.073	3.3±0.5	3.4±0.5	1.3±0.2
1–0 S(1)	2.122	20.1±0.3	16.8±0.6	9.3±0.3
2–1 S(2)	2.154	···	1.1±0.2	···
1–0 S(0)	2.223	5.2±0.3	4.4±0.3	···
2–1 S(1)	2.248	5.2±0.7	3.3±0.4	1.7±0.5
1–0 Q(1)	2.407	15±1	20±2	9±2
1–0 Q(2)	2.413	6±1	12±1	···
1–0 Q(3)	2.424	13±1	17±1	···
1–0 Q(4)	2.437	6±1	10±2	···
1–0 Q(5)	2.455	6±1	17±2	···
Atomic and Ionic lines				
[N I] $^2P_{3/2,1/2} - ^2D_{5/2}$+ [N I] $^2P_{3/2,1/2} - ^2D_{3/2}$	1.040+1.041	15.7±0.7[a]		
[Fe II] $a^4D_{7/2} - a^4F_{9/2}$	1.644	0.9±0.3		

Notes: [a]S/N between 2 and 3.

Table E.4: a) Observed lines in BHR71: HH320A/B and HH321A/B.

Term	$\lambda(\mu m)$	$F \pm \Delta F(10^{-15}$ erg cm^{-2} s$^{-1})$			
H_2 Lines		HH320 A	HH320 B	HH321 A	HH321 B
2–0 S(9)	1.053	19±2	10±2	5±2[a]	···
2–0 S(8)	1.057	8±2	6±2	···	···
2–0 S(7)	1.064	10±1	13±1	12.9±0.5	···
2–0 S(6)	1.073	9±1	7±1	5.2±0.5	···
2–0 S(5)	1.085	24±1	17.9±0.7	20.3±0.4	···
2–0 S(4)	1.100	11.1±0.8	7.3±0.7	6±3[a]	···
2–0 S(3)	1.117	18±1	15.2±0.9	21±1	···
3–1 S(9)	1.122	13±2	7±1	···	···
3–1 S(7)	1.130	6±1	7.3±0.8	···	···
2–0 S(2)+ 3–1 S(6)	1.138+1.140	21±2	10.0±0.8	9.4±0.6	···
3–1 S(5)	1.152	20±1	11.6±0.8	11.3±0.6	···
2–0 S(1)	1.162	18±1	15±1	16.9±0.6	···
3–1 S(4)	1.167	8±1	4.2±0.8	3.0±0.4	···
3–1 S(3)	1.186	13.7±0.8	8.0±0.6	8.8±0.7	···
2–0 S(0) + 4–2 S(10)	1.189+1.190	5.3±0.8	···	2.8±0.6	···
4–2 S(9) + 4–2 S(8)	1.196+1.199	5±1	···	···	···
4–2 S(7) + 3–1 S(2)	1.205+1.207	6±2	7±2[a]	3.5±0.6	···
4–2 S(5)	1.226	10±2	6±2	5±1	···
3–1 S(1)	1.233	9±1	7.7±0.7	5.6±0.8	···
2–0 Q(1)	1.238	9±1	8.0±0.7	8.8±0.8	···
2–0 Q(2) + 4–2 S(4)	1.242+1.242	5±1	5.0±0.6	4.4±0.7	···
2–0 Q(3)	1.247	10±1	7.6±0.9	9.5±0.8	···
2–0 Q(4)	1.254	5.8±0.6	2.6±0.8	3.8±0.8	···
4–2 S(3) + 3–1 S(0)[1]	1.261+1.262	16±1	5.9±0.8	13±1	···

Notes: [a]S/N between 2 and 3.
[1]For HH320 A and HH321 A this line is also blended with the 2-0 Q(5).

Table E.4: a) *(continued)* Observed lines in BHR71: HH320A/B and HH321A/B.

Term	$\lambda(\mu m)$	$F \pm \Delta F(10^{-15}$ erg cm^{-2} s$^{-1})$			
H_2 Lines		HH320 A	HH320 B	HH321 A	HH321 B
2–0 Q(5)	1.263	···	10±1	···	···
2–0 Q(6)	1.274	···	2.2±0.6	···	···
4–2 S(2) + 2–0 Q(7)	1.285+1.287	8±1	6±1	9.0±0.8	···
2–0 Q(8)	1.302	4.1±0.9	···	1.8±0.3	···
4–2 S(1)	1.311	6.5±0.9	3.7±0.7	3.9±0.3	···
3–1 Q(1)	1.314	···	···	4.1±0.5	···
2–0 Q(9)	1.319	7±2	2.5±0.8	5.0±0.4	···
3–1 Q(3)	1.324	5.2±0.6	4±1	···	···
3–1 Q(4) + 2–0 O(3)	1.333+1.335	8.3±0.7	6.5±0.9	7.1±0.4	···
3–1 Q(5) + 4–2 S(0)	1.342+1.342	9±1	5.1±0.9	4.3±0.4	···
5–3 S(3)	1.347	4.6±0.6	1.9±0.7 [a]	1.9±0.7[a]	···
4–2 Q(5) + 2–0 O(5)	1.429+1.432	7±2	7±1	···	···
3–1 Q(11)	1.448	···	3.3±0.8	···	···
5–3 Q(2) + 4–2 Q(9)	1.498+1.499	···	···	1.7±0.3	···
3–1 O(5)	1.522	4.1±0.6	5±2[a]	6±1	···
2–0 O(7)	1.546	2.7±0.7	···	3.1±0.6	···
5–3 O(2) + 5-3 Q(7)	1.561+1.563	···	···	1.4±0.5[a]	···
2–0 O(8) + 5–3 O(3)	1.610+1.613	···	···	3.1±0.9	···

Notes: [a]S/N between 2 and 3.

Table E.4: a) *(continued)* Observed lines in BHR71: HH320A/B and HH321A/B.

Term	$\lambda(\mu m)$	$F \pm \Delta F(10^{-15}$ erg cm^{-2} s$^{-1})$			
H_2 Lines		HH320 A	HH320 B	HH321 A	HH321 B
4–2 O(5)	1.622	···	···	2.8±0.2	···
3–1 O(7)	1.645	3±1	4±2[a]	6±2	···
1–0 S(11)	1.650	4±1	···	2.9±0.4	···
1–0 S(10)[2]	1.666	2.5±0.8	···	9±2	···
1–0 S(9)	1.688	13.2±0.8	9.8±0.4	19±1	···
1–0 S(8)	1.715	10±1	6±1	11±2	···
1–0 S(7)	1.748	47±1	32±2	54.9±0.9	4±1
1–0 S(6)	1.788	31±1	21±3	41.9±0.9	···
1–0 S(3)	1.958	99±6	78±2	150±2	24±2
2–1 S(4)	2.004	7.7±0.9	7±1	12±2	4±1
3–2 S(6)	2.013	1.3±0.6[a]	···	···	···
1–0 S(2)	2.034	48±1	39±1	74±2	10±2
3–2 S(5)	2.066	2.5±0.5	2.7±0.6	4±1	···
2–1 S(3)	2.073	21.8±0.8	13.9±0.6	33±1	···
1–0 S(1)	2.122	125±2	98±2	212±3	35±1
2–1 S(2)	2.154	7.9±0.9	5.4±0.4	15±1	···
3–2 S(3)	2.201	4.8±0.7	3.6±0.5	6.8±0.8	···
1–0 S(0)	2.223	29±1	22±1	48±2	10±1
2–1 S(1)	2.248	14±1	11.4±0.9	22±1	···
2–1 S(0)	2.355	6±1	4±2[a]	13±1	···
3–2 S(1)	2.386	···	···	3±1	···
1–0 Q(1)	2.407	83±1	79±4	148±3	40±1
1–0 Q(2)	2.413	41±4	36±4	73±3	17±2
1–0 Q(3)	2.424	95±3	80±4	179±7	43±3
1–0 Q(4)	2.437	38±4	31±4	66±3	···
1–0 Q(5)	2.455	43±4	33±4	85±3	···
1–0 Q(6)	2.476	23±5	···	40±5	···
1–0 Q(7)	2.500	40±8	···	47±5	···
0–0 S(13)	3.847	29±6	···	···	···

Notes: [a]S/N between 2 and 3.
[2]For HH321 A this line is also blended with the 2-0 O(9).

Table E.4: b). Observed lines in BHR71: condensations.

Term	$\lambda(\mu m)$	$F \pm \Delta F(10^{-15}$ erg cm^{-2} s$^{-1})$				
H_2 Lines		Knot 1	Knot 2	Knot3	Knot 4	Knot 5
2–0 S(9)	1.053	···	···	···	7±2	···
2–0 S(7)	1.064	···	···	5±2[a]	10±2	···
2–0 S(6)	1.073	···	···	···	5±2[a]	···
2–0 S(5)	1.085	···	···	8±2	11±2	···
2–0 S(4)	1.100	···	···	···	4±1	···
2–0 S(3)	1.117	···	···	7±2	10±2	···
2–0 S(2) +	1.138+	···	···	7±3[a]	8±3[a]	···
3–1 S(6)	1.140					
3–1 S(5)	1.152	···	···	6±3[a]	8±3[a]	···
2–0 S(1)	1.162	···	···	8±2	11±3	···
3–1 S(3)	1.186	···	···	···	7±1	···
2–0 S(0)	1.189	···	···	···	4±1	···
3–1 S(1)	1.233	···	···	···	3±1	···
2–0 Q(1)	1.238	···	···	5±2[a]	5±1	···
2–0 Q(3)	1.247	···	···	6±2	7±2	···
2–0 Q(5)	1.263	···	···	4±2[a]	6±2	···
2–0 Q(6)	1.274	···	···	···	4±2[a]	···
4–2 S(2) +	1.285+	···	···	···	5±2[a]	···
2–0 Q(7)	1.287					
3–1 Q(3)	1.324	···	···	···	3±1	···
3–1 Q(4) +	1.333+1.335	···	···	5±1	3±1	···
2–0 O(3)						
1–0 S(9)	1.688	···	···	2.9±0.9	3.4±0.5	···
1–0 S(8)	1.715	···	···	···	···	···

Notes: [a]S/N between 2 and 3.

Table E.4: (b) *(continued)* Observed lines in BHR71: condensations.

Term	$\lambda(\mu m)$	$F \pm \Delta F(10^{-15}$ erg cm^{-2} s$^{-1})$				
H_2 Lines		Knot 1	Knot 2	Knot3	Knot 4	Knot 5
1–0 S(7)	1.748	7±1	7.2±0.7	15±1	17±1	7±1
1–0 S(6)	1.788	7±2	3.4±0.6	11±2	13±2	5±2[a]
1–0 S(3)	1.958	32±2	15±2	59.1±0.9	58±2	12±2
2–1 S(4)	2.004	6±3[a]	···	···	···	···
1–0 S(2)	2.034	11.4±0.8	10±1	24±1	27±2	10±1
2–1 S(3)	2.073	···	4.2±0.6	5±1	6±1	5±1
1–0 S(1)	2.122	29.8±0.9	21.4±0.7	60±1	65±1	25.8±0.5
2–1 S(2)	2.154	···	···	···	···	···
1–0 S(0)	2.223	9.2±0.8	7±2	15±1	13.7±0.8	7±1
2–1 S(1)	2.248	···	···	7±1	7.7±0.8	4±1
1–0 Q(1)	2.407	28±2	19±1	57±2	50±4	17±1
1–0 Q(2)	2.413	15±4	6±1	24±2	17±4	7±2
1–0 Q(3)	2.424	26±2	17±1	53±2	47±4	20±1
1–0 Q(4)	2.437	···	7±2	22±3	18±4	9±3
1–0 Q(5)	2.455	···	···	13±4	13±3	12±4

Notes: [a]S/N between 2 and 3.

Table E.5: Observed lines in HH99 A.

Term	λ (μm)	$F \pm \Delta F$ (10^{-16} erg cm^{-2} s^{-1})
H_2 lines		
2–0 S(7)	1.064	8.1 ± 2.9[a]
2–0 S(6)	1.073	8.0 ± 4.0[a]
2–0 S(5)	1.085	8.5 ± 2.8
3–1 S(5)	1.152	3.6 ± 1.6[a]
2–0 S(1)	1.162	6.6 ± 2.2
2–0 Q(7)	1.287	4.3 ± 1.1
1–0 S(9)	1.688	5.7 ± 2.2[a]
1–0 S(7) + [Fe II] $a^4P_{3/2} - a^4D_{7/2}$	1.748+1.749	27.6 ± 2.6
1–0 S(6)	1.788	18.4 ± 2.8
1–0 S(3)	1.958	246.0 ± 8.7
2–1 S(4)	2.004	6.6 ± 1.8
1–0 S(2)	2.034	62.2 ± 2.2
2–1 S(3)	2.073	12.0 ± 1.8
1–0 S(1)	2.122	163.2 ± 2.4
2–1 S(2)	2.154	7.8 ± 1.2
1–0 S(0)	2.223	42.3 ± 1.1
2–1 S(1)	2.248	17.7 ± 1.3
2–1 S(0)	2.355	12.0 ± 4.4[a]
1–0 Q(1)	2.407	187.1 ± 3.8
1–0 Q(2)	2.413	75.4 ± 4.1
1–0 Q(3)	2.424	169.0 ± 4.6
1–0 Q(4)	2.437	52.3 ±10.7
Atomic and Ionic lines		
[C I] $^1D_2 - ^3P_1$	0.983	23.9 ± 4.6
[C I] $^1D_2 - ^3P_2$	0.985	71.4 ± 4.6
[S II] $^2P_{3/2} - ^2D_{3/2}$	1.029	7.4 ± 1.5
[S II] $^2P_{3/2} - ^2D_{5/2}$	1.032	4.6 ± 1.3
[Fe II] $a^4D_{7/2} - a^6D_{9/2}$	1.257	50.4 ± 1.5
[Fe II] $a^4D_{7/2} - a^6D_{7/2}$	1.321	18.6 ± 1.8
[Fe II] $a^4D_{7/2} - a^4F_{9/2}$	1.644	58.6 ± 2.2
[Fe II] $a^4D_{5/2} - a^4F_{7/2}$	1.678	4.8 ± 1.6
[Fe II] $a^4D_{7/2} - a^4F_{7/2}$ + [Fe II] $a^4P_{5/2} - a^4D_{7/2}$	1.810+1.811	20.1 ± 6.5

Notes: [a]S/N between 2 and 3.

Table E.6: Observed lines in HH99 B0.

Term	λ (μm)	$F \pm \Delta F$ (10^{-16} erg cm^{-2} s^{-1})
H_2 lines		
2–0 S(9)	1.053	4.9 ± 2.0[a]
2–0 S(7)	1.064	13.4 ± 2.7
2–0 S(6)	1.073	7.4 ± 1.9
2–0 S(5)	1.085	17.6 ± 2.3
2–0 S(4)	1.100	9.1 ± 4.0[a]
3–1 S(5)	1.152	6.4 ± 1.3
2–0 S(1)	1.162	5.6 ± 1.2
3–1 S(4)	1.167	3.7 ± 1.2
3–1 S(3)	1.186	5.4 ± 2.0[a]
2–0 S(0)	1.189	3.6 ± 1.1
3–1 S(2)	1.207	3.4 ± 1.4[a]
4–2 S(6)	1.214	3.2 ± 1.2[a]
4–2 S(5)	1.226	3.9 ± 1.2
3–1 S(1)	1.233	5.7 ± 0.7
2–0 Q(1)	1.238	4.6 ± 1.0
2–0 Q(2) + 4-2S(4)	1.242+1.242	3.6 ± 0.8
2–0 Q(3) + [Fe II] $a^4D_{3/2} - a^6D_{5/2}$	1.247+1.248	4.0 ± 1.4[a]
2–0 Q(4)	1.254	2.9 ± 0.6
4–2 S(3) + 3-1S(0)	1.261+1.262	6.7 ± 1.2
2–0 Q(5)	1.263	5.2 ± 1.7
2–0 Q(7)	1.287	5.2 ± 0.9
4–2 S(1)	1.311	5.0 ± 1.8[a]
2–0 O(3)	1.335	5.7 ± 1.3
3–1 Q(5) + 4-2S(0)	1.342+1.342	5.9 ± 1.2
1–0 S(9)	1.688	14.2 ± 2.0
1–0 S(8)	1.715	12.1 ± 1.8
1–0 S(7) + [Fe II] $a^4P_{3/2} - a^4D_{7/2}$	1.748+1.749	47.5 ± 1.4

Notes: [a]S/N between 2 and 3.

Table E.6: *(continued)* Observed lines in HH99 B0.

Term	λ (μm)	$F \pm \Delta F$ (10^{-16} erg cm^{-2} s^{-1})
H_2 lines		
1–0 S(6)	1.788	34.6 ± 1.3
1–0 S(3)	1.958	199.6 ± 6.5
1–0 S(2)	2.034	61.0 ± 1.8
3–2 S(5)	2.066	7.2 ± 1.4
2–1 S(3)	2.073	18.3 ± 1.4
1–0 S(1)	2.122	147.4 ± 1.4
3–2 S(4)	2.127	4.5 ± 0.7
2–1 S(2)	2.154	13.1 ± 1.4
3–2 S(3)	2.201	8.5 ± 1.4
1–0 S(0)	2.223	48.8 ± 1.1
2–1 S(1)	2.248	26.6 ± 1.2
3–2 S(2)	2.287	7.0 ± 1.2
2–1 S(0)	2.355	14.2 ± 1.3
1–0 Q(1)	2.407	212.4 ± 4.3
1–0 Q(2)	2.413	84.7 ± 4.3
1–0 Q(3)	2.424	209.5 ± 4.3
1–0 Q(4)	2.437	67.1 ± 4.1
1–0 Q(5)	2.455	54.5 ± 4.9
1–0 Q(6)	2.476	48.9 ±11.7
1–0 Q(7)	2.500	140.8 ±15.0

Notes: [a]S/N between 2 and 3.

Table E.6: *(continued)* Observed lines in HH99 B0.

Term	λ (μm)	$F \pm \Delta F$ (10^{-16} erg cm^{-2} s^{-1})
Atomic and Ionic lines		
[C I] $^1D_2 - ^3P_1$ + [C I] $^1D_2 - ^3P_2$	0.983+0.985	66.1 ± 5.6
[S II] $^2P_{3/2} - ^2D_{3/2}$	1.029	10.3 ± 1.7
[S II] $^2P_{3/2} - ^2D_{5/2}$	1.032	9.5 ± 1.2
[S II] $^2P_{3/2} - ^2D_{3/2}$	1.034	5.6 ± 1.0
[N I] $^2P_{3/2,1/2} - ^2D_{5/2}$ + [N I] $^2P_{3/2,1/2} - ^2D_{3/2}$	1.040+1.041	11.4 ± 2.2
He I $^3S_1 - ^3P^o_{0,1,2}$	1.083	7.9 ± 2.1
[Fe II] $a^4D_{7/2} - a^6D_{9/2}$	1.257	119.1 ± 1.0
[Fe II] $a^4D_{1/2} - a^6D_{1/2}$	1.271	8.1 ± 1.7
[Fe II] $a^4D_{3/2} - a^6D_{3/2}$	1.279	10.5 ± 2.9
Paβ	1.282	4.8 ± 2.0[a]
[Fe II] $a^4D_{5/2} - a^6D_{5/2}$	1.295	16.6 ± 1.8
[Fe II] $a^4D_{3/2} - a^6D_{1/2}$	1.298	4.7 ± 1.0
[Fe II] $a^4D_{7/2} - a^6D_{7/2}$	1.321	41.0 ± 1.8
[Fe II] $a^4D_{5/2} - a^6D_{3/2}$	1.328	10.3 ± 2.0
[Fe II] $a^4D_{5/2} - a^4F_{9/2}$	1.534	19.4 ± 1.5
[Fe II] $a^4D_{3/2} - a^4F_{7/2}$	1.600	11.0 ± 2.1
[Fe II] $a^4D_{7/2} - a^4F_{9/2}$	1.644	133.9 ± 1.5
[Fe II] $a^4D_{5/2} - a^4F_{7/2}$	1.678	12.3 ± 2.4
[Fe II] $a^4D_{3/2} - a^4F_{5/2}$	1.711	5.2 ± 1.8[a]
[Fe II] $a^4D_{1/2} - a^4F_{3/2}$	1.745	8.2 ± 1.9
[Fe II] $a^4D_{3/2} - a^4F_{3/2}$	1.798	6.4 ± 2.7[a]
[Fe II] $a^4D_{7/2} - a^4F_{7/2}$ + [Fe II] $a^4P_{5/2} - a^4D_{7/2}$	1.810+1.811	36.9 ± 3.8

Notes: [a]S/N between 2 and 3.

Table E.7: Observed lines in HH99 B1 (slit 1).

Term	λ (μm)	$F \pm \Delta F$ (10^{-16} erg cm^{-2} s^{-1})
H_2 lines		
2–0 S(7)	1.064	12.2 ± 2.2
2–0 S(5)	1.085	12.1 ± 2.1
3–1 S(8)	1.124	2.8 ± 0.9
2–0 S(2)	1.130	8.5 ± 2.8
3–1 S(7)	1.138	6.4 ± 1.9
3–1 S(5)	1.152	10.7 ± 2.5
2–0 S(1)	1.162	15.4 ± 3.5
3–1 S(3)	1.186	7.8 ± 2.0
2–0 S(0)	1.189	5.1 ± 1.8[a]
3–1 S(2)	1.207	3.7 ± 1.0
4–2 S(5)	1.226	4.4 ± 1.7[a]
3–1 S(1)	1.233	7.9 ± 2.0
2–0 Q(1)	1.238	10.2 ± 2.8
2–0 Q(2) + 4-2S(4)	1.242+1.242	5.6 ± 1.6
2–0 Q(3)	1.247	9.0 ± 1.8
2–0 Q(4)	1.254	2.9 ± 0.7
4–2 S(3) + 3-1S(0)	1.261+1.262	5.2 ± 0.9
2–0 Q(5)	1.263	4.6 ± 0.8
3–1 Q(5) + 4-2S(0)	1.342+1.342	7.4 ± 0.6
3–1 Q(7)	1.368	6.6 ± 2.4[a]
1–0 S(9)	1.688	15.9 ± 2.6
1–0 S(8)	1.715	16.6 ± 3.1
1–0 S(7)	1.748	52.2 ± 4.0
1–0 S(6)	1.788	52.4 ± 2.5
1–0 S(3)	1.958	456.5 ± 7.1

Notes: [a]S/N between 2 and 3.

Table E.7: *(continued)* Observed lines in HH99 B1 (slit 1).

Term	λ (μm)	$F \pm \Delta F$ (10^{-16} erg cm^{-2} s^{-1})
H_2 lines		
2–1 S(4)	2.004	11.3 ± 2.5
1–0 S(2)	2.034	128.3 ± 1.9
2–1 S(3)	2.073	24.6 ± 2.4
1–0 S(1)	2.122	280.5 ± 1.6
3–2 S(4)	2.127	4.2 ± 1.9[a]
2–1 S(2)	2.154	21.1 ± 1.5
3–2 S(3)	2.201	7.0 ± 1.8
1–0 S(0)	2.223	74.2 ± 1.5
2–1 S(1)	2.248	25.8 ± 5.8
2–1 S(0)	2.355	12.3 ± 2.4
3–2 S(1)	2.386	9.7 ± 2.2
1–0 Q(1)	2.407	287.4 ±10.0
1–0 Q(2)	2.413	125.0 ±10.2
1–0 Q(3)	2.424	246.9 ± 9.4
1–0 Q(4)	2.437	94.8 ±10.2
1–0 Q(5)	2.455	58.5 ± 9.9
1–0 Q(6)	2.476	71.7 ±8.9
1–0 Q(7)	2.500	212.5 ±28.6
Atomic and ionic lines		
[C I] $^1D_2 - ^3P_1$ + [C I] $^1D_2 - ^3P_2$	0.983+0.985	30.6 ±10.0
[Fe II] $a^4D_{7/2} - a^6D_{9/2}$	1.257	27.0 ± 1.0
[Fe II] $a^4D_{5/2} - a^4F_{9/2}$	1.534	9.5 ± 1.7
[Fe II] $a^4D_{7/2} - a^4F_{9/2}$	1.644	38.3 ± 3.8

Notes: [a]S/N between 2 and 3.

Table E.8: Observed lines in HH99 B1 (slit 2).

Term	λ (μm)	$F \pm \Delta F$ (10^{-16} erg cm^{-2} s^{-1})
H_2 lines		
2–0 S(3)	1.117	8.9 ± 1.9
3–1 S(9) + 3-1S(10) + 3-1S(11)	1.120+1.120+1.121	8.5 ± 2.2
3–1 S(8)	1.124	5.5 ± 1.7
3–1 S(7)	1.130	7.9 ± 1.8
2–0 S(2)	1.138	4.7 ± 1.1
3–1 S(6)	1.140	6.1 ± 1.2
3–1 S(5)	1.152	8.6 ± 1.3
2–0 S(1)	1.162	7.7 ± 2.0
3–1 S(3)	1.186	5.4 ± 0.9
2–0 S(0)	1.189	5.1 ± 1.7
4–2 S(5)	1.226	3.6 ± 1.2
3–1 S(1)	1.233	3.7 ± 1.4[a]
2–0 Q(1)	1.238	6.1 ± 1.6
2–0 Q(3)	1.247	5.3 ± 1.4
2–0 Q(4)	1.254	2.9 ± 0.6
4–2 S(3) + 3-1S(0)	1.261+1.262	4.8 ± 1.3
2–0 Q(5)	1.263	3.3 ± 1.2[a]
2–0 O(3)	1.335	4.1 ± 1.4
3–1 Q(5) + 4-2S(0)	1.342+1.342	4.7 ± 1.4
1–0 S(9)	1.688	13.1 ± 2.3
1–0 S(8)	1.715	12.1 ± 3.0
1–0 S(7)	1.748	36.7 ± 2.7
1–0 S(6)	1.788	21.0 ± 2.6
1–0 S(3)	1.958	119.0 ± 1.7

Notes: [a]S/N between 2 and 3.

Table E.8: *(continued)* Observed lines in HH99 B1 (slit 2).

Term	λ (μm)	$F \pm \Delta F$ (10^{-16} erg cm^{-2} s^{-1})
H_2 lines		
1–0 S(2)	2.034	39.1 ± 0.9
2–1 S(3)	2.073	9.5 ± 1.6
1–0 S(1)	2.122	102.0 ± 0.7
2–1 S(2)	2.154	4.3 ± 0.6
1–0 S(0)	2.223	28.5 ± 1.2
2–1 S(1)	2.248	14.4 ± 1.0
2–1 S(0)	2.355	8.1 ± 2.1
1–0 Q(1)	2.407	114.0 ± 3.4
1–0 Q(2)	2.413	48.8 ± 3.9
1–0 Q(3)	2.424	106.0 ± 4.1
1–0 Q(4)	2.437	61.0 ± 5.7
1–0 Q(5)	2.455	26.2 ± 4.9
Atomic and Ionic lines		
[Fe II] $a^4D_{3/2} - a^6D_{5/2}$	1.248	4.4 ± 1.6[a]
[Fe II] $a^4D_{7/2} - a^6D_{9/2}$	1.257	34.0 ± 1.6
[Fe II] $a^4D_{7/2} - a^6D_{7/2}$	1.321	9.8 ± 1.4
[Fe II] $a^4D_{5/2} - a^4F_{9/2}$	1.534	4.9 ± 2.1[a]
[Fe II] $a^4D_{7/2} - a^4F_{9/2}$	1.644	48.9 ± 2.2
[Fe II] $a^4D_{5/2} - a^4F_{7/2}$	1.678	5.3 ± 2.3[a]
[Fe II] $a^4D_{3/2} - a^4F_{5/2}$	1.711	7.5 ± 2.4
[Fe II] $a^4D_{1/2} - a^4F_{3/2}$	1.745	7.8 ± 2.3
[Fe II] $a^4D_{7/2} - a^4F_{7/2}$ + [Fe II] $a^4P_{5/2} - a^4D_{7/2}$	1.810+1.811	10.2 ± 2.4

Notes: [a]S/N between 2 and 3.

Table E.9: Observed lines in HH99 B2.

Term	λ (μm)	$F \pm \Delta F$ (10^{-16} erg cm^{-2} s^{-1})
H_2 lines		
2–0 S(3)	1.117	2.8 ± 0.8
3–1 S(9) + 3-1S(10) + 3-1S(11)	1.120+1.120+1.121	2.6 ± 0.8
3–1 S(7)	1.130	4.6 ± 0.9
2–0 S(2)	1.138	3.2 ± 0.8
3–1 S(5)	1.152	3.2 ± 0.9
2–0 S(1)	1.162	4.7 ± 1.2
3–1 S(3)	1.186	4.6 ± 1.1
4–2 S(5)	1.226	2.0 ± 0.9[a]
3–1 S(1)	1.233	2.3 ± 1.1[a]
2–0 Q(1)	1.238	3.1 ± 1.1[a]
2–0 Q(3)	1.247	4.6 ± 1.1
4–2 S(3) + 3-1S(0)	1.261+1.262	2.7 ± 0.8
2–0 Q(7)	1.287	3.5 ± 0.7
2–0 O(3)	1.335	2.3 ± 0.6
1–0 S(9)	1.688	9.4 ± 3.0
1–0 S(8)	1.715	7.3 ± 1.7
1–0 S(7) + [Fe II] $a^4P_{3/2} - a^4D_{7/2}$	1.748+1.749	22.4 ± 1.9
1–0 S(6)	1.788	17.1 ± 1.7
1–0 S(3)	1.958	68.0 ± 1.1
2–1 S(4)	2.004	3.7 ± 1.4[a]
1–0 S(2)	2.034	23.3 ± 1.2
2–1 S(3)	2.073	6.2 ± 1.2

Notes: [a]S/N between 2 and 3.

Table E.9: *(continued)* Observed lines in HH99 B2.

Term	λ (μm)	$F \pm \Delta F$ (10^{-16} erg cm^{-2} s^{-1})
H_2 lines		
1–0 S(1)	2.122	63.4 ± 1.1
3–2 S(4)	2.127	1.4 ± 0.5[a]
2–1 S(2)	2.154	4.6 ± 1.1
3–2 S(3)	2.201	3.7 ± 1.3[a]
1–0 S(0)	2.223	20.0 ± 1.1
2–1 S(1)	2.248	10.8 ± 1.2
2–1 S(0)	2.355	4.8 ± 1.3
1–0 Q(1)	2.407	105.0 ± 3.6
1–0 Q(2)	2.413	43.6 ± 3.5
1–0 Q(3)	2.424	106.0 ± 3.5
1–0 Q(4)	2.437	45.6 ± 4.0
1–0 Q(5)	2.455	19.9 ± 3.4
1–0 Q(6)	2.476	37.5 ±16.8
Atomic and Ionic lines		
[Fe II] $a^4D_{7/2} - a^6D_{9/2}$	1.257	32.1 ± 0.8
[Fe II] $a^4D_{5/2} - a^6D_{5/2}$	1.295	3.0 ± 1.0
[Fe II] $a^4D_{7/2} - a^6D_{7/2}$	1.321	10.8 ± 0.9
[Fe II] $a^4D_{5/2} - a^6D_{3/2}$	1.328	1.9 ± 0.6
[Fe II] $a^4D_{5/2} - a^4F_{9/2}$	1.534	7.1 ± 1.3
[Fe II] $a^4D_{3/2} - a^4F_{7/2}$	1.600	3.2 ± 1.1[a]
[Fe II] $a^4D_{7/2} - a^4F_{9/2}$	1.644	43.5 ± 1.2
[Fe II] $a^4D_{1/2} - a^4F_{5/2}$	1.664	5.1 ± 1.3
[Fe II] $a^4D_{5/2} - a^4F_{7/2}$	1.678	8.8 ± 2.4
[Fe II] $a^4D_{3/2} - a^4F_{5/2}$	1.711	4.1 ± 1.9[a]
[Fe II] $a^4D_{7/2} - a^4F_{7/2}$ + [Fe II] $a^4P_{5/2} - a^4D_{7/2}$	1.810+1.811	36.9 ± 3.8

Notes: [a]S/N between 2 and 3.

Table E.10: Observed lines in HH99 B3.

Term	λ (μm)	$F \pm \Delta F$ (10^{-16} erg cm^{-2} s^{-1})
H_2 lines		
3–1 S(5)	1.152	7.2 ± 2.0
2–0 S(1)	1.162	10.0 ± 1.2
3–1 S(4)	1.169	3.9 ± 1.2
3–1 S(3)	1.186	3.9 ± 0.9
2–0 S(0)	1.189	2.8 ± 0.8
4–2 S(5)	1.226	4.6 ± 1.2
3–1 S(1)	1.233	5.5 ± 1.2
2–0 Q(1)	1.238	6.8 ± 1.9
2–0 Q(3)	1.247	3.5 ± 0.7
2–0 Q(4)	1.254	1.7 ± 0.6[a]
4–2 S(3) + 3-1S(0)	1.261+1.262	4.8 ± 1.0
2–0 Q(5)	1.263	4.8 ± 1.1
4–2 S(2)	1.285	3.4 ± 1.6[a]
2–0 Q(7)	1.287	5.7 ± 1.8
4–2 S(1)	1.311	5.6 ± 2.3[a]
3–1 Q(1)	1.314	5.3 ± 2.0[a]
2–0 O(3)	1.335	4.6 ± 1.3
3–1 Q(5) + 4-2S(0)	1.342+1.342	3.8 ± 1.2
1–0 S(9)	1.688	12.5 ± 3.0
1–0 S(8)	1.715	9.7 ± 1.8
1–0 S(7) + [Fe II] $a^4P_{3/2} - a^4D_{7/2}$	1.748+1.749	39.5 ± 3.4
1–0 S(6)	1.788	29.7 ± 2.7
1–0 S(3)	1.958	103.0 ± 6.1
2–1 S(4)	2.004	4.1 ± 1.3
1–0 S(2)	2.034	37.7 ± 1.8
3–2 S(5)	2.065	5.9 ± 2.2[a]
2–1 S(3)	2.073	13.1 ± 1.6
1–0 S(1)	2.122	120.0 ± 1.1
2–1 S(2)	2.154	9.8 ± 0.8
3–2 S(3)	2.201	8.0 ± 2.6
1–0 S(0)	2.223	39.9 ± 1.5

Notes: [a]S/N between 2 and 3.

Table E.10: *(continued)* Observed lines in HH99 B3.

Term	λ (μm)	$F \pm \Delta F$ (10^{-16} erg cm^{-2} s^{-1})
H_2 lines		
2–1 S(1)	2.248	26.4 ± 1.2
3–2 S(2)	2.287	5.2 ± 1.8[a]
2–1 S(0)	2.355	13.0 ± 2.3
3–2 S(1)	2.386	9.7 ± 1.9
1–0 Q(1)	2.407	223.3 ± 3.6
1–0 Q(2)	2.413	93.1 ± 3.8
1–0 Q(3)	2.424	221.1 ± 3.4
1–0 Q(4)	2.437	89.3 ± 3.6
1–0 Q(5)	2.455	36.8 ± 3.4
1–0 Q(6)	2.476	111.2 ± 9.0
Atomic and Ionic lines		
[Fe II] $a^4D_{3/2} - a^6D_{5/2}$	1.248	3.2 ± 0.7
[Fe II] $a^4D_{7/2} - a^6D_{9/2}$	1.257	20.6 ± 0.9
[Fe II] $a^4D_{1/2} - a^6D_{1/2}$	1.271	7.1 ± 1.2
[Fe II] $a^4D_{3/2} - a^6D_{3/2}$	1.279	5.9 ± 1.1
[Fe II] $a^4D_{7/2} - a^6D_{7/2}$	1.321	13.5 ± 1.7
[Fe II] $a^4D_{7/2} - a^4F_{9/2}$	1.644	41.0 ± 0.5

Notes: [a]S/N between 2 and 3.

Appendix F

The Orion molecular cloud outflow

The Orion Molecular Cloud, OMC-1, is, at a distance of approximately 450 pc (Genzel & Stutzki, 1989), the nearest and best studied region currently undergoing massive star formation. A photodissociation region (PDR) is sandwiched between the molecular cloud and a blister H II region, which lies to the edge of OMC-1. Both the PDR and the H II region are excited by the photoionizing stars in the Trapezium, which is located in front of OMC-1. Partially ionized globules and edge-on photoionization fronts are associated with the Trapezium (Hester et al., 1991; O'Dell et al., 1991). Within the molecular cloud, in the region of the Becklin-Neugebauer object (BN) (Menten & Reid, 1995), lie several highly luminous and deeply embedded proto-stellar sources. One of these sources, the radio source "I", $\approx$ 8" south east of BN, is associated with the energetic Orion molecular outflow.

Rosenthal et al. (2000) used the Short-Wavelength-Spectrometer on the Infrared Space Observatory (ISO) to obtain near- and mid-spectra toward the brightest H_2 emission peak (Peak 1) of the Orion molecular cloud (OMC-1) outflow. The observations were centred on a point in Peak 1 with an aperture of 14″ x 20″ for $\lambda < 12$ μm, 14″ $\times$ 27″ at 12–27.5 μm, 20″ $\times$ 27″ at 27.5–29 μm and 20″ $\times$ 33″ at 29–45.2 μm. In addition to 56 H_2 ro-vibrational and

pure rotational lines, they detected H I recombination lines, atomic and ionic fine structure lines (including the [Si II] 34.8 μm and [Fe II] 17.936, 25.988 and 35.777 μm lines), molecular lines of CO and H_2O and PAH features. Such emission is typical of that expected from the shocks associated with outflows and Le Bourlot et al. (2002) successfully modelled the H_2 emission with a two component (40 and 60 km s^{-1}) C-type shock model. However, they found that this model underestimated the observed intensity of the 34.8 μm [Si II] transition by some five orders of magnitude. They suggested that the [Si II] observations may, at least partly, be a result of contributions from regions other than the shocked gas. Here, an attempt is made to model the [Fe II] lines in order to investigate this theory further. In the next Section the models used and the results from them are described the models used and give our results; in Section F.0.2 the results are discussed and in the final Section of this Chapter these findings are summarised.

F.0.1 Model and Results

In the work presented below, only C-type shock models were used (at the time the work was carried out the code had not been adapted to model J-type shocks with magnetic precursors). Both electrons and neutral perturbers (H_2, H and He) were considered in the excitation model for Fe^+. Subsequent work showed that perturbers are inefficient at exciting Fe^+ because electron spin conservation (assuming LS coupling) means that only H and electrons can excite Fe^+ out of the ground state a^6D term, in which most of the Fe^+ population is assumed to initially reside (see Chapter 3 and Appendix C.1 for further detail).

The [Fe II] line intensities observed by Rosenthal et al. (2000) are labelled as I_{obs} and are given in the first row of Table F.1, where [Fe II] intensities predicted by several shock models are also presented. The shock models used by Le Bourlot et al. (2002) ($n_{\rm H} = 10^4$ cm^{-3}, B=100 μG, $v_{\rm s} = 40$ and 60 km s^{-1}) produced [Fe II] line intensities (labelled I^1 and I^2 in rows 2 and 3 of Table

F.1) that are much smaller than those observed. Experimentation with shock parameters indicated the model that best fit the [Fe II] observations was a 54 km s^{-1} C-type shock with an initial density of $n_H = 10^5$ cm^{-3} and magnetic field of B=400 μG: the intensities from this model are labelled as I^3 and are given in row 4 of Table F.1. However, this model still could not reproduce the observations, especially the 25.988 and 35.777 μm lines. Of particular concern was the fact that the 35.777 μm line was so poorly reproduced, while the 17.936 μm transition agreed to within a factor of two with the observations. The upper levels of these two transitions are only 0.09 eV apart (see Figure 3.1, page 51, Chapter 3).

Table F.1: Comparison between shock models and observations of [Fe II] line intensities. The last two rows present the calculated intensities for v_s = 54 km s^{-1} models in which the new Fe-chemistry (I_{Fe}) has been removed and in which PAHs are destroyed in the shock (I_{PAH}), respectively (see Section F.0.2).

λ (μm)	17.936	25.988	35.777
term	$a^4F_{9/2} - a^4F_{7/2}$	$a^6D_{9/2} - a^6D_{7/2}$	$a^4F_{5/2} - a^4F_{3/2}$
I_{obs}	2.56x10^{-4}	3.70x10^{-3}	1.22x10^{-3}
I^1	1.82x10^{-5}	5.68x10^{-5}	1.56x10^{-6}
I^2	8.23x10^{-8}	1.66x10^{-6}	5.15x10^{-9}
I^3	1.83x10^{-4}	2.76x10^{-4}	1.28x10^{-5}
I^3_{Fe}	2.09x10^{-4}	3.14x10^{-4}	1.47x10^{-5}
I^3_{PAH}	1.98x10^{-4}	4.08x10^{-4}	1.36x10^{-5}

Notes:
[1] v_s=60 km s^{-1}, $n_H = 10^4$ cm^{-3}, B=100 μG
[2] v_s=40 km s^{-1}, $n_H = 10^4$ cm^{-3}, B=100 μG
[3] v_s=54 km s^{-1}, $n_H = 10^5$ cm^{-3}, B=400 μG
All intensities in erg s^{-1} cm^{-2} sr^{-1}

F.0.2 Discussion

It is important to understand, first of all, why the observations of the [Fe II] lines could not be reproduced and, secondly, why the 35.777 μm transition is so poorly modelled in comparison to the 17.936 μm line. Several possible

solutions were considered, which are dealt with case-by-case below. From here on only the 54 km s^{-1} shock model, and modifications to it, are considered.

Statistical Equilibrium

Although it is an unlikely scenario, if the gas were not in statistical equilibrium it is possible that the population in the $a^4F_{5/2}$ term could be significantly less than in the $a^4F_{9/2}$ term, giving rise to the weaker intensity predicted for the 35.777 μm line. Statistical equilibrium can be tested for by checking that the length scale for a collision between Fe^+ and, the most abundant collision partner, H_2, is less than the width of the shock. At the peak of the shock, v_i=7.9 $\times 10^5$ cm s^{-1}, $n(H_2)$=2.44 $\times 10^4$ and the rate for deexcitation of Fe^+ by H_2 is 7.34 $\times 10^{-10}$ cm^3 s^{-1}, which gives L=4.4$\times 10^{10}$ cm. The width of the shock is of order 3 $\times 10^{15}$ cm, see Fig. F.1, so as expected, this possible solution is discounted.

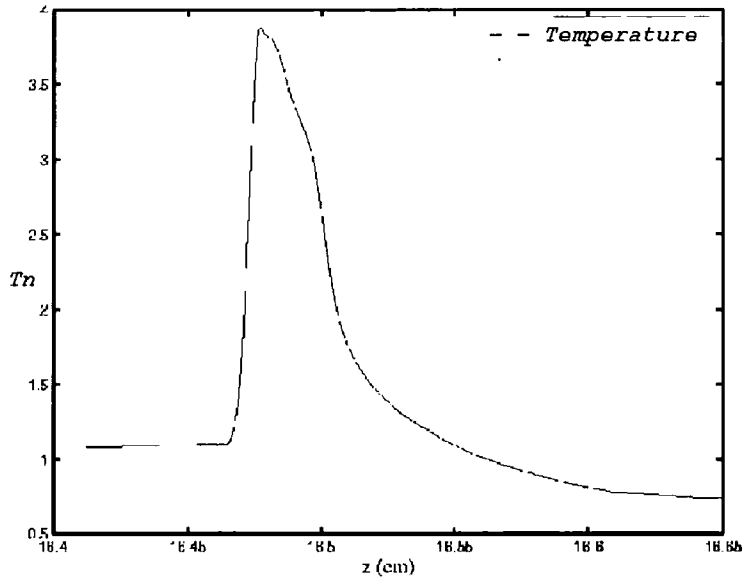

Figure F.1: Neutral temperature profile for the 54 km s^{-1} shock with initial $n_H = 10^5$ cm^{-3} and B=400 μG. The shock width is $\approx 3\times 10^{15}$ cm.

Iron Chemistry

A rudimentary FeO-producing chemistry (G. P. des Forêts, private communication) was included in the model prior to this work:

Neutral reactions:

$Fe + O_2 \rightarrow FeO + O$	$k = 2.1 \times 10^{-10}$ exp[-10200/T_n] cm^3 s^{-1}
$Fe + H_2O \rightarrow FeO + H_2$	$k = 1.0 \times 10^{-10}$ exp[-9300/T_n] cm^3 s^{-1}
$Fe + OH \rightarrow FeO + H$	$k = 1.0 \times 10^{-10}$ exp[-1550/T_n] cm^3 s^{-1}
$FeO + H_2 \rightarrow FeOH + H$	$k = 1.0 \times 10^{-10}$ exp[-12000/T_n] cm^3 s^{-1}

Ion neutral reactions:

$H_3^+ + FeO \rightarrow FeOH^+ + H_2$	$k = 2.0 \times 10^{-9}$ cm^3 s^{-1}
$He^+ + FeO \rightarrow Fe^+ + O + He$	$k = 1.7 \times 10^{-9}$ cm^3 s^{-1}
$FeOH^+ + e^- \rightarrow FeO + H$	$k = 3.0 \times 10^{-7} (T_e/300)^{-0.5}$ cm^3 s^{-1}
$FeOH^+ + e^- \rightarrow Fe + OH$	$k = 3.0 \times 10^{-7} (T_e/300)^{-0.5}$ cm^3 s^{-1}

However, the rates used are somewhat uncertain. Therefore, the Fe and Fe^+ abundances were calculated with and without this chemistry in order to investigate its impact on the results. In Figure F.2 the abundances of Fe and Fe^+ are plotted for the cases where the FeO-producing chemistry is included in the model and where it is not. The FeO-producing chemistry results in the formation of Fe-bearing molecules (FeO, FeOH, $FeOH^+$) and a post-shock abundance of Fe plus Fe^+ that is 10% of the elemental (total) abundance of Fe. Removing the Fe-chemistry doubles the abundance of Fe plus Fe^+ in the post-shock gas to 20% of the total Fe abundance. However, this has little effect on our comparison with the observations, see row 5 in Table F.1.

Ionization of Fe

Fe is ionized in the shock via charge transfer reactions with ions, such as H^+. It is expected that in the post-shock gas $n(Fe^+) \gg n(Fe)$, it is often assumed that the post-shock iron is fully ionized; however, the model finds that most of the iron remains in its neutral form, see Fig. F.2. This is a possible explanation for the small intensities of the [Fe II] lines in relation to the observations and

so a few ways in which the post-shock abundance of Fe^+ can be increased are considered.

I *Length Scale*

Inspection of the abundance profiles of Fe and Fe^+, see Fig. F.2, show that the conversion of Fe to Fe^+ is not completed over the shock. In order to check that this is consistent with the profile (e.g., density) predicted by the shock model, the scale length, L, of the Fe to Fe^+ reactions is calculated and compared to the shock width.

$$L = \frac{v_n}{kn_e}, \tag{F.1}$$

The neutral velocity, v_n, at the peak of the shock is 4.89 $\times 10^6$ cm s^{-1}; the rate coefficient, k, for the charge transfer reaction is of the order 10^{-9} cm^3 s^{-1}. As many ions, including H^+ (the most abundant ion) are involved in this process, the total ion density, which is equal to the electron density, n_e, may be used. Inserting these values into F.1 gives a scale length of, $L \approx 2 \times 10^{16}$ cm. As can be seen from Fig. F.1, the width of the shock is approximately 3 $\times 10^{15}$ cm; therefore Fe cannot be fully converted to Fe^+ via charge transfer reactions over the width of this shock.

II *Availability of Ions*

The charge transfer reactions take the form of

$$X^+ + Fe \rightarrow X + Fe^+,$$

where X^+ is the ion (for example, H^+, H_3^+ and H_3O^+). If these ions are not available (or very scarce) then the charge transfer reaction will not occur (or will occur very slowly). In Table F.2 the pre- and post-shock values of the summed relative abundances of the ions involved in the Fe to Fe^+ charge transfer reactions are listed, along with the relative abundances of Fe and Fe^+.

There it can be seen that some 98% of the ions are neutralised through the conversion of Fe to Fe^+ and other reactions during the shock compression. The post-shock abundance of Fe is 3 orders of magnitude greater than that of Fe^+ and so even if the remaining 2% of ions were used to convert Fe to Fe^+ a greater post-shock abundance of Fe^+ then Fe would still not result. Therefore, whilst the length scale of the Fe to Fe^+ charge transfer reaction is greater than the width of the shock it seems likely that the neutralisation of ions is the primary reason for the cessation of the Fe to Fe^+ charge transfer reactions, and hence the small $n(Fe^+)/n(Fe)$ ratio in the post-shock gas.

Table F.2: Pre- and post-shock relative abundances of Fe, Fe^+ and the summed contributions of the ions involved in the Fe to Fe^+ charge transfer reactions.

Species	Pre-shock Relative Abundances	Post-shock Relative Abundances
Ions	1.28×10^{-8}	2.54×10^{-10}
Fe^+	4.10×10^{-10}	3.78×10^{-9}
Fe	1.45×10^{-8}	2.94×10^{-6}

III *PAHs*

Polycyclic aromatic hydrocarbons (PAHs) are very large molecules and it is not unreasonable to assume that, if the shock is sufficient to destroy or partially destroy grains, then PAHs may also be destroyed in the shock.

In a C-type shock wave, the rate at which PAHs neutralise Fe^+, through ion-neutral and ion-ion reactions (see Section 3.2.2 in Chapter 3), is greater than the rate of electron recombination, which is the only other reaction to convert Fe^+ to Fe. Therefore, reactions with PAHs are the dominant mechanism for neutralising Fe^+. If the PAHs were destroyed in the shock then significantly less Fe^+ would be converted back into Fe, resulting in an increase in the degree of ionization of the gas.

The destruction of PAHs in the shock was very crudely modelled by removing the PAHs from the calculation. In order to maintain the overall $n(C)/n_{\rm H}$ ratio, the carbon that had been removed from the gas in the form of PAHs was assumed instead to be bound in the grain cores. It was found that the 'destruction' of PAHs in the shock increased the amount of Fe^+ in the post-shock gas, but not to a higher abundance than Fe, see Fig. F.2. The shock is also narrowed because, as stated above, the removal of PAHs acts to increase the ionization of the gas, which leads to an increased coupling between the neutral and charged fluids (des Forêts et al., 1988).

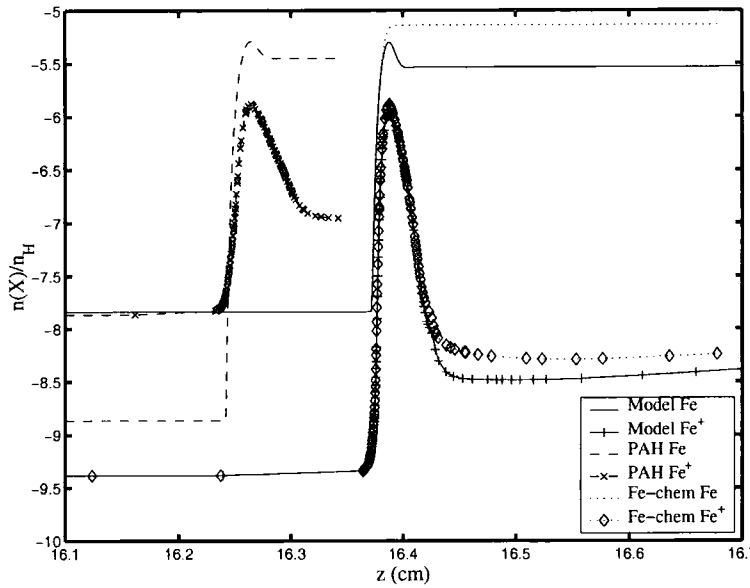

Figure F.2: Fe and Fe^+ profiles for the 54 km s^{-1} shock with initial $n_{\rm H}$ = 10^5 cm^{-3} and B=400 μG with no alterations (solid lines), PAH 'destruction' (dashed lines) and with the new Fe-chemistry removed (dotted lines).

Aperture Size and Observations

Le Bourlot et al. (2002) suggested that the observations of Rosenthal et al. (2000) include more than the outflow, as their calculation of the 34.8 μm [Si II] line intensity was some five orders of magnitude smaller than the observation. The fact that here the [Fe II] lines are also underestimated by, in some cases, several orders of magnitude supports this idea. The aperture sizes of the

ISO-SWS can be large: $14'' \times 20''$ for $\lambda < 12$ μm; $14'' \times 27''$ at 12 to 27.5 μm; $20'' \times 27''$ at 27.5 to 29 μm and $20'' \times 33''$ at 29 to 45.2 μm so the three [Fe II] lines are observed with three different sized apertures, with each longer wavelength line captured in a larger aperture. Rosenthal et al. (2000) centred their observations at the centre of the brightest hydrogen peak in the OMC-1 outflow (peak 1). However, near the outflow region is what (Schultz et al, 1999) have termed a 'wisp': a structure just northeast of the Becklin-Neugebauer object (BN) (Menten & Reid, 1995) that appears in Paα, [Fe II], Hα, [S II] and [N II]. The hydrogen recombination lines indicate that this is a photoexcitation region, probably due to the Trapezium just to the south of BN. All of the apertures that Rosenthal et al. (2000) use are large enough to detect emission from the wisp (see Figures. 1 in Rosenthal et al. (2000) and Schultz et al. (1999)) and, obviously, a larger aperture will detect a greater area of the wisp. This could explain why there is more Fe^+ observed than the shock model predicts and why the model gets progressively worse with increasing wavelength.

The contribution that may be expected from the wisp may be calculated. The wisp extends over approximately $20'' \times 2.5''$ (O'Dell et al., 1991). From Fig. 1 of Rosenthal et al. (2000) it can be seen that approximately 22.5 square arcsec of the wisp is in the larger aperture and approximately 17.5 square arcsec is in the smaller aperture. The larger aperture is $20'' \times 30''$ and is used to observe the 35.777 micron line and the smaller aperture is $20'' \times 27''$ and is used to observe the 17.936 and 25.988 micron lines. Schultz et al. (1999) observe a 50 square arcmin area in the 1.644 μm line of [Fe II] and find a flux of 0.6×10^{-5} Jy per square arcsec (upper limit). It is assumed that all of this flux is due to the wisp: this is an overestimate as there are other [Fe II] sources in the field. The [Fe II] flux contribution from the wisp is therefore $50 \times 50 \times 0.6 \times 10^{-5}$ Jy $= 1.5 \times 10^{-2}$ Jy, or 1.5×10^{-25} erg cm^{-2} s^{-1} Hz^{-1}. The frequency of the 1.644 μm line is 1.83×10^{14} Hz and the filters used by Schultz et al. (1999) are 1 % bandpass. Hence, the frequency range of the observations is 1.83×10^{12} Hz and the flux due to the wisp is 2.75×10^{-13} erg cm^{-2} s^{-1}. In order

to be able to compare this flux with the observations, the angular size of the source must be considered. The total extent of the wisp is 50 square arcsecond so each aperture receives a contribution of 2.34 $\times 10^{-4}$ erg cm^{-2} s^{-1} sr^{-1}. For comparison, the intensity of the 1.644 μm line predicted by the 54 km s^{-1} model 7.61 $\times$ 10^{-5} erg cm^{-2} s^{-1} sr^{-1}. The values calculated for the wisp here are upper limits but it seems likely that there is a strong contribution from the wisp to the the observations of Rosenthal et al. (2000).

The work on HH outflows presented in Chapter 5 showed that the [Fe II] emission in those objects also cannot be modelled by a C-type shock but required the higher degree of ionization found in J-type shocks. It is possible that such a situation could also be apply to Orion.

F.0.3 Conclusions for Orion

The best model that was found to reproduce the [Fe II] lines observed by Rosenthal et al. (2000) towards peak 1 in the Orion star forming region outflow is a 54 km s^{-1} C-type shock with initial density of $n_{\rm H}$=10^5 cm^{-3} and an initial magnetic induction of B=400 μG. However, this model produces [Fe II] line intensities that are a factor of two smaller than the 17.936 μm line intensity; an order of magnitude smaller than the 25.988 μm line intensity and two orders of magnitude smaller than the 35.777 μm line intensity. Several possible explanations for this discrepancy were considered and it was concluded that it is probable that the sizes of the apertures that Rosenthal et al. (2000) use are such that they detect emission from a photoexcitation emission region, known as the 'wisp', to the northeast of the outflow they were observing. However, it is also possible that the observed [Fe II] may originate in regions of higher ionization (possibly due to a J-type shock) than the H_2 emission.

Appendix G

The Sagittarius B2 Outflow

Sgr B2 is a massive ($\approx 7 \times 10^6$ $M_\odot$, approx 45 pc in diameter) and very active star forming region. It lies at a distance of 8.5 kpc from the sun and close, approximately 100 pc (Lis & Goldsmith, 1989), to the Galactic Centre. The Sgr B2 region contains three compact star forming cores with which H II regions and outflows are associated (Vogel et al., 1987). These cores are labelled M (Main or Middle), N (North), S (South) and SW (South West) and are roughly aligned in a N-S direction. These cores are surrounded by a dense ($n_{\rm H} \approx 10^5$ cm^{-3}) and warm ($\approx$ 100 K) envelope, which extends about 5 pc in the N-S direction and 2.5 pc in the E-W direction (Hüttemeister et al., 1993b). The dense envelope is itself surrounded by a hot (> 300 K) and tenuous ($\approx 10^3$ cm^{-3}) envelope, which is observed mostly in molecular absorption lines. From observations of metastable ammonia lines, Hüttemeister et al. (1995) suggested a component with an even higher temperature of approximately 600 K was also present. Possible heat sources for this hot and extended envelope include a high cosmic ray flux (Wilson et al., 1982) and C-type shocks (Flower et al., 1995).

In addition to heating the gas through which they pass, shocks also erode dust grains, thereby releasing species from their mantles (e.g., NH_3) and grains (e.g., Fe) into the gas (see Chapter 3). Once in the gas, Fe is rapidly ionized to Fe^+ but it may be able to form molecules, such as FeO, in the shock wave.

Previous work (Flower et al., 1995) has shown that the metastable levels of ammonia (Hüttemeister et al., 1993a, 1995) observed in absorption towards Sgr B2 are consistent with the predictions of a shock model. The recent (tentative) observation of FeO in absorption towards Sgr B2 made by Walmsley et al. (2002) presents an opportunity to test the hypothesis that FeO may also be produced in a shock wave.

Flower et al. (1995) constructed a shock model for this region which successfully reproduced the NH_3 observations (see below for further details). Similar models to that of Flower et al. (1995) were explored to compare with the new observations of FeO. Additional constraints on the models come from comparisons with the column densities derived from observations of other species. The Sgr B2 region is highly active and complex; different features are characterised by their rest velocity. The H II regions behind the layer of hot gas have a rest velocity between $60<V_{LSR}<70$ km s^{-1}. Therefore, following a suggestion by C. M. Walmsley (private communication), the modelling targetted observations towards one H II region, Sgr B2(M), between $60<V_{LSR}<70$ km s^{-1}. Finally, at the time that this work was carried out the code had not been adapted to model J-type shocks with magnetic precursors, therefore, only C-type shocks were considered.

G.0.4 Comparison with previous work

The modelling work presented here follows on from the work of Flower et al. (1995) (hereafter FPW) who showed that the metastable levels of NH_3 up to $(J, K)=(14, 14)$ observed in absorption towards Sgr B2 by Hüttemeister et al. (1993a) and Hüttemeister et al. (1995) could be modelled using a 25 km s^{-1} C-type shock with low initial density and small magnetic field, when sputtering and grain erosion were considered. The code they used, MHD_VODE, has evolved considerably since their work was published and, of direct relevance here, calculations of the distribution of Fe^+ level populations and an FeO-producing chemistry (G. P. des Forêts, private communication, see Appendix

F) have been added. It was also found that there was an error in the code used by FPW: the differential compression of the negatively charged grains had been omitted, which produced a wider and cooler shock than should be expected.

FPW found that it was possible to model the first fifteen metastable levels of ammonia observed towards Sgr B2 with a shock speed of 25 km s^{-1}, a pre-shock gas density of $n_{\rm H}$ of 500 cm^{-3} and a magnetic field of 5 μG. It was found that, due to the changes made to the code since 1995, using these conditions resulted in a sonic point in the flow; the shock remained continuous when an initial magnetic induction of 8 μG was adopted. The shock produced by this model is just over four times narrower than that of FPW, having a length of about a third of a parsec compared to 1.5 pc, and has a correspondingly higher peak neutral temperature, $T_{\rm n}$=1.38$\times$10^3 K compared to 611 K. These differences are entirely due to changes in the code since 1995 rather than increasing the magnetic field slightly, which would tend to decrease the temperature. The main effect is probably due to the inclusion of the differential compression of the negatively charged grains.

The populations in the metastable levels of ammonia were calculated in the same way as described in Flower et al. (1995). That is, the collisional excitation rates were extrapolated from the deexcitation rate coefficients of Danby et al. (1988), which were calculated for levels up to (J = 6, K = 6) and for a temperature of 300 K, assuming detailed balance. An excitation temperature, $T_{ex}(K, K)$ was estimated, taking the likely conditions in Sagittarius B2 into account, in order that the model results could be compared with observed quantity, $N(K, K)/T_{ex}(K, K)$. The column density of the levels populations were calculated at each step of the integration.

The initial composition of grain mantles used in this study were the same as that of FPW, rather than that tabulated in Chapter 3 and are listed in Table G.1. FPW assumed that the grain cores consisted only of C and O, with relative abundances of 1.63$\times$10^4 and 1.43$\times$10^4, while in the work presented

here it was assumed that Si, Mg and Fe were also bound in grain cores. The relative abundances of the species assumed to be in the grain cores for this study are, in some cases, different to those given in Chapter 3 and are listed in Table G.2. One further difference between the two studies is the fractional abundance of PAHs, $n(\mathrm{PAH})/N_{\mathrm{H}}$, which here was taken to be a factor of ten smaller than the 10^{-6} used by FPW (and in Chapter 5). Instead, in the model presented here, there is a correspondingly greater abundance of C and H in the gas phase.

Table G.1: Initial composition of grains mantles: Table 3 of Flower et al. (1995)

X	$n(\mathrm{X})/n_{\mathrm{H}}$
CH_4	1.207×10^{-6}
CO	1.207×10^{-6}
CO_2	1.207×10^{-6}
H_2O	1.137×10^{-5}
O_2	1.137×10^{-5}
NH_3	1.867×10^{-6}
N_2	1.867×10^{-6}
H_2S	1.850×10^{-6}

Table G.2: Initial composition of grains cores

X	$n(\mathrm{X})/n_{\mathrm{H}}$
C	2.12×10^{-4}
O	1.43×10^{-4}
Si	3.58×10^{-5}
Mg	3.85×10^{-5}
Fe	3.23×10^{-5}

G.0.5 Comparison with predictions of shock models

It was expected that any changes to the model for the NH_3 emission would be small; nonetheless, a range of shock speeds, from 25 to 60 km s^{-1} were

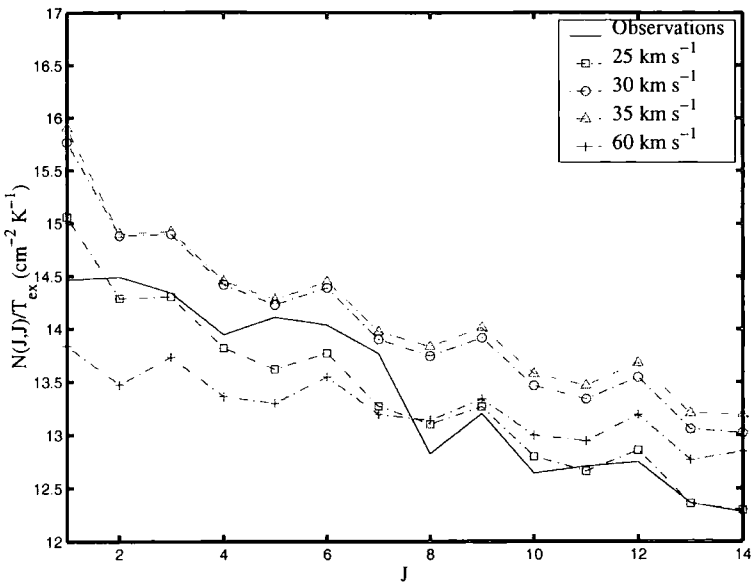

Figure G.1: Ratio of column density to excitation temperature against rotational quantum number for shock speeds of 25 (squares), 30 (circles), 35 (triangles) and 60 (crosses) km s^{-1}. The observations are marked by a solid line: for clarity the observed points have been left unmarked in this and subsequent figures. Shock speeds in the vicinity of 25 km s^{-1} fit the observations best.

considered. In Fig. G.1 the calculated column density divided by excitation temperature are plotted against rotational angular momentum quantum number of the level for models with shock speeds of 25 (squares), 30 (circles), 35 (triangles) and 60 (crosses) km s^{-1}; a solid line marks the observed quantities, from Hüttemeister et al. (1993b) and (Hüttemeister et al., 1995). It is clear from Fig. G.1 that, as expected, a model with $v_s \approx 25$ km s^{-1} provides the best fit to the observations. The models with shock velocities of 30 and 35 km s^{-1} overestimate the column densities over the whole range of the observations. The 60 km s^{-1} model underestimates the lower levels but over estimates the higher ones because the higher temperatures attained in faster shock waves tend to shift the population to the higher levels. Similar discrepancies were found for shocks with velocities between 35 and 60 km s^{-1} and, in order to keep the plot uncluttered, are not shown in Figure G.1.

Once it was established that a shock speed in the region of 25 km s^{-1} models

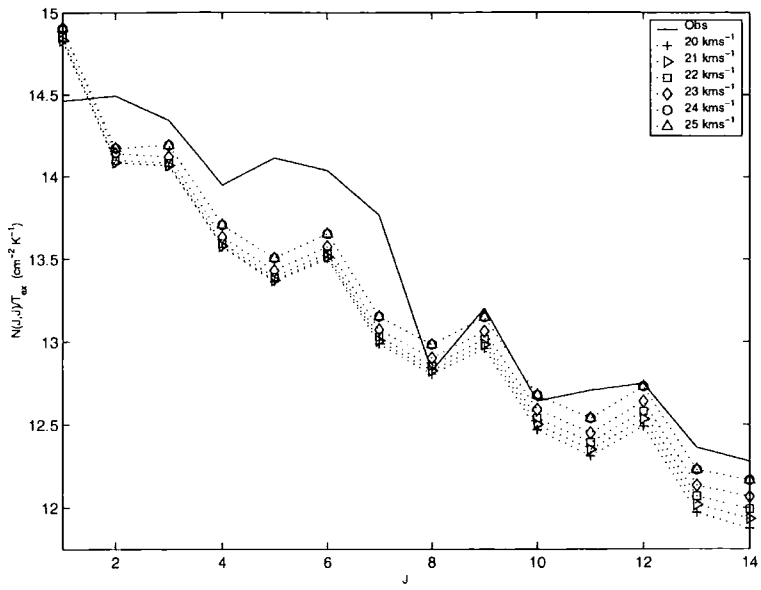

Figure G.2: Ratio of column density to excitation temperature against rotational quantum number for shock speeds of 20-25 km s^{-1}.

the metastable levels of ammonia reasonably well, models with shock velocities around this value were investigated in order to pinpoint the best shock speed. In Figures G.2 and G.3 the column density divided by excitation temperature against J for models with v_s=20-25 and 24-28 km s^{-1}, respectively, are plotted: once again the observations are indicated by a solid line. Models with shock velocities below 24 km s^{-1} generally underestimate the observed column densities. In Figure G.3 it can be seen that models with shock velocities of 27 and 28 km s^{-1} almost always overestimate the column densities. The models do not follow the form of the observations, which have less population in the higher J levels with respect to the models. However, of the remaining three models (v_s= 24 (crosses), 25 (right-facing triangles) and 26 (squares) km s^{-1}) the 25 km s^{-1} model provides the best fit over the range of the observations.

Column densities of several species (listed in Table G.3), in addition to the FeO column density, were collected from the literature in order to compare with the column densities predicted by such a 25 km s^{-1} shock model. It can be seen that the column densities of H, H_2, O and S-bearing species, with the

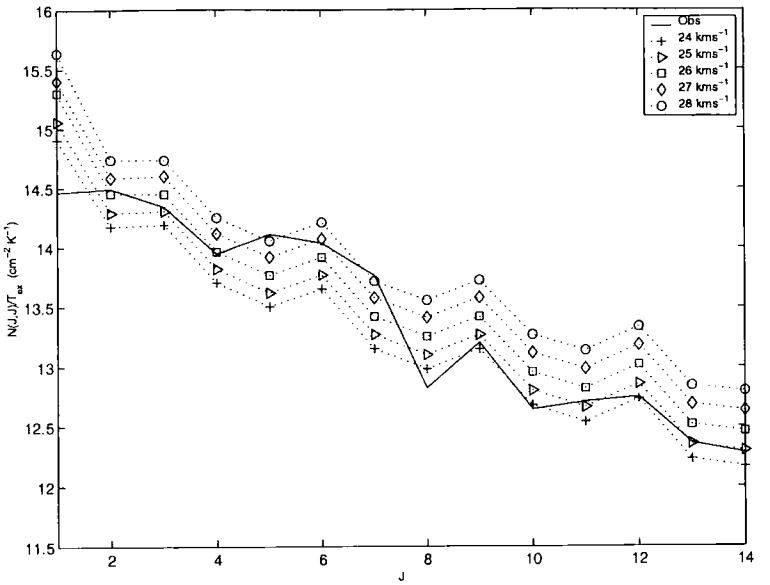

Figure G.3: Ratio of column density to excitation temperature against rotational quantum number for shock speeds of 24-28 km s^{-1}

exception of CS, are underestimated by several orders of magnitude. However, the shock-related species that are of more relevance to this study, namely FeO, OH, NH_3, SiO and H_3O^+, are reasonably well reproduced. These findings shall be discussed in the next Section.

Table G.3: Comparison of observed column densities with those from a 25 km s^{-1} model.

Species	Model	Observation (cm^{-2})	V_{LSR}	Reference
FeO	4.5×10^{12}	$\approx10^{12}$	62	Walmsley et al. (2002)
FeO/SiO	2×10^{-2}	2×10^{-3}	62	Walmsley et al. (2002)
FeO/H_2	1.4×10^{-9}	3×10^{-11}	62	Walmsley et al. (2002)
H	5.9×10^{18}	7.7×10^{20} - 1.2×10^{22}	-100 - 40	Lis et al. (2001)
H_2	3.3×10^{21}	10^{22}-10^{25}	-100 - 40	e.g Hüttemeister et al. (1993b)
O	1.9×10^{16}	2.5×10^{18}–9.6×10^{18}	-78–30	Lis et al. (2001)
OH	1.9×10^{17}	$> 3.6\times10^{15}$	62	Storey et al. (1981)
		1.2×10^{17}	$\approx$60	Bieging (1976)
H_3O^+	8.8×10^{13}	(para) 9×10^{13}	60	Goicoechea &
		(ortho) 7.2×10^{13}	60	Cernicharo (2001)
NH_3	1.6×10^{16}	9×10^{17}	50	Vogel et al. (1987)
		3×10^{16}	65	Ceccarelli et al. (2002)
NO	2.5×10^{16}	9.33×10^{15}	60–64	Halfen et al. (2001)
CS	4.3×10^{14}	(Red) 6.6×10^{14}	50–80	Mehringer (1995)
		(Blue) 7.3×10^{14}	50-80	Mehringer (1995)
SO	9.7×10^{14}	6.2×10^{17}	55–60	Nummelin et al. (2000)
		8.9×10^{15}–1.7×10^{16}	50–65	Goldsmith et al. (1987)
SO_2	2.0×10^{16}	5.0×10^{18}	55–60	Nummelin et al. (2000)
OCS	2.2×10^{12}	5.1×10^{15}	62	Nummelin et al. (2000)
OCS	2.2×10^{12}	5.8×10^{15}–8.7×10^{15}	50–65	Goldsmith et al. (1987)
HCS^+	4.4×10^{11}	6.9×10^{13}	62	Nummelin et al. (2000)
SO^+	4.6×10^{12}	1.9×10^{14}	62	Nummelin et al. (2000)
SiO	2.6×10^{14}	9.6×10^{13}	65	Nummelin et al. (2000)
		(Red) 5.0×10^{14}	45–85	Liu et al. (1998)
		(Blue) 6.0×10^{15}	45–85	Liu et al. (1998)
		$>5\times10^{14}$	45–88	Peng et al. (1995)

G.0.6 Discussion

NH_3

FPW found that levels above (J, K)=(6, 6) were underpopulated and they suggested that the temperature of the gas may have been underestimated by their model. The version of the code used for this work produced a narrower shock with a higher peak temperature and, indeed, the model fits the observations quite well above (J, K)=(8, 8). However, below these levels the column density to excitation temperature ratios of the 25 km s^{-1} shock are smaller than the observed quantities (see Figures G.1-G.3).

Other species

The column densities calculated for H, H_2 and O are due only to the shock: the probability that these species are present along the line of sight outside of the shocked gas is not taken into account, and this is a likely reason for the difference between calculation and observation. The disparity between the observations and calculations for the S-bearing species is suspected to be in some way due to the chemistry used.

The ability of the model to accurately predict the FeO column density was of particular interest because it was the first ever observation of this species towards Sgr B2 (Walmsley et al., 2002) that prompted this investigation. WBFS concluded that their results were compatible with a FeO column density of order 10^{12} cm^{-2} and the column density found for FeO of 4.5 $\times$ 10^{12} cm^{-2} is in reasonable agreement with this value. WBFS estimate a value of 0.002 for [FeO]/[SiO], based on their FeO column density and the SiO observation of Peng et al. (1995). The value for this ratio predicted by the model, 0.02, differs by an order of magnitude. However, this is due to a combination of factors of two and five difference in the values computed by the model for the column densities of SiO and FeO, respectively, rather than order of magnitude

differences in one or the other species, which might indicate a problem with the model. It more difficult to say anything substantial about the [FeO]/[H_2] ratio as the column density of H_2 is very poorly known. The value found for [FeO]/[H_2] of 1.4×10^{-9} is much larger than WBFS's estimate of 3×10^{-11} but that is due to the fact that the model underestimate the column density of H_2.

It can be seen in Table G.3 that observations have provided quite different column densities for some species: NH_3 has been observed to have a column density of 9×10^{17} cm^{-2} (Vogel et al., 1987) and 3×10^{16} cm^{-2} (Ceccarelli et al., 2002); observations of the SiO column density range from 9.6×10^{13} (Nummelin et al., 2000) to 6×10^{15} cm^{-2} (Liu et al., 1998) and the two OH column densities (Storey et al., 1981; Bieging, 1976) differ by two orders of magnitude. In the cases of NH_3 and SiO it is worth noting that the calculated column densities best match observations that were made in velocity ranges closest to the 60–70 km s^{-1} range that was targetted. For ammonia, the 9×10^{17} cm^{-2} observation (Vogel et al., 1987) was found to be at peak absorption at 50 km s^{-1} whereas the 3×10^{16} cm^{-2} observation (Ceccarelli et al., 2002), which the predicted column density of 1.6×10^{16} cm^{-2} is in good agreement with, was at peak absorption at 65 km s^{-1}. In the case of SiO, the observations of Liu et al. (1998) and Peng et al. (1995) both peak at $V_{LSR} \approx 65$ km s^{-1} while the observation of Nummelin et al. (2000) peaks at $V_{LSR} \approx 115$ km s^{-1}. The computed column density of SiO is slightly nearer to the values found by Peng et al. (1995) and by Liu et al. (1998) in the red lobe. The computed column density of CS is also in better agreement with the column density found towards the red lobe than the blue (Mehringer, 1995). When considering the OH observations, it should be noted that the column density of Storey et al. (1981) is a lower limit as they assume an optically thin case. Storey et al. (1981) consider the difference between their result and that of Bieging (1976), with which the predicted column density is in good agreement, to indicate that there is a large FIR optical depth.

G.0.7 Conclusions for Sgr B2

Sgr B2(M) can be simply modelled with a 1D, planar, 25 km s^{-1} C-type shock with an initial density of 500 cm^{-3} and magnetic field of 8 μG. With such a model the observations in the 60< V_{LSR} <70 km s^{-1} range of column densities of the shock-related species OH, NH_3, SiO, FeO and H_3O^+ can be matched to within a factor of two. This model also reproduces tolerably well the metastable levels of ammonia up to (J, K)=(14, 14) with the levels above (J, K)=(8, 8) giving the best fit.

Bibliography

Abgrall, H. & Roueff, E. 1989, A&ASS, 79, 313

Allen, C. W. 1983, Astrophysical Quantities (3rd ed; London: Athlone)

Anders, E. & Grevesse, N. 1989, Geochim. Cosmochim. Acta, 53, 197

Andre, P., Ward-Thompson, D., & Barsony, M. 2000, Protostars and Planets IV, 59

Anthony-Twarog, B. J. 1982, AJ, 87, 1213

Böhm, K. & Matt, S. 2001, PASP, 113, 158

Bacciotti, F. & Eislöffel, J. 1999, A&A, 342, 717

Bachiller, R. 1996, ARA&A, 34, 111

Bachiller, R., Tafalla, M., & Cernicharo, J. 1994, ApJL, 425, L93

Bally, J. & Devine, D. 1994, ApJL, 428, L65

Bally, J., Heathcote, S., Reipurth, B., Morse, J., Hartigan, P., & Schwartz, R. 2002, AJ, 123, 2627

Bally, J. & Lada, C. J. 1983, ApJ, 265, 824

Beck-Winchatz, B., Böhm, K., & Noriega-Crespo, A. 1996, AJ, 111, 346

Beck-Winchatz, B., Böhm, K. H., & Noriega-Crespo, A. 1994, PASP, 106, 1271

Benedettini, M., Giannini, T., Nisini, B., Tommasi, E., Lorenzetti, D., Di Giorgio, A. M., Saraceno, P., Smith, H. A., & White, G. J. 2000, A&A, 359, 148

Bieging, J. H. 1976, A&A, 51, 289

Black, J. H. & van Dishoeck, E. F. 1987, ApJ, 322, 412

Bohigas, J., Persi, P., & Tapia, M. 1993, A&A, 267, 168

Bontemps, S., Andre, P., & Ward-Thompson, D. 1995, A&A, 297, 98

Bourke, T. L. 2001, ApJL, 554, L91

Bourke, T. L., Garay, G., Lehtinen, K. K., Koehnenkamp, I., Launhardt, R., Nyman, L., May, J., Robinson, G., & Hyland, A. R. 1997, ApJ, 476, 781

Bourke, T. L., Hyland, A. R., & Robinson, G. 1995, MNRAS, 276, 1052

Brandt, J. C., Stecher, T. P., Crawford, D. L., & Maran, S. P. 1971, ApJL, 163, L99+

Brown, P. N., Byrne, G. D., & Hindmarsh, A. C. 1989, SIAM J. Sci. Stat. Comp, 10, 1038

Buehrke, T., Mundt, R., & Ray, T. P. 1988, A&A, 200, 99

Cabrit, S. & Raga, A. 2000, A&A, 354, 667

Campbell, B., Persson, S. E., Strom, S. E., & Grasdalen, G. L. 1988, AJ, 95, 1173

Canto, J., Raga, A. C., & Binette, L. 1989, Revista Mexicana de Astronomia y Astrofisica, 17, 65

Cardelli, J. A., Clayton, G. C., & Mathis, J. S. 1989, ApJ, 345, 245

Carr, J. S. 1993, ApJ, 406, 553

Ceccarelli, C., Baluteau, J.-P., Walmsley, M., Swinyard, B. M., Caux, E., Sidher, S. D., P., C., Gry, C., M., K., & Prusti, T. 2002, A&A, 383, 603

Cernicharo, J. & Reipurth, B. 1996, ApJL, 460, L57+

Chernin, L. M. & Masson, C. R. 1995, ApJ, 443, 181

Chiéze, J. P., Pineau des Forêts, G., & Flower, D. R. 1998, MNRAS, 295, 672

Chini, R., Krugel, E., Haslam, C. G. T., Kreysa, E., Lemke, R., Reipurth, B., Sievers, A., & Ward-Thompson, D. 1993, A&A, 272, L5+

Cohen, M., Harvey, P. M., & Schwartz, R. D. 1985, ApJ, 296, 633

Cohen, N. & Westberg, K. R. 1983, Journal of Physical and Chemical Reference Data, 12, 531

Corliss, C. & Sugar, J. 1982, Journal of Physical and Chemical Reference Data, 11, 135

Corporon, P. & Reipurth, B. 1997, in IAU Symp. 182: Herbig-Haro Flows and the Birth of Stars, 85P–+

Danby, G., Flower, D. R., Valiron, P., Schilke, P., & Walmsley, C. M. 1988, MNRAS, 235, 229

Davis, C. J. & Eisloeffel, J. 1995, A&A, 300, 851

Davis, C. J., Mundt, R., & Eisloeffel, J. 1994, ApJL, 437, L55

Davis, C. J., Mundt, R., Eisloffel, J., & Ray, T. P. 1995, AJ, 110, 766

Davis, C. J., Ray, T. P., Eisloeffel, J., & Corcoran, D. 1997, A&A, 324, 263

Davis, C. J., Smith, M. D., Eislöffel, J., & Davies, J. K. 1999, MNRAS, 308, 539

de Gouveia dal Pino, E. & Opher, R. 1990, Revista Mexicana de Astronomia y Astrofisica, vol. 21, 21, 477

des Forêts, G. P., Flower, D. R., & Dalgarno, A. 1988, MNRAS, 235, 621

Dove, J. E. & Mandy, M. E. 1986, ApJL, 311, L93

Draine, B. T. 1978, ApJS, 36, 595

—. 1980, ApJ, 241, 1021

Draine, B. T., Roberge, W. G., & Dalgarno, A. 1983, ApJ, 264, 485

Elias, J. H. 1980, ApJ, 241, 728

Falle, S. A. E. G., Innes, D. E., & Wilson, M. J. 1987, MNRAS, 225, 741

Fernandes, A. J. L. & Brand, P. W. J. L. 1995, MNRAS, 274, 639

Field, G. B., Rather, J. D. G., Aannestad, P. A., & Orszag, S. A. 1968, ApJ, 151, 953

Flower, D. R. 1989, Journal of Physics B Atomic Molecular Physics, 22, 2319

Flower, D. R., Le Bourlot, J., Pineau des Forêts, G. P., & Cabrit, S. 2003, MNRAS, 341, 70

Flower, D. R. & Pineau des Forêts, G. 1995, MNRAS, 275, 1049

—. 2003, MNRAS, 343, 390

Flower, D. R., Pineau des Forets, G., Field, D., & May, P. W. 1996, MNRAS, 280, 447

Flower, D. R., Pineau des Forêts, G., & Hartquist, T. 1985, MNRAS, 216, 775

Flower, D. R., Pineau-Des-Forets, G., & Hartquist, T. W. 1986, MNRAS, 218, 729

Flower, D. R., Pineau des Forêts, G., & Walmsley, C. M. 1995, A&A, 294, 815

Flower, D. R. & Pineau des Forêts, G. P. 1999, MNRAS, 308, 271

Garay, G., Köhnenkamp, I., Bourke, T. L., Rodríguez, L. F., & Lehtinen, K. K. 1998, ApJ, 509, 768

Genzel, R. & Stutzki, J. 1989, ARA&A, 27, 41

Giannini, T., M^{c}Coey, C., Caratti o Garatti, A., Nisini, B., Lorenzetti, D., & Flower, D. R. 2004, A&A, 419, 999

Gibb, A. G. & Heaton, B. D. 1993, A&A, 276, 511

Gibb, A. G. & Little, L. T. 1998, MNRAS, 295, 299

Gibb, E. L., Whittet, D. C. B., Schutte, W. A., Boogert, A. C. A., Chiar, J. E., Ehrenfreund, P., Gerakines, P. A., Keane, J. V., Tielens, A. G. G. M., van Dishoeck, E. F., & Kerkhof, O. 2000, ApJ, 536, 347

Goldsmith, P. F., Snell, R. L., Hasegawa, T., & Ukita, N. 1987, ApJ, 314, 525

Gredel, R. 1994, A&A, 292, 580

—. 1996, A&A, 305, 582

Gredel, R. & Reipurth, B. 1993, ApJL, 407, L29

—. 1994, A&A, 289, L19

Gueth, F., Guilloteau, S., Dutrey, A., & Bachiller, R. 1997, A&A, 323, 943

Halfen, D. T., Apponi, A. J., & Ziurys, L. M. 2001, ApJ, 561, 244

Haro, G. 1952, ApJ, 115, 572

Harris, A. W., Gry, C., & Bromage, G. E. 1984, ApJ, 284, 157

Hartigan, P., Curiel, S., & Raymond, J. 1989, ApJL, 347, L31

Hartigan, P., Edwards, S., & Ghandour, L. 1995, ApJ, 452, 736

Hartigan, P. & Graham, J. A. 1987, AJ, 93, 913

Hartigan, P., Raymond, J., & Hartmann, L. 1987, ApJ, 316, 323

Hartmann, L. & Raymond, J. C. 1984, ApJ, 276, 560

Heck, L., Flower, D. R., & Pineau Des Forêts, G. 1990, Computer Physics Communications, 58, 169

Herbig, G. H. 1951, ApJ, 113, 697

Hester, J. J., Gilmozzi, R., O'dell, C. R., Faber, S. M., Campbell, B., Code, A., Currie, D. G., Danielson, G. E., Ewald, S. P., Groth, E. J., Holtzman, J. A., Kelsall, T., Lauer, T. R., Light, R. M., Lynds, R., O'Neil, E. J., Shaya, E. J., & Westphal, J. A. 1991, ApJL, 369, L75

Hilton, J. & Lahulla, J. F. 1995, A&ASS, 113, 325

Hodapp, K. & Ladd, E. F. 1995, ApJ, 453, 715

Hollenbach, D. & McKee, C. F. 1989, ApJ, 342, 306

Hüttemeister, S., Wilson, T. L., Bania, T. M., & Martin-Pintado, J. 1993a, A&A, 280, 255

Hüttemeister, S., Wilson, T. L., Henkel, C., & Mauersberger, R. 1993b, A&A, 276, 445

Hüttemeister, S., Wilson, T. L., Lemme, C., Dahmen, G., & Henkel, C. 1995, A&A, 294, 667

Jones, A. P., Tielens, A. G. G. M., & Hollenbach, D. J. 1996, ApJ, 469, 740

Jones, A. P., Tielens, A. G. G. M., Hollenbach, D. J., & McKee, C. F. 1994, ApJ, 433, 797

Kaufman, M. J. & Neufeld, D. A. 1996a, ApJ, 456, 611

—. 1996b, ApJ, 456, 250

Kingdon, J. B. & Ferland, G. J. 1996, ApJS, 106, 205

Kwan, J. 1977, ApJ, 216, 713

Larson, R. B. 2003, Reports on Progress in Physics, 66, 1651

Launay, J. M. & Roueff, E. 1977, A&A, 56, 289

Le Bourlot, J., Pineau des Forêts, G., & Flower, D. R. 1999, MNRAS, 305, 802

Le Bourlot, J., Pineau des Forêts, G., Flower, D. R., & Cabrit, S. 2002, MNRAS, 32, 985

Lemaire, J.-L., Field, D., Pineau Des Forets, G., & Callejo, G. 2002, in SF2A-2002: Semaine de l'Astrophysique Francaise, 31–+

Lis, D. C. & Goldsmith, P. F. 1989, ApJ, 337, 704

Lis, D. C., Keene, J., Philips, T. G., Schilke, P., Werner, M. W., & Zmuidzinas, J. 2001, ApJ, 561, 823

Liu, S. H., Mehringer, D. M., Miao, Y., & Snyder, L. E. 1998, ApJ, 501, 680

Mandy, M. E. & Martin, P. G. 1993, ApJS, 86, 199

Marraco, H. G. & Rydgren, A. E. 1981, AJ, 86, 62

Martin, P. G. & Mandy, M. E. 1995, ApJL, 455, L89+

Mathis, J. S., Rumpl, W., & Nordsieck, K. H. 1977, ApJ, 217, 425

May, P. W., Forêts, G. P., Flower, D. R., Field, D., Allan, N. L., & Purton, J. A. 2000, MNRAS, 318, 809

M^{c}Coey, C., Giannini, T., Flower, D. R., & Caratti o Garatti, A. 2004, MNRAS, in press, astro-ph/0406262

Mehringer, D. M. 1995, ApJ, 454, 782

Mendoza, C. 1983, in IAU Symp. 103: Planetary Nebulae, 143–172

Menten, K. M. & Reid, M. J. 1995, ApJL, 445, L157

Micono, M., Massaglia, S., Bodo, G., Rossi, P., & Ferrari, A. 1998, A&A, 333, 1001

Morse, J. A., Heathcote, S., Cecil, G., Hartigan, P., & Raymond, J. C. 1993, ApJ, 410, 764

Mullan, D. J. 1971, MNRAS, 153, 145

Nahar, S. N. 1995, A&A, 293, 967

Neckel, T. & Staude, H. J. 1987, ApJL, 322, L27

Neufeld, D. A. & Kaufman, M. J. 1993, ApJ, 418, 263

Nisini, B., Caratti o Garatti, A., Giannini, T., & Lorenzetti, D. 2002, A&A, 393, 1035

Noriega-Crespo, A., Cotera, A., Young, E., & Chen, H. 2002, ApJ, 580, 959

Nummelin, A., Bergman, P., Hjalmarson, Å., Friberg, P., Irvine, W. M., Millar, T. J., Ohishi, M., & Saito, S. 2000, ApJS, 128, 213

Nussbaumer, H. & Rusca, C. 1979, A&A, 72, 129

Nussbaumer, H. & Storey, P. J. 1988, A&A, 193, 327

O'Dell, C. R., Wen, Z., & Hester, J. J. 1991, PASP, 103, 824

Osterbrock, D. E. 1961, ApJ, 134, 347

Peng, Y., Vogel, S. N., & Carlstrom, J. E. 1995, ApJ, 455, 223

Pequignot, D. & Aldrovandi, S. M. V. 1976, A&A, 50, 141

Pettersson, B. 1984, A&A, 139, 135

Pikel'Ner, S. B. 1967, in IAU Symposium, ed. H. Van Woerden, Vol. 31, 129

Pineau des Forêts, G., Flower, D. R., Aguillon, F., Sidis, V., & Sizun, M. 2001, MNRAS, 323, L7

Pineau des Forêts, G., Flower, D. R., & Chiéze, J.-P. 1997, in IAU Symposium, ed. B. Reipurth & C. Bertout, Vol. 182, 199

Quinet, P., Le Dourneuf, M., & Zeippen, C. J. 1996, A&ASS, 120, 361

Raga, A. C., Binette, L., Canto, J., & Calvet, N. 1990, ApJ, 364, 601

Raga, A. C., Riera, A., Masciadri, E., Beck, T., Böhm, K. H., & Binette, L. 2004, AJ, 127, 1081

Reipurth, B. 1989, Nature, 340, 42

Reipurth, B. & Bally, J. 2001, ARA&A, 39, 403

Reipurth, B. & Cernicharo, J. 1995, in Revista Mexicana de Astronomia y Astrofisica Conference Series, 43–+

Reipurth, B., Chini, R., Krugel, E., Kreysa, E., & Sievers, A. 1993, A&A, 273, 221

Reipurth, B. & Graham, J. A. 1988, A&A, 202, 219

Reipurth, B., Hartigan, P., Heathcote, S., Morse, J. A., & Bally, J. 1997, AJ, 114, 757

Reynolds, R. J. 1976, ApJ, 206, 679

Richmyer, R. D. & Morton, K. W. 1957, Difference Methods for Initial-value Problems (Interscience Publishers)

Rieke, G. H. & Lebofsky, M. J. 1985, ApJ, 288, 618

Rosenthal, D., Bertoldi, F., & Drapatz, S. 2000, A&A, 356, 705

Roueff, E. & Le Bourlot, J. 1990, A&A, 236, 515

Savage, B. D. & Sembach, K. R. 1996, ARA&A, 34, 279

Schroder, K., Staemmler, V., Smith, M. D., Flower, D. R., & Jaquet, R. 1991, Journal of Physics B Atomic Molecular Physics, 24, 2487

Schultz, A. S. B., Colgan, S. W. J., Erickson, E. F., Kaufman, M. J., Hollenbach, D. J., O'Dell, C. R., Young, E. T., & Chen, H. 1999, ApJ, 511, 282

Schwartz, P. R., Gee, G., & Huang, Y.-L. 1988, ApJ, 327, 350

Schwartz, R. D. 1978, ApJ, 223, 884

Schwartz, R. D., Cohen, M., & Williams, P. M. 1987, ApJ, 322, 403

Seaton, M. J. 1968, Advances in Atomic and Molecular Physics (Volume 4: Academic Press Inc. New York)

—. 1979, MNRAS, 187, 73P

Seidensticker, K. J. & Schmidt-Kaler, T. 1989, A&A, 225, 192

Smith, M. D. 1994, MNRAS, 266, 238

Smith, M. D. & Brand, P. W. J. L. 1990, MNRAS, 243, 498

Smith, M. D., Brand, P. W. J. L., & Moorhouse, A. 1991, MNRAS, 248, 451

Smith, M. D., Khanzadyan, T., & Davis, C. J. 2003, MNRAS, 339, 524

Smith, M. D. & Mac Low, M.-M. 1997, A&A, 326, 801

Snell, R. L., Loren, R. B., & Plambeck, R. L. 1980, ApJL, 239, L17

Sofia, U. J. & Meyer, D. M. 2001, Bulletin of the American Astronomical Society, 33, 1438

Spitzer, L. 1962, Physics of Fully Ionized Gases (Physics of Fully Ionized Gases, 2nd ed. Publisher: New York: Interscience; Springer, 2000. Editedy by Arthur N. Cox. ISBN: 0387987460)

Spitzer, L. J. & Scott, E. H. 1969, ApJ, 158, 161

Staemmler, V. & Flower, D. R. 1991, Journal of Physics B Atomic Molecular Physics, 24, 2343

Stone, J. M. & Hardee, P. E. 2000, ApJ, 540, 192

Storey, J. W. V., Watson, D. M., & Townes, C. H. 1981, ApJL, 244, 27

Umemoto, T., Iwata, T., Fukui, Y., Mikami, H., Yamamoto, S., Kameya, O., & Hirano, N. 1992, ApJL, 392, L83

Vogel, S. N., Genzel, R., & Palmer, P. 1987, ApJ, 316, 243

Walmsley, C. M., Bachiller, R., Pineau des Forêts, G., & Schilke, P. 2002, ApJL, 556, 109

Weaver, R., McCray, R., Castor, J., Shapiro, P., & Moore, R. 1977, ApJ, 218, 377

Wilgenbus, D., Cabrit, S., Pineau des Forêts, G., & Flower, D. R. 2000, A&A, 356, 1010

Wilking, B. A., McCaughrean, M. J., Burton, M. G., Giblin, T., Rayner, J. T., & Zinnecker, H. 1997, AJ, 114, 2029

Wilson, T. L., Ruf, K., Walmsley, C. M., Martin, R. N., Batrla, W., & Pauls, T. A. 1982, A&A, 115, 185

Zhang, H. L. & Pradhan, A. K. 1995, A&A, 293, 953